Title
Biogeochemical and Physical Controls Governing Nitrogen Loss within Oxygen Minimum Zones

Author
McCoy, Daniel Edward

Publication Date
2023

Peer reviewed|Thesis/dissertation

UNIVERSITY OF CALIFORNIA

Los Angeles

Biogeochemical and Physical Controls Governing Nitrogen Loss within Oxygen Minimum Zones

A dissertation submitted in partial satisfaction
of the requirements for the degree
Doctor of Philosophy in Atmospheric and Oceanic Sciences

by

Daniel Edward McCoy

2023

ABSTRACT OF THE DISSERTATION

Biogeochemical and Physical Controls
Governing Nitrogen Loss within Oxygen Minimum Zones

by

Daniel Edward McCoy
Doctor of Philosophy in Atmospheric and Oceanic Sciences
University of California, Los Angeles, 2023
Professor Daniele Bianchi, Chair

In contrast to other biogeochemical tracers, nitrogen in the ocean exists in a myriad of chemical forms, each with its own distinct properties and reactivity. These diverse chemical forms of nitrogen, including organic and inorganic compounds, are collectively involved in a unique and dynamic microbially-mediated cycle which is tightly intertwined with the overall functioning of marine ecosystems and has significant implications for the global cycles of carbon, phosphorous, and oxygen. While nitrogen is predominantly cycled between bioavailable forms in the ocean, additional anaerobic metabolic pathways emerge when the concentration of dissolved oxygen drops to suboxic or anoxic levels within the ocean's oxygen-minimum-zones (OMZs). These pathways produce gaseous dinitrogen (N_2) and nitrous oxide (N_2O), a potent greenhouse agent and contributor to ozone depletion, which together lead to a loss of bioavailable nitrogen from the oceans to the atmosphere. This dissertation provides a comprehensive analysis of these microbial pathways in OMZs, and further explores their sensitivity to both physical and biogeochemical variability.

In Chapter 2, we describe the development of a general algorithm used to expand the observational record of a special class of subsurface, predominantly anticyclonic oceanic eddies known as submesoscale coherent vortices (SCVs). These eddies have been shown to

play an oversized role in propagating water masses in the intermediate and deeper parts of the ocean, and were recently identified as hot-spots of N_2 and N_2O production. By applying the algorithm to the global Argo float array, we detect nearly 4000 new global observations of these eddies. Furthermore, we demonstrate that their formation takes place in regional hot-spots, allowing us to quantify their contributions to local heat and salt anomalies due to their formation and propagation.

In Chapter 3, we incorporate a new model of the oceanic nitrogen cycle into an eddy-resolving 3D regional ocean model of the Eastern Tropical South Pacific, an upwelling region and hot-spot of nitrogen loss and N_2O outgassing. The model accurately simulates both aerobic and anaerobic transformations responsible for N_2 and N_2O production, and provides a realistic representation of the large scale physical circulation. By decomposing the N_2O tracer in the 3D model, we are able to attribute contributions from local biogeochemical sources and sinks, explore the role of the physical circulation in supplying N_2O to the region, and ultimately quantify the drivers of N_2O outgassing to the atmosphere.

Finally, Chapter 4 builds upon the findings of Chapter 3. Specifically, we deploy a higher resolution version of the 3D model to explore how mesoscale-driven heterogeneity governs the production of N_2 and N_2O in the Eastern Tropical South Pacific. By filtering biogeochemical tracer fields into "mean" and "eddy" components (e.g., fields governed by low/high frequency and large/small spatial scales, respectively), we demonstrate that oxygen variability induced by ephemeral eddies and filaments stimulates nitrogen loss to the atmosphere, but by preferential producing N_2 at the expense of N_2O consumption. These findings reveal that the mesoscale circulation plays a critical role in regulating N_2O production, and further implies that coarse-grained biogeochemical models may overestimate the fluxes to the atmosphere from these regions.

The dissertation of Daniel Edward McCoy is approved.

James W. Moffett

James C. McWilliams

Andrew L. Stewart

Daniele Bianchi, Committee Chair

University of California, Los Angeles

2023

TABLE OF CONTENTS

LIST OF FIGURES

LIST OF TABLES

ACKNOWLEDGMENTS

This dissertation's research has been made possible by a strong collaboration with my thesis advisor, Daniele Bianchi. I am deeply appreciative of his mentorship and invaluable guidance throughout this entire graduate program. I would also like to extend my gratitude to all my coauthors and mentors who have consistently challenged me to improve my approach to scientific research. Chapters 3 and 4 particularly benefitted from insights provided by Pierre Damien, Simon Yang, and Daniel Clements. Andrew Stewart also played a key role in designing the methodology and analyses presented in Chapter 2.

In the midst of this academic journey, I cannot overlook the non-scientific support that has been crucial to my success. First and foremost, I owe an immeasurable debt of gratitude to my best friend and wife, Alexandra Bailey, for her unwavering patience, support, and constant encouragement. I would also like to express my appreciation to the diverse group of friends and colleagues who helped me maintain my sanity through this stressful journey, as well as my family for their enduring patience and unwavering belief in me. Lastly, to my loyal companion, Honey, whose presence and unconditional love continues to provide immeasurable joy to my everyday life.

Chapter 2 is reproduced from McCoy et al. (2020) (available in Progress in Oceanography), Chapter 3 is reproduced from McCoy et al. (2023) (accepted in Global Biogeochemical Cycles), and Chapter 4 is being prepared for submission to Geophysical Research Letters. Material from the Chapters 2 and 3 are reproduced with permission from the publishers. Chapter 2 is based upon work supported by the U.S. National Science Foundation under grants OCE-1635632, OCE-1847687, and OCE-1751386. It was made possible through the International Argo Program and the national programs that contribute to it. I would also like to thank Victor Ciaramitaro and James Huntley for initial analysis of SCVs in Argo data. Chapters 3 and 4 are based upon work supported by the U.S. National Science Foundation under grant OCE-1847687. I'd like to acknowledge the computational support by the Extreme Science and Engineering Discovery Environment (XSEDE) through allocation TG-OCE17001.

VITA

2007–2011 B.S. (Global Environmental Science), University of Hawai'i at Manoa.

2012 Field Assistant, Ocean Technology Group

2012–2017 Research Associate, Hawai'i Ocean Time-series

2017–2020 M.S. (Atmospheric and Oceanic Sciences), UCLA.

PUBLICATIONS

McCoy, D., Damien, P., Clements, D., Yang, S., & Bianchi, D. Mesoscale variability enhances fixed nitrogen loss and suppresses nitrous oxide production in oxygen minimum zones, *in preparation for Geophysical Research Letters 2023*

Bianchi, D, **McCoy, D.**, & Yang, S. Formulation, optimization and sensitivity of NitrOMZv1.0, a biogeochemical model of the nitrogen cycle in oceanic oxygen minimum zones, *Geoscientific Model Development Discussions 2023*

McCoy, D., Damien, P., Clements, D., Yang, S., & Bianchi, D. Pathways of nitrous oxide production in the eastern tropical South Pacific oxygen minimum zone, *Global Biogeochemical Cycles 2023*

Pham, A., Damien, P., **McCoy, D.**, Mar, M., Kessouri, F., McWilliams, J., Moffett, J.,& Bianchi, D. The shelf-to-basin transport of iron along the northern U.S. west coast, *in preparation for Global Biogeochemical Cycles 2023*

McCoy, D., Bianchi, D., & Stewart, A. Global observations of submesoscale coherent vortices in the ocean, *Progress in Oceanography 2020*

McCoy, D., McManus, M., Kotubetey, K., Kawelo, H., Young, C., D'Andrea, B., Ruttenberg, K., & Alegado, R. Large-scale climatic effects on traditional Hawaiian fishpond aquaculture, *PLoS ONE 2017*

CHAPTER 1

Introduction to the oceanic nitrogen cycle

Nitrogen (N) occupies a central role in biogeochemistry. As a limiting nutrient for primary productivity, nitrogen ultimately influences the cycling of carbon, phosphorous, and oxygen (Zehr & Ward, 2002; Gruber, 2004; Arrigo, 2005; Capone et al., 2008; Voss et al., 2013; Pajares & Ramos, 2019), but stands out among other major elements in the ocean due to its existence in a greater variety of chemical forms and oxidation states (Capone et al., 2008; Lam & Kuypers, 2011). Marine organisms leverage this versatility, undertaking numerous chemical transformations as part of their metabolism (Capone et al., 2008; Kuypers et al., 2018). As a consequence, biological processes heavily influence the oceanic nitrogen budget, distinguishing it from the budgets for other limiting nutrients (e.g., iron, phosphorous (P), and silicon), which instead are dominated by riverine or atmospheric inputs (Codispoti et al., 2001).

The process that quantitatively dominates the oceanic N cycle is the photosynthetic fixation of carbon and nitrogen into organic matter by marine phytoplankton at the ocean surface (Capone et al., 2008). Since most phytoplankton appear to have a relatively fixed cell quota for protein, lipids, carbohydrates, and DNA/RNA, they tend to assimilate bioavailable or "fixed" forms of nitrogen such as ammonium (NH_4^+), nitrate (NO_3^-), and nitrite (NO_2^-) in approximately constant ratios with other nutrients (Redfield et al., 1963; Anderson & Sarmiento, 1994). The majority of the resulting organic matter is either respired or remineralized by heterotrophic bacteria in the euphotic zone (Capone et al., 2008). This process transforms organic nitrogen back to fixed inorganic forms, which supports the continuous growth of phytoplankton populations in a tightly interconnected loop referred to as "regenerated" production (Dugdale & Goering, 1967; Eppley & Peterson, 1979). However, since a

small fraction is exported to the dark interior ocean, surface concentrations of fixed N are low while the deep ocean is enriched. To enable "new" production at the ocean surface, ocean circulation and mixing is needed to resupply inorganic nitrogen to the euphotic zone (Dugdale & Goering, 1967; Eppley & Peterson, 1979). This interplay between biological and physical processes (the biological pump) plays a significant role in determining the concentration of CO_2 in the atmosphere, and ultimately is a crucial component of Earth's climate system (Broecker & Peng, 1982; Capone et al., 2008).

The preferred electron acceptor for organic matter remineralization is oxygen (O_2), and since modern oceans are well oxygenated, marine organisms involved with the oceanic N cycle are typically associated with aerobic lifestyles (Lam & Kuypers, 2011). The vast majority of heterotrophic bacteria use O_2 to oxidize organic carbon to CO_2 as a source of energy, releasing NH_4^+ (ammonification, the reverse process of NH_4^+ assimilation) as they lack the ability to oxidize it further to NO_2^- or NO_3^-. This latter step is undertaken by specialized groups of chemolithotrophic bacteria and archaea, which use the oxidation of NH_4^+ to NO_2^-, and NO_2^- to NO_3^-, as a source of energy. This process, known as nitrification (B. Ward & Zafiriou, 1988), links the most oxidized (NH_4^+) and most reduced (NO_3^-) forms of fixed N and exerts a strong control on their individual distributions, leading to NO_3^- accumulation in the deep oxygenated ocean and generally low NH_4^+ and NO_2^- concentrations elsewhere. Notably, the first step of nitrification (NH_4^+ oxidation) produces nitrous oxide (N_2O) as a by-product (Hooper & Terry, 1979; Goreau et al., 1980; Nevison et al., 2003), an ozone-depleting agent and powerful greenhouse gas that is roughly 300 times more potent than carbon dioxide (Suntharalingam et al., 2000; Ravishankara et al., 2009). The oceanic emission of N_2O constitutes roughly 20% to the total emission of N_2O into the atmosphere (Canadell et al., 2021), providing an additional link between the ocean N cycle and Earth's climate (Capone et al., 2008; Lam & Kuypers, 2011).

1.1 Nitrogen loss from oxygen-minimum-zones

Due to weak ventilation and O_2 consumption through remineralization, a small fraction

($< 4\%$) of the global oceans contain low O_2 concentrations such that oxic respiration and nitrification can hardly be sustained (Wyrtki, 1962; Karstensen et al., 2008; Keeling et al., 2010). Two of these major oxygen-minimum-zones (OMZs) are found beneath productive eastern boundary upwelling systems (EBUS) in the tropical North and South Pacific (ETNP and ETSP), while a third exists in the northeastern Arabian Sea (Gruber & Sarmiento, 1997). Although most life avoids such low-O_2 conditions, OMZs foster heterotrophic bacteria capable of remineralizing organic matter with NO_3^- (abundant in deep waters due to nitrification), the next preferred alternative electron acceptor (Froelich et al., 1979), in a process known as denitrification. This process generates N_2O (as an intermediary) and dinitrogen (N_2) (Bianchi et al., 2012; DeVries et al., 2013), the most abundant form of nitrogen in the ocean that is only available to N_2-fixing diazotrophs (Eugster & Gruber, 2012; Luo et al., 2012). Furthermore, the NH_4^+ released from organic matter is oxidized to N_2 in OMZs by chemolithotrophic anammox bacteria (anaerobic NH_4^+ oxidation) (Könneke et al., 2005). Accordingly, N_2 production is mainly restricted to OMZs and anoxic sediments, while N_2O is a key intermediary in both the nitrification and denitrification transformation pathways (Babbin et al., 2015). This biological production of N_2O and N_2 in OMZs represents a loss of fixed N from the ocean to the atmosphere (Naqvi et al., 2010; Yang et al., 2020).

As a result of these additional anaerobic pathways, the inventory of nitrogen is perhaps the one elemental cycle that is most affected by oceanic OMZs (Lam & Kuypers, 2011). Large fixed N losses from OMZs (Gruber & Sarmiento, 1997; Deutsch et al., 2001) in part causes the residence time of fixed N is be about one order of magnitude shorter than for phosphorous (Gruber & Galloway, 2008; Wang et al., 2019), driving a notable stoichiometric deficit in seawater N:P ratios ($\sim$14.7:1, from the relatively constant value of 16:1) (Redfield et al., 1963; Anderson & Sarmiento, 1994) that limits surface production over large swaths of the ocean (Tyrrell, 1999). Moreover, the N_2O yield from nitrification has been observed to increase at lower O_2 (Goreau et al., 1980; Nevison et al., 2003), such as within steep O_2 gradients surrounding anoxic OMZ waters (Babbin et al., 2015). Therefore, the conditions in and around OMZs host unique environments where multiple oxidative and reductive nitrogen transformations coexist, resulting in an almost complete N cycle (Lam & Kuypers, 2011).

This allows OMZ regions to account for up to 50% of total oceanic N_2O emissions to the atmosphere (Naqvi et al., 2010; Codispoti, 2010; Babbin et al., 2015; Arévalo-Martínez et al., 2016; Yang et al., 2020) and 30 - 50% of total N_2 production (Gruber & Galloway, 2008; Codispoti, 2010), despite only occupying roughly 1% of the total ocean volume (Lam & Kuypers, 2011). Meanwhile, analyses of contemporary and historical data sets suggest an intensification of the world's OMZs has been occurring over the past few decades (Stramma et al., 2008, 2010), which models project to continue into the future (Cabré et al., 2015; J. J. Busecke et al., 2019; Kwiatkowski et al., 2020). As a consequence, the oceans are likely to experience further fixed N loss, which in turn will constrain primary production and ultimately reduce the ocean's capacity to sequester atmospheric CO_2 (Falkowski, 1997).

1.2 Modelling the nitrogen cycle

Numerous studies on microbial processes in OMZs in the past few decades (Codispoti & Christensen, 1985; B. Ward & Zafiriou, 1988; Lam & Kuypers, 2011) have facilitated the development of ocean biogeochemical models capable of informing the expression of N cycle transformations in dynamic environments. From the beginning, these models have included NO_3^- and NH_4^+ assimilation by phytoplankton and subsequent nitrification (Fasham et al., 1990; Sarmiento et al., 1993; Moore et al., 2004). With the advent of more complex Earth System Models, biogeochemical representations have progressively expanded to include more detailed representations of the N cycle, including N_2 fixation, denitrification and N_2O production (Aumont et al., 2015; Séférian et al., 2020; Stock et al., 2020; Long et al., 2021). However, these models frequently employ oversimplified empirical parameterizations to represent nitrogen transformations, overlooking the complexities inherent in the network of nitrogen reactions and their controls (Bianchi et al., 2022). New understandings surrounding the processes governing N_2O and N_2 production have stimulated a resurgence of model development in the field.

For example, despite the discovery of anammox as an alternative N loss pathway to heterotrophic denitrification in recent decades (Dalsgaard et al., 2003; Kuypers et al., 2003;

Könneke et al., 2005), models often conflate anammox and denitrification into a single N_2 production term. Additionally, observations of supersaturated N_2O concentrations within the suboxic gradients surrounding the anoxic core of OMZs (where no nitrification can occur) (Martens-Habbena et al., 2009) had been historically linked to enhanced production from nitrification (Cohen & Gordon, 1978). Thus, models that include N_2O cycling predominantly rely on parameterizations that link N_2O production to nitrification or aerobic respiration (Suntharalingam et al., 2000; Nevison et al., 2003; Jin & Gruber, 2003; Manizza et al., 2012), with denitrification typically modelled as an exclusive sink of N_2O (and thus, a source of N_2) in the ocean (Suntharalingam et al., 2000; Codispoti et al., 2001; Jin & Gruber, 2003; Battaglia & Joos, 2018). Yet recent studies have questioned the relative contribution from nitrification to total N_2O production by demonstrating the existence of progressive O_2 sensitivities for the distinct enzymes regulating step-wise denitrification rates (Körner & Zumft, 1989; Kalvelage et al., 2011; Dalsgaard et al., 2014; Babbin et al., 2015; Ji et al., 2015). In the same low O_2 environments where enhanced nitrification-production has been observed, N_2O accumulation from the denitrification pathway can occur as NO_2^- reduction proceeds while N_2O reduction is inhibited, in a process referred to as "incomplete" denitrification (Babbin et al., 2015). This discovery has raised questions around the relative contributions from nitrification and denitrification pathways to supersaturated N_2O in suboxic OMZ waters, and their overall significance to total N_2O production.

While ocean biogeochemical models have progressively expanded our understanding of OMZ nitrogen cycling, they omit key tracers and processes such as NO_2^- and "incomplete" denitrification (Lam & Kuypers, 2011; Kalvelage et al., 2013; Babbin et al., 2014, 2015, 2017; Buchwald et al., 2015). With recent studies demonstrating significant N_2O production from the denitrification pathway (Babbin et al., 2015), and due to the global significance of N loss within OMZs (Codispoti et al., 2001), accurate representation and parameterization of the nitrogen transformation rates within ocean models is needed to constrain current rates of N_2 and N_2O production. This in turn will improve our ability to predict future responses to climate forcing and deoxygenation.

1.3 The Eastern Tropical South Pacific

The Peruvian upwelling ecosystem extends from the southern extent of Chile ($\sim 45^o S$) to northern Peru ($\sim 4^o S$). It belongs to the four major EBUS, which together account for about 11% of the global ocean "new" production (Bakun & Parrish, 1982; Chavez & Messié, 2009; Arévalo-Martínez et al., 2016). In general, EBUS are located along the eastern flanks of subtropical gyres, where equatorward winds stimulate the formation of expansive eastern boundary currents at the ocean surface (Colas et al., 2013). The interaction between these currents, the coastline, and the Earth's rotation induces a shallow offshore surface Ekman transport, which gives way to the upwelling of cooler waters from below (Chavez & Messié, 2009; Rykaczewski & Dunne, 2010; Jacox & Edwards, 2012). As these deep waters rise to the surface, they bring with them an abundance of nutrients, such as NO_3^- and phosphate, which in turn fuels phytoplankton growth capable of sustaining higher trophic levels including fish populations (Bakun & Parrish, 1982; Huyer, 1983; Chavez & Messié, 2009). Consequently, this coastal upwelling exerts a pronounced influence on sea surface temperature and primary production, leaving a distinct mark on these oceanic properties (Chavez & Messié, 2009).

While southern Chile experiences more intense upwelling during boreal summer (Pennington et al., 2006), upwelling-favorable conditions exist year-round along the Peruvian and northern Chile coastlines, fueling high rates of surface primary productivity and organic matter export (Chavez & Messié, 2009). On sinking, organic matter remineralization promotes O_2 consumption in the underlying water column (Wyrtki, 1962; Capone et al., 2008; Stramma et al., 2008). Additionally, due to a location in the South Pacific tropical shadow zone of the thermocline (which extends westward from the eastern boundary between the equatorward edges of the subtropical gyres)(Luyten et al., 1983), supply of O_2 from the ventilated subtropical gyres to the ETSP is weak (Karstensen et al., 2008; Stramma et al., 2010). As a consequence, the relatively O_2-rich eastward tropical currents are the major advective sources of oxygen to the equatorward side of the ETSP OMZ (Karstensen et al., 2008; Stramma et al., 2010). However, despite additional lateral O_2 supply from mesoscale eddies (Gnanadesikan et al., 2013; Bettencourt et al., 2015), O_2 remains depleted within

the OMZ core (Kwiecinski & Babbin, 2021), leading to functional anoxia (Thamdrup et al., 2012). Due to these characteristics, the ETSP hosts the second largest OMZ by area, extending 1000 km offshore of the Peruvian shelf with a maximum thickness greater than 600 m (Fuenzalida et al., 2009).

1.4 The role of the physical circulation

Enhanced and persistent mesoscale activity occurs in the ETSP compared to other upwelling regions (Chaigneau et al., 2009; Chelton et al., 2011). Along the Peruvian coast, instability of the equatorward Humboldt current generates nonlinear mesoscale eddies which propagate coastal biogeochemical and physical properties offshore (Chelton et al., 2007; Chaigneau et al., 2008; Arévalo-Martínez et al., 2016). As the mean currents are weak at depth, this eddy variability strongly influences the flow and intermittently supplies O_2-rich water to the OMZ (Czeschel et al., 2011; Gnanadesikan et al., 2013; Bettencourt et al., 2015), leading to heterogeneity in nitrogen cycling (Altabet et al., 2012; Stramma et al., 2013; Bourbonnais et al., 2015; Löscher et al., 2016). For example, Altabet et al. (2012) demonstrated the role of coastal eddies in trapping and transporting organic matter offshore, which locally stimulates N_2 production via enhanced heterotrophic denitrification (Babbin et al., 2014). Eddies have also been shown to inject nutrients into the euphotic zone by lifting the upper thermocline, leading to increased production and organic matter flux to the deep ocean (McGillicuddy et al., 2007).

In addition to mesoscale eddies, EBUS generate a distinctive class of smaller, subsurface, predominantly anticyclonic eddies known as submesoscale coherent vortices (McWilliams, 1985; Pelland et al., 2013; Hormazabal et al., 2013; Molemaker et al., 2015). These eddies have been shown to play an oversized role in propagating water masses in the intermediate and deeper parts of the ocean (Richardson et al., 2000; Hormazabal et al., 2013; Z. Zhang et al., 2015; Pegliasco et al., 2015; Jithin & Francis, 2021; X. Zhang et al., 2022). In the ETSP, they are known to form from the destabilization of the poleward flowing Peru-Chile Undercurrent (Hormazabal et al., 2013; Combes et al., 2015; Thomsen et al., 2016), which

carries relatively warm, salty, and O_2-poor waters of equatorial origin (Contreras et al., 2019). Due to their characteristically long lifetimes and highly nonlinear nature, these eddies can effectively transport low-O_2 waters into the nearby subtropical gyre (Frenger et al., 2018). As a consequence, they have been attributed to expanding the influence of OMZs (Landolfi et al., 2013), and are known hot-spots of N loss and N_2O production in otherwise aerobic waters (Altabet et al., 2012; Bourbonnais et al., 2015; Löscher et al., 2016; Arévalo-Martínez et al., 2016; Grundle et al., 2017).

The presence of a vibrant eddy circulation suggests that the evolution of nitrogen tracers in the ETSP cannot be understood simply in terms of the advection by the time-mean circulation, background diffusion, and local sources and sinks (Pasquero, 2005). At any instant, eddies distort the tracer field and form local tracer anomalies. As has been shown by many previous studies, correlations between eddy-scale current and tracer anomalies can lead to an eddy-induced transport which, in some cases, can significantly augment the mean biogeochemical transport (Falkowski et al., 1991; Lathuilière et al., 2010; Gruber et al., 2011; Gaube et al., 2014). This recognition has generated a variety of techniques for representing the influence of turbulent tracer dispersion induced by unresolved eddies in course models (e.g., Gent & Mcwilliams (1990) and Fox-Kemper et al. (2008))

A common approach to representing the influence of eddies and filaments is the inclusion of a parameterized enhanced molecular diffusion term applied to resolved tracer gradients. Despite its frequent application to modelling studies, limitations of this parameterization (the gradient-diffusion hypothesis) have been noted for reactive tracers (Prend et al., 2021), of which all forms of marine N, except N_2, qualify. A pioneering study by Lévy et al. (2013) highlighted this bias by exploring the role of "eddy reactions", which arise due to eddy-driven heterogeneity in the distribution of reactive biogeochemical tracers and the nonlinear nature of biogeochemical reactions (e.g., Michaelis-Menten substrate uptake for nutrients, light limitation in nitrifying microbes and phytoplankton, and O_2 inhibition for anaerobic processes) (K. A. Johnson & Goody, 2011; Dalsgaard et al., 2014). The contribution from eddy nitrogen reactions may be large in OMZs regions such as the ETSP, where both biogeochemical and physical forcings act to generate environmental heterogeneity. Thus, challenges

remain in estimating modern global ocean N loss and N_2O outgassing due to uncertainties surrounding the spatial and temporal variability of the processes governing their evolution in OMZs (Bourbonnais et al., 2015; Arévalo-Martínez et al., 2016).

1.5 Science questions and outline

In this first Chapter of my dissertation, I have outlined our region of interest (the Eastern Tropical South Pacific), the biogeochemical reactions relevant to N_2 and N_2O production, and provided a background into the important role the physical circulation plays. I have similarly highlighted the importance of resolving the questions surrounding N loss and N_2O production, given the expected expansion of OMZs in future climates.

Due to the global implications of nitrogen cycling within OMZ regions, this dissertation investigates the physical and biogeochemical interactions that shape modern rates of N_2O and N_2 production in the ETSP. To this end, I carried out a series of projects aimed at describing the processes relevant to their production. Together, these projects will add great value to the ocean community by providing insights into one of the most important oceanographic regions governing the outgassing of N_2O and the inventory of fixed N.

In Chapter 2, we specifically sought to address the following scientific questions:

- Where are "hot-spots" of SCV formation in the world ocean?
- For regional hot-spots, what water masses are impacted by SCV transport?
- What are the potential regional generation mechanisms?
- Where SCVs appear, what are their contributions to local heat and salt anomalies?

To provide insights into these questions, we developed and applied a general algorithm to the global Argo float array in order to detect SCV encounters from chance profile measurements. We ultimately expanded the record of SCVs in the global ocean by including nearly 4000 additional observations. We grouped detections into regional populations, and used water mass analyses and previous literature on SCVs to link populations to formation regions,

allowing for a speculation on possible mechanisms of formation. We further used theory and statistics to demonstrate SCVs can leave a significant imprint on the hydrographic properties of waters masses in regions of high SCV density.

In Chapter 3, we aimed to quantify several important processes impacting the evolution of N_2O within the ETSP:

- What are the respective contributions to local ETSP N_2O production from nitrification and "incomplete" denitrification?
- What role does advection play in transporting remotely-generated N_2O to the ETSP?
- What processes dominate the ultimate outgassing of N_2O?

To accomplish this, we made use of a new model of the oceanic N cycle known as NitrOMZ (**Nitr**ogen cycling in **O**xygen **M**inimum **Z**ones), which we previously detailed in a separate manuscript that is not presented herein (Bianchi et al., 2022). Briefly, the model explicitly represents the major forms of nitrogen found in seawater as prognostic tracers, and parameterizes the transformations that connect them as a function of seawater chemistry. Crucially, NitrOMZ includes the process of anammox, separately represents each denitrification step (allowing for "incomplete" denitrification), and simulates N_2O production from NH_4^+ oxidation.

We initially implemented the model in an idealized 1D representation of the ETSP water column (Bianchi et al., 2022), and used a formal optimization procedure to extract parameter sets capable of recovering measured tracer and rate distributions from recent hydrographic measurements (Kalvelage et al., 2013; Ji et al., 2015; Peng et al., 2016; Babbin et al., 2017, 2020). The optimization revealed systematic variations in the sensitivity of denitrification processes to O_2, and was consistent with recent incubation experiments (Dalsgaard et al., 2014) in suggesting progressive O_2 intolerances exist for the denitrification steps. We similarly used observations to constrain the parameters governing N_2O production from nitrification (Goreau et al., 1980; Nevison et al., 2003), ultimately generating parameter values within the range of recent studies (Ji et al., 2018; Santoro et al., 2021). We then embedded

NitrOMZ into the Regional Ocean Modelling System (ROMS) (Shchepetkin & McWilliams, 2005; Shchepetkin, 2015), a primitive-equation, hydrostatic, topography-following general ocean circulation model. This allowed us to more accurately simulate aerobic and anaerobic nitrogen transformations, and the physical circulation, within a characteristic OMZ upwelling region. We compiled a budget of N_2O to elucidate the contributions from both denitrification and nitrification to total N_2O production. We also highlighted the role of the large scale tropical circulation in supplying outgassing-favorable N_2O to the ETSP. These results provide new insight into the sources of N_2O outgassing in this dynamic region.

Our goal in Chapter 4 was to explore the contributions from mean and eddy N cycle reactions to total N_2O production and fixed N loss within the ETSP OMZ in order to assess the following questions:

- How do nitrogen transformations in the ETSP respond to mesoscale tracer heterogeneity?
- What are the mean and eddy reaction contributions to N_2O and N_2 production in the ETSP?

To address these questions, we applied a higher resolution version of the model applied in Chapter 3 to better simulate the evolution of smaller scale features like mesoscale eddies, SCVs, and filaments in the ETSP. We used monthly-filtered tracer fields to represent a "mean field approximation" of the ETSP, in analogy to tracer fields resolved by a coarse-grained model. Using an offline version of the N cycle transformations in the model, we extracted the contributions from the low frequency circulation, allowing for an investigation into the role that mesoscale-driven heterogeneity in the OMZ plays in regulating fixed N loss.

Finally, in Chapter 5, I summarize the advances presented in this dissertation. I highlight the importance and need for continued efforts, and outline the ongoing and future work inspired by the work presented here.

CHAPTER 2

Global Observations of Submesoscale Coherent Vortices in the Ocean

This chapter contains the published manuscript (McCoy et al., 2020), available from Progress in Oceanography, without any changes.

2.1 Introduction

Anticyclonic oceanic eddies with subsurface velocity maxima populate many areas of the world ocean and exert a regional influence on heat, salt, and nutrient transport (Richardson et al., 2000; Nauw et al., 2006; Pegliasco et al., 2015; Frenger et al., 2018). They have been detected within the near-surface, intermediate, and near-bottom layers of the ocean, and are characterized by horizontal scales that range from the submesoscale (¡10 km) to the internal Rossby radius of deformation (10 – 100 km) (McWilliams, 1985; D'Asaro, 1988; Nauw et al., 2006; Molemaker et al., 2015). A defining characteristic of these eddies is the doming and bowling of isopycnal surfaces around a weakly stratified, gradient-wind balanced water mass (McWilliams, 1985; Gordon et al., 2002; Nauw et al., 2006) that also exhibits anomalously low potential vorticity (PV) (Meunier et al., 2018). Intrathermocline eddies (ITEs) are variants that displace the main thermocline and are thought to be generated by a variety of mechanisms that include: 1) subduction of mode waters at frontal boundaries (Spall, 1995; Hogan & Hurlburt, 2011); 2) isolation of pre-existing mesoscale anticyclones from the surface by advection or restratification (Hogan & Hurlburt, 2011); 3) a reduction of PV along fronts by counter-directional winds on the frontal jet (A. C. Thomas et al., 2009); 4) intense local upwelling driven by eddy-wind interactions that induces isopycnal doming (McGillicuddy,

2014). Sub-thermocline variants common to eastern boundary upwelling systems (EBUS) are frequently termed submesoscale coherent vortices (SCVs, (McWilliams, 1985)). They have been shown to be primarily generated via subsurface currents that undergo flow separation near capes or promontories, followed by submesoscale instabilities and roll-up into coherent vortices (D'Asaro, 1988; Molemaker et al., 2015; Thomsen et al., 2016). Here we use the term SCV to describe both types of eddies, due to their similar dynamical structures and role in subsurface ocean circulation.

Interest in SCVs is motivated by their occasional propagation within or below the pycnocline, where relatively weak turbulent mixing allows for a slower decay compared to mesoscale eddies (McWilliams, 1985; Collins et al., 2013). Observations also suggest a preference for anticyclonic rotation and isolation of core water mass over many cycles due to the rapid rotation (McWilliams, 1985; Schütte et al., 2016). These characteristics allows for individual SCVs to exist for several years, while efficiently transporting nutrients and other material properties thousands of kilometers away from their formation regions (Richardson et al., 2000; Frenger et al., 2018). For example, Lukas & Santiago-Mandujano (2001) detected an SCV with a radius of at least 15 km to the North of the Hawaiian Islands that was virtually depleted in dissolved oxygen throughout its core. The highly atypical hydrographic properties within the eddy relative to the surrounding water suggested formation off the southern tip of Baja California several years prior to detection.

The long lifetimes and unique dynamics of SCVs suggest that they are important in shaping the distribution and variability of heat, salt, and biogeochemical tracers over large swaths of the ocean. Notably, compared to surface intensified eddies, SCVs differ strongly in both their efficiency in carrying water mass anomalies, and the resulting biogeochemical responses within the encapsulated waters (Schütte et al., 2016). A study by Frenger et al. (2018) used a global eddying ocean biogeochemical model to suggest that SCVs shed from Pacific EBUS accounted for roughly 10% of the offshore transport of nutrients from those systems along the isopycnals where eddies are found, while Pelland et al. (2013) estimated that up to 44% of the heat and salt loss from the California undercurrent is a result of SCV generation along its pathway. Perhaps most striking are the Mediterranean outflow

eddies or 'Meddies' that appear in the North Atlantic Ocean as blobs of dense, salty, weakly stratified Mediterranean Sea water (McWilliams, 1985; Bower et al., 1997; Richardson et al., 2000; Barbosa Aguiar et al., 2013; Bashmachnikov et al., 2015). Settling to around 1000 m before adjusting and acquiring their characteristic anticyclonic rotation, they could account for roughly 40% of the Mediterranean outflow, and contribute to the westward salinity flux within the Mediterranean salt tongue (Bower et al., 1997; Richardson et al., 2000). Additionally, the isolation of SCV core properties may also establish a distinct biogeochemical environment and subsequent biological community compared with the surrounding waters (Löscher et al., 2015; Frenger et al., 2018). Low-oxygen SCVs, such as those shed from EBUS, have been shown to be hot-spots of fixed nitrogen losses and production of nitrous oxide, a powerful greenhouse gas (Altabet et al., 2012; Arévalo-Martínez et al., 2015; Löscher et al., 2015; Grundle et al., 2017).

After propagation from source regions, the core properties of SCVs often strongly contrast with surrounding waters, allowing easy detection as vertically confined, weakly stratified, Gaussian-shaped water mass anomalies (J. Simpson et al., 1984; McWilliams, 1985; Z. Zhang et al., 2015). Examples from the observational record include California Undercurrent 'Cuddies' (Garfield et al., 1999; Chaigneau et al., 2011; Pelland et al., 2013; Collins et al., 2013), Peru-Chile 13C Water Eddies (G. C. Johnson & McTaggart, 2010; Chaigneau et al., 2011; Hormazabal et al., 2013), Labrador Sea outflow eddies (Bower et al., 2013), Beaufort Sea eddies (D'Asaro, 1988; Zhao et al., 2018), Persian Gulf eddies (L'Hégaret et al., 2016), Red Sea outflow eddies ((Shapiro & Meschanov, 1991), and the ITE's of the Northwest Pacific (Gordon et al., 2002; Hogan & Hurlburt, 2011; Z. Zhang et al., 2015) and Southern Indian (Nauw et al., 2006; Dilmahamod et al., 2018) Oceans. Yet, despite the multitude of studies documenting individual SCV populations, their global occurrence, properties, and generation frequency remain poorly constrained.

While the advent of satellite altimetric observations facilitated the study of surface-intensified eddies (Chelton et al., 1998; Chaigneau et al., 2011; Gaube et al., 2018), the weak or undetectable sea-surface signature of SCVs restricts their observational record to mostly chance encounters with shipboard instrumentation or autonomous sampling platforms. Over

the past two decades, the global array of roughly 4000 operational Argo floats has produced nearly 2 million hydrographic profiles of the upper 2000 meters of the ocean, offering a unique opportunity to study SCVs. This vast number of profiles provides robust estimates of regional climatological water column properties, which can be exploited to detect SCVs based on their anomalous hydrographic signatures (G. C. Johnson & McTaggart, 2010; Pegliasco et al., 2015; Z. Zhang et al., 2015; Li et al., 2017).

In this paper, we develop a general algorithm to identify Argo float profiles that crossed the interior of SCVs, expanding similar methods used by G. C. Johnson & McTaggart (2010) and Z. Zhang et al. (2015) to study regional SCV populations. Based on theory and observations, we identify SCVs within Argo profiles using three primary criteria. First, a SCV must contain a vertically confined, Gaussian-shaped water mass anomaly, indicative of remote subsurface advection. Second, the water mass anomaly must be weakly stratified, corresponding to doming/bowling of isopycnals above and below the water mass, respectively. Finally, horizontal velocities estimated from hydrographic properties must suggest a local maxima within the range of the SCV. We establish specific detection criteria corresponding to these conditions, based on: (1) spiciness, a measure of density-compensated thermohaline variability, (2) buoyancy frequency, a measure of the vertical stratification, and (3) dynamic height anomaly, a measure of the horizontal pressure gradient force.

By applying the algorithm to the global Argo array, we detect roughly 4000 "spicy-core" SCVs (anomalously warm and salty) and "minty-core" SCVs (anomalously cold and fresh). We analyze the properties of these detections to shed light on the regional variability and generation mechanisms of SCVs, and their impacts on heat and salt distribution. The rest of the paper is organized as follows: section 2.2 discusses the Argo data set and the algorithm used to detect SCVs; section 2.3 describes the global and regional results after application of the detection method; section 2.4 discusses possible generation mechanisms associated with large coherent populations of SCV detections; and section 2.5 provides estimates of their numbers and expected contribution to heat and salt budgets globally.

2.2 Methods

2.2.1 Data and Quality Control

We downloaded Argo float profiles from August 1997 to January 2020 from the U.S. Argo global data center (GDAC). Vertical levels without 'good' or 'probably good' quality control flags were rejected, and delayed-mode or adjusted values were used whenever available. Questionable float profiles based on a list provided by the GDAC ('grey-listed' floats) were removed. We further applied the following quality control criteria to remove casts with poor vertical resolution. We rejected casts that did not contain data from 0 to 100 dbar, or data greater than 700 dbar; profiles with vertical spacing greater than 65 dbar between 100 – 700 dbar were also excluded. Of the profiles that passed these criteria, any data between 0 – 1000 dbar were accepted until the difference between pressure levels was greater than 65 dbar. For the casts deeper than 1000 dbar, a 105 dbar resolution threshold was applied past that point. Finally, profiles were removed if they contained less than 40 vertical levels, or if they contained potential density inversions below the mixed layer (defined by the depth where potential density exceeds the surface value by 0.03 kg m^{-3} (de Boyer Montégut et al., 2004)).

Of the initial 1,992,246 float profiles, 336,861 (17%) were rejected based on these criteria (Figure A.1). Quality controlled temperature and salinity profiles were then linearly interpolated to a 10 dbar pressure grid from 0 to 2000 dbar, before deriving spiciness, absolute salinity, conservative temperature, and potential density. Derived buoyancy frequency (N^2) profiles on the 10 dbar grid were found to contain significant small-scale noise. To minimize this noise, we derived buoyancy frequency profiles from temperature and salinity profiles that were interpolated to a finer 2 dbar grid and smoothed with a Gaussian filter with a bandwidth of 10 dbar, before interpolating them back to the 10 dbar grid.

2.2.2 Anomalous Water Mass Detection

To identify water mass anomalies associated with remotely-generated SCVs, we compared each profile with the nearest monthly climatological profile from the Roemmich-Gilson Argo Climatology (Roemmich & Gilson, 2009). In order to better preserve water mass properties, we derived and interpolated climatological profiles of spiciness and buoyancy frequency to each cast potential density, before subtracting them to obtain anomaly profiles along isopycnals. We chose to subtract properties along density rather than pressure because of to the preferential movement of water masses along isopycnal surfaces (Talley et al., 2011). When climatological temperature or salinity profiles were not available at the cast location (such as near the coast), we computed an average climatological profile using data from neighboring cells. Float profiles that could not be paired with climatological profiles were excluded (Figure A.1).

To quantify the water mass variability at each profile location, we gathered spiciness and buoyancy frequency anomalies from all profiles conducted within 220 km of the cast coordinates that were also conducted within +- 45 days of the cast date, regardless of year (Figure 2.1A). We then calculated the interquartile range (IQR), or the difference between the 75th and 25th percentile, to quantify the statistical spread of anomalies at each density level. These spatial and temporal thresholds are similar to those applied in Pegliasco et al. (2015), and were chosen to prevent false detections in regions with large horizontal temperature and salinity gradients and/or significant seasonal variability. Profiles without at least 60 comparable casts fitting the above criteria were excluded. After organizing all values into percentiles, we defined upper and lower outlier thresholds at each density level as the 75% value plus 1.5 times the IQR, and the 25% value minus 1.5 times the IQR, respectively (Tukey, 1977). We analyzed IQR statistical thresholds rather than mean and standard deviations because the IQR is less sensitive to large outliers.

The upper and lower IQR thresholds in spiciness anomaly were applied to identify isopycnal surfaces with anomalously high or low spiciness, which we labeled as spicy (anomalously warm and salty) or minty (anomalously cold and fresh) water mass intrusions, respectively

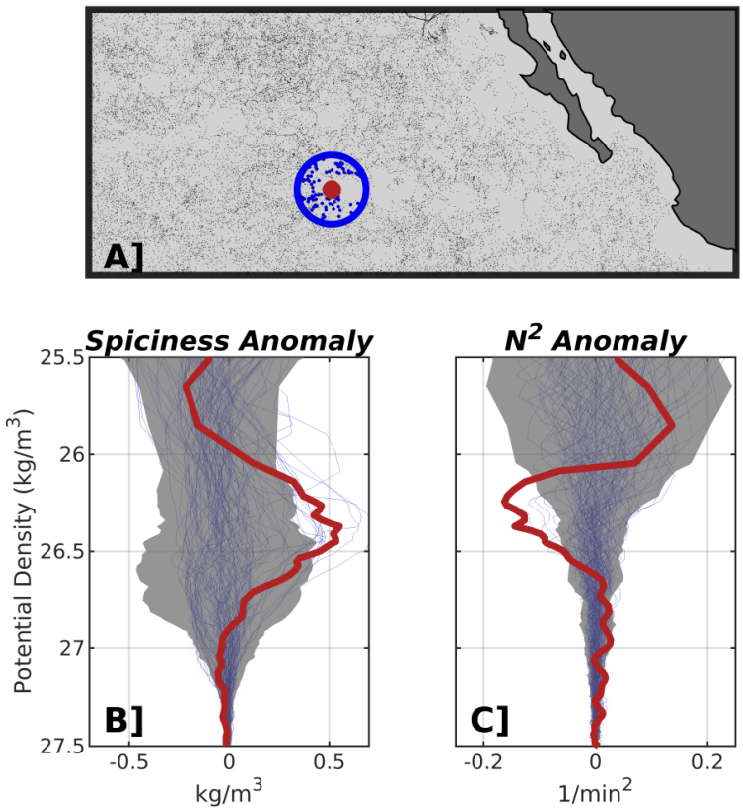

Figure 2.1: Example of Argo cast exceeding spiciness and buoyancy frequency anomaly thresholds for SCV detection. (A) Locations of Argo float 4900860, cycle 347 (thick red point), and all floats within a 220 km radius circle that were conducted within ± 45 days of the cast date, regardless of year (blue points); all other Argo casts are shown as faint grey dots. (B) Spiciness anomaly versus potential density for both the cast (red curve) and the nearby comparable Argo casts (blue curves). Shaded gray regions represent calculated IQR thresholds along each isopycnal. (C) Same as (B), but for squared buoyancy frequency anomaly. Note the thresholds being exceeded in both plots at a density of roughly 26.4 kg m^{-3}.

(shaded regions in Figure 2.1B). Likewise, lower IQR thresholds in buoyancy frequency anomaly (Figure 2.1C) were used to identify anomalously weak stratification within the core of each intrusion (section 2.2.4). While the 25% and 75% IQR threshold limits are commonly applied in statistical outlier detection (Tukey, 1977), they are rather restrictive. Thus, weakly stratified water mass intrusions detected using these thresholds likely represent

an underestimate of their true number in the ocean. However, adopting these strict criteria provides the benefit of reducing false positives, thus generating robust detections that can be confidently attributed to SCV identification.

To avoid detecting surface features such as mesoscale eddies, we limit our detection routine to subsurface isopycnals only. Since SCVs have been previously identified within or below the upper pycnocline (here defined as the vertical level of greatest stratification), we restricted our search to isopycnals below this depth. To estimate this level at each cast location, we used the depth of maximum climatological N^2 (Figure A.2), a criterion that robustly isolated isopycnals near the surface with very large IQR. Any cast which featured at least two consecutive isopycnal surfaces below this depth, spaced apart by 10 dbar, which exceeded either of the spiciness thresholds discussed above was kept for further analysis.

2.2.3 Gaussian Model Fit

In order to detect the presence of anomalously weak stratification associated with spicy or minty water mass intrusions, we required an estimate of the vertical thickness of each intrusion. Since observations of SCVs suggest that their vertical structure is well represented by a Gaussian monopole (McWilliams, 1985; Pelland et al., 2013), to estimate the vertical thickness or extent H we fit a one-term Gaussian model to spiciness anomaly profiles (calculated along isopycnals) in pressure space of the form:

$$Ae^{-\left(\frac{z-z_o}{h}\right)^2}, \tag{2.1}$$

where A is the maximum absolute spiciness anomaly exceeding the IQR threshold, z is the pressure profile, z_o is the pressure of A, and h is the scale height. By fitting the model, we set H to be the distance encompassed by $z_\mathrm{o} \pm 2$ standard deviations (σ) of the Gaussian model:

$$H = 4\sigma = 2\sqrt{2}h\,. \tag{2.2}$$

To find the best fit of the Gaussian model to the spiciness anomaly profile, we allowed A to vary by $\pm 20\%$, H to vary between 100 – 1200 dbar, and z_o to vary by $\pm 20\%$ of H. We then

calculated the sum of squared residuals for all combinations by reducing the vertical spiciness anomaly profile to within each estimated H. After careful inspection of fit solutions, we only considered combinations where: 1) the squared two-dimensional correlation coefficient (R^2) between the reduced profile and model was greater than 0.5; 2) the root-mean-squared error normalized to the min/max of the reduced spiciness profiles (NRMSE hereafter) was less than 0.5; 3) profile data exists within the extent of the predicted H; and 4) A was greater than 0.1 kg m^{-3}. We chose the best combination in a least-square sense to estimate H, while simultaneously rejecting profiles which could not fit the above parameters or thresholds (purple dashed curve in Figure 2.2B). In practice, this eliminated intrusions that were (1) not well represented by a vertical Gaussian structure, (2) too thin (¡ 100 dbar), or (3) too thick (¿1200 dbar) and thus not likely to be a result of an SCV.

2.2.4 Weakly Stratified Core Detection

After successfully fitting Gaussian curves to spicy and minty intrusions, we sought anomalously weak stratification within the vertical extent of each water mass, indicative of bowling/doming of isopycnals around the intrusion. However, inspection of profiles which succeeded in fitting the model occasionally revealed noisy signatures in buoyancy frequency anomaly along isopycnals. Since the weak stratification characteristic of SCVs should be most evident within waters just above and below the core of the feature, we defined an additional core vertical thickness or extent (H_{core}) using the σ value from the Gaussian fitting routine:

$$H_{\text{core}} = 2\sigma = \sqrt{2}h\,. \tag{2.3}$$

Using the above estimate, we set two strict criteria to check for weak stratification. First, the buoyancy frequency anomaly profile must be less than the lower N^2 IQR threshold at a depth within the core limits, to represent the abnormally low stratification associated with SCVs. Second, the vertical mean of N^2 anomaly within this range must also be less than zero to avoid false detections due to occasionally noisy signals (e.g. Figure 2.2D). Profiles that did not fit the above stratification criteria were rejected.

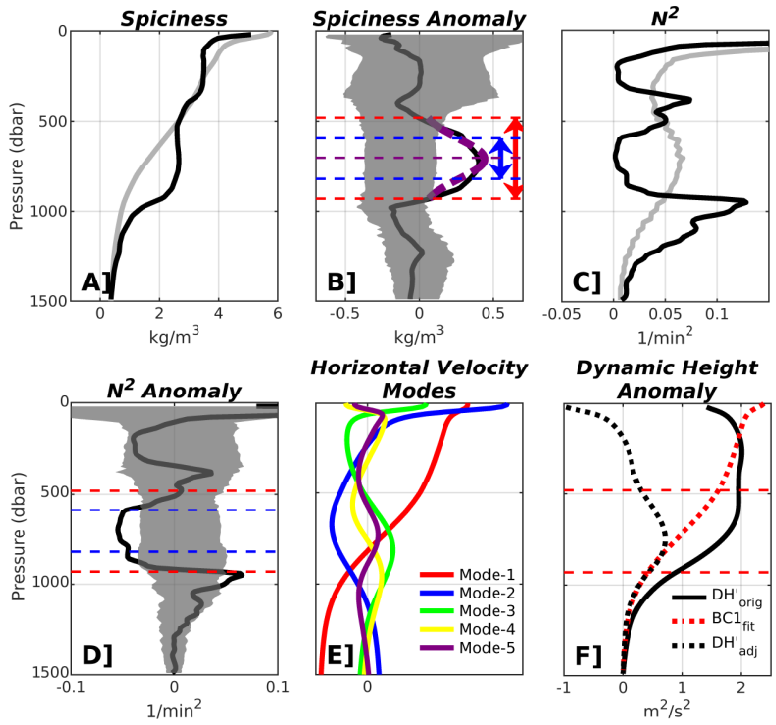

Figure 2.2: (A) Spiciness versus pressure from Argo cast 69027, cycle 151 (black curve), and its local Argo climatology (grey curve). (B) Spiciness anomaly (derived along isopycnals) versus pressure (black curve) and the Gaussian model result (purple dashed curve). Dashed red lines represent estimates of the vertical thickness of the SCV, whereas dashed blue lines represent estimates of the SCV core thickness. The dashed purple line represents the estimate of the SCV core isopycnal/pressure. Shaded gray regions represent IQR thresholds used for the detection. (C,D) Same as (A,B), but for squared buoyancy frequency and squared buoyancy frequency anomaly. (E) The first five baroclinic horizontal velocity modes (dimensionless) vs. pressure, calculated from the climatological buoyancy frequency profile. (F) Original dynamic height anomaly (solid black curve), the first baroclinic horizontal velocity mode fit (dashed red curve), and the final adjusted dynamic height anomaly profile (dashed black curve).

2.2.5 Subsurface Velocity Maxima Detection

Satisfying the interior horizontal velocity maxima criteria is difficult without in-situ subsurface current data. However, the dynamic height differences between two nearby casts can be used as an estimate for the geostrophic velocity streamfunction, assuming flow at depth

is relatively weak compared to surface velocities; note that this is a poor assumption within the vicinity of boundary currents and the Antarctic Circumpolar Current (ACC) (Ollitrault & Colin de Verdière, 2014). We take advantage of the fact that the majority (86%) of quality controlled floats began their casts at depths greater than 1000 dbar, where horizontal velocities are usually small (Talley et al., 2011). To test for a local extremum in the horizontal velocity, we calculated the dynamic height profile vs. pressure for both the detected SCV profile and the local Argo climatological profile. We started this calculation from the greatest cast pressure p_{ref}, with the dynamic height anomaly $DH'_{\mathrm{o}}(z)$ defined as the difference along isobars between the two profiles:

$$DH'_{\mathrm{o}}(z) = \left(-\frac{1}{g}\int_{p_{\mathrm{ref}}}^{p_{\mathrm{z}}} \frac{1}{\rho_{\mathrm{cast}}} dp \right) - \left(-\frac{1}{g}\int_{p_{\mathrm{ref}}}^{p_{\mathrm{z}}} \frac{1}{\rho_{\mathrm{clim}}} dp \right). \tag{2.4}$$

We translated our velocity maximum criterion into finding a peak in $DH'_{\mathrm{o}}(z)$ (i.e. geostrophic streamfunction) within the vertical extent estimate provided by the Gaussian model. Initial results indicated that slight misplacements of the pycnocline in pressure space between the SCV and the climatological profile can lead to large dynamic height anomalies along isobars, which dominated any SCV dynamic signature within the profile. This finding is not surprising given that, away from oceanic margins, the vertical structure of the ocean is almost entirely described by the barotropic and first baroclinic modes (Wunsch, 1997; Szuts et al., 2012). Thus, heaving caused by internal wave motions is an additional source of error in the dynamic height anomaly calculation.

To isolate and remove the impact of first baroclinic mode structures, we decomposed the climatological profile into vertical modes following Gill (1982) and Chelton et al. (1998). Briefly, we solved for the linear dynamical modes brought about by the standard eigenvalue problem of internal wave theory, using a Matlab routine written by Klink (1999). We extracted the first baroclinic horizontal velocity mode (ψ_{BC1}) produced by the routine (e.g. Figure 2.2E) and estimated the corresponding modal amplitude (α_{BC1}) by restricting the modal structure to be zero at p_{ref}, before applying a non-linear least-squares optimization to solve for the best fit to the dynamic height anomaly profile. To avoid over-fitting the $BC1$ projection to $DH'_{\mathrm{o}}(z)$ profile sections with large SCV dynamic signatures, we ignored data

between the vertical extent of the SCV in pressure space, as well as data within the mixed layer. Thus, the dynamic height anomaly attributed to first baroclinic mode structures and the adjusted dynamic height anomaly used for detection purposes are respectively defined as:

$$DH'_{\mathrm{BC1}}(z) = \alpha_{\mathrm{BC1}}\psi_{\mathrm{BC1}}(z), \tag{2.5a}$$

$$DH'_{\mathrm{adj}}(z) = DH'_{\mathrm{o}}(z) - DH'_{\mathrm{BC1}}(z). \tag{2.5b}$$

In practice, the above method performed well in removing large runaway dynamic height anomalies when they appeared in the record by filtering out the impact of first baroclinic mode structures (e.g. Figure 2.2F). However, baroclinic modes are likely an imperfect distinction between SCV structures and other mesoscale flows. Thus, removing the first mode component may delete part of the SCV structure. Our restriction to subsurface-intensified eddies suggests this is only a minor component of the circulation, and we note that the majority of profiles were largely unaffected by this approach (Figure A.3). A more in-depth analysis of our strategy with dedicated SCVs observations would help refine this method further. We used the adjusted dynamic height anomaly ($DH'_{\mathrm{adj}}(z)$) to test for the presence of a local peak in dynamic height anomaly within the vertical extent of each intrusion, rejecting any profiles which did not exhibit this feature, while defining those that passed all the above criteria as spicy or minty-core SCVs.

2.2.6 SCV Characterization

Previous studies suggest that the SCV radius is comparable to their internal Rossby deformation radius (McWilliams, 1985; Pelland et al., 2013; Z. Zhang et al., 2015). Following the methods of Dewar & Meng (1995) and Z. Zhang et al. (2015), we used estimates of SCV scale height (h, converted from dbar to m), core-isopycnal background buoyancy frequency (N_{clim}), and the local Coriolis parameter (f) for each detected SCV to infer the first baroclinic deformation radius and thus an idealized horizontal scale L, defined as:

$$L = \frac{N_{\mathrm{clim}}h}{f}\,. \tag{2.6}$$

While for some cases the above calculation represents the upper-limit of SCV length scales (McWilliams, 1985; Pelland et al., 2013), results from Z. Zhang et al. (2015) and Li et al. (2017) suggest this is a realistic estimate.

We note that the above estimates of h and L do not strongly depend on the assumption that each Argo float profile perfectly pierced the SCV through its center, which is likely false for most cases. Insofar as the three-dimensional SCV shape can be described by separate functions in the vertical and horizontal directions (McWilliams, 1985), the vertical SCV scale h will not depend on the distance of the profile from the eddy center. Likewise, our estimate of the horizontal extent L of an eddy only invokes the background stratification N_{clim} as an additional quantity. However, we also note that our method does not include consideration of the threshold of detectability for SCVs based on individual profiles, which would be influenced by the strength of the SCV, and the position of each profile relative to the SCV core.

2.2.7 SCV Time-series

After detecting SCVs using the above methods, inspection of initial results revealed several instances of individual Argo floats detecting SCVs over consecutive 10-day cycles, suggesting that repeat sampling of the same eddy may be common with Argo. This is not surprising given the Lagrangian nature of Argo floats when stationed at their parking depths, which is often at 1000 m and potentially within the dynamical influence of SCVs. To reduce over-counting when compiling regional statistics, we sorted SCVs according to their float identification and cycle numbers, and grouped detections until they were more than 2 cycles ($\sim$ 30 days) apart of each other. Doing so provided us with time-series of profiles through the same SCV (e.g. Figure 2.3B – D). When gathering SCV statistics such as core isopycnal and vertical thickness, we used the average from all profiles within an individual time-series to represent the SCV in histograms and property maps (see sections 2.3.1 – 2.3.4). Additionally, the locations and dates of consecutive profiles allow for an estimate of SCV drift direction and speed, which can be used to draw inferences regarding the influence of regional SCV

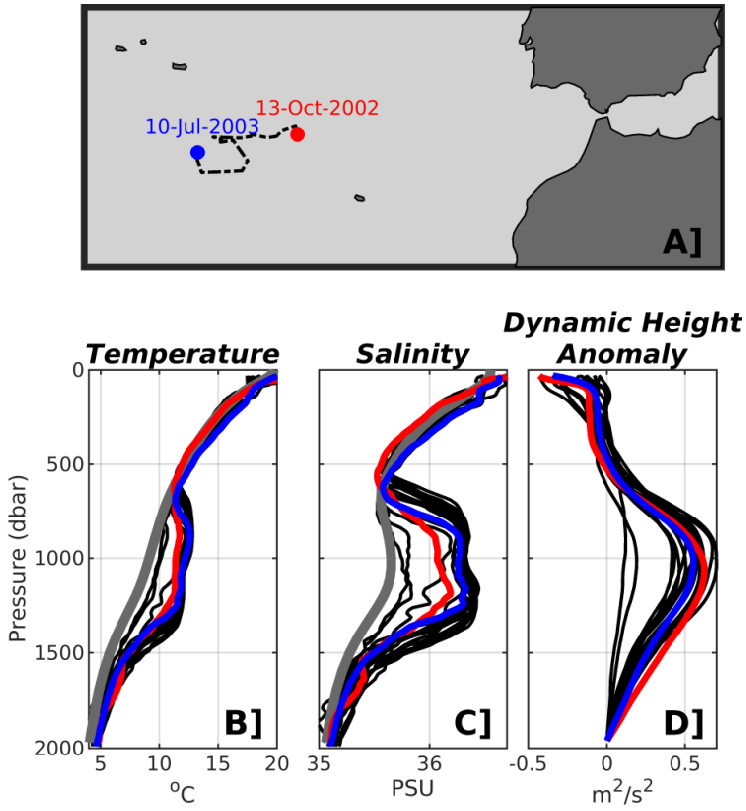

Figure 2.3: (A) Locations of an example SCV time-series from Argo float 6900181, cycles 4-5, 8-12, 15, 18, 20, 22-28, 30-31 off of the northwest African coastline, with the first and final detection shown as red and blue circles. Panels B, C, and D show each casts' temperature, salinity, and dynamic height anomaly profile vs. pressure, respectively. Red and blue curves represent the initial and final casts, and thick gray curves in (B) and (C) show the averaged climatological profile from all casts.

populations.

2.3 Results

After application of the SCV detection algorithm to the global Argo array, we identify 2501 casts piercing spicy-core SCVs, and 1583 casts piercing minty-core SCVs over more than 20 years of available data (Figure 2.4A). By grouping detections from consecutive Argo casts

(see section 2.2.7), we are able to record 383 spicy-core SCV time-series and 169 minty-core SCV time-series, reducing the number of unique SCVs to 1716 spicy-core and 1258 minty-core detections. Visual inspection of their initial locations (Figure 2.4B–E) reveals populations in every ocean basin; additionally, the correspondence between detected SCVs and previously identified Argo SCV populations such as those from G. C. Johnson & McTaggart (2010), Pegliasco et al. (2015), and Z. Zhang et al. (2017) supports the detection criteria described in section 2.2.2.

Spicy-core SCV detections generally outnumber minty-core detections throughout the subtropics and mid-latitudes, and vice-versa for high-latitude regions, as observed in the North Pacific and Southern Ocean. Maps of average core properties and vertical thickness estimates are shown in Figures 2.5 and 2.6 for spicy-core and minty-core SCVs, respectively. Several regions show SCVs with similar hydrographic characteristics, such as widespread spicy-core populations in the Eastern Tropical Pacific, suggesting common formation mechanisms in those regions. In an effort to describe regional SCV variability and identify coherent populations, we divide each ocean into north and south basins, before further separating the eastern and western parts (i.e. Northeast Pacific, see black polygons in Figure 2.4A). We also separate the Southern Ocean due to a high number of coherent minty-core SCV detections, by defining a region poleward of 40°S. We then construct histograms of SCV core statistics to facilitate property comparisons across and within basins. The following sections discuss SCV detections and their statistics organized by ocean basin, highlighting notable hot-spots and coherent SCV populations wherever they appear. A more fine-grained characterization of our detections is further presented for reference in Appendix A.4.

2.3.1 Pacific SCVs

In the Northwest Pacific, we find 249 spicy-core SCVs spatially concentrated along the western boundary, ranging from the Philippine Islands to the east of Japan, up to the latitude of the Kuril Islands chain, with sparser detections throughout the western end of the low-latitude subtropical gyre. Distributions of core hydrographic properties (Figure

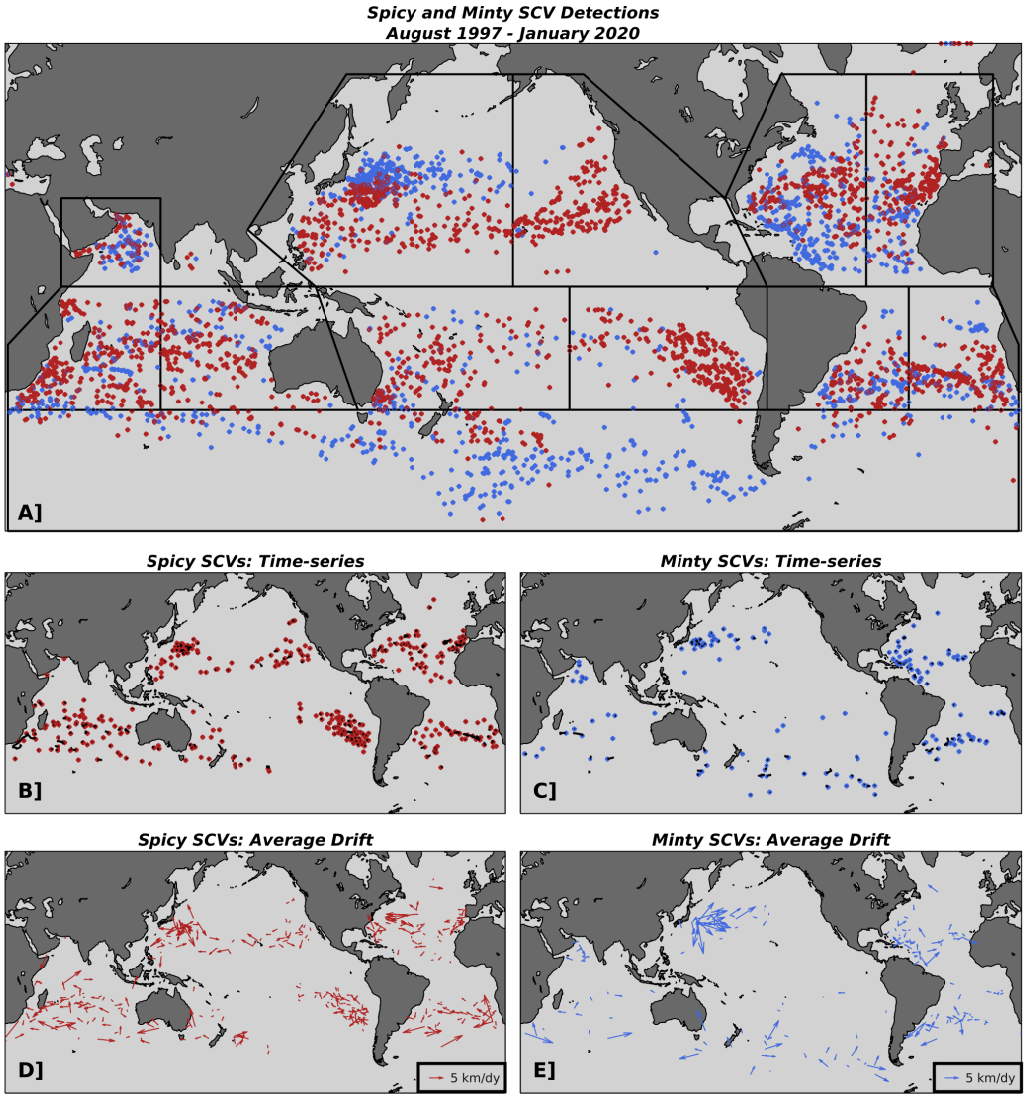

Figure 2.4: (A) Locations of all spicy-core (red) and minty-core (blue) SCVs detected from Argo floats over the period of August 1997 to January 2020. Polygons used to group SCV statistics for regional analyses (Figures 2.7 – 2.9) are shown in black. (B,C) Initial locations of spicy-core and minty-core SCV time-series, shown as red and blue dots respectively, from repeatedly sampled SCVs measured from consecutive Argo float casts. Time-series trajectories are shown as thin black lines. (D,E) Average drift speed and direction (shown as vector arrows) calculated from each spicy-core and minty-core SCV time-series, respectively.

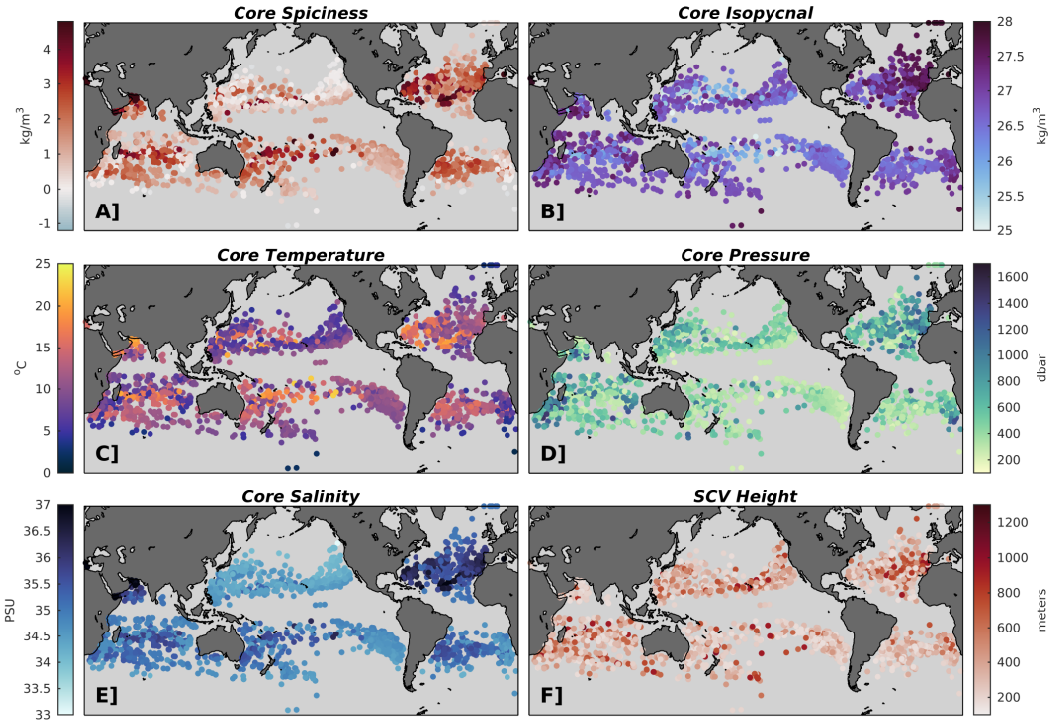

Figure 2.5: Spicy-core SCV detection locations, coloured by (A) core absolute spiciness, (B) core isopycnal, (C) core temperature, (D) core pressure, (E) core salinity, and (F) SCV vertical thickness.

2.7) and their respective scatter maps (Figure 2.5) suggest that at least two overlapping populations exist. Most are found along the western boundary between 26.5 – 27.2 kg m^{-3}, with core temperatures and salinities between 5 – 10°C and 34.2 – 35 PSU respectively; a smaller number of SCVs, mostly within the subtropical gyre, contain cores at 25.8 – 26.2 kg m^{-3}, with core temperatures of 10 – 16°C.

Within the same region, we also identify 274 minty-core SCVs concentrated in the Kuroshio extension at slightly higher latitudes and over a larger geographical area than the co-located spicy-core SCVs (Figure 2.6). In general, the cores of these minty SCVs are found on the same isopycnal range as the larger population of spicy-core SCVs, but with slightly decreased temperature and salinity values. Additionally, the minty-core SCVs show a trend of decreasing temperature and spiciness with latitude (Figure 2.6A and C). Core pressure and vertical thickness distributions are very similar across spicy and minty-core

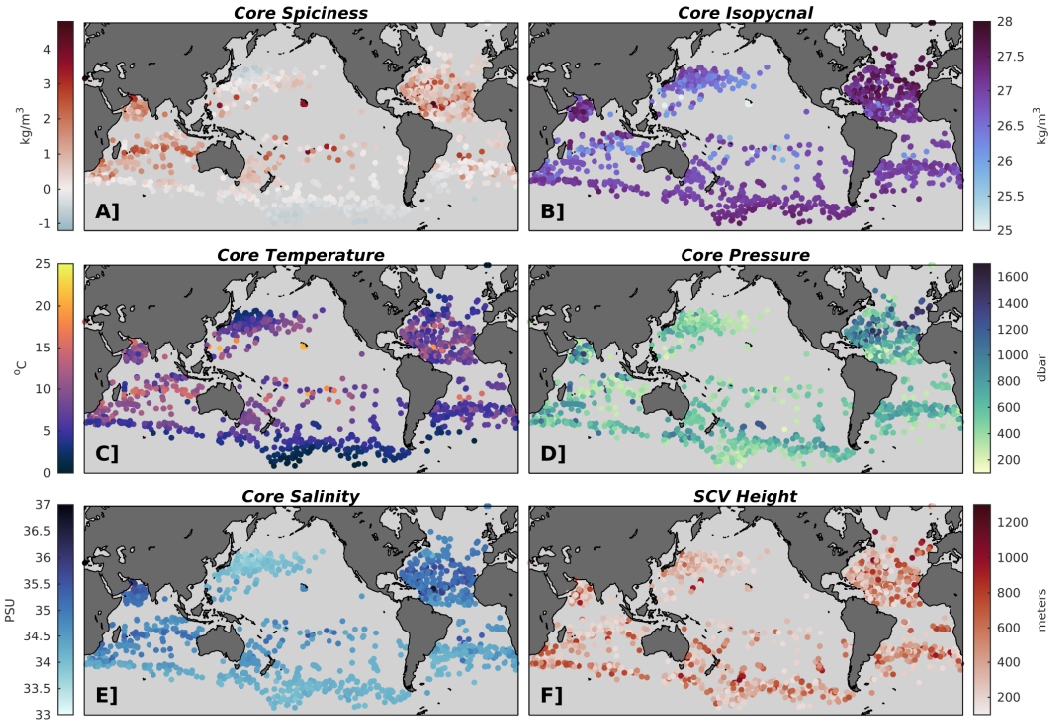

Figure 2.6: Same as Figure 2.5, but for minty-core SCV detections.

SCVs, suggesting that the majority propagate at 300 – 800 dbar, with thicknesses of 500 m or less. A relatively large number of SCV time-series are observed to the east of Japan, with no obvious preference for drift direction, identifying this region as a potential source of long-lived SCVs throughout the Northwest Pacific (Figure 2.4B – E).

In contrast to the northwest populations, the Northeast Pacific is largely characterized by predominately spicy-core SCVs (160 detections versus 10 minty-core) that appear to be one coherent population based on both property distributions and scatter maps (Figures 2.7 and 2.5). Histograms show relatively small spread and indicate that their typical core temperature and salinity range from 6 – 12°C and 34.1 – 34.6 PSU, respectively. Most are found propagating at core pressures and isopycnals of 250 – 700 dbar and 26.2 – 26.8 kg m^{-3} respectively, with typical vertical thickness of 250 – 500 m. Spatially, they are distributed along the eastern boundary from the Baja California Peninsula to Vancouver Island, extending out to the Hawaiian Islands. This pattern can be explained by drift

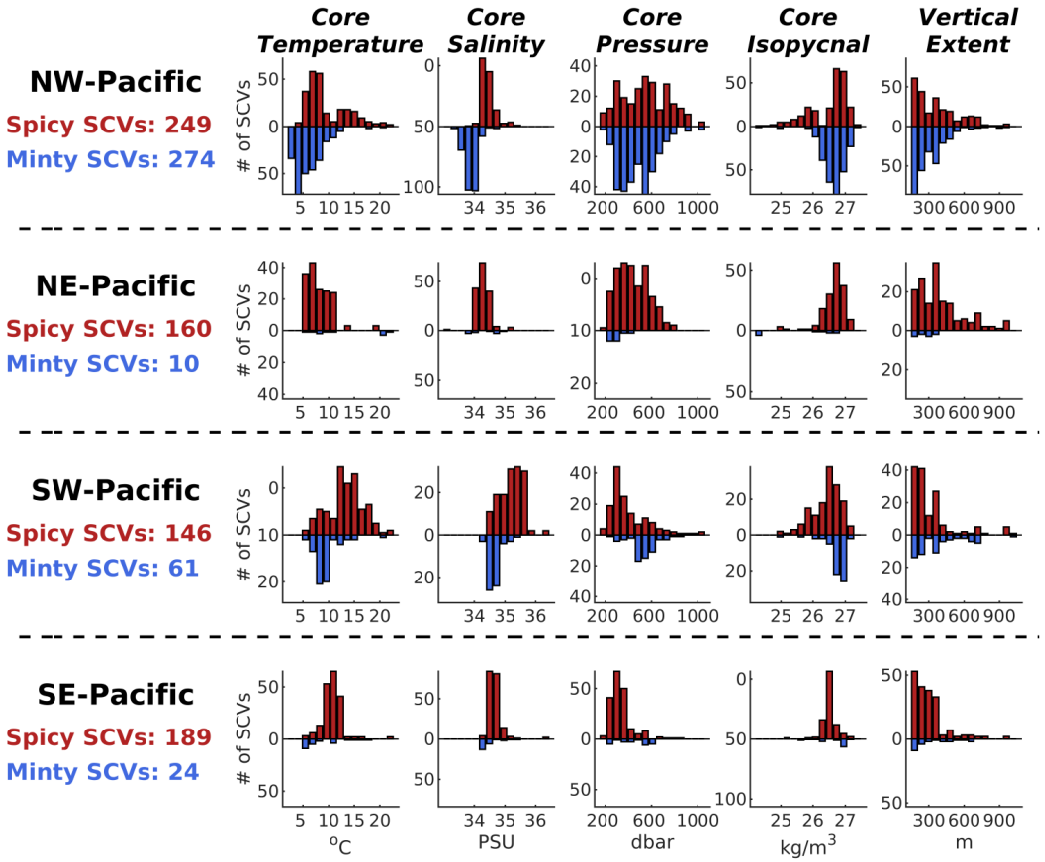

Figure 2.7: Histograms of SCV core temperature, core salinity, core pressure, core isopycnal, and vertical thickness from the northwest, northeast, southwest, and southeast Pacific regions (respectively). Regions are outlined in Figure 2.4. Red bars show spicy-core SCV distributions, and blue bars minty-core SCVs.

observations from the numerous SCV time-series within the region, as evidenced by panels B and D in Figure 2.4, which collectively indicate southwestward propagation from the eastern boundary into the subtropical gyre. Similar to the minty-core population in the Northwest Pacific, SCV property maps in Figure 2.5 indicate that SCV cores become slightly less warm and salty and propagate along denser isopycnals as they are detected more poleward.

SCV spatial distributions within the South Pacific largely mirror those from the North Pacific; both spicy-core and minty-core SCVs are detected in the western end of the basin, whereas spicy-core SCVs dominate detections in the east. Minty-core SCVs in the Southwest

Pacific (61 detections) are mostly observed between Australia and New Zealand and show uni-modal distributions across many properties. Typical SCVs exhibit core temperatures of 5 – 10°C, salinity values of 34.1 – 34.7 PSU, and propagate along core isopycnals between 26.9 – 27.1 kg m^{-3} at depths of 500 – 700 dbar (Figure 2.7). However, despite consistent properties across detections in this region, there is a notable lack of SCV time-series, suggesting that these may be relatively short-lived features. Spicy-core SCVs (146 detections) are also prevalent east of Australia, notably with more time-series observations, but at slightly lower latitudes and with additional scattered observations spread throughout the western end of the subtropical gyre. Compared to the minty-core detections, spicy-core SCVs show a much wider range of SCV core values with several peaks; however, mapped properties in Figure 2.5 show ∼3 distinct populations occupying waters to the west, north, and southeast of New Zealand.

The Southeast Pacific shares remarkably similar population characteristics with the Northeast Pacific spicy-core detections, albeit with less spread. Distributions from the 189 spicy-core detections in the region show SCVs with core temperatures and salinity values between 8 – 12°C and 34.1 – 34.8 PSU, respectively, which propagate along a small range of isopycnals (26.2 – 26.8 kg m^{-3}). They are concentrated along the coast of Chile and extend into the subtropics, as indicated by the spatial extent of detections and the numerous SCV time-series showing predominantly northwestern propagation (Figure 2.4). As for the Northeast Pacific SCVs, detections exhibit a pattern of SCV cores becoming slightly cooler and fresher as they are observed more poleward. The similar distributions and spatial patterns of both the northeastern and southeastern spicy-core detections in the Pacific suggests that a common generation mechanism consistently produces spicy-core SCVs along the eastern boundary of the Pacific, which are capable of reaching the interiors of the subtropical gyres.

2.3.2 Atlantic SCVs

The North Atlantic exhibits more spatial variability in detections when compared to the other basins, possibly because of the relatively smaller basin width; however several notable

patterns emerge. Of the 163 spicy-core SCVs identified throughout the Northwest Atlantic, a population of relatively warm (15 – 20°C) and salty (36.0 – 36.3 PSU) SCVs is observed extending northeast from the Florida coastline into the central North Atlantic along the $\sim$ 26.5 isopycnal, at depths of roughly 300 – 700 dbar (shown clearly by the high spiciness values in Figure 2.5A). In the Eastern North Atlantic, where we identify 152 spicy-core SCVs, a population of SCVs with slightly colder core temperatures (10 – 15°C) propagating along denser isopycnals ($\sim$ 27.5 kg m^{-3}) appears to originate along the eastern boundary near the Iberian peninsula, overlapping with the western population throughout the central Atlantic (Figure 2.8). SCV time-series detections (Figure 2.4) further indicate that these distributions belong to two separate populations, which emanate from the Gulf Stream region in the western Atlantic and the Mediterranean outflow in the east, and eventually overlap in the central Atlantic, albeit at different depths. Finally, the low-latitude North Atlantic also includes a separate smaller, coherent population of spicy-core SCVs. Time-series from this population indicate that they propagate westward, which, coupled with their spatial property distributions in Figure 2.5, suggests a source near the Canary Islands.

Minty-core SCVs in the Northwest Atlantic (212 detections) are heavily concentrated along the western boundary, from the northeastern coast of Brazil to Nova Scotia, whereas the 86 detections in the Northeast Atlantic are largely found in two clusters centered near the Canary Islands and off the coast of Mauritania. Distributions of core properties for both sub-basins show significant spread across all properties, yet indicate that most minty-core SCVs propagate along isopycnals ranging from 27.0 – 28.0 kg m^{-3}, with core salinity values of 34.5 – 35.5 PSU (Figure 2.8). The Western North Atlantic, however, exhibits peaks at slightly colder core temperatures ($\sim$ 4 – 6°C versus 7 – 9°C), and at the 27.0 – 27.2 kg m^{-3} isopycnal range (versus a more even distribution in the east). SCV property maps in Figure 2.6 show less coherent spatial patterns in the Western North Atlantic than in the east, where in general the SCVs near the Canary Islands exhibit slightly saltier cores than the Mauritania population to the south. SCV time-series are found all throughout the western population of minty-core SCVs, whereas they are only detected within the Canary population in the east (Figure 2.4).

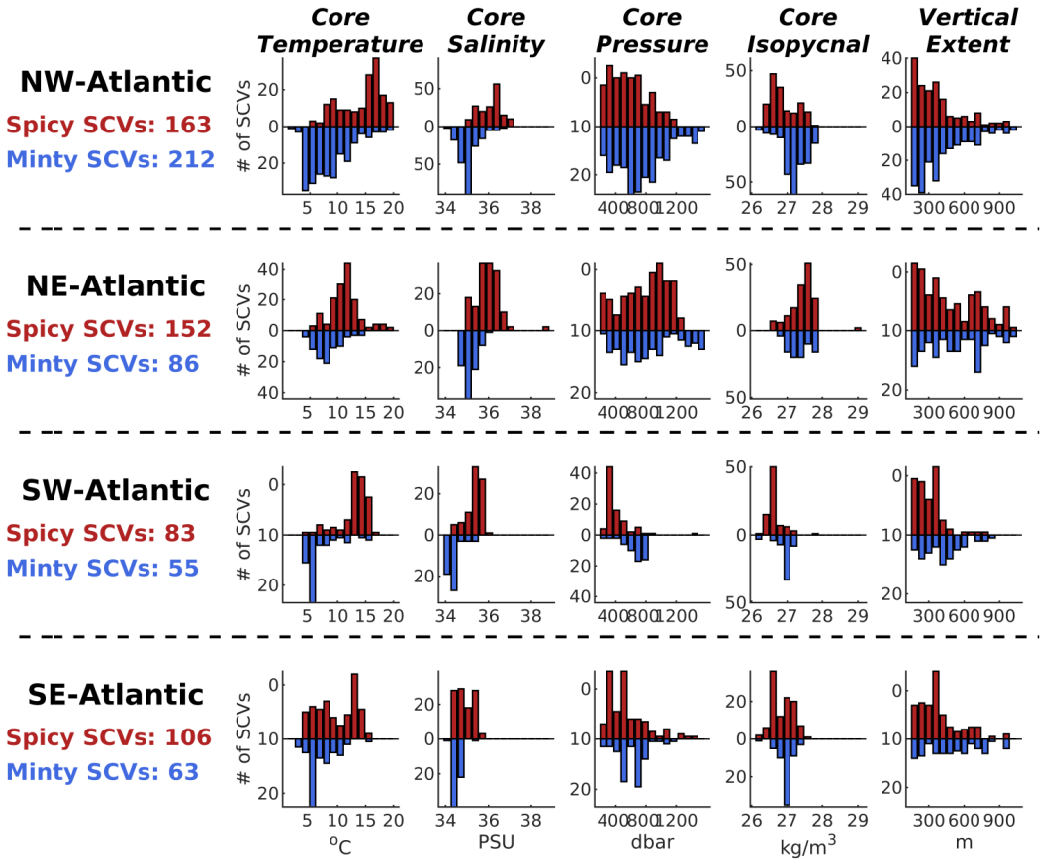

Figure 2.8: Same as Figure 2.7, but for the northwest, northeast, southwest, and southeast Atlantic regions (respectively).

The South Atlantic basin is largely defined by a zonal band at roughly 30°S of both spicy and minty-core SCVs, extending between Namibia and the southernmost extent of Brazil (Figures 2.5 and 2.6), with westward propagating SCV of both types (Figure 2.4). The 83 spicy-core SCVs throughout the Southwest Atlantic show uni-modal property distributions, with SCVs generally propagating at $\sim$ 400 dbar along the 26.5 kg m^{-3} isopycnal, while exhibiting core temperature and salinity values ranging between 12 – 16°C and 35 – 36 PSU respectively (Figure 2.8). Minty-core SCVs in both the West (55 detections) and the East (63) South Atlantic have remarkably similar properties, suggesting one coherent population propagating at roughly 600 – 800 dbar along the $\sim$ 27.0 kg m^{-3} isopycnal, with core temperatures of roughly 4 – 6°C, and salinity values between 34.0 – 34.5 PSU. In

contrast, the Southeast Atlantic spicy-core SCV distributions (106 detections) are bi-modal, but show similar peaks in core temperature, salinity, pressure, and isopycnal as in the western spicy-core SCVs. The secondary peak across property distributions results from a separate population of deeper ($\sim$ 800 dbar versus $\sim$ 400 dbar) spicy-core SCVs with relatively colder (5 – 10°C) and fresher (34.0 – 34.5 PSU) cores that are zonally distributed along the eastern boundary between South Africa and Angola (seen clearly in Figure 2.5A). This population also exhibits the pattern observed in the spicy detections within the eastern regions of the Pacific and North Atlantic, where SCV spiciness decreases poleward.

2.3.3 Indian SCVs

SCV detections within the North Indian Ocean are concentrated within the Arabian Sea, where we found 40 spicy-core and 64 minty-core detections. Spicy-core SCVs with relatively warm and salty cores ($\sim$ 17°C and ¿37 PSU) are detected near the Gulf of Oman and the Red Sea outflow regions. However, detections in the offshore region to the east show more heterogeneous properties, as evidenced by the spread in histograms from Figure 2.9. Notably, the only spicy-core SCV time-series detected in this region are confined to the outflow regions (Figure 2.4). Minty-core SCVs are mostly found overlapping with the offshore spicy-core SCVs in the central Arabian Sea, where they also exhibit significant spread across core properties, albeit with significantly more numerous time-series detections as evidenced by Figure 2.4. While both spicy and minty SCV core pressures show a wide range, nearly all SCVs exhibit vertical thickness of less than 400 meters.

In the Southern Indian Ocean, we detect 313 spicy-core SCVs mostly distributed along zonal bands with contrasting core properties between Madagascar and Australia (Figure 2.5). The center of the basin between 20 – 25°S exhibits SCVs with relatively high values of temperature and salinity compared to the zonal bands at lower and higher latitudes. SCV time-series are prevalent throughout the region and generally show westward propagation, with slightly more observations in the central zonal band. This result, coupled with the similarities in distributions across both eastern and western spicy-core SCVs (Figure 2.9),

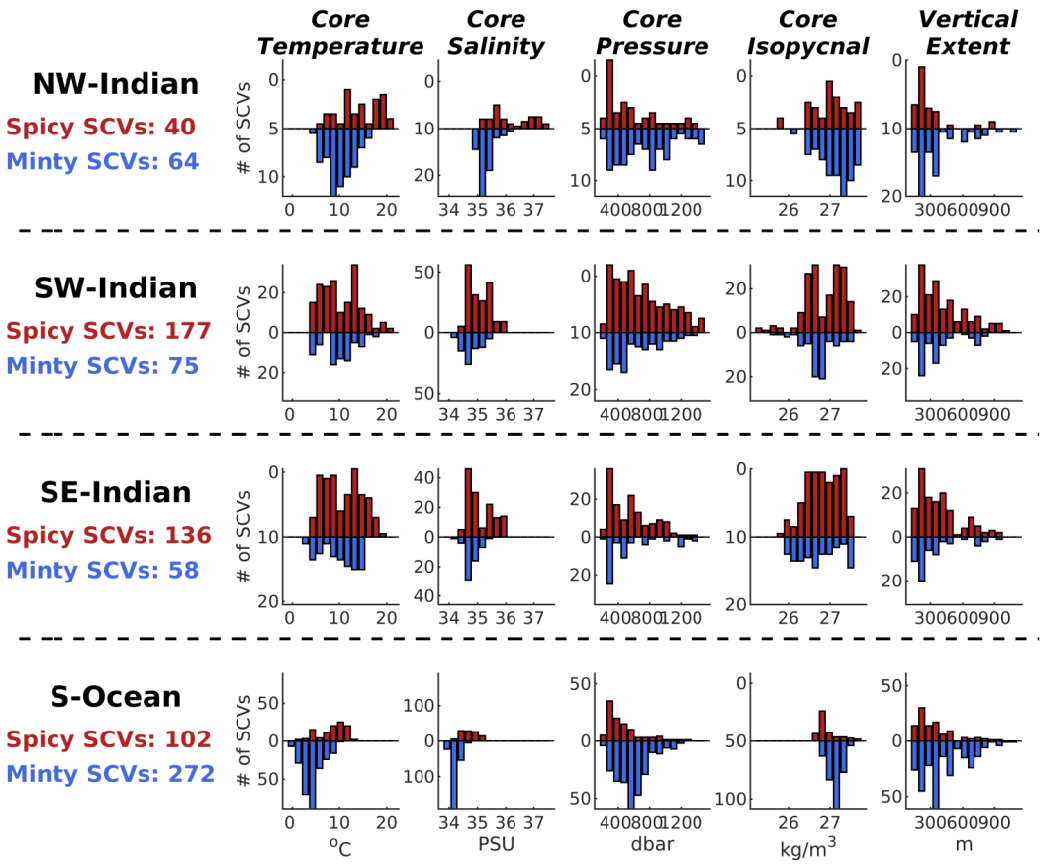

Figure 2.9: Same as Figure 2.7, but for the northwest, southwest, and southeast Indian and Southern Ocean regions (respectively).

suggests a connection across the basin between the two populations. Minty-core SCVs (133 detections) are similarly identified at the same low and high latitudes as spicy-core SCVs, but in contrast are largely absent throughout the 20 – 25°S band. Despite large spread in core distributions (Figure 2.9), SCV property maps in Figure 2.6 again show similarities across zonal sections. Finally, the southeast coast of South Africa and to a lesser extent the waters off of Tanzania are additional zones of spicy and minty-core SCV observations. However, property maps suggest high variability in their characteristics, despite several prevalent spicy-core time-series detections.

2.3.4 Southern Ocean SCVs

Minty-core SCVs with coherent properties are identified along a high-latitude band throughout the Southern Ocean (defined here as poleward of 40°S). Distributions (Figure 2.9) and SCV property maps (Figure 2.6) show remarkable consistency across detections, with a notable pattern of slightly greater core temperature ($\sim$ 5 – 8°C versus $\sim$ 0 – 5°C) within the high latitude Indian Ocean compared to the Pacific. Nearly all detected SCVs propagate at core pressures of 300 – 800 dbar along core isopycnals ranging from 26.9 – 27.5 kg m^{-3}, which, coupled with similarities in core temperature and salinity, suggest a common formation mechanisms throughout the Southern Ocean in the vicinity of the ACC. Given their proximity to the minty-core detections, spicy-core SCVs identified at high latitudes throughout the South Indian basin and to the southeast of New Zealand in the Pacific may also have a generation source associated with the ACC.

2.4 Discussion

Global and regional maps of SCV properties (Figures 2.5 through 2.9) reveal several notable SCV populations with coherent properties, such as the wide-spread spicy SCVs along the eastern boundary of the Pacific Ocean and the zonal band of minty SCVs throughout the Southern Ocean. These results strongly suggests generation of SCVs with similar hydrographic features in those regions. However, in order to estimate the regional frequency of SCV generation, we need to account for the uneven spatial sampling density of Argo. Notable locations such as the Kuroshio extension have a much higher number of Argo casts within the record than the Southern Ocean, for example, as observed after binning Argo casts into 4° x 4° latitude/longitude cells (Figure 2.10A). After accounting for this discrepancy in sampling density, we estimate the SCV frequency by binning detections within the same grid, as shown in panels B – D of Figure 2.10. This provides a metric to identify zones with relatively high frequency of SCV observations that are also characterized by consistent SCV properties.

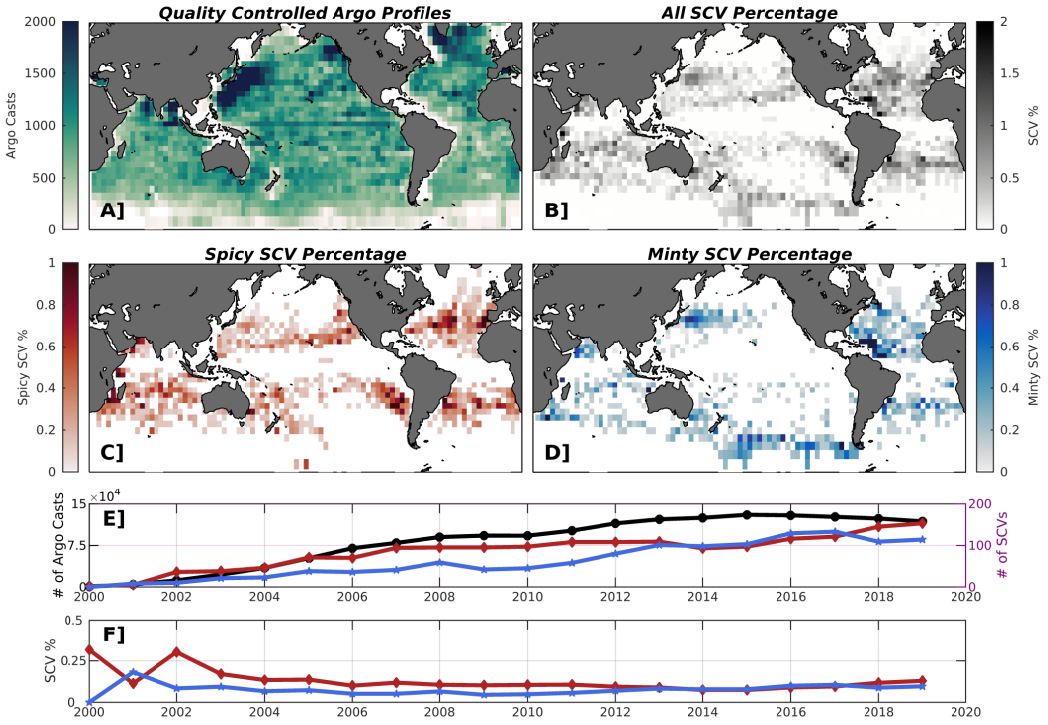

Figure 2.10: (A) Number of quality controlled Argo profiles within 4° x 4° longitude/latitude grid boxes. (B) Percentage of unique SCV detections. Panel C and D show the gridded percentages from spicy-core and minty-core detections (respectively). (E) Time-series of the total number of quality controlled Argo casts (black line, left y-axis) and the total number of unique spicy-core and minty-core detections (red and blue lines, right y-axis). (F) Annual SCV percentage of spicy-core (red) and minty-core (blue) SCVs.

Figures 2.4 and 2.10 reveal several remarkable hot-spots that exhibit the presence of SCV time-series, a higher spatial density of detections, and relatively coherent SCV-core properties. Notably, these criteria are common in close proximity to: 1) major eastern boundary upwelling systems (EBUS); 2) outflow from marginal seas such as the Mediterranean and Red Seas; 3) large oceanic fronts such as the ACC and those associated with western boundary current separation. The following sections explore possible generation mechanisms associated with these regions. To do so, we gather populations of SCVs near these oceanic features and connect their characteristics with regionally persistent currents

and water masses. When necessary, to characterize hydrographic profiles of water masses, we identify approximate temperature and salinity curves by averaging Argo profiles near their geographic source regions using 5° latitude/longitude cells. We also highlight persistent fronts using a mean sea surface dynamic topography derived from jointly analyzed data of drifters, satellite altimetry, wind, and gravity for the decade 1992-2012 (retrieved online from http://apdrc.soest.hawaii.edu/datadoc/mdot.php). Fronts associated with the ACC are demonstrated using results from the WOCE Southern Ocean Atlas (Orsi & Whitworth, 2005).

2.4.1 Poleward Flow Along Eastern Boundaries

The four major EBUS in the Pacific and Atlantic are the California, Peru-Humboldt, Canary, and Benguela upwelling systems. These regions are found along the eastern flanks of their respective subtropical gyres, driven by persistent equatorward winds along their meridional coastlines (Bakun & Nelson, 1991). The resulting equatorward currents in each EBUS (the California Current, the Peru-Humboldt Current, the Canary Current, and the Benguela Current, respectively) carry high-latitude waters, whereas characteristic undercurrents flowing at mid-depths over the shelf and slope (Chavez & Messié, 2009) carry subsurface equatorial waters poleward. The global SCV detections highlight each EBUS as sites of frequent long-lived SCV generation, as evidenced by Figures 2.4 and 2.10; thus the unique wind-forced dynamics of these systems appear to promote SCV generation.

Model simulations of eastern boundary undercurrents (Molemaker et al., 2015) have shown that they develop anticyclonic vertical vorticity along their poleward path due to the effect of bottom drag against the continental slope. Separation from the slope near ridges or areas of strong topographic curvature causes offshore diversion, followed by centrifugal and submesoscale instabilities, vigorous mixing, and organization of the flow into anticyclonic vortices (Dewar et al., 2015; Molemaker et al., 2015; Southwick et al., 2016). To explore the role of these undercurrents in the generation of SCVs detected near EBUS, we compare the temperature and salinity of equatorial surface currents and poleward undercurrents with

similar T-S curves from SCV detections.

In the North Pacific, the California Current advects relatively cold, fresh and oxygen-rich Pacific Subarctic Upper Water (PSUW) equatorward from roughly 45 ° N (Lynn & Simpson, 1987; Thomson & Krassovski, 2010), whereas the poleward California Undercurrent transports relatively warm, salty and oxygen-poor Pacific Equatorial Water (PEW) as far North as the Aleutian Islands (Thomson & Krassovski, 2010). Panel A in Figure 2.11 provides details from a subset of SCVs detected off of the California upwelling system. Spicy-core SCVs are detected from the Baja California Peninsula to as far as Vancouver Island, with spatial distributions and SCV time-series suggesting southwestward propagation towards the Hawaiian Islands, consistent with β-plane drift westward and equatorward (Cushman-Roisin & Beckers, 2011). A representative profile off of Baja California (star marker in Figure 2.11A) reveals a typical peak in salinity centered just below the salinity minimum at 200 dbar, surrounded by anomalously high temperatures throughout the SCV extent. These characteristics, along with the uni-modal distribution of core isopycnal centered at roughly 26.6 kg m^{-3}, match descriptions of 'Cuddies' from the literature, likely generated from the California Undercurrent via the processes outlined above (J. J. Simpson & Lynn, 1990; Chaigneau et al., 2011; Pelland et al., 2013; Collins et al., 2013; Garfield et al., 1999; Li et al., 2017; Steinberg et al., 2018). Indeed, T-S diagrams of detected SCVs versus curves of PEW (dashed black curve in Figure 2.11A) and PSUW (solid black curve) show a high influence of PEW in their cores, despite many being detected well offshore of the coastline.

Equatorward offshore flow in the South Pacific is dominated by the Peru-Humboldt Current, which transports relatively cold and fresh Subantarctic Surface Water (SASW) from the north of the Subantarctic Front along the coasts of Chile and Peru (Schneider et al., 2003). Countering the surface flow is the Peru-Chile Undercurrent, of similar origin to the California Undercurrent, wherein PEW water flows from the equator southward along the continental slope of South America (G. C. Johnson & McTaggart, 2010). Panel B in Figure 2.11 outlines a subset of spicy-core SCVs detected off of the Peru-Humboldt upwelling system. A representative SCV from the region (star marker in 2.11B) reveals typical SCV cores below the halocline, with pronounced salinity maxima at roughly 300 – 500 dbar, and

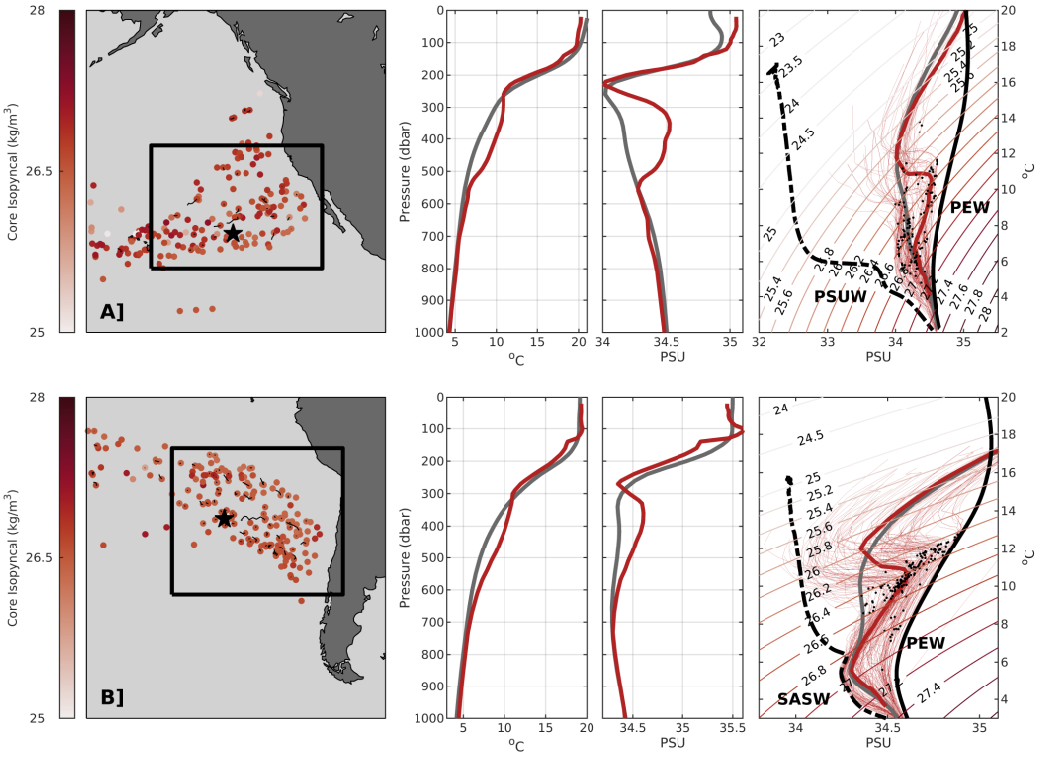

Figure 2.11: (A) Locations, colored by core isopycnal, and hydrographic properties of spicy-core SCVs detected near the California upwelling system. Thin black lines indicate propagation of SCVs with multiple casts. Temperature and salinity profiles and diagrams are constructed from the star marker profile (Argo float 4900691, cycle 85, solid red curve), with the grey curve representing the climatological profile for that cast's location and month. T-S curves for all other detections with the boxed region are shown as thin red lines, with black dots representing core temperature and salinity values. (B) Same as (A), but for the spicy-core SCVs off of the Peru-Humboldt upwelling system, with the example profile from Argo float 3900328 cycle 141. Approximate curves of Pacific Equatorial Water (PEW, both panels), Pacific Subarctic Upper Water (PSUW, panel A) and Subantarctic Surface Water (SASW, panel B) are also shown.

anomalously warm temperatures down to 600 dbar or deeper. A relatively large number of SCVs in this region are sampled multiple times by the same floats (thin black lines) and show northwestward propagation, consistent with β-plane drift. Descriptions of anticyclonic eddies in this region (G. C. Johnson & McTaggart, 2010; Chaigneau et al., 2011; Colas et

al., 2012; Hormazabal et al., 2013; Combes et al., 2015) attribute formation to the same undercurrent processes outlined above for Cuddies, leading to spicy-core SCVs. Similar to the North Pacific population, T-S diagrams suggest that SCVs in this region contain a high percentage of PEW versus SASW, placing their origin within the undercurrent.

The Canary Current system extends from the coast of Morocco to Cape Blanc, Mauritania and is distinct from the other EBUS due to opposite hydrographic characteristics. The equatorward current advects relatively warm and salty North Atlantic Central Water (NACW) equatorward, whereas relatively cooler, fresher, and nutrient-rich South Atlantic Central Water (SACW) is advected poleward at the surface by the Mauritania Current (Kämpf & Chapman, 2016), and similarly to the south of Cape Blanc by a poleward undercurrent along the shelf break (Schütte et al., 2016; Klenz et al., 2018). Panel A in Figure 2.12 shows the Mauritania detections, which in contrast to other EBUS are characterized by predominately minty-core SCVs. From the limited observations, histograms suggest that most minty-core SCVs off of Mauritania propagate between 400 – 800 dbar along the 26.9 – 27.4 isopycnal surfaces, with typical core temperatures and salinities ranging between 6 – 10°C and 34.8 – 35.2 PSU respectively. Profiles from the region (see star marker example in Figure 2.12A) reveal that most cores are positioned well below the base of the shallow pycnocline, where they appear as a homogeneous layer of relatively cold and fresh water that often represents the salinity minimum. The T-S diagram for the population clearly shows an influence of SACW in their cores, which is relatively cold and fresh in the North Atlantic (hence, the minty-core populations). Several other studies have reported on similar subsurface eddies with cores of anomalously low temperature and salinity in the Mauritania region, often described as "dead zone" anticyclonic mode water eddies (ACME) because of the low oxygen concentration (Karstensen et al., 2015; Schütte et al., 2016; Grundle et al., 2017; Thomsen et al., 2019; Hauss et al., 2016), with several found to last up to 200 days (Karstensen et al., 2017). Thus, while further observations are still needed, the above results suggest SCVs generation in this region via undercurrent instabilities, likely at prominent topographic features (Schütte et al., 2016), which encapsulate volumes of SACW before advection westward into the subtropical gyre.

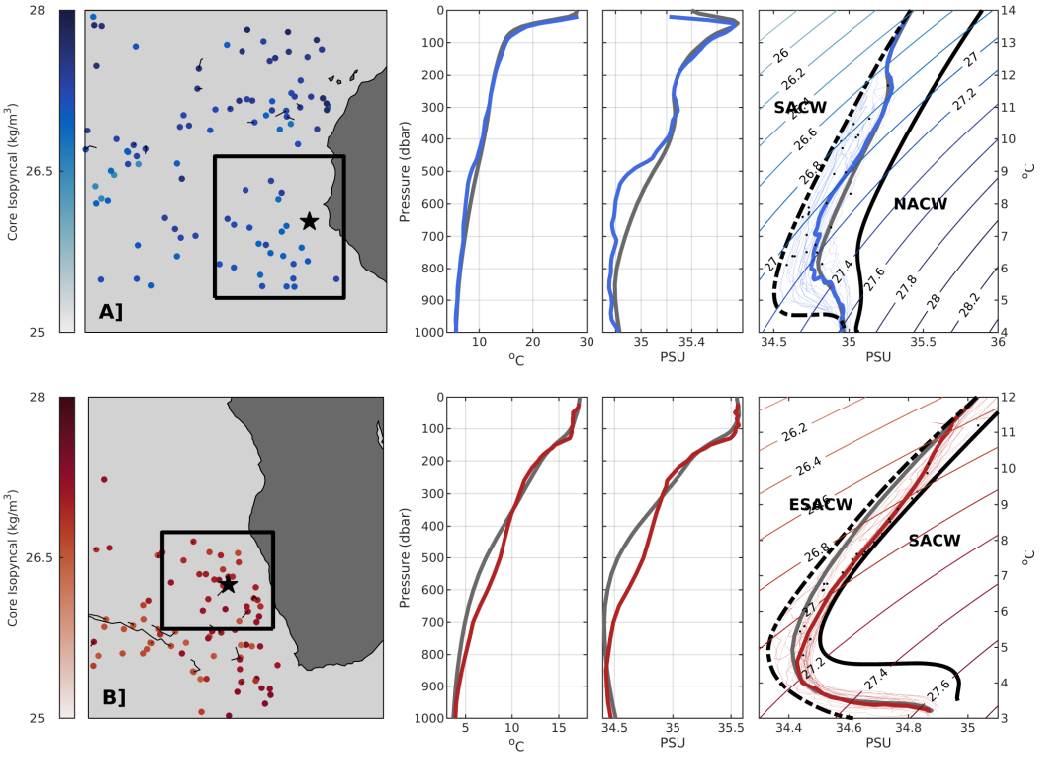

Figure 2.12: (A) Same as panel A in Figure 2.11, but for the minty-core SCVs detected off of the Mauritania coastline. The example profile is from Argo float 6900919 cycle 130. (B) Same as (A), but for the spicy-core SCVs detected off of the Benguela upwelling system, with the example profile from Argo float 1901238 cycle 38. Approximate curves of South Atlantic Central Water (SACW, both panels), North Atlantic Central Water (NACW, panel A) and Eastern South Atlantic Central Water (ESACW, panel B) are also shown.

The Benguela upwelling system along the west coast of Africa in the South Atlantic is driven by the equatorward Benguela Current, which carries cold Eastern South Atlantic Central Water (ESACW) from Africa's southern tip to roughly 15 – 16 ° S. At its northernmost extent, the Benguela Current meets the poleward Angola Current, which transports relatively warmer and saltier SACW (as opposed to the colder and fresher counterparts in the North Atlantic) to form the Angola-Benguela front zone (Lass & Mohrholz, 2008). The Angola current periodically (typically September to November and February to April) breaks through the front to continue poleward as the Benguela Undercurrent along the shelf (Lass

et al., 2000; Mohrholz et al., 2001), supplying subsurface SACW to the northern Benguela system (Siegfried et al., 2019). Panel B in Figure 2.12 describes the spicy-core SCVs detected off of Namibia, which show generally similar distributions in core properties to the Mauritania minty-core SCVs. An example profile for the region shows a core of relatively warm and salty water at roughly the same depth as the example shown for Mauritania. Similar to the North Atlantic minty-core SCVs off of Mauritania, T-S diagrams suggest that Benguela spicy-core SCVs contain higher percentages of SACW, indicative of an origin within the Benguela Undercurrent. Pegliasco et al. (2015) documented subsurface anticyclonic eddies originating from the Benguela Current, while model simulations from Frenger et al. (2018) also suggested that similar, low-oxygen eddies in the region are generated via undercurrent instabilities. T-S signatures of the SCVs generated within that study largely agree with our Benguela detections, providing more evidence of an origin within the undercurrent.

In summary, our results highlight the eastern boundary of the Pacific Ocean as significant sources of long-lived and far-reaching SCVs. This conclusion mirrors those of several previous studies (G. C. Johnson & McTaggart, 2010; Pelland et al., 2013; Frenger et al., 2018), which suggest that these SCVs could modify the mean properties of the Pacific subtropical gyres by introducing warm, salty, and oxygen-poor/nutrient-rich PEW waters. A similar mechanism may also occur in the Atlantic, via westward propagation of SACW waters, but on a smaller scale given the large disparity in detections. Regardless, SCVs generated from these systems may alter the characteristics of both local and adjacent water masses by exporting poleward undercurrent signatures away from EBUS, while also contributing to subtropical gyre tracer budgets (Frenger et al., 2018).

2.4.2 Marginal Sea Overflow

Dense water outflows originating from marginal seas and continental shelves are major components of the Earth climate system, given their contributions to intermediate and deep water masses of the world's oceans (Stewart, 1982; Vic et al., 2015). After flowing into the open ocean, instability processes govern the dispersal of overflow waters, which can take

place over hundreds or thousands of kilometers depending on the basin dynamics (Legg et al., 2009; Vic et al., 2015). For example, overflow from the Mediterranean encounters a region with relatively low background eddy activity, allowing for a gravity current which, after achieving neutral buoyancy, is deflected to form a boundary-intensified poleward flow (Bower et al., 1997; Legg et al., 2009) similar to an EBUS undercurrent. Other notable outflows, such as the Persian Gulf outflow near the Gulf of Oman and the spread of Red Sea Water in the Gulf of Aden, equilibrate at shallower depths and encounter vigorous mesoscale variability which actively participates in spreading the dense plumes (Vic et al., 2015; Morvan et al., 2019). Given their ability to transport water mass volumes over significant distances, SCVs could play a role in spreading these overflow waters away from the formation regions.

Perhaps the most notable and well studied examples are the Mediterranean outflow eddies ('Meddies'). Large segments of the boundary-intensified overflow jet have been shown to separate near the southwestern tip of the Iberian peninsula in the form of warm, salty Mediterranean Water lenses of roughly 20 km diameter (Bower et al., 1997; Richardson et al., 2000; McWilliams, 2019), with one or two vertically aligned cores typically centered between 800 and 1200 m (Bashmachnikov et al., 2015). Those that avoid collision can last for several (4–5) years, propagating as far as the mid-Atlantic ridge (Richardson et al., 2000; Ménesguen et al., 2012; Barbosa Aguiar et al., 2013) before dissipation by double-diffusive mixing (Radko & Sisti, 2017). With estimates suggesting that they support about 50% of the westward salt flux from the Mediterranean (Bower et al., 1997; Richardson et al., 2000), these SCVs have a far-reaching impact on the tracer budget of the North Atlantic, in addition to their contribution to the Mediterranean salt tongue, one of the prominent hydrographic features of the mid-depth North Atlantic (Richardson et al., 2000).

Panel A in Figure 2.13 outlines a subset of spicy-core SCVs identified near the Mediterranean outflow. Temperature and salinity profiles from the population are in good agreement with previous descriptions of Meddies, showing large temperature (~ 4°C) and salinity (~ 1 PSU) anomalies centered at roughly 1000 dbar. As reported in other studies, a large number contain two cores at roughly 800 and 1200 dbar and are sampled over consecutive Argo cycles for many months (see Figure 2.3 for a notable example). The adjacent region next to the

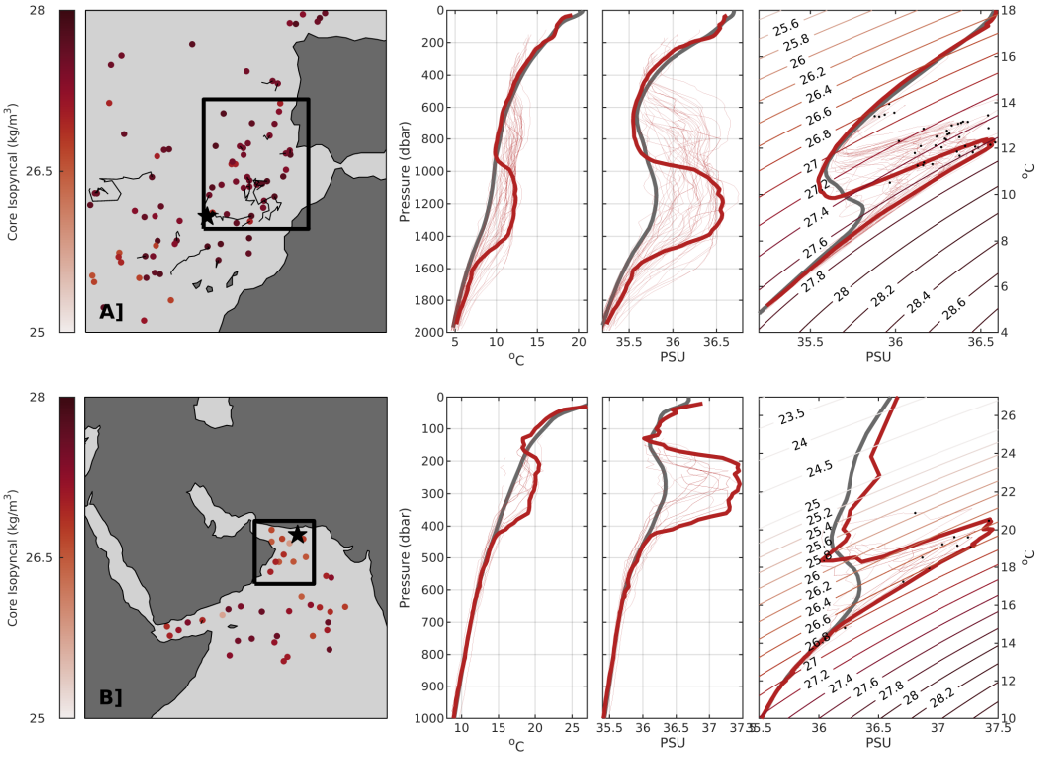

Figure 2.13: (A) Locations, colored by core isopycnal, and hydrographic properties of spicy-core SCVs detected near the Mediterranean outflow. Thin black lines indicate propagation of SCVs with multiple casts. Temperature and salinity profiles and diagram are constructed from the star marker profile (Argo float 1900349, cycle 8, solid red curve), with the grey curve representing the climatological profile for that cast's location and month. Data for all other detections with the boxed region are shown as thin red lines, with black dots representing core temperature and salinity values. (B) Same as (A), but for spicy-core SCVs detected near the Gulf of Oman, with the example profile from Argo float 2902387, cycle 159.

Mediterranean outflow also exhibits some of the highest frequency in SCV detection across the ocean ($\sim$ 1% of all Argo casts in that region, Figure 2.10), with panel D in Figure 2.4 suggesting that many are long lasting. Together, these results support the role of Meddies in modulating the heat and salt budget of the North Atlantic by periodically advecting volumes of Mediterranean water, often over several thousand kilometers.

The Arabian Sea is also influenced by two separate outflows originating in the Persian

Gulf and the Red Sea, which settle at 250–300m and 600–1000m depths into the Gulf of Oman and into the Gulf of Aden, respectively (Morvan et al., 2019). In contrast to the Gulf of Cadiz with Mediterranean outflow water, the Arabian Sea is home to a relatively energetic mesoscale eddy field that provides a different dynamical regime for the spreading of outflow waters (Bower & Furey, 2012; Carton et al., 2012; Morvan et al., 2019; Vic et al., 2015). Mesoscale surface eddies have been shown in modelling studies and in-situ observations to divert the outflow paths away from the coast, advecting them instead along curved trajectories corresponding to the local eddy vorticity (Carton et al., 2012). As these eddies approach the coast, frictional effects due to the slanted bottom boundary layer generate opposite-signed relative vorticity on the slope in the form of elongated filaments of outflow waters. Strong lateral shear leads to instabilities that break apart these filaments into submesoscale vortices with cores of outflow water, which then propagate away from their region of formation if paired with a surface eddy (Molemaker et al., 2015; Morvan et al., 2019; Vic et al., 2015).

Panel B in Figure 2.13 shows a collection of detections identified near the Gulf of Oman. Profiles indeed show anomalous cores of hot and salty water at roughly 200 – 300 dbar, indicative of Persian Gulf overflow waters, and compare well with previously reported anticyclonic lenses observed in this region (L'Hégaret et al., 2016). However, as noted by Bower & Furey (2012) and L'Hégaret et al. (2016), SCVs at these outflows are generally short-lived due to their generation along western boundaries, where strong horizontal shear by mesoscale eddies and westward self-propagation back towards the source region may lead to rapid destruction.

As shown in previous studies, the generation of SCVs at major outflows plays a non-negligible role in transport and dispersion of these regionally important water masses. The same mechanism responsible for producing SCVs at EBUS (subsurface boundary current separation) generates Meddies, while SCVs generated within the Arabian Sea outflows appear to be more ephemeral due to their formation within more energetic western boundary systems. This further highlights the importance of dynamical differences along eastern versus western ocean boundaries. In more quiescent environments found near eastern boundaries, SCVs are capable of transporting origin water masses over great distances, whereas vigorous

mesoscale activity along western boundaries may confine their regional reach.

2.4.3 Mode Water Eddies

As revealed by Figures 2.4 and 2.10, frequent and long-lived SCVs occur within regions of mode water formation. Mode waters originate from deep mixed layers caused by winter convection (Hanawa & Talley, 2001; Xu et al., 2016), occurring in conjunction with persistent fronts that often separate these homogeneous water masses from more stratified waters. Notable examples include subtropical mode waters associated with the western boundary current extensions of the subtropical gyres (the Kuroshio, Gulf Stream, East Australian, Brazil and Agulhas Currents), and the Subantarctic Mode Water forming equatorward of the ACC (Hanawa & Talley, 2001). SCVs could generate along these fronts as a result of meander-driven subduction driving low potential vorticity mode water into the stratified interior, where an anticyclonic circulation occurs due to vortex compression (Spall, 1995; L. N. Thomas, 2008). Thus, SCVs may trap mode water and propagate it far from frontal regions, potentially playing a role in mode water dispersal in the stratified interior.

Observations of SCVs from these regions show thick subsurface cores composed of homogeneous, oxygen-rich waters (Oka, 2009; Z. Zhang et al., 2015; Xu et al., 2016; Schütte et al., 2016; Li et al., 2017; Barcelo-Llull et al., 2017; Shi et al., 2018), which, along with our results, support SCVs generation by mode water subduction. Detections from Figures 2.4 to 2.6 reveal large coherent populations of both spicy- and minty-core SCVs inhabiting the Kuroshio, East Australia, Gulf Stream, Aghulas, and Brazil Current regions (where subtropical mode waters are subducted) (Hanawa & Talley, 2001). Panel A in Figure 2.14 shows representative profiles and temperature-salinity diagrams from both spicy- and minty-core SCVs detected in the vicinity of the Kuroshio extension, which closely match the results of Z. Zhang et al. (2015) and Li et al. (2017). These studies speculated that both spicy- and minty-core SCVs propagate through this region, and are possibly formed by frontal convergence and subduction of winter mixed-layer water along the persistent fronts of the Kuroshio. Other studies have shown that, along with large volumes of North Pacific Subtropical Mode Water

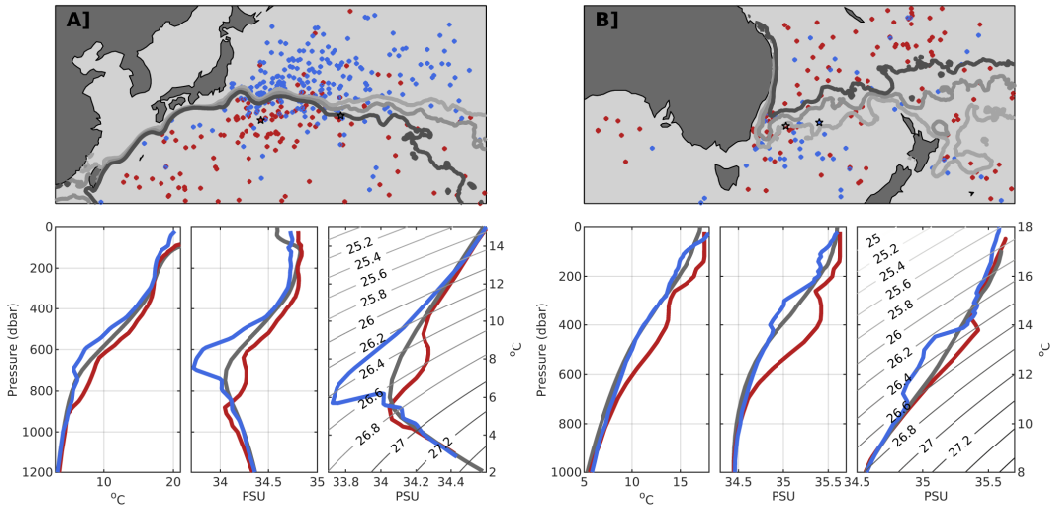

Figure 2.14: (A) Locations and hydrographic properties of spicy-core (red) and minty-core (blue) SCVs detected near the Kuroshio extension. Temperature and salinity profiles and diagram are constructed from the star marker profiles for an example spicy-core SCV (Argo float 2900156, cycle 34, solid red curve) and minty-core SCV (Argo float 29010, cycle 75, solid blue curve), with the grey curve representing the climatological profile for the spicy-core SCV's location and cast month. Climatological dynamic topography contour lines (100cm, 110cm, and 120cm) are also plotted. (B) Same as (A), but for spicy-core SCVs detected near the East Australia Current. The example spicy-core SCV is from Argo float 5901235, cycle 36 (red curve) and the example minty-core SCV is from Argo float 5903639, cycle 223 (blue curve); climatological dynamic topography contour lines (70 cm, 80 cm, and 90 cm) are also shown.

(NPSTMW, $\sim$ 25.2 kg m^{-3}), two types of North Pacific Central Mode Water (NPCMW) form between the Kuroshio Extension front and Kuroshio Bifurcation front, for a lighter variety ($\sim$ 25.8 – 26.2 kg m^{-3}), and between the Kuroshio Bifurcation front and the Subarctic front, for a slightly denser variety ($\sim$ 26.3 – 26.4 kg m^{-3}, (Oka & Suga, 2005)).

The bimodal distributions for spicy-core SCVs in the Northeast Pacific (Figure 2.7) may result from subduction of both NPSTMW and the lighter NPCMW, whereas the unimodal distributions for minty-core SCVs suggest a generation along the Subarctic front from the denser NPCMW (Z. Zhang et al., 2015). This is also supported by the more poleward occur-

rence of minty-core SCVs compared to spicy-core SCVs in the region. A similar mechanism may be responsible for the SCVs detected along the East Australia Current extension (Figure 2.14B), which shows similar spatial patterns and vertical structures. Both spicy and minty-core SCVs with core isopycnals of approximately 26.4 kg m^{-3} are identified near the separation zone of the East Australia current, with minty-core SCVs distributed more poleward by several degrees latitude. In addition, spicy-core SCVs propagating to the north of New Zealand (Figure 2.5) are co-located with the formation region for South Pacific Subtropical Mode Water (SPSTMW), exhibiting very similar characteristics to this water mass (15 – 19°C, 35.5 PSU, 26.0 kg m^{-3}, (Hanawa & Talley, 2001)).

SCVs detections along the western boundary of the Atlantic may also have connections to mode waters. North Atlantic Subtropical Mode Water (NASTMW) is characterized by temperature, salinity, and potential density values of $\sim$ 18°C, 36.5 PSU, and 26.5 kg m^{-3}, respectively, and is formed just south of the Gulf Stream Extension to cover the western extent of the subtropical gyre (Hanawa & Talley, 2001). Core property distributions (Figure 2.8) and spatial patterns (Figure 2.5) from spicy-core SCVs detected within the Northwest Atlantic match well with these characteristics, suggesting that these SCVs may form from, and eventually help spread NASTMW throughout the North Atlantic. Spatial distributions and histograms for spicy-core SCVs in the South Atlantic, with the exception of the Benguela SCVs discussed in section 2.4.1, also align well with the properties and formation region of South Atlantic Subtropical Mode Water (SASTMW, 12 – 18°C, 35.2 – 36.2 PSU, 26.2 – 26.6 kg m^{-3}).

Thus, subduction of mode waters at western boundary current fronts may be a common SCV generation mechanism throughout the western boundary of oceanic basins, just as undercurrent instabilities lead to generation along the eastern boundaries. Additionally, due to beta drift, the propagation direction would be mostly westward, which often contrasts with the large scale circulation of mode water formation regions (Shi et al., 2018). However, the process of subduction of saline subtropical surface mixed layer water is not necessarily restricted to the western extent of subtropical gyres. Nauw et al. (2006) speculated that SCV observed throughout the Indian Ocean were generated via the South Indian Tropical Front

between the tropics and subtropics in the eastern part of the South Indian subtropical gyre. We also detect SCVs throughout this region, which, together with their results, suggests that other frontal structures likely generate SCVs.

Finally, a major component of the Southern Ocean overturning circulation consists of the northward export of Subantarctic Mode Water (SAMW) and Antarctic Intermediate Water (AAIW) across the Subantarctic Front – the southern boundary of the subtropical gyres, which together ventilate large areas of the lower thermocline in the Southern Hemisphere (Hanawa & Talley, 2001; Sallée et al., 2010; Cerovečki et al., 2013). SAMW forms in deep winter mixed layers poleward of the Subantarctic Front, and is characterized by wide ranges of temperature, salinity, and potential density of 4 – 15°C, 34.2 – 35.8 PSU, and 26.5 – 27.1 kg m^{-3} respectively. Colder and fresher SAMW is found in the Pacific, whereas warmer and saltier waters form in the Southwestern Atlantic (Cerovečki et al., 2013).

Figure 2.15 shows a typical profile from the minty-core SCVs detected along the Subantarctic Front, which exhibits a core of homogeneous temperature and salinity between roughly 400 – 700 dbar. Contour lines highlight the approximate locations of the Subantarctic Front (grey) and Polar Front (black) from the WOCE Southern Ocean Atlas (Orsi & Whitworth, 2005), which are poleward of the majority of minty-core SCVs detections throughout the Southern Ocean. Additionally, histograms of core temperature, salinity, and isopycnal for the minty-core SCVs of the Southern Ocean (Figure 2.9), Southwest Atlantic, and Southeast Atlantic (Figure 2.8) exhibit similar peaks and spread, which match hydrographic characteristics of SAMW. This result is highlighted by the similarities in mapped minty-core SCV properties throughout the high-latitude Southern Ocean (Figure 2.6), suggesting a connection between these geographic regions via formation and propagation of SAMW mode water SCVs.

Previous studies have suggested that SCVs with vertically homogeneous hydrographic properties are formed at upper ocean fronts (Spall, 1995; Gordon et al., 2002; L. N. Thomas, 2008) where isopycnals from the thermocline outcrop in the winter mixed layer. At these fronts, mode waters are subducted into the thermocline, and sometimes forms isolated lenses (Nauw et al., 2006). Our results suggest that SCVs actively transport mode waters away from

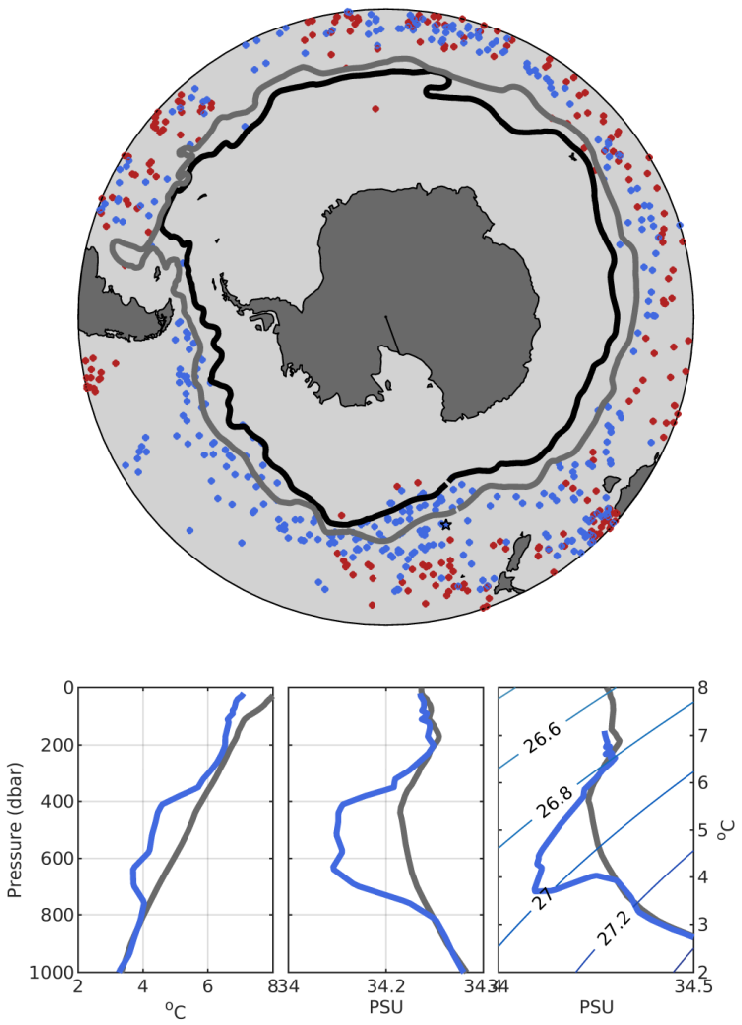

Figure 2.15: Locations and hydrographic properties of spicy-core SCVs (red) and minty-core SCVs (blue) detected near the Antarctic Circumpolar Current. Contour lines represent the location of the Polar Front (black) and Subantarctic Front (grey) from the WOCE Southern Ocean Atlas (Orsi & Whitworth, 2005). Temperature and salinity profiles and diagram are constructed from the star marker profile (Argo float 1901435, cycle 217, solid blue curve), with the grey curve representing the climatological profile for that cast's location and month.

their formation regions. As shown in Figure 2.10, $\sim 1\%$ of Argo profiles from these regions detected SCVs, highlighting a relatively high generation frequency. However, more research is needed to quantify their importance on regional and global scales. Regardless, their

potential to transport recently ventilated waters may impact oxygen and nutrient budgets by periodically injecting oxygen-rich, nutrient-poor waters into the stratified interior.

2.5 SCV Impacts

Our detections show regional generation of SCVs that can propagate temperature, salinity, and other tracer anomalies over basin scales, as observed for Meddies and Cuddies. To illustrate the potential to significantly modify local and remote water mass properties, we provide a first-order estimate of the heat and freshwater contributions from detectable SCVs at any given location in the ocean. To this end, we first utilize detection statistics from Figure 2.10 and regional averages of SCV scale height and radius to build a simple model of SCV distribution based on scaling arguments (Appendix A.1 and A.2), and use it to provide a first-order estimate of their frequency in the ocean. We then use similar scaling arguments applied to regionally averaged temperature and salinity anomalies to estimate the heat and salt content lost or gained at any given point in the ocean because of the presence of SCVs.

After dividing the ocean into 4° by 4° latitude/longitude cells, a first-order upper-bound estimate (Appendix A.1) of the spatial density distribution of SCVs (n_{scv}, in units of # km^{-2}) can be written as

$$n_{\mathrm{scv}} = \frac{N_{\mathrm{d}}}{N_{\mathrm{a}}} \frac{1}{\pi \alpha^2 \overline{L^2}}\,, \tag{2.7}$$

where N_{d} is the number of detected spicy or minty SCVs, N_{a} is the number of quality controlled Argo casts, L is SCV scale length (km), α is a scaling factor (here set to 1, see Appendix A.1), and the overbar represents the average calculated from all spicy or minty SCVs within the grid cell. Similar to (2.7), a first-order lower-bound estimate of the average heat anomaly caused by the presence of SCVs at any given location in the ocean ($\delta H'$, in units of J m^{-2}, Appendix A.2) can be defined as

$$\delta H' = \gamma\, \rho\, C_{\mathrm{p}}\, \frac{N_{\mathrm{d}}}{N_{\mathrm{a}}}\, \frac{\pi^{\frac{1}{2}} \overline{T'_{\mathrm{d}}\, h\, L^2}}{\overline{L^2}}\,, \tag{2.8}$$

where γ is a scaling factor (here set to 1, see Appendix A.2), ρ is average ocean density (1027 kg m^{-3}), C_{p} is the specific heat capacity of seawater (3850 J kg^{-1}°C^{-1}), T'_{d} is the detected

core temperature anomaly (°C), and h is the SCV scale height. The salt anomaly ($\delta S'$, in units of g m^{-2}) is given by

$$\delta S' = \gamma \, \rho \, \frac{N_\mathrm{d}}{N_\mathrm{a}} \, \frac{\pi^{\frac{1}{2}} \overline{S'_\mathrm{d} \, h \, L^2}}{\overline{L^2}} \, , \tag{2.9}$$

where S'_d is the detected core salinity anomaly (g kg^{-1}).

Figure 2.16 shows the result from these equations applied to the same 4° x 4° latitude/longitude grid shown in Figure 2.10. Panels A and B provide estimates of the spatial density of spicy-core and minty-core SCVs throughout the ocean respectively. Both plots reveal increasing numbers of SCVs at higher latitudes. Many of the grid cells throughout the Southern Ocean show values of 1 – 2 SCVs per 100 x 100 km^2; other regions with high SCV spatial density include the North Atlantic, Mediterranean outflow, and Southwest Atlantic regions for spicy-core SCVs, and the Kuroshio and Labrador Sea regions for minty-core SCVs. According to the arguments in Dewar & Meng (1995), high-latitude SCVs are expected to be smaller due to the decrease in the first baroclinic radius of deformation with latitude, which scales inversely with the Coriolis frequency (f) and linearly with the buoyancy frequency N. Thus, the area of SCVs (hence, the probability of being detected by randomly-located Argo profiles) increases with the square of the radius, which is much larger near the equator, compared to polar regions. This makes SCVs comparably easier to detect at low latitudes, implying that the same relative number of detections at low versus high latitudes in Figure 2.10 corresponds to a larger spatial density of SCVs at higher latitudes.

However, as revealed in panels C – F in Figure 2.16, the relatively high spatial density observed throughout the high latitudes does not necessarily correspond to a similar amplification in anomalous heat (MJ m^{-2}) and salt (g m^{-2}) brought about by SCVs. Although SCVs are more frequently found in these regions, their area and volume are smaller than those observed at lower latitudes. Therefore, the higher frequency of SCVs at higher latitudes is compensated by their smaller volumes, leading to comparable heat and salt anomalies. Rather, we find that the influence of spicy-core SCVs on heat and salt peaks near the overflow regions and throughout the Pacific EBUS (sections 2.4.1 and 2.4.2). This result is not surprising given the large temperature and salinity anomalies associated with dense, warm and salty overflow waters (Figure 2.13), and the PEW advected by the Cali-

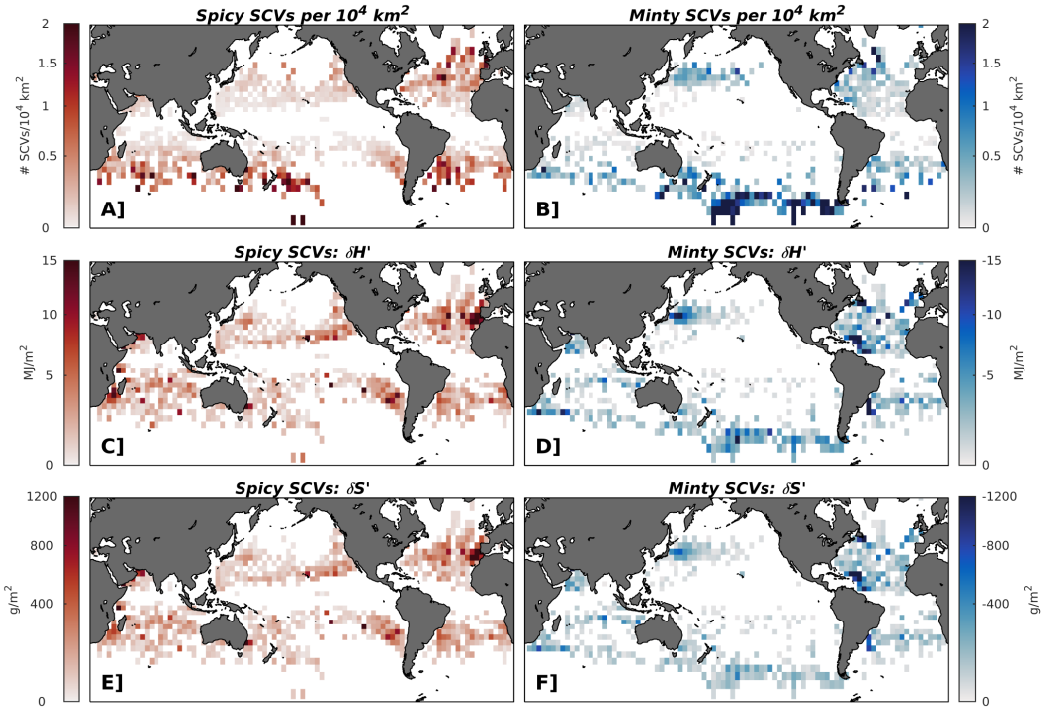

Figure 2.16: (A,B) Estimate of the number of SCVs per 100 x 100 km^2, derived for each 4° x 4° longitude/latitude grid cell for spicy-core SCVs and minty-core SCVs, respectively. (C,D) Average heat anomaly caused by the presence of SCVs, δH' (MJ m^{-2}), calculated from all spicy-core and minty-core SCVs, respectively, within each grid cell. (E,F) Average salt anomaly caused by the presence of SCVs, δS' (g m^{-2}), calculated from all spicy-core and minty-core SCVs, respectively, within each grid cell.

fornia and Peru-Humboldt Undercurrents (Figure 2.11). Similarly, while amplified heat and salt contributions from minty-core SCVs were co-located with high spatial densities near the Kuroshio extension, the Labrador Sea, and throughout the Southern Ocean, notable peaks were also identified off of the Caribbean region in the North Atlantic. Temperature and salinity anomalies associated with North Brazil Current subsurface eddies had been previously described by Fratantoni & Richardson (2006); our findings provide further evidence that these SCVs may play an important role on the upper ocean hydrography of this region.

Our results provide more evidence that SCV generation and propagation modify the hy-

drographic properties of both nearby and remote regions, in particular by spreading heat and salt from EBUS undercurrents, overflows, and mode waters. We further reveal unexpected amplifications for regions such as the Caribbean and Labrador Sea. The net transport of heat and salt by SCVs may ultimately alter the properties of water masses as they form and decay, in turn affecting ocean circulation.

It is important to stress that the simple model on which Figure 2.16 is based depends on a simplification of the real distribution, structure, and hydrographic impact of SCVs. For example, it does not consider important elements such as the life cycle of SCVs, their propagation and dissipation, and their interaction with the sampling strategy of Argo floats. It also estimates average anomalies caused by the presence of SCVs, but not by their dissipation. Furthermore, the number of detections depends on several parameters of our detection algorithm, including relatively strict IQR thresholds (section 2.2.2). Thus, we are likely under sampling the true number of SCVs, and our analysis likely represents a conservative estimate on the effect of relatively strong SCVs. Regardless, it provides a first order estimate of essential quantities needed to characterize the impact of SCVs on oceanic circulation, including transport of heat and salt, and should be seen as a first step towards the development of more realistic models of the distribution of SCVs.

2.6 Summary

In this study, we developed a method for detecting subsurface anticyclonic eddies (SCVs) using spiciness, stratification, and dynamic height anomalies derived from Argo float profiles. By utilizing the high spatial and temporal resolution sampling provided by the nearly 4000 operational Argo floats, we detected 1716 spicy-core and 1258 minty-core SCVs in the Argo record, showing that subsurface anticyclonic eddies populate vast swaths of the global ocean. Based on the statistics of detected SCVs, we infer the location and characteristics of regional SCV populations, highlighting several hot-spots of formation that tend to generate long-lived SCVs (Figures 2.4, 2.5, 2.6, and 2.10).

Among these, poleward undercurrents associated with EBUS and the Mediterranean out-

flow appear to produce abundant SCVs capable of reaching the subtropical gyres. Based on a comparison with surrounding waters, these SCVs may provide a significant source of undercurrent water to these regions, while also potentially weakening undercurrent signatures as they flow poleward. Mode water formation regions near persistent fronts associated with western boundary currents and the ACC also appear as hot-spots of SCV formation, suggesting an important role for SCVs in spreading mode waters.

Finally, we provided a first-order estimate of the number of SCVs and their contribution to heat and salt wherever they appear. Our results suggest that SCVs play a role in modulating water properties in the subtropical gyres and mid-latitude subduction regions, which in turn may alter interior water mass characteristics. Quantifying the impact of SCVs on heat, salt and tracer fluxes will benefit from a more detailed characterization of SCV frequency, movement, dissipation, and three-dimensional shape. This will likely require more accurate statistical models of the structure and life cycle of SCVs, constrained by Argo and other observations, as well as the use of high-resolution numerical models.

CHAPTER 3

Pathways of Nitrous Oxide Production in the Eastern Tropical South Pacific Oxygen Minimum Zone

This chapter contains an accepted manuscript (McCoy et al., 2023), available from Global Biogeochemical Cycles, without any changes.

3.1 Introduction

Nitrous oxide (N_2O) is a powerful greenhouse gas that is roughly 300 times more potent than carbon dioxide (CO_2) and is projected to become the most important ozone-depleting anthropogenic emission by the end of the 21st century (Ravishankara et al., 2009; Canadell et al., 2021). Recent analyses of the global N_2O budget over the decade of 2007 - 2016 suggest that anthropogenic emissions are responsible for up to 40% of total N_2O sources to the atmosphere, mostly from agriculture, whereas outgassing from the ocean accounts for roughly 20% (Canadell et al., 2021). The production of N_2O in the ocean is linked to the remineralization of organic matter (OM) via both aerobic and anaerobic pathways, and, as a consequence, is tightly coupled to the oceanic oxygen (O_2) distribution (Freing et al., 2012; Babbin et al., 2015; Ji et al., 2015; Arévalo-Martínez et al., 2016; Yang et al., 2020). While sea surface N_2O measurements are typically found to be saturated with respect to atmospheric concentrations over much of the world ocean, the most intense hot-spots of N_2O outgassing are found in the Eastern Tropical North Pacific (ETNP), the Eastern Tropical South Pacific (ETSP), and the Arabian Sea. Here, high organic matter export rates and sluggish lateral circulation result in steep O_2 gradients that surround anoxic (here defined as $O_2 < 5\ mmol\ m^{-3}$) waters, also known as oxygen minimum zones (OMZ)(Codispoti,

2010; Arévalo-Martínez et al., 2016; Ji et al., 2018; Yang et al., 2020). Although OMZs only account for roughly 1% of the total ocean volume, the dynamic marine nitrogen cycling that occurs in these regions results in up to 50% of total oceanic N_2O emissions to the atmosphere (Codispoti, 2010; Babbin et al., 2015; Arévalo-Martínez et al., 2016; Yang et al., 2020).

The ETSP hosts the second largest OMZ by area and comprises the Humboldt Current System, one of the four major Eastern Boundary Upwelling Systems, which extends from the southern extent of Chile ($\sim 45^o S$) to northern Peru ($\sim 4^o S$) (Chavez & Messié, 2009; Santoro et al., 2021). While southern Chile experiences more intense upwelling during boreal summer (Pennington et al., 2006), upwelling-favorable conditions exist year-round along the Peruvian and northern Chile coastlines, fueling high rates of surface primary productivity, organic matter export (Chavez & Messié, 2009), and subsurface O_2 depletion. The ETSP OMZ is located in a so-called "shadow zone" of the thermocline (Luyten et al., 1983), where the supply of O_2 by subduction and advection from the ventilated subtropical gyre is limited. Instead, O_2 transport mostly occurs by a combination of zonal advection by eastward tropical currents such as the Equatorial Undercurrent (EUC) and the Southern Subsurface Countercurrents (SSCC) (Karstensen et al., 2008; Stramma et al., 2010), and by mesoscale eddies (Gnanadesikan et al., 2013; Bettencourt et al., 2015). The balance between high remineralization rates and weak O_2 supply leads to functional anoxia in the OMZ core (Thamdrup et al., 2012), resulting in a pronounced subsurface nitrite (NO_2^-) maximum, and a strong fixed-nitrogen deficit (Kalvelage et al., 2013). An additional characteristic of the ETSP is the relatively sharp transition from anoxic to suboxic ($5\ mmol\ m^{-3} < O_2 < 10\ mmol\ m^{-3}$) waters along the OMZ boundary. These O_2 gradients host both aerobic (e.g., nitrification) and anaerobic (e.g., denitrification) nitrogen transformations, which result in N_2O supersaturation around the anoxic core (Babbin et al., 2015; Kock et al., 2016). Upwelling of these N_2O-laden waters eventually leads to local hot-spots of N_2O outgassing (Arévalo-Martínez et al., 2016; Ji et al., 2018; Yang et al., 2020).

Nitrification is a two-step aerobic process wherein ammonium (NH_4^+, here used interchangeably with ammonia, NH_3) produced by remineralization of organic matter (pathway 1 in Figure 3.1) is oxidized to NO_2^- and subsequently to nitrate (NO_3^-) by ammonia-oxidizing

bacteria (AOB) and archaea (AOA), and nitrite-oxidizing bacteria (NOB) (pathways 2 and 4, respectively) (Lam & Kuypers, 2011). N_2O production occurs as a byproduct of ammonia oxidation (pathway 3), resulting in a positive correlation between apparent oxygen utilization (AOU) and supersaturated N_2O concentrations in many areas of the ocean (Cohen & Gordon, 1978; Walter et al., 2006). This process has been further quantified by active production of $^{15}N_2O$ in ^{15}N tracer incubation experiments (Yoshida et al., 1989). Due to a reported shift in N_2O production from hydroxylamine oxidation to nitrifier-denitrification (Wrage et al., 2001; Stein & Yung, 2003), the yield of N_2O production from NO_2^- has been observed to increase at decreasing O_2 in cultures with ammonia-oxidizing bacteria and archaea (Goreau et al., 1980; Löscher et al., 2012). This increase likely leads to enhanced nitrification-derived N_2O production within steep suboxic gradients around the anoxic core of OMZs (Nevison et al., 2003; Ji et al., 2015, 2018; Santoro et al., 2021).

N_2O also forms during step-wise denitrification (the reduction of NO_3^- to NO_2^- to N_2O to N_2) under suboxic and anoxic conditions (pathways 5 - 7 in Figure 3.1). Recent field measurements suggest that NO_3^- is also a direct substrate for N_2O production, presumably involving NO_2^- reduction inside the cell of denitrifying microorganisms (Ji et al., 2015, 2018; Frey et al., 2020). In the anoxic core of OMZs, widespread consumption of N_2O occurs via N_2O reduction, the only known biological process able to remove N_2O from the water column (although the possibility of N_2O fixation has been reported, see Farías et al. (2013)). Recent studies have highlighted how the different steps, each mediated by distinct enzymes and likely different microorganisms (Ganesh et al., 2014; Kuypers et al., 2018), are subject to variable O_2 sensitivities, wherein NO_3^-, NO_2^-, and N_2O reduction are progressively inhibited by O_2 (Körner & Zumft, 1989; Kalvelage et al., 2011; Dalsgaard et al., 2014; Babbin et al., 2015; Ji et al., 2015). Therefore, the same suboxic gradients that lead to enhanced N_2O production from nitrification can also lead to N_2O accumulation from denitrification, as both NO_3^- and NO_2^- reduction proceed while N_2O reduction is inhibited, in a process referred to as "incomplete" denitrification (Babbin et al., 2015).

Production of N_2O at low O_2 from both nitrification and denitrification, and their shared NO_2^- intermediary, complicate the interpretation of in situ observations (Ji et al., 2015,

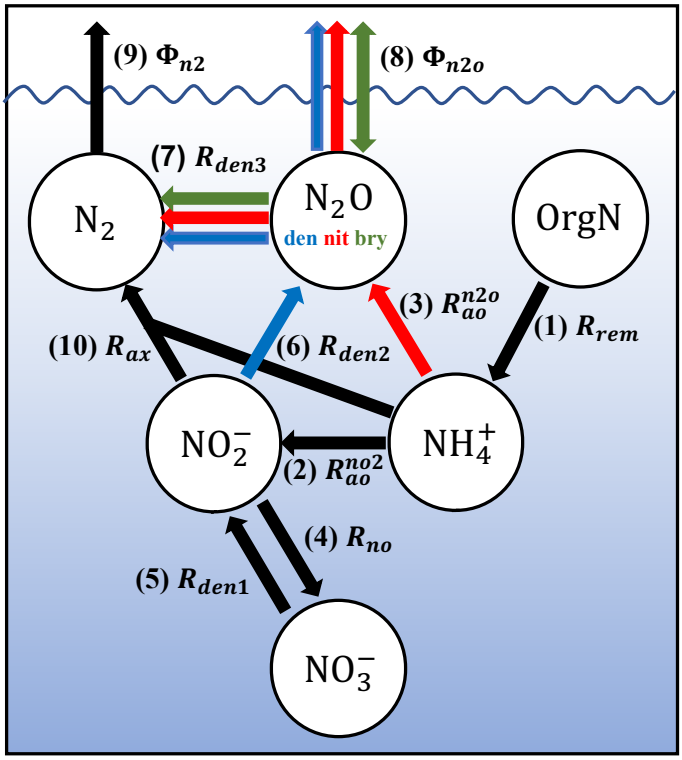

Figure 3.1: Schematic of the oceanic nitrogen cycle (ignoring biological uptake) as represented in ROMS. Transformation pathways include: (1, R_{rem}) oxic remineralization of nitrogen in organic matter (OrgN) to ammonium; (2, R_{ao}) ammonium oxidation to nitrite; (3, R_{ao}^{n2o}) ammonium oxidation to nitrous oxide; (4, R_{no}) nitrite oxidation; (5, R_{den1}) nitrate reduction; (6, R_{den2}) nitrite reduction; (7, R_{den3}) decomposed nitrous oxide reduction; (8, Φ_{n2o}) decomposed nitrous oxide air-sea flux; (9, Φ_{n2}) dinitrogen air-sea flux; and (10, R_{ax}) anaerobic ammonium oxidation (anammox). Colored arrows correspond to the sources and sinks of the decomposed N_2O tracers discussed in Section 3.2.4; N_2O originating from denitrification (N_2O_{den}, blue), N_2O originating from nitrification (N_2O_{nit}, red), and N_2O originating from model boundaries (N_2O_{bry}, green).

2018; Santoro et al., 2021). In these regions, observations typically reveal an OMZ anoxic core characterized by a secondary NO_2^- maximum and undersaturated N_2O concentrations, suggesting coupled step-wise or "complete" denitrification. N_2O supersaturation in the upper and lower oxyclines has been linked to the enhanced production by nitrification at low O_2 (Cohen & Gordon, 1978). This is challenged by recent studies noting the lack of a linear relationship with AOU and high abundances of gene markers for NO_2^- reduction, which suggest simultaneous production by nitrification and incomplete denitrification (Babbin et

al., 2015; Arévalo-Martínez et al., 2016; Ji et al., 2018), as further supported by isotopic evidence (Bourbonnais et al., 2017; Casciotti et al., 2018).

Incomplete denitrification due to progressive O_2 tolerances is missing from most biogeochemical models, which predominantly employ simple parameterizations to represent N_2O production as a function of nitrification, while denitrification is typically modelled as a net sink of N_2O at low O_2 (Suntharalingam et al., 2000; Jin & Gruber, 2003; Ji et al., 2018; Battaglia & Joos, 2018). By resolving O_2-dependent decoupling of N_2O production and consumption, Babbin et al. (2015) suggested that N_2O production rates from denitrification may be up to two orders of magnitude larger than those from nitrification near the core of OMZs, albeit closely balanced by N_2O reduction.

While the uncertainty surrounding N_2O production in the ocean has been reduced in recent years following improved estimates of ocean (Yang et al., 2020), terrestrial, and anthropogenic N_2O sources (Tian et al., 2020; Canadell et al., 2021), barriers remain in accurately projecting future air-sea fluxes because of poorly constrained contributions from nitrification and denitrification. The observed expansion of OMZs (Stramma et al., 2008; Schmidtko et al., 2017; Oschlies et al., 2018) is expected to continue over the 21st century, although the extent of future changes in low O_2 and anoxic water volumes remains uncertain (Cabré et al., 2015; Bianchi et al., 2018; J. J. M. Busecke et al., 2022). Accurate parameterization of N_2O cycling in global ocean models is thus crucial to simulate realistic future scenarios. This is critical given that OMZ regions remain poorly resolved in current global Earth system models (Cabré et al., 2015; J. J. M. Busecke et al., 2022; Séférian et al., 2020), which generally fail to capture fine-scale circulation such as the zonal jet systems that ventilate the tropical Ocean (Kessler, 2006; Duteil et al., 2014; J. J. Busecke et al., 2019; Duteil et al., 2021).

To address these sources of uncertainty, we incorporate a new model of the OMZ nitrogen cycle (NitrOMZ) (Bianchi et al., 2022) into an eddy-resolving three-dimensional (3-D) regional ocean model of the ETSP that simulates local N_2O production and consumption from nitrification and denitrification. The model, constrained by in situ ETSP observations of nitrogen cycle tracers and transformation rates, allows for an examination of the N_2O balance within a typical OMZ upwelling system. To attribute the sources of N_2O outgassing

flux to different processes, we use the 3-D model to track contributions from nitrification, denitrification, and physical transport into the model domain. This analysis reveals the importance of incomplete denitrification and transport of remotely-generated N_2O for air-sea fluxes, with implications for future N_2O emissions in a changing ocean.

The rest of the paper is organized as follows: Section 3.2 describes the 3-D model configuration and setup, a brief summary of N_2O production pathways in NitrOMZ, and the N_2O tracer decomposition strategy; Section 3.3 provides a short validation of model solutions, summarizes the results of the simulations, and describes the ETSP N_2O balance; Section 3.4 discusses the results and implications, and concludes the paper.

3.2 Methods

3.2.1 Model configuration

The physical component of the model consists of the Regional Ocean Modeling System (ROMS) (Shchepetkin & McWilliams, 2005; Shchepetkin, 2015), a primitive-equation, hydrostatic, topography-following general ocean circulation model. The model domain extends from -111.38^oW to -66.62^oW and from 42.52^oS to 3.41^oN and is chosen to resolve key oceanographic features of the ETSP such as the EUC (Figure 3.2c), the wind-driven South Pacific gyre (contour lines in Figure 3.2a and 3.2b), and the horizontal extent of the OMZ (Figure 3.3a). Its grid consists of 402 x 502 points with a nominal resolution of 10 kilometers and 42 topography-following vertical levels with higher resolution at the surface and bottom. The model time-step is 800 seconds, and output is saved as monthly means.

For this study, low-frequency interannual variability is ignored to instead focus on a climatological steady-state. Initial conditions and monthly climatological boundary forcing (applied at the northern, western, and southern boundaries) for temperature, salinity, surface elevation, and horizontal velocity are taken from an existing Pacific-wide ROMS simulation (Lemarié et al., 2012). Normal-year-forcing of daily freshwater and turbulent heat fluxes are estimated using bulk formulae (Large, 2006) applied to ERA-interim (ERAi) reanalysis

data for the year 1979 (Simmons et al., 2006; Dee et al., 2011). Because of known biases in ERAi, which overestimates shortwave and underestimate longwave fluxes (Brodeau et al., 2010), we applied corrections from the DRAKKAR Forcing Set version 5.2 to heat fluxes (Dussin et al., 2014). Daily climatological wind stress is taken from the QuickSCAT-based Scatterometer Climatology of Ocean Winds (Risien & Chelton, 2008). The resulting simulation produces a realistic climatological picture of the hydrographic properties, gyre circulation, and equatorial current structure of the ETSP (Figure 3.2a - c) when compared to validation products (Figure 3.2d - f).

The physical model is coupled online to the Biogeochemical Elemental Cycling (BEC) model from Moore et al. (2004) using the same equations and parameter settings as in Frischknecht et al. (2017) with the exception of the nitrogen cycling component, which was expanded for the NitrOMZ model (Bianchi et al., 2022)(see Section 3.2.2). Initial conditions and boundary forcing of biogeochemical nutrient concentrations (NO_3^-, PO_4^{3-}, $Si(OH)_4$ and O_2) are taken from monthly climatological observations from the 2013 World Ocean Atlas (H. E. Garcia, Boyer, et al., 2013; H. E. Garcia, Locarnini, et al., 2013). NH_4^+, NO_2^-, and N_2 boundary conditions are set to 0 but adjust rapidly within the domain. Iron data are taken from the Community Earth System Model (CESM) as in Deutsch et al. (2021), and DIC and alkalinity from GLODAP (Lauvset et al., 2016), with a reference year of 2002.

Initial conditions and monthly boundary forcing at the northern, western, and southern boundaries for N_2O were generated from a 3-D machine-learning reconstruction based on in situ data from the MEMENTO (Kock & Bange, 2015) database, integrated with additional cruises (Yang et al., 2020). Due to the strong coupling between N_2O and O_2 concentrations, and to avoid aliasing between monthly gridded O_2 estimates and individual snapshot measurements of N_2O, we first average monthly N_2O measurements onto a 1-degree horizontal grid before applying the same machine learning approach described in Yang et al. (2020). Air-sea gas exchange at the surface is modeled according to Wanninkhof (1992), using a constant atmospheric mixing ratio of 300 ppb, which is taken as a typical concentration for the 20th century.

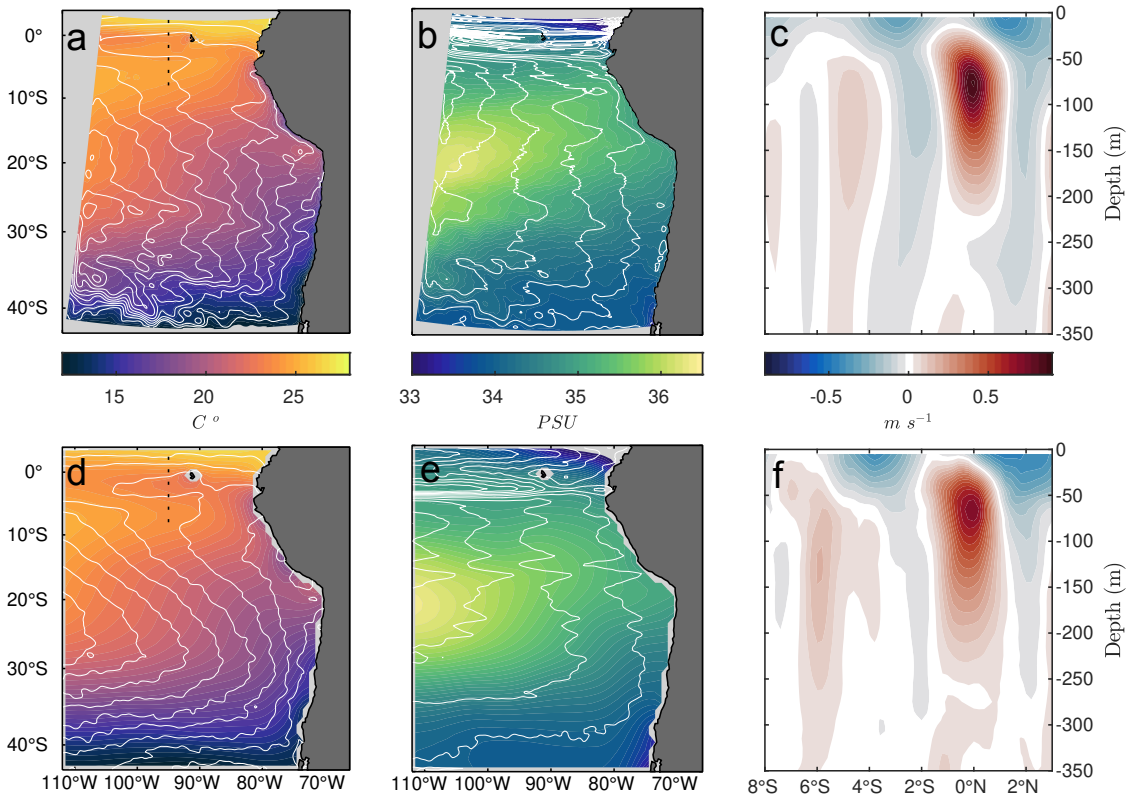

Figure 3.2: (a,d) Average sea-surface temperature from model years 41 - 50 (top) and World Ocean Atlas 2018 (bottom). Contours highlight sea-surface height at 5 *cm* intervals, with validation data obtained by averaging AVISO data between 2000 to 2018. Dashed lines mark the transect location in panels (c) and (f). (b,e) Same as in panels (a) and (d), but for sea-surface salinity; contours highlight calculated geostrophic velocity streamlines, with validation data derived from AVISO. (c,f) Zonal velocity sections along the equator at 95^oW from ROMS (top) and G. C. Johnson et al. (2002) (bottom).

3.2.2 NitrOMZ model formulation

The NitrOMZ model explicitly resolves the main set of nitrogen cycle transformations associated with the remineralization of sinking organic matter in low O_2 environments (summarized in Figure 3.1, with formulations presented in Supporting Information B.2). These include the following chemolithotrophic reactions: aerobic NH_4^+ oxidation (here used interchangeably with ammonia oxidation) to N_2O ($R_{ao}^{n_2o}$) and NO_2^- (R_{ao}), aerobic NO_2^- oxidation to NO_3^- (R_{no}), and anaerobic NH_4^+ oxidation with NO_2^- to N_2 (anammox, R_{ax}). NitrOMZ partitions

organic matter remineralization in ROMS-BEC (see Supporting Information B.1) to include three additional heterotrophic denitrification steps: NO_3^- reduction to NO_2^- (R_{den1}), NO_2^- reduction to N_2O (R_{den2}), and N_2O reduction to N_2 (R_{den3}). Thus, the model expands BEC by allowing production of N_2O via both nitrification and denitrification, as summarized in Sections 3.2.2.1 and 3.2.2.2.

Further details on the formulation and parameterization of the the model are discussed in Bianchi et al. (2022). Briefly, the model contains 23 parameters that control the N cycle, most of which are poorly constrained by observations and can plausibly span a range of values. Initially, we set the maximum aerobic remineralization rate (k_{rem}) and the NH_4^+ and NO_2^- half saturation constants for NH_4^+ and NO_2^- oxidation ($K_{ao}^{o_2}$ and $K_{no}^{o_2}$, respectively) to literature values (Babbin et al., 2015; Bristow et al., 2016), before optimizing the remaining parameters in a 1-D setup against a cost function constructed from in situ observations of tracers and N transformation rates from the ETSP (Kalvelage et al., 2013; Ji et al., 2015; Peng et al., 2016; Babbin et al., 2017, 2020). We adopt the final parameter set shown in Table B.4, which was slightly tuned from the optimal solution presented in Bianchi et al. (2022) (see Sections 3.2.2.1 and 3.2.2.2).

3.2.2.1 N_2O sources and sinks: nitrification

Production of N_2O via nitrification is modelled as a by-product of NH_4^+ oxidation ($R_{ao}^{n_2o}$, pathway 3 in Figure 3.1), with enhanced yields at lower O_2. Both NH_4^+ and NO_2^- oxidation (R_{ao} and R_{no}, respectively) are suppressed near the surface by light inhibition (see Supporting Information B.4) and competition for NH_4^+ and NO_2^- by phytoplankton as in Frischknecht et al. (2017). Therefore, nitrification is largely restricted to below the euphotic zone while also being suppressed at low O_2. The partitioning between N_2O and NO_2^- production from NH_4^+ oxidation is calculated using the function proposed by Nevison et al. (2003), derived by fitting measured N_2O and NO_2^- yields ($f_{ao}^{n_2o}$ and $f_{ao}^{no_2}$, respectively) to O_2 concentrations (Goreau et al., 1980):

$$\frac{f_{ao}^{n_2o}}{f_{ao}^{no_2}} = 0.01 \cdot (\frac{a}{[O_2]} + b). \tag{3.1}$$

N_2O production by nitrification, in units of $mmol$ N m^{-3} s^{-1}, is therefore represented as:

$$R_{ao}^{n_2o} = R_{ao} \cdot f_{ao}^{n_2o}, \tag{3.2}$$

with a similar function for NO_2^- production.

The parameterization from Nevison et al. (2003), based on the observed relationship between N_2O excess and apparent oxygen utilization, which was consistent with N_2O yields from cultured AOB (Goreau et al., 1980), implicitly represents a shift in N_2O production from NH_4^+ oxidation as a byproduct of hydroxylamine oxidation (at high O_2) to nitrifier-denitrification (at low O_2) (Wrage et al., 2001; Stein & Yung, 2003). Recent studies suggest that AOA (which often greatly outnumber AOB in marine environments) can also produce N_2O via a hybrid mechanism, with lower yield than observed in their bacterial counterparts (Stieglmeier et al., 2014; Kozlowski et al., 2016; Trimmer et al., 2016; Hink, Nicol, & Prosser, 2017; Hink, Lycus, et al., 2017). Since NitrOMZ does not separately model production from AOA and AOB, we initially set distinct values of the parameters a and b (Table B.4) to the optimized values from the Opt_{sel} solution (0.4 and 0.2, respectively) from Bianchi et al. (2022). We later tuned them to 0.3 and 0.1 respectively, to reflect results from a series of recent in situ measurements of N_2O production from the ETSP and ETNP OMZs (Ji et al., 2015, 2018; Santoro et al., 2021). We also slightly increased the maximum NH_4^+ and NO_2^- oxidation rates (k_{ao} and k_{no} respectively, see Supporting Information B.2) from Opt_{sel} values to bring surface concentrations of NO_2^- and NH_4^+ closer to zero. The parameter values for a and b cause NH_4^+ oxidation to predominantly produce NO_2^- at high O_2 concentrations (R_{ao}). As O_2 becomes scarce, overall NH_4^+ oxidation decreases, while production of N_2O ($R_{ao}^{n_2o}$) relative to NO_2^- increases following equations 3.1 and 3.2.

3.2.2.2 N_2O sources and sinks: denitrification

In the denitrification pathway, N_2O is produced via NO_2^- reduction ($R_{den2}^{n_2o}$, pathway 6 in Figure 3.1) at low O_2:

$$R_{den2}^{n_2o} = f_{den2} \cdot R_{rem}^{tot} \cdot Q_{den}^{N:C}, \tag{3.3}$$

where f_{den2} is the local fraction of total organic matter remineralization (R_{rem}^{tot}) routed to NO_2^- reduction (see Supporting Information B.3), and $Q_{den}^{N:C}$ the nitrogen to carbon ratio from denitrification (472/2/106) following Anderson & Sarmiento (1994). Similarly, N_2O is consumed via N_2O reduction to N_2 ($R_{den3}^{n_2}$, pathway 7 in Figure 3.1) at low O_2:

$$R_{den3}^{n_2} = f_{den3} \cdot R_{rem}^{tot} \cdot Q_{den}^{N:C}. \tag{3.4}$$

Each denitrification rate in NitrOMZ is calculated using a step-specific O_2 inhibition term. Similar to Dalsgaard et al. (2014), Babbin et al. (2015), and Ji et al. (2018), we model a progressive O_2 inhibition of the three denitrification steps ($K_{den1}^{O_2} > K_{den2}^{O_2} > K_{den3}^{O_2}$). As a consequence, complete denitrification to N_2 via N_2O reduction ($R_{den3}^{n_2}$) occurs in anoxic waters as each step proceeds unimpeded. However, at low but non-zero O_2, the decoupling of steps allows for N_2O accumulation from incomplete denitrification (production > consumption).

Following initial model validation, we increased the original Opt_{sel} O_2 inhibition parameter for NO_2^- reduction ($K_{den2}^{o_2}$) from 1.3 to 2.3 $mmol$ O_2 m^{-3}. This widens the N_2O production window in suboxic waters from incomplete denitrification to better match the magnitude of observed subsurface N_2O maxima in the ETSP OMZ. This permits NO_2^- reduction at slightly higher O_2 than is typically reported (Dalsgaard et al., 2014), which may reflect the lack in the model of direct N_2O production from NO_3^- suggested by recent studies (Ji et al., 2018; Frey et al., 2020).

3.2.3 N_2O balance

In the model, net N_2O production (J^{n_2o}, in units of $mmol$ N_2O m^{-3} s^{-1}) results from the balance of nitrification and denitrification terms (equations (3.2-3.4)):

$$J^{n_2o} = 0.5 \cdot (R_{den2}^{n_2o} + R_{ao}^{n_2o}) - R_{den3}^{n_2}. \tag{3.5}$$

Here, 0.5 converts the NO_2^- reduction rate ($R_{den2}^{n_2o}$) and the N_2O production rate from ammonia oxidation ($R_{ao}^{n_2o}$) from units of $mmol$ N m^{-3} to units of $mmol$ N_2O m^{-3}.

The resulting N_2O balance is closed to numerical precision within each grid cell of the

model, and scaled up to arbitrary 3-D domains:

$$\frac{d[\mathrm{N_2O}]}{dt} = J^{n_2o} + T^{n_2o} - \Phi^{n_2o}. \tag{3.6}$$

Here, $d[\mathrm{N_2O}]/dt$ is the climatological $\mathrm{N_2O}$ rate of change calculated as the difference between snapshots at the beginning and end of each month, T^{n_2o} the transport component calculated as the divergence of advection/diffusion fluxes, J^{n_2o} the sum of biological sources and sinks (equation (3.5)), and Φ^{n_2o} the air-sea flux controlled by gas exchange. We define a budget domain that captures the extent of the ETSP OMZ horizontally (dashed blue box in Figure 3.3a) and vertically from the surface to 1000 m depth.

3.2.4 $\mathrm{N_2O}$ tracer decomposition

In the model, $\mathrm{N_2O}$ concentrations can change under the effect of physical (advection from the model boundaries, air-sea gas exchange at the surface) or biogeochemical (nitrification, denitrification) terms. We quantify the contributions to the total $\mathrm{N_2O}$ from individual terms by decomposing the $\mathrm{N_2O}$ tracer as follows:

$$N_2O = N_2O_{nit} + N_2O_{den} + N_2O_{bry}. \tag{3.7}$$

Here, $\mathrm{N_2O}_{nit}$ tracks the fraction of $\mathrm{N_2O}$ produced by $\mathrm{NH_4^+}$ oxidation within the domain (R_{ao}^{n2o}, equation (3.2)), whereas $\mathrm{N_2O}_{den}$ tracks $\mathrm{N_2O}$ produced by $\mathrm{NO_2^-}$ reduction ($R_{den2}^{n_2o}$, equation (3.3)) as outlined in Sections 3.2.2.1 and 3.2.2.2 (pathways 3 and 6, respectively, in Figure 3.1). Physical contributions are accounted by the remaining tracer, $\mathrm{N_2O}_{bry}$, which tracks air-sea gas exchange (discussed further below) and the transport of $\mathrm{N_2O}$ from the horizontal boundaries.

By construction, the conservation equations for the individual tracers sum up to the conservation equation for total $\mathrm{N_2O}$ (equation 3.6). Thus, while each tracer has a unique source, they are all subject to consumption by $\mathrm{N_2O}$ reduction at a rate proportional to the

individual tracer's fractional contribution to total N_2O concentration in a linear fashion:

$$R^{nit}_{den3} = \frac{N_2O_{nit}}{N_2O} \cdot R^{n_2}_{den3}, \tag{3.8a}$$

$$R^{den}_{den3} = \frac{N_2O_{den}}{N_2O} \cdot R^{n_2}_{den3}, \tag{3.8b}$$

$$R^{bry}_{den3} = \frac{N_2O_{bry}}{N_2O} \cdot R^{n_2}_{den3}, \tag{3.8c}$$

Accordingly, the biogeochemical sources-minus-sinks for each decomposed tracer (J terms, in units of $mmol$ N_2O m^{-3}) are:

$$J^{n_2o}_{nit} = (0.5 \cdot R^{n_2o}_{ao}) - R^{nit}_{den3}, \tag{3.9a}$$

$$J^{n_2o}_{den} = (0.5 \cdot R^{n_2o}_{den2}) - R^{den}_{den3}, \tag{3.9b}$$

$$J^{n_2o}_{bry} = -R^{bry}_{den3}. \tag{3.9c}$$

Note that the N_2O_{bry} tracer has no biogeochemical source in the domain and can only be consumed by N_2O reduction (R^{bry}_{den3}).

Transport of each decomposed tracer (T terms) is saved online as the divergence of advection/diffusion fluxes as in equation 3.6. All N_2O advected into the domain from the boundaries is tagged as N_2O_{bry}. That is, concentrations for N_2O_{bry} at the lateral boundaries are identical to N_2O, and for N_2O_{nit} and N_2O_{den} are zero. Air-sea fluxes (Φ terms) follow the same formulation as for total N_2O, but with mixing ratios set to zero for all tracers except N_2O_{bry}, for which they are set to the total values. As a consequence, fluxes of N_2O derived from nitrification and denitrification ($\Phi^{nit}_{n_2o}$ and $\Phi^{den}_{n_2o}$, respectively) are restricted to outgassing, whereas the flux of N_2O derived from the model boundaries ($\Phi^{bry}_{n_2o}$) allows for both ingassing (when N_2O_{bry} is below saturation) and outgassing (above saturation).

To initialize the decomposition tracers, we set the initial N_2O_{bry} to observed N_2O, and N_2O_{nit} and N_2O_{den} to zero. Thus, N_2O_{nit} and N_2O_{den} exclusively track production within the domain after initialization (Figure B.1). We then run a 50 year simulation to allow domain-integrated biogeochemical tracers to reach a seasonal quasi-steady state (Figure B.2). While this period may not be sufficient to fully equilibrate the decomposition tracers in the deep ocean, we can capture their proportion in the upper ocean and analyze their contributions to the total N_2O balance.

3.3 Results

3.3.1 Model validation

Figure 3.3 shows the extent and thickness of the modelled OMZ from model years 41 - 50 (Figure 3.3a) and various validation products (Figure 3.3b - e). The simulated OMZ is centered offshore of the Peruvian and Ecuadorian coastline at roughly 8^oS and extends from the Galapagos islands at the equator to nearly 15^oS. This represents a displacement both equatorward and offshore compared to observations, which suggest a more coastal OMZ between southern Peru and Chile; a similar shift in potential vorticity as the model progresses from initialization (Figure B.3) points to a slight bias in the representation of the physical circulation near the boundary between the subtropical gyre and the tropical current system. The thickness of waters with less than 10 $mmol$ O_2 m^{-3} ranges mostly between 300 - 500 m and extends to roughly 105^oW. Considering that O_2 reconstructions based on spatial interpolation of in situ profiles underestimate the volume of anoxic waters (Bianchi et al., 2012), the inset bar plot in Figure 3.3a suggests that the ROMS simulation is overall within range of OMZ volume predictions across several thresholds ranging from 5 $mmol$ O_2 m^{-3} (Kwiecinski & Babbin, 2021) to 20 $mmol$ O_2 m^{-3} (Dunn, 2012; Bianchi et al., 2012; H. Garcia et al., 2019).

Taking into account the slight equatorward geographic shift in the model OMZ, nitrogen tracer (NO_3^-, NO_2^-, and N_2O) sections at 250 m in Figure 3.4a - c compare well with observational products (Figure 3.4d - f). The simulation is able to replicate the observed drawdown of NO_3^- and N_2O, and the increase in NO_2^- within the core of the OMZ, resulting from denitrification. The magnitude and spatial patterns of open ocean concentrations are similarly reproduced, such as the low NO_3^- and N_2O concentrations observed in the subtropical gyre at 25^oS. The oxic to suboxic transition zone (inshore of the 20 $mmol$ O_2 m^{-3} contour in Figure 3.4) also reveals an increase in N_2O concentrations that skillfully reproduces observations.

Model profiles centered over the OMZ (Figure 3.4g - i) show low concentrations at the surface for NO_3^-, NO_2^-, and N_2O. As depth increases, local maxima in NO_2^- and N_2O are observed at $\sim$100 m coincident with low but non-zero O_2. Just below this depth, where O_2

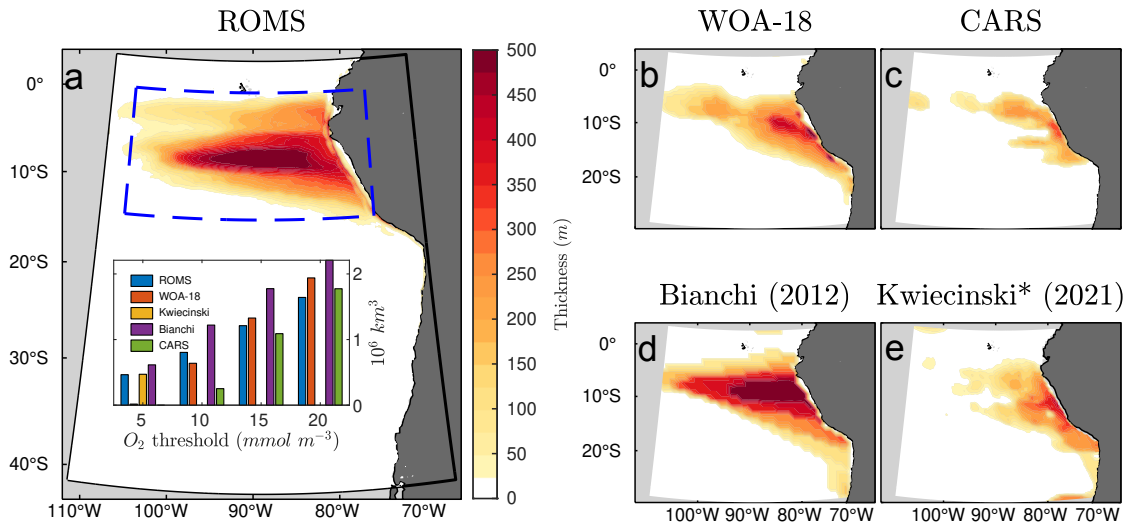

Figure 3.3: (a) ROMS Peru-Chile 10 km domain, with averaged OMZ thickness ($O_2 < 10\ mmol\ m^{-3}$) from model years 41 - 50. The inset bar plot shows OMZ volume from ROMS and validation products based on 5, 10, 15, and 20 $mmol\ m^{-3}$ thresholds. The N_2O budget region is also shown as the area encompassed by dashed blue lines, extending vertically from the surface to 1000 m. (b-d) OMZ thickness ($O_2 < 10\ mmol\ m^{-3}$) from World Ocean Atlas 2018, CSIRO Atlas of Regional Seas (CARS), and the Objective mapping 2 product from Bianchi et al. (2012). (e) OMZ thickness ($O_2 < 5\ mmol\ m^{-3}$) from Kwiecinski & Babbin (2021).

drops further to anoxic levels, local minima in NO_3^- and N_2O appear along with a large peak in NO_2^- of roughly 4 $mmol\ m^{-3}$. Beneath the anoxic OMZ, a second N_2O peak appears of slightly greater magnitude (~60 μmol N_2O m^{-3}) than the shallower maximum (~50 μmol N_2O m^{-3}). Depth-dependent distributions from shipboard measurements (Kalvelage et al., 2013; Cornejo & Farías, 2012; Krahmann et al., 2021) (pink shading) generally show good agreement between model and observations. The smaller vertical extent of the modeled OMZ NO_2^- maximum and N_2O minimum is likely caused by a slightly thinner oxygen deficient layer than observed. Also note that the geographical location of shipboard measurements differs from the ROMS averaging box due to the equatorward and offshore OMZ shift discussed above. Despite this geographical bias, Figure 3.4g - i demonstrates similarity in the expression of anaerobic nitrogen cycle processes at locations with comparable O_2 profiles. Remaining inconsistencies, such as the shallower depth of the observed upper N_2O maxima,

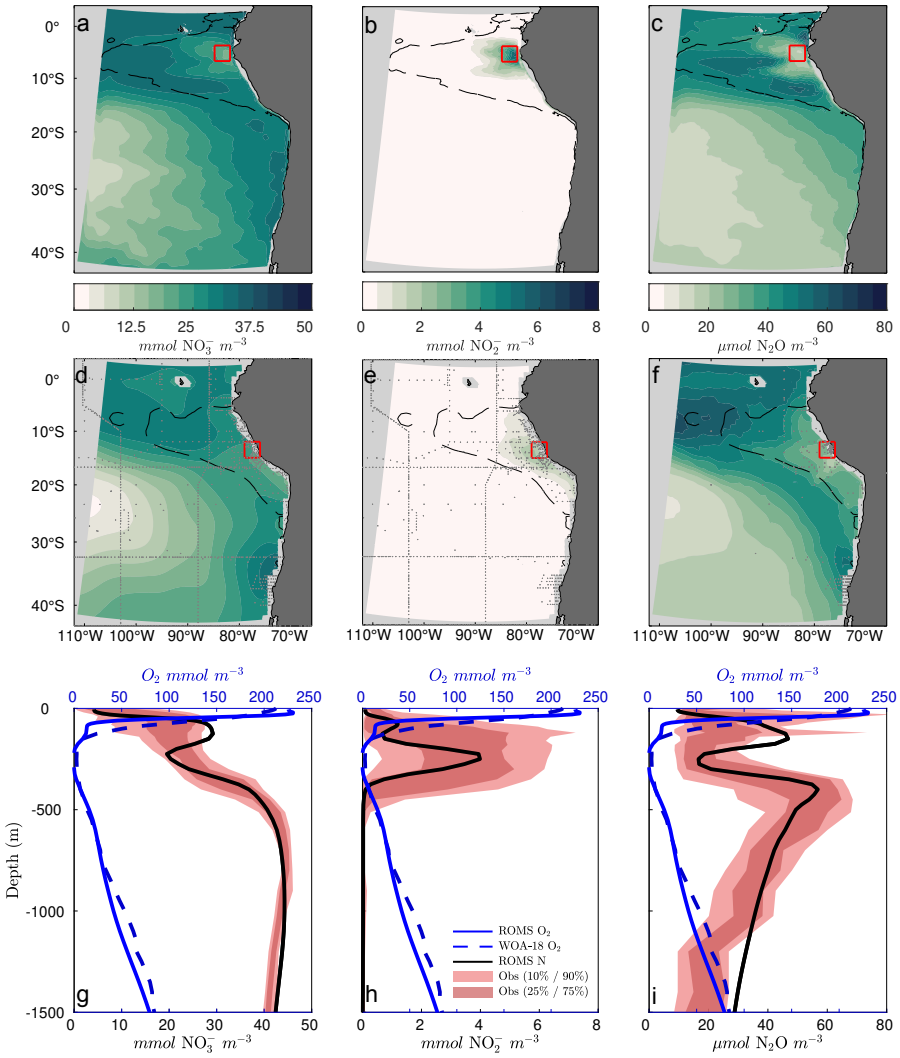

Figure 3.4: (a-c) ROMS averaged NO_3^-, NO_2^-, and N_2O at 250 m from model years 41 - 50. Dashed black lines highlight the 20 $mmol$ O_2 m^{-3} contour. (d-f) NO_3^- at 250 m from World Ocean Atlas 2018, and NO_2^- and N_2O at 250 m from machine learning estimates. Grey markers show the location of shipboard samples. (g-i) Averaged profiles of NO_3^-, NO_2^-, and N_2O from ROMS (black curves) extracted from within the OMZ (red boxes in panels a - c). Shaded regions show the 10th/90th and 25th/75th percentiles of shipboard observations from Kalvelage et al. (2013), Cornejo & Farías (2012), and Krahmann et al. (2021) conducted within the red boxes in panels d - f. Solid blue curves show ROMS O_2 whereas the dashed blue curves show averaged World Ocean Atlas 2018 O_2 over the shipboard sampling region.

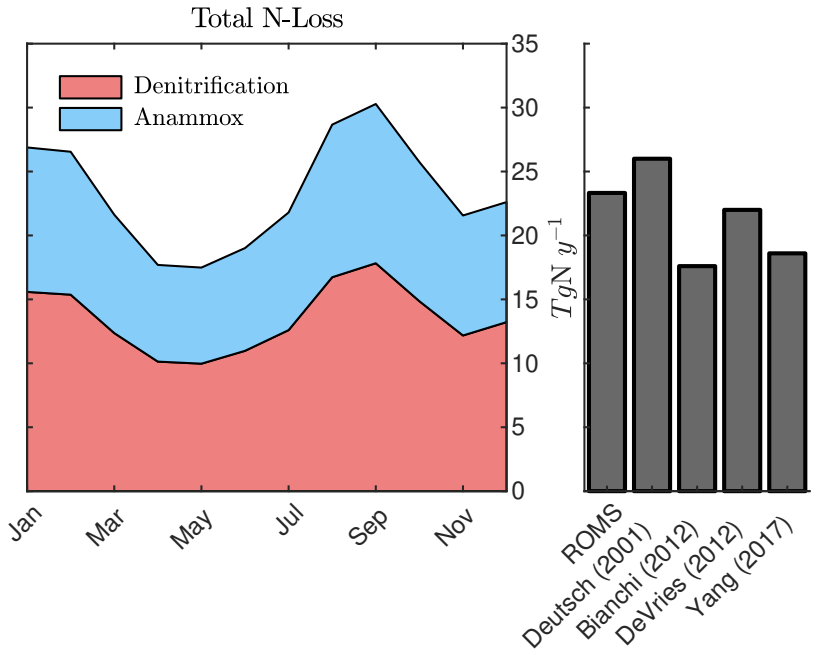

Figure 3.5: (left) Monthly averaged fixed nitrogen loss from ROMS via canonical denitrification and anammox from models year 41 - 50. (right) ETSP estimates of total annual averaged nitrogen loss from ROMS, Deutsch et al. (2001), Bianchi et al. (2012), DeVries et al. (2013), and Yang et al. (2017).

can be explained by the proximity of observations to the coast, as compared to the more offshore location used to average model profiles.

Finally, given the importance of accurately representing water column denitrification, we compared total fixed nitrogen loss in ROMS via denitrification and anammox to other ETSP estimates (Figure 3.5). We simulate a consistent N loss fraction of roughly 58%/42% from denitrification/anammox (respectively) throughout the year, consistent with recent studies (Peng et al., 2016). The total water-column fixed nitrogen loss in the model is 23.3 TgN yr^{-1}, within the range of observational estimates for the region (Deutsch et al., 2001; Bianchi et al., 2012; DeVries et al., 2013; Yang et al., 2017), and with seasonal variability mostly driven by changes in denitrification rates (red shading). Thus, despite a geographic shift, the model produces a realistic OMZ and associated nitrogen cycle tracers and rates.

3.3.2 N_2O production in the ETSP

A transect at 8^oS crossing the core of the model OMZ in Figure 3.6 reveals the subsurface structure of tracers and reactions relevant to N_2O production in the ETSP. We model a large discrepancy in magnitude between NO_3^- and NO_2^- reduction rates ($R^{no_2}_{den1}$-$R^{n_2o}_{den2}$, Figure 3.6a) throughout the OMZ, which in part maintains the relatively high NO_2^- concentrations shown by Figure 3.6d. The difference between NO_2^- reduction and N_2O reduction ($R^{n_2o}_{den2}$-$R^{n_2}_{den3}$, Figure 3.6b), in contrast, is much smaller in magnitude but switches sign along the transect. Within the anoxic core (< 5 $mmol$ O_2 m^{-3}, dotted black contour in Figure 3.6), N_2O reduction exceeds NO_2^- reduction causing widespread net N_2O consumption (blue shading) of nearly 0.2 μmol N m^{-3} d^{-1} (Figure 3.6b). The resulting N_2O zonal gradients (Figure 3.6e) show consistent offshore subsurface N_2O minima that coincide with peak concentrations of NO_2^- at the same depth range (Figure 3.6d). These patterns suggests that all three modelled denitrification steps proceed with minimal O_2 inhibition within the anoxic core, supporting a zone of complete denitrification to N_2 and thus active fixed N loss.

Along the exterior of the anoxic core, Figure 3.6b indicates that O_2 gradients preferentially inhibit N_2O reduction ($R^{n_2}_{den3}$) and allow incomplete denitrification. Accordingly, net N_2O consumption transitions to net production (red shading) of a similar $\sim$0.2 μmol N m^{-3} d^{-1} magnitude (Figure 3.6b). Beyond suboxic waters ($O_2 > 10$ $mmol$ m^{-3}, dashed black contour line in Figure 3.6), net production from denitrification abruptly ceases. The transect also reveals maximum N_2O production from NH_4^+ oxidation ($R^{n_2o}_{ao}$, Figure 3.6c) peaks at roughly 0.02 μmol N m^{-3} d^{-1} and is largely restricted to a thin, mostly oxygenated layer at roughly 100 - 150 m that mirrors vertical maxima in POC flux (not shown) and the primary NO_2^- maximum in Figure 3.6d. Notably, the rate is slightly amplified within the 5 $mmol$ O_2 m^{-3} contour (dotted black contours in Figure 3.6c), revealing enhanced N_2O yield at low O_2.

The relative contributions to total N_2O concentrations (Figure 3.6e) from the decomposed N_2O tracers (Figure 3.6f - h) highlight the disparity between biogeochemical N_2O sources in the ETSP. Within the anoxic OMZ core, residual N_2O concentrations of $\sim$10 to 20 μmol

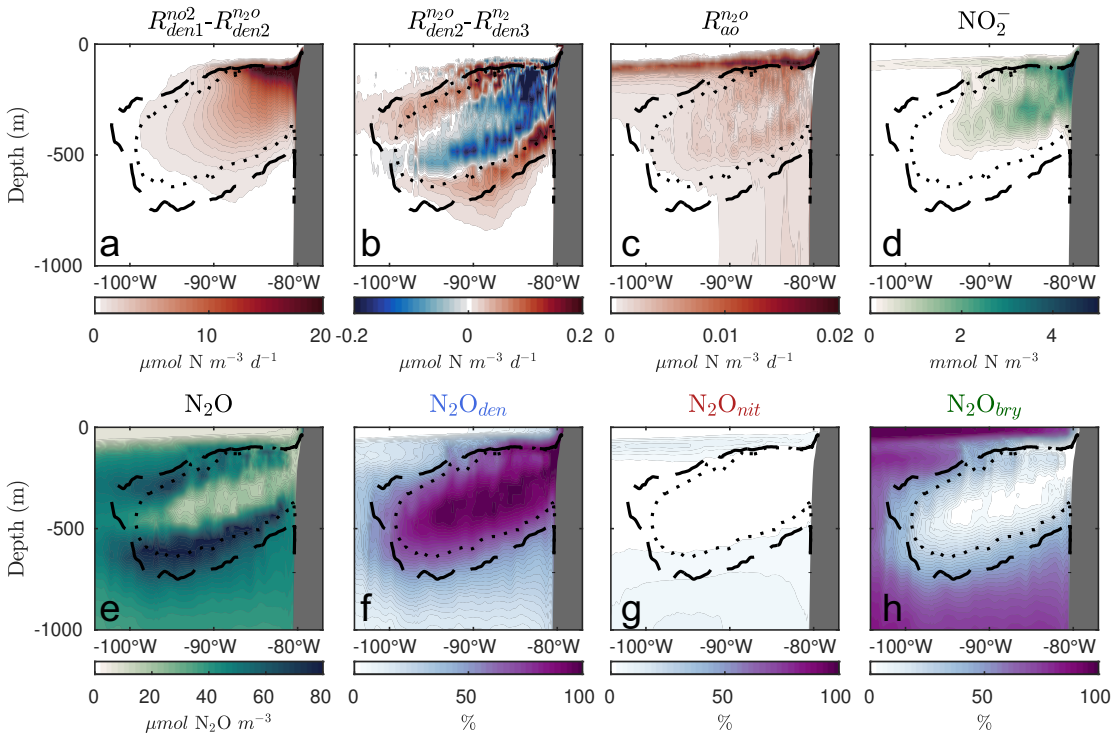

Figure 3.6: (a) Averaged net NO_2^- production from denitrification for model years 41 - 50 along a transect from the coast at 8^oS. The dotted and dashed black curves in highlight the 5 and 10 $mmol\ O_2\ m^{-3}$ contours, respectively. (b-e) Same as in panel (a), but for N_2O production from denitrification (b), N_2O production from nitrification (c), NO_2^- (d), and N_2O (e). Panels (f) - (h) show the relative contributions to the N_2O in panel (e) from each decomposed N_2O tracer (N_2O_{den}, N_2O_{nit}, and N_2O_{bry}).

m^{-3} persist (Figure 3.6e), and are nearly completely derived from denitrification via NO_2^- reduction (N_2O_{den}, Figure 3.6f). Considering the patterns in Figure 3.6b, this indicates a balance in the anoxic core between advection of N_2O_{den} produced along the OMZ fringe and local N_2O consumption. As O_2 increases beyond suboxic levels, the contribution of N_2O_{den} diminishes, while the contribution from the boundaries (N_2O_{bry}) begins to account for the remainder. In contrast, N_2O from nitrification (N_2O_{nit}, Figure 3.6g) contributes up to 10% to total N_2O along the transect, with a maximum at roughly 100 m depth, suggesting that incomplete denitrification is the main biogeochemical contributor ($\mathcal{O}(10)$ times greater production) to local N_2O production throughout the OMZ.

A similar transect showing the sources-minus-sinks (J terms, equations (3.5) and (3.9a,3.9b,3.9c)) of each decomposed N_2O tracer further highlights the disparity between different processes (Figure B.4). Production and consumption of N_2O by denitrification ($J^{n_2o}_{den}$, Figure B.4b) largely mirror the sources and sinks of total N_2O (J^{n_2o}, Figure B.4a), which are mostly confined to the OMZ. In contrast, N_2O produced by nitrification ($R^{n_2o}_{ao}$, Figure 3.6c) largely escapes consumption by denitrification throughout the transect, except near the coast, and therefore contributes to total N_2O concentrations primarily in the upper ocean at roughly 100 m depth ($J^{n_2o}_{nit}$, Figure B.4c), in agreement with Figure 3.6g.

Notably, the contribution of N_2O transported into the OMZ from the model boundaries (N_2O_{bry}) is rapidly reduced at low O_2 (Figure 3.6h). Indeed, Figure B.4d reveals significant OMZ consumption of N_2O_{bry} ($J^{n_2o}_{bry}$), especially at shallower depths, helping to explain the small contribution of N_2O_{bry} to total N_2O concentrations throughout most of the OMZ. Thus, the ETSP is revealed as a sink of remotely generated N_2O transported into the domain. Additionally, while production from incomplete denitrification is generally confined to suboxic waters (dashed black contour in Figure 3.6b), significant concentrations of N_2O from denitrification (N_2O_{den}) in oxygenated waters suggest export of N_2O_{den} out of the OMZ. Together, these results highlight an important role for circulation in redistributing N_2O within the ETSP.

3.3.3 Contributions of different processes to the N_2O balance

The monthly-averaged time-series from model years 41 - 50 of integrated net biogeochemical sources-minus-sinks (J terms) for N_2O (equation (3.5)) and each decomposed N_2O tracer (equation (3.9a),3.9b,3.9c) are shown in Figure 3.7a. In general, the ETSP is a net source of N_2O from August to February (J^{n_2o}, black line in Figure 3.7a). Net production is predominantly driven by denitrification ($J^{n_2o}_{den}$, blue line), which provides a consistent source of N_2O throughout the year while also driving the bulk of monthly variability in net N_2O production (J^{n_2o}). In contrast, production from nitrification ($J^{n_2o}_{nit}$, red line) is net positive throughout the year, but only accounts for a small proportion of the total. Since N_2O transported from

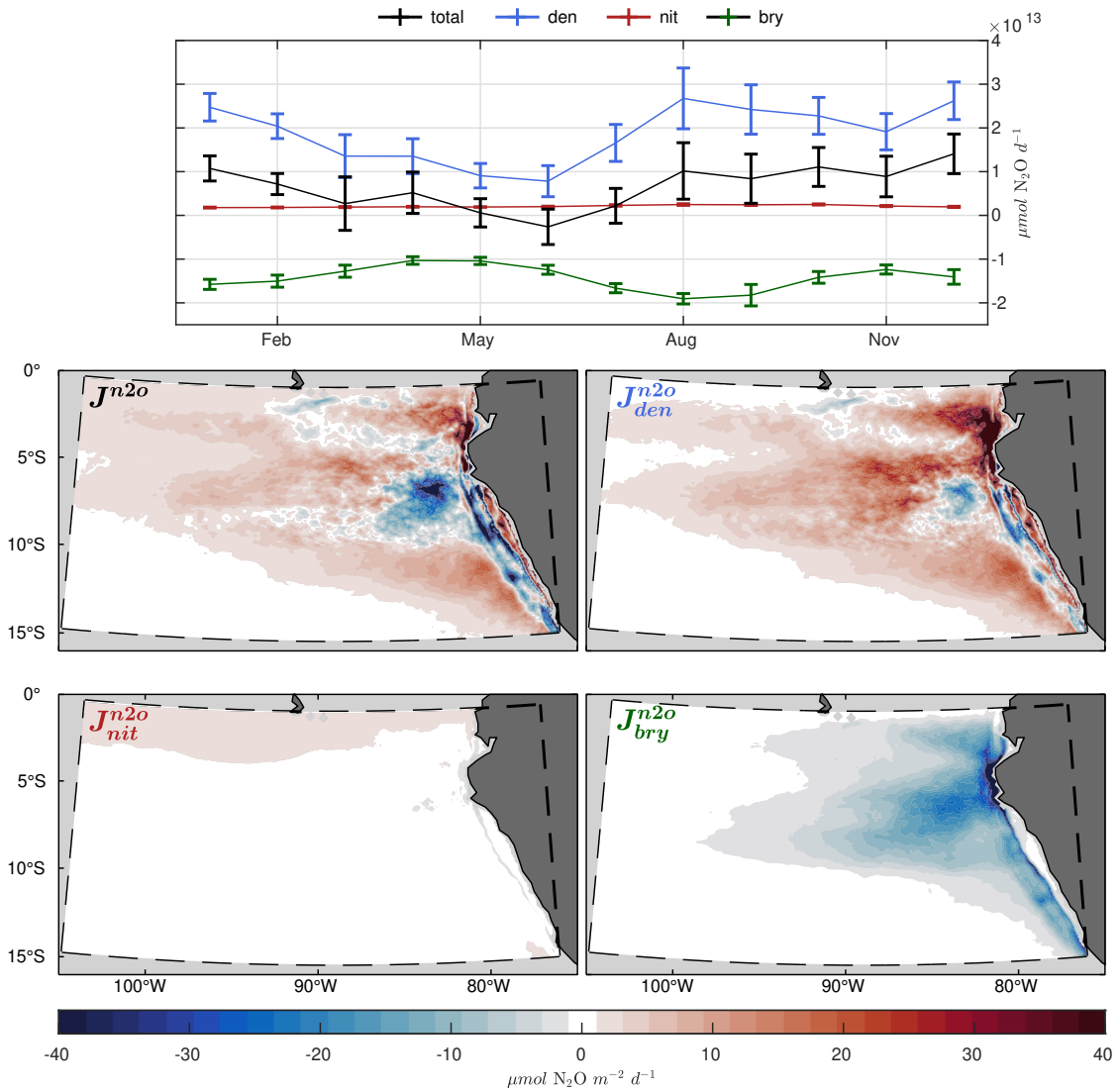

Figure 3.7: (top) Time-series of integrated biological sources-minus-sinks (J terms) for N_2O (black) and each of the decomposed N_2O tracers. Error bars show monthly average and standard deviation from model years 41 - 50. (bottom panels) Vertically integrated sources-minus-sinks for total N_2O and the decomposed N_2O tracers from the OMZ budget domain, averaged from model years 41 - 50.

the boundaries (N_2O_{bry}) lacks production terms within the domain, $J^{n_2o}_{bry}$ (green line) reveals consistent consumption by denitrification throughout the year.

Vertically integrating the sources-minus-sinks over the budget domain for the total N_2O tracer (J^{n_2o}, Figure 3.7b) and for the N_2O originating from NO_2^- reduction ($J^{n_2o}_{den}$, Figure

3.7c) reveals similar spatial patterns, showing a hot-spot of vigorous net consumption (blue shading) centered at roughly 8^oS and 80^oW that abruptly transitions to net production (red shading) in the surrounding ocean. The spatial patterns for the remaining N_2O tracers are distinct. The integrated sources-minus-sinks of N_2O from nitrification ($J^{n_2o}_{nit}$, Figure 3.7d) reveal a region of net production mainly along the northern boundary that is partly compensated by net consumption immediately adjacent to the coastline. In contrast, the consumption of N_2O originating from the model boundaries ($J^{n_2o}_{bry}$, Figure 3.7e) takes place over much of the OMZ, with enhanced loss near the coast.

The OMZ is therefore characterized by a coastal hot-spot of net N_2O consumption that depletes locally produced N_2O from both denitrification and, to a lesser extent, nitrification ($J^{n_2o}_{den}$ and $J^{n_2o}_{nit}$, blue and red lines in Figure 3.7a, respectively) and N_2O originating from outside the domain ($J^{n_2o}_{bry}$, green line in Figure 3.7a). Outside the coastal hot-spot, the prevalence of incomplete denitrification in the steep O_2 gradients bounding the anoxic OMZ more than compensates for consumption via complete denitrification at the coast, and makes the OMZ a net annual production source of N_2O (Figure 3.7a). As expected at quasi steady-state, advective and diffusive terms (T), shown in Figure B.5, largely balance the sources-minus-sinks in Figure 3.7.

The resulting N_2O air-sea flux (Φ^{n_2o}, black lines in Figure 3.8a) peaks in July and is positive throughout the year, indicating that the ETSP OMZ is a constant source of N_2O to the atmosphere with higher outgassing rates throughout the upwelling season (boreal summer). The major contributing components to the flux are N_2O originating from the model boundaries ($\Phi^{n_2o}_{bry}$) and locally produced N_2O from denitrification ($\Phi^{n_2o}_{den}$), which exhibit similar seasonal cycles as in the total flux (Φ^{n_2o}), albeit with different geographical distributions. The spatial pattern of total N_2O air-sea flux (Φ^{n_2o}) can be described as a combination of $\Phi^{n_2o}_{bry}$ and $\Phi^{n_2o}_{den}$ patterns; the outgassing flux of N_2O from denitrification ($\Phi^{n_2o}_{den}$) is concentrated near the coast with a structure closely mirroring the coastal hot-spot of consumption shown by Figure 3.7c, whereas the flux of N_2O originating from boundaries ($\Phi^{n_2o}_{bry}$) takes place mostly along the northern boundary of the budget region (albeit with maximum outgassing near the coast). Finally, the magnitude of air-sea flux from local nitrification ($\Phi^{n_2o}_{nit}$) is small but

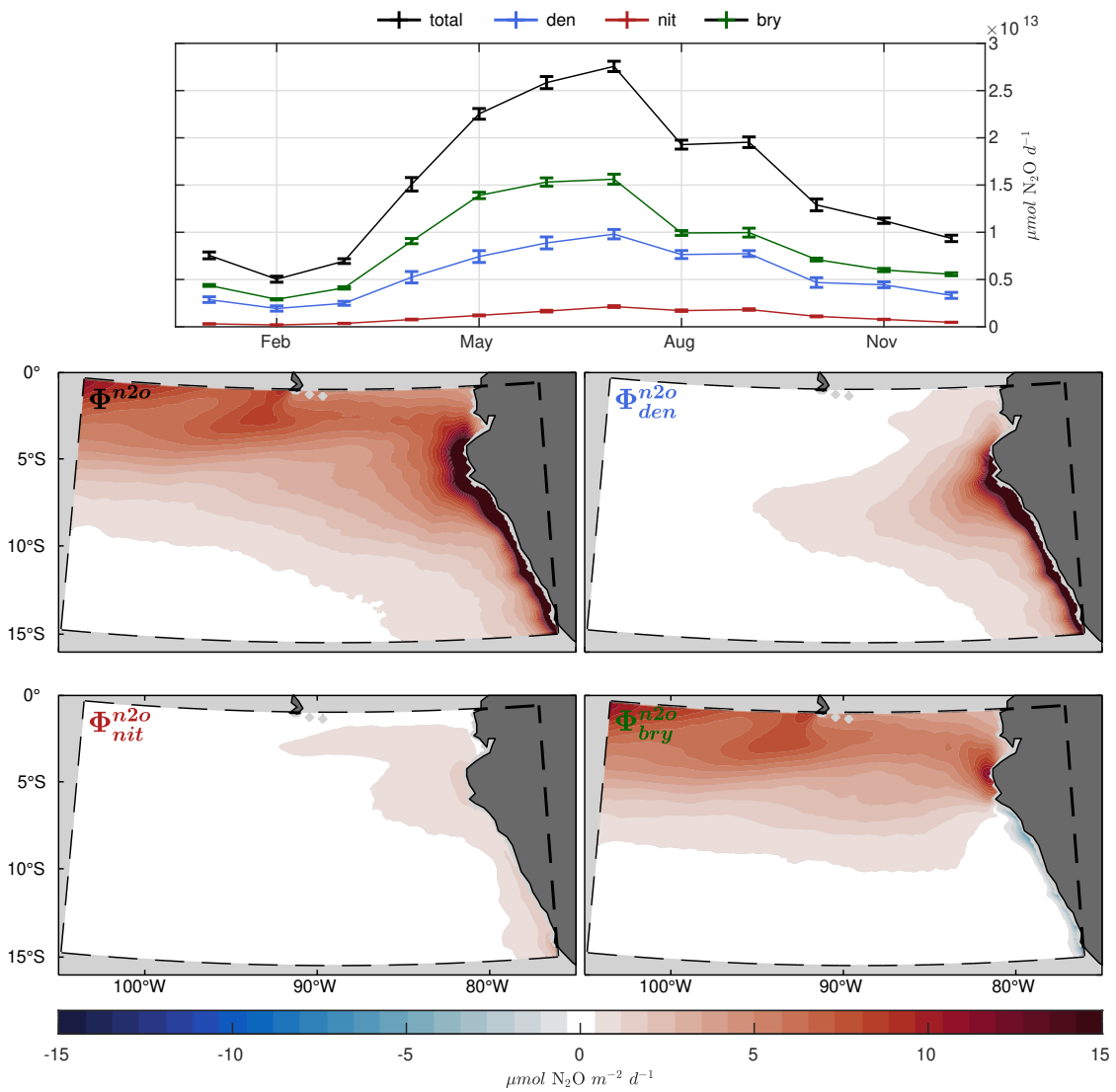

Figure 3.8: Same as in Figure 3.7, but for air-sea flux (Φ) of total N_2O and each of the decomposed N_2O tracers.

net positive, and shows a similar July maximum peaking near the coast.

3.3.4 N_2O balance in the ETSP

A schematic of the annual mean N_2O balance (Figure 3.9) over model years 41 - 50 shows that N_2O production in the OMZ is dominated by incomplete denitrification (191.6 $\pm$ 26.3 $Gg\,N\,y^{-1}$), whereas nitrification contributes a smaller fraction (21.4 $\pm$ 0.6 $Gg\,N\,y^{-1}$). Conversely, consumption of N_2O from the model boundaries (N_2O_{bry}) drives a net N_2O loss

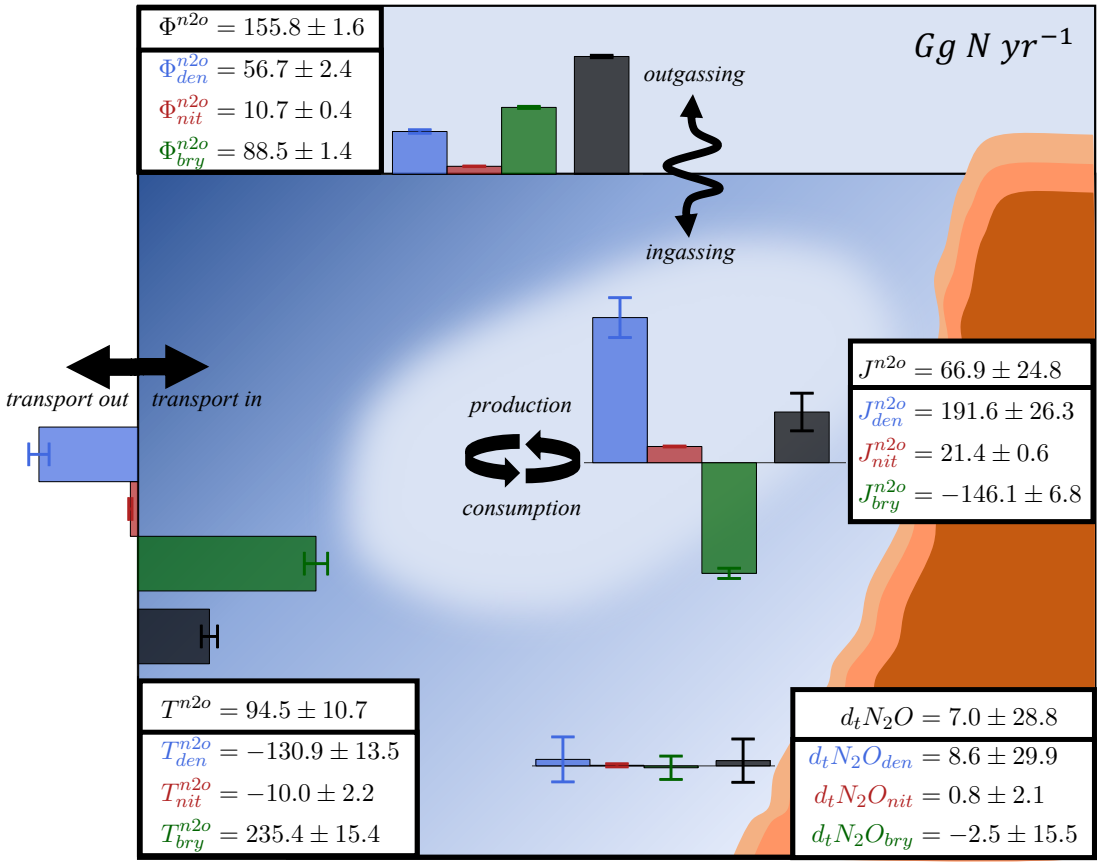

Figure 3.9: Schematic of the ETSP OMZ N_2O tracer budget, with calculated averages and standard deviations ($Gg\,N\,y^{-1}$) of net air-sea flux (Φ), advection (T), sources-minus-sinks (J), and the annual rate of change (d_t) from model years 41 - 50. Bar plots indicate both the direction of, and relative magnitude of, budget averages and standard deviations.

(-146.1 $\pm$ 6.8 $Gg\,N\,y^{-1}$). The excess production makes the ETSP a net N_2O source to the atmosphere (66.9 $\pm$ 24.8 $Gg\,N\,y^{-1}$). This production takes place predominantly on the fringe of the OMZ both vertically and horizontally, where thick suboxic layers support net N_2O accumulation from denitrification (Figures 3.6b and 3.7c).

The budget also suggests that the corresponding outgassing pathways from local production sources are somewhat inefficient. The annual export of 130.9 $\pm$ 13.5 and 10 $\pm$ 2.2 $Gg\,N\,y^{-1}$ of N_2O originating from denitrification and nitrification ($T^{n_2o}_{den}$ and $T^{n_2o}_{nit}$, respectively) indicates that ~68% and ~46% of their net production ($J^{n_2o}_{den}$ and $J^{n_2o}_{nit}$, respectively) ultimately avoids outgassing within the domain via export at the model boundaries. Despite

the surprising magnitude of these export rates, high net import of N_2O from the model boundaries ($T_{bry}^{n_2o}$, 235.4 $\pm$ 15.4 $Gg\,N\,y^{-1}$) represents a net source of 94.5 $\pm$ 10.7 $Gg\,N\,y^{-1}$ into the OMZ region. Separating the advective fluxes into zonal, meridional, and vertical components reveals zonal fluxes along the western boundary of the domain as the primary interface of N_2O exchange with the surrounding ocean, organized as alternating narrow bands of N_2O import (Figure B.6a, red shading) and export (blue shading). The net transport is driven by N_2O supplied through the boundaries (N_2O_{bry}, Figure B.6d), with the most intense import along the equator at roughly 150 m depth (see also Figure 3.6h). In contrast, denitrification-driven export (Figure B.6b) is focused further to the south (roughly 8^oS) and at deeper depths (200 - 500 m, also evident in Figure 3.6f).

After accounting for boundary exchanges and local subsurface production and consumption, all tracers reveal net outgassing with contributions from N_2O originating from the boundaries and denitrification ($\Phi_{bry}^{n_2o}$ and $\Phi_{den}^{n_2o}$, respectively) contributing $\sim$56% and $\sim$36%, respectively, to the annual 155.8 $\pm$ 1.6 $Gg\,N\,y^{-1}$ outgassed to the atmosphere. N_2O originating from nitrification ($\Phi_{nit}^{n_2o}$) contributes only $\sim$7% on an annual basis. Thus, the picture that emerges is that of an ETSP OMZ characterized by: (1) A consistent supply of N_2O originating outside the ETSP from predominantly zonal subsurface currents in the tropical band (Figures B.5, and B.6d); (2) Advection of N_2O into a coastal hot-spot where vigorous consumption leads to significant N loss; (3) Net N_2O production predominantly by denitrification within suboxic gradients surrounding the OMZ (Figures 3.6b and 3.7c); (4) Significant export of N_2O produced by denitrification to the exterior ocean (Figures B.5, and B.6b); (5) Consumption of locally produced and externally derived N_2O; and (6) Year-round air-sea flux of N_2O driven predominantly by N_2O imported into the domain and produced locally by denitrification that upwell and outgas along the northern extent of the OMZ and along the coast, respectively (Figure 3.8c,d).

3.4 Discussion and Conclusions

We developed a climatological, eddy-resolving simulation of the ETSP OMZ that reproduces the main patterns in the spatial distribution of observed nitrogen tracers and transformation rates. Despite enhanced yields at low O_2 (equation (3.1)), we find that the local net contribution from nitrification, after accounting for consumption by denitrification, represents only ∼11% of the total biogeochemical N_2O sources in the ETSP (Figure 3.9). Water column maxima in N_2O production by NH_4^+ oxidation follow vertical maxima in POC flux, which occur well above the oxycline throughout much of the domain east of -90^{o}W (Figure 3.6c). Closer to shore, as the OMZ core shoals to ∼100 m, some proportion of the N_2O produced by nitrification (Figure 3.7d) is subsequently mixed into anoxic waters and consumed by N_2O reduction. The major contribution of nitrification to N_2O production takes place immediately adjacent to the coast, where low O_2 waters at shallow depths lead to enhanced production (Figure 3.6c) and an efficient outgassing route. As a result, the air-sea flux pattern in Figure 3.8d shows negligible contributions from nitrification throughout most of the domain, with the exception of coastal outgassing driven by upwelling. While the contribution from nitrification to N_2O production in the model is sensitive to the choice of the parameters in equation (3.1), the values used in this study are constrained by observations (Section 3.2.2) and fall within the range of previous estimates (Ji et al., 2018; Santoro et al., 2021) that suggest weak nitrification production. Therefore, similar to the results of Ji et al. (2015, 2018) and Babbin et al. (2015), our simulation suggests that local production by nitrification is not a dominant pathway for N_2O outgassing in this region.

Instead, N_2O production is dominated by incomplete denitrification along the suboxic fringes of the anoxic OMZ core (Figure 3.6b,f and Figure 3.7a,c), in agreement with recent studies (Babbin et al., 2015; Bourbonnais et al., 2017; Ji et al., 2018). In general, the three step-wise denitrification rates shows a strong seasonal dependence and are primarily controlled by the timing of organic matter supply from the euphotic zone (Figure B.7) rather than variability in low O_2 volumes throughout the year (Figure B.8). Within the anoxic core of the OMZ, we find large net N_2O consumption rates (Figure 3.6b), in agreement

with recent measurements (Kock et al., 2016; Casciotti et al., 2018; Kelly et al., 2021) and modeling studies (Bourbonnais et al., 2017). This indicates short residence times for N_2O produced via NO_2^- reduction (N_2O_{den}) due to the strong coupling between denitrification steps at low O_2. Significant net N_2O production by denitrification (J_{den}^{n2o}) occurs where high rates of vertical POC flux overlap with an anoxic to suboxic O_2 gradient. There, the difference in O_2 tolerance thresholds leads to a relatively small residual between large NO_2^- and N_2O reduction rates within the domain (Figure 3.6b)(Babbin et al., 2015). Along with N_2O consumption and the inhibition of aerobic remineralization in the anoxic core, this leads to the characteristic double peak structure in N_2O profiles (Figure 3.6e).

The vertical depth range occupied by anoxic to suboxic gradients plays a key role in determining regions of net production or consumption via denitrification. For instance, the integrated net production by denitrification in Figure 3.7c reveals consumption along the northern extent of the Peruvian coast at roughly 8^oS. Considering this pattern, Figure 3.6b shows relatively sharp O_2 gradients above and below the OMZ around -85^{o}W, indicating that N_2O consumption is particularly strong near the coast, where thin but shallow suboxic layers are found. In contrast, suboxic layers become thicker offshore, resulting in conditions more favorable to N_2O production. Therefore, the high rates of coastal outgassing observed in Figure 3.8c are at least partially driven by net transport from more productive surrounding waters (Figure B.5).

Our results demonstrate the role of advection in redistributing N_2O within the ETSP. Notably, the EUC and SSCC are major conduits of N_2O transport into the OMZ domain. This is demonstrated by the large fractional contributions of boundary-derived N_2O at 150 m throughout the eastern extent of the transect in Figure 3.6h, which match subsurface patterns in Figure B.6d. These results are consistent with those from Yang et al. (2020), who highlighted the tropics in the Eastern Pacific as an important outgassing region with seasonality driven predominantly by the timing of upwelling (May to September). While a significant fraction of the imported N_2O is ultimately advected into the anoxic OMZ to be consumed (Figures 3.6h and 3.7e), the remainder is responsible for the bulk ($\sim$56%) of the outgassing flux over the OMZ domain. As the N_2O budget and boundary export schematic in

Figures 3.9 and B.6 show, circulation also plays a key role in exporting the majority (roughly 68%) of local denitrification-derived N_2O production out of the OMZ. Much of this export takes place along the western boundary (Figure B.6b), but at more southerly latitudes and at deeper depths compared to the import of external N_2O from the boundaries (T^{n2o}_{bou}).

Our regional simulations do not allow us to explore the fate of this exported N_2O. Global or basin-wide simulations would enable tracking the interplay of N_2O sources and sinks within and outside OMZs. Using water mass analysis and isotopic measurements, Carrasco et al. (2017) found stronger correlations between N_2O and N^* from waters equatorward of 20^oS in the ETSP compared to subtropical waters further south, suggesting that equatorial waters with high N_2O were linked to a source from denitrification. As these N^* signals propagate far into the western Pacific along the equator (Deutsch et al., 2001), it is possible that a significant portion of the imported N_2O originates from eastward equatorial currents that recirculate N_2O (and N^*) produced by denitrification in the ETSP. This may help explain the high N_2O concentrations in offshore water waters measured by Santoro et al. (2021). Isotopic measurements along the equator may help resolve these emerging questions.

The residual between rapid N_2O production and consumption by denitrification is heavily coupled to O_2 dynamics and thus a major portion of N_2O outgassing in this region is likely sensitive to future changes in OMZ magnitude and geometry. Observations suggest that deoxygenation over the past 50 years has led to expansion of OMZ volumes and shoaling of the upper oxycline (Stramma et al., 2008; Schmidtko et al., 2017). Yet, whether this has caused a positive or negative impact on N_2O production likely depends on the relative changes of anoxic versus suboxic volumes. If future climate change results in an increase in the volume of suboxic waters, as suggested by Earth system model projections (Cabré et al., 2015; Kwiatkowski et al., 2020; J. J. Busecke et al., 2019), it would increase production from both incomplete denitrification and nitrification, leading to a positive climate feedback (Battaglia & Joos, 2018). A parallel reduction in the volume of anoxic waters (Bianchi et al., 2018; J. J. Busecke et al., 2019) would also limit N_2O consumption, strengthening this feedback.

Future changes in the oxycline depth via projected stratification or wind changes (Kwiatkowski

et al., 2020; J. J. Busecke et al., 2019; Bakun, 1990) may alter the coupling between local N_2O production and outgassing over OMZs, while also affecting the export of N_2O into the nearby gyres. The lack of interannual forcing in our study leaves gaps in understanding ENSO impacts. OMZ geometry and denitrification rates are sensitive to ENSO variability (Yang et al., 2017), thus N_2O production and outgassing are likely to exhibit significant year-to-year changes. Interannually forced, high-resolution simulations are needed to resolve these questions. Future versions of the model should also improve the representation of N_2O sources to included additional pathways, namely hybrid production from AOA (Stieglmeier et al., 2014; Kozlowski et al., 2016; Trimmer et al., 2016) and direct N_2O production from NO_3^- (Ji et al., 2018; Frey et al., 2020). New measurements of these N cycle transformations across environmental gradients will help constraining the relative contributions of these processes.

CHAPTER 4

Mesoscale Variability Enhances Fixed Nitrogen Loss and Suppresses Nitrous Oxide Production in Oxygen Minimum Zones

This chapter contains a draft of a manuscript, to be submitted.

4.1 Introduction

Nitrogen (N) exists in many chemical forms and oxidation states in the ocean, linked together by a dynamic microbial cycle (Zehr & Ward, 2002; Kuypers et al., 2018). Bioavailable or "fixed" N, such as nitrate (NO_3^-), nitrite (NO_2^-), and ammonium (NH_4^+, here used interchangeably with ammonia, NH_3) are used to synthesize organic matter or provide energy for metabolisms via redox reactions (Capone et al., 2008; Kuypers et al., 2018). Loss of fixed N occurs in anaerobic environments where N transformations produce dinitrogen gas (N_2) (Codispoti, 2007; Dalsgaard et al., 2012) and nitrous oxide (N_2O), an ozone-depleting agent and powerful greenhouse gas (Suntharalingam et al., 2000; Ravishankara et al., 2009; IPCC, 2013). Hot-spots of fixed N loss occur in oxygen minimum zones (OMZ) such as those found in the Arabian Sea, the Eastern Tropical North Pacific, and the Eastern Tropical South Pacific (ETSP) (Codispoti & Christensen, 1985; Deutsch et al., 2001; Bianchi et al., 2012; DeVries et al., 2013). Despite only occupying roughly 1% of the ocean volume (Lam & Kuypers, 2011), up to 50% of oceanic N_2O emissions to the atmosphere (Codispoti, 2010; Arévalo-Martínez et al., 2016; Yang et al., 2020) and 30 - 50 % of total N_2 production (Gruber & Galloway, 2008; Codispoti, 2010) occur in these regions.

As O_2 approaches anoxia (here defined as $O_2 < 5$ mmol m^{-3}), aerobic remineralization ceases and is followed by stepwise heterotrophic denitrification ($NO_3^- \rightarrow NO_2^- \rightarrow N_2O \rightarrow N_2$), which generates both N_2O (as an intermediary) and N_2 (B. B. Ward et al., 2009; Babbin et al., 2015; Kalvelage et al., 2013). The release of NH_4^+ from remineralization further stimulates fixed N loss. In oxygenated waters, small amounts of N_2O are generated as a byproduct of NH_4^+ oxidation by nitrification, with higher yields at lower O_2 concentrations (Goreau et al., 1980; Nevison et al., 2003; Ji et al., 2015; Santoro et al., 2021). In oxygen-deficient waters, N_2 is produced by anaerobic oxidation of NH_4^+ with NO_2^- (anammox) (Kuypers et al., 2003; Lam et al., 2009; Dalsgaard et al., 2012). Recent studies have shown that denitrification is more sensitive than anammox to O_2, with each reduction step progressively more inhibited by O_2 due to regulation by distinct enzymes (Körner & Zumft, 1989; Kalvelage et al., 2011; Dalsgaard et al., 2014). This suggests that elevated N_2O concentrations along the fringe of OMZs are the result of incomplete denitrification, as NO_3^- and NO_2^- reduction proceed, while N_2O reduction is suppressed at low but non-vanishing O_2 (Babbin et al., 2015; Frey et al., 2020; Bianchi et al., 2022; McCoy et al., 2023).

The ETSP hosts the second largest OMZ by area in the global ocean (Fuenzalida et al., 2009; Bianchi et al., 2012). Enhanced and persistent mesoscale activity occurs in this region (Chaigneau et al., 2009; Chelton et al., 2011). Variability at the oceanic mesoscale shapes the transport of biogeochemical tracers due to eddy-scale correlations between currents and tracer concentrations, for example by intermittently supplying O_2 to the OMZ (Czeschel et al., 2011; Gnanadesikan et al., 2013; Bettencourt et al., 2015). Yet, because of computational limitations, models employed to simulate extensive regions like the ETSP over long time scales are typically coarse in horizontal resolution. A recognition of eddy-induced transport has generated a variety of techniques to represent their unresolved influence in such models (e.g., Gent & Mcwilliams (1990) and Fox-Kemper et al. (2008)).

Mesoscale activity also generates heterogeneity in biogeochemical tracers. Because many biogeochemical transformations depend nonlinearly on tracer concentrations, and have comparable timescales to turbulent tracer fluctuations (Mahadevan & Campbell, 2002; Pasquero, 2005; Prend et al., 2021), chemical heterogeneity can lead to amplification or reduction of

transformation rates at the scale of eddies (herein referred to as "eddy reactions") (Goodman & Robinson, 2008; Lévy et al., 2012; Wallhead et al., 2013; Martin et al., 2015; Prend et al., 2021). As a consequence, biogeochemical rates estimated from a "mean field approximation" (e.g., from properties averaged over temporal or spatial scales greater than those of eddies) can fail to capture the magnitude of transformation rates in a fluctuating environment (Rovinsky et al., 1997; Brentnall, 2003; Lévy et al., 2013; Martin et al., 2015). For example, Lévy et al. (2013) used an eddy-resolving biogeochemical model of the North Atlantic to suggest that eddy reactions augment primary production and grazing rates by between 5 - 30% relative to the mean state.

N cycle reactions responsible for N_2 and N_2O production are highly nonlinear in their response to environmental variability, in particular oxygen concentrations, suggesting a significant role for eddy reactions. In this study, we examine the role of eddy heterogeneity on fixed N loss and N_2O production, which is usually ignored by coarse models of ocean biogeochemistry used to study OMZ processes (Cabré et al., 2015; Martinez-Rey et al., 2015; Kwiatkowski et al., 2020; J. J. M. Busecke et al., 2022). To this end, we apply an eddy-mean decomposition formalism (Lévy et al., 2013, 2024) to a realistic eddy-resolving simulation of the ETSP OMZ (McCoy et al., 2023) to quantify the importance of eddy reactions on N_2 and N_2O production.

4.2 Methods

4.2.1 Model configuration

We employ an identical model configuration for the ETSP as in McCoy et al. (2023), but with a finer horizontal resolution of 5 km (from 10 km) to better resolve mesoscale eddies. The domain extends from -111.38^oW to -66.62^oW and from 42.52^oS to 3.41^oN, and captures the horizontal extent of the ETSP OMZ, the equatorial current system, and the wind-driven subtropical gyre circulation (Figure 4.1a).

The physical component consists of the Regional Ocean Modeling System (ROMS), a

primitive-equation, hydrostatic, topography-following general ocean circulation model (Shchepetkin & McWilliams, 2005; Shchepetkin, 2015). ROMS is coupled online to the Biogeochemical Elemental Cycling (BEC) model (Moore et al., 2004; Deutsch et al., 2021) with an expanded representation of OMZ biogeochemistry (NitrOMZ) (Bianchi et al., 2022). We analyze daily output from a 10-year simulation initialized with the 10 km configuration (McCoy et al., 2023), following a one year adjustment period. Model setup and forcings, and a description of NitrOMZ, are summarized in Sections C.1 and C.2 of the Supporting Information, and described in detail in previous publications (McCoy et al., 2023; Bianchi et al., 2022).

4.2.2 N_2 and N_2O production

In the model, the net N_2O and N_2 production rates (J_{N_2O} and J_{N_2}, in units of mmol N m^{-3} s^{-1}), are given by:

$$J_{N_2O} = R^{n2o}_{ao} + R^{n2o}_{den2} - R^{n2}_{den3}, \tag{4.1}$$

$$J_{N_2} = R^{n2}_{den3} + R^{n2}_{ax}. \tag{4.2}$$

Here, R^{n2o}_{ao} is the rate of N_2O production from NH_4^+ oxidation (pathway 2b in Figure 4.1c, following equations (C.8) - (C.10)), R^{n2o}_{den2} and R^{n2}_{den3} are the denitrification steps of NO_2^- reduction and N_2O reduction, respectively (pathways 5 and 6, following equations (C.1) to (C.4)), and R^{n2}_{ax} is the anammox rate (pathway 7, equation (C.8)).

These rates follow the same formulation as in McCoy et al. (2023) (Section C.2 of the Supporting Information; Table S1), and include multiple nonlinear terms: (1) All reactions follow a Michaelis-Menten kinetics to represent uptake of oxidants and reductants (K. A. Johnson & Goody, 2011); (2) Anaerobic processes are inhibited exponentially in the presence of O_2 (Dalsgaard et al. (2014)); (3) The N_2O yield during NH_4^+ oxidation (R^{n2o}_{ao}) increases rapidly at low O_2 (Goreau et al., 1980; Ji et al., 2018).

4.2.3 Eddy-mean decomposition of tracer equations

The conservation equation for a biogeochemical tracer (C) can be written as:

$$\frac{\partial \mathrm{C}}{\partial t} = -\nabla(\mathbf{u}\mathrm{C}) + \frac{\partial}{\partial z}\left(\kappa \frac{\partial \mathrm{C}}{\partial z}\right) + J_{\mathrm{C}}. \tag{4.3}$$

Here, $\mathbf{u}$ and κ are the velocity vector (u,v,w) and the vertical eddy diffusivity, resulting in the advective transport and turbulent diffusion terms, and J_{C} encapsulates biogeochemical sources and sinks.

The eddy-mean decomposition requires filtering equation (4.3) to separate contributions from large scale, low frequency "mean" fields from higher frequency "eddy" fluctuations. For example, the decomposition of C follows:

$$\mathrm{C} = \overline{\mathrm{C}} + \mathrm{C}'. \tag{4.4}$$

Here, the filter consists of monthly climatological averages from 10 years of model output. Eddy fluctuations (C') therefore represent tracer heterogeneity at sub-monthly time scales, which is mostly driven by mesoscale variability (Le Traon, 1991; Morrow & Le Traon, 2012).

Following the approach of Lévy et al. (2013), substituting C for $\overline{\mathrm{C}} + \mathrm{C}'$ and $\mathbf{u}$ for $\overline{\mathbf{u}} + \mathbf{u}'$ in equation (4.3), and applying the monthly climatological filter leads to:

$$\frac{\partial \overline{\mathrm{C}}}{\partial t} = -\nabla(\overline{\mathrm{C}}\overline{\mathbf{u}}) - \nabla(\overline{\mathrm{C}'\mathbf{u}'}) + \frac{\partial}{\partial z}\left(\kappa \frac{\partial \overline{\mathrm{C}}}{\partial z}\right) + J_{\overline{\mathrm{C}}} + J'_{\mathrm{C}} \tag{4.5}$$

where:

$J_{\overline{\mathrm{C}}} = \sum R_{(\overline{\mathrm{x}_1},\ldots,\overline{\mathrm{x}_N})}$

$J'_{\mathrm{C}} = \sum [\overline{R} - R_{(\overline{\mathrm{x}_1},\ldots,\overline{\mathrm{x}_N})}]$.

The first three terms on the right hand side of equation (4.5) are the mean and eddy advective fluxes and the mean turbulent diffusion, and reveal a coupling between the mean tracer ($\overline{\mathrm{C}}$) balance and eddy-induced transport that is not explored further here. To compute mean reactions ($R_{(\overline{\mathrm{x}_1},\ldots,\overline{\mathrm{x}_N})}$), we calculate N monthly climatological fields ($\overline{\mathrm{x}_1}, \ldots, \overline{\mathrm{x}_N}$) and solve an offline version of the biogeochemical model equations (Section C.2 of Supporting Information). The resulting eddy reactions are then found using an analogous decomposition to equation (4.4), i.e., $R' = R - R_{(\overline{\mathrm{x}_1},\ldots,\overline{\mathrm{x}_N})}$.

4.2.4 Sign and amplitude of eddy reactions

To attribute eddy reactions to correlations between specific tracer pairs, we follow the approach of Lévy et al. (2013), and approximate monthly-averaged reaction rates ($\overline{R}$) with a Taylor series expansion:

$$\overline{R} \approx \underbrace{R_{(\overline{\mathrm{x}_1},\ldots,\overline{\mathrm{x}_N})}}_{\text{mean reaction}} + \underbrace{\sum_i \frac{\partial R_{(\overline{\mathrm{x}_1},\ldots,\overline{\mathrm{x}_N})}}{\partial \mathrm{x}_i}\overline{\mathrm{x}_i'}}_{\text{identically zero}} + \underbrace{\frac{1}{2}\sum_{i,j} \frac{\partial^2 R_{(\overline{\mathrm{x}_1},\ldots,\overline{\mathrm{x}_N})}}{\partial \mathrm{x}_i \partial \mathrm{x}_j}\overline{\mathrm{x}_i'\mathrm{x}_j'} + \mathcal{O}(\overline{\mathrm{x}_i'^3})}_{\text{eddy reaction}}. \tag{4.6}$$

For purely linear reactions, equation (4.6) would reduce to $R_{(\overline{\mathrm{x}_1},\ldots,\overline{\mathrm{x}_N})}$, and monthly-averaged rates would therefore depend on mean reactions only. For nonlinear reactions, since $\overline{\mathrm{x}_i'} = 0$, the linear terms also reduce to zero, and the monthly-averaged eddy reaction rates can be estimated with knowledge of eddy tracer variances and pairwise covariances ($\overline{\mathrm{x}_i'\mathrm{x}_j'}$), and the second derivatives of the model functional dependencies, evaluated using the mean state ($\partial^2 R_{(\overline{\mathrm{x}_1},\ldots,\overline{\mathrm{x}_N})}/\partial \mathrm{x}_i \partial \mathrm{x}_j$). Equation (4.6) allows to quantify the respective contribution of different tracer correlations to the total eddy reaction rate. Here we ignore third order and higher terms, assuming small fluctuations; this approximation is supported by our results (Section 4.3.3).

4.3 Results

4.3.1 Mean state and eddy variability

The model produces a realistic representation of the physical circulation and biogeochemistry of ETSP (see Figure 4.1a, d-g; a detailed validation is presented in McCoy et al. (2023)). Briefly, it simulates a wide-spread and persistent OMZ centered at roughly -8^{o}S that extends offshore to nearly 100^{o}W, with a ventilated wind-driven subtropical gyre to the southeast (Figure 4.1a). The monthly filter successfully separates mesoscale-driven eddy tracer heterogeneity from mean distributions set by the low frequency circulation, as the variability seen in daily-averaged snapshots is significantly smoothed in mean fields (see Figure C.1 for N tracers). This allows for eddy tracers (e.g., O_2' in Figure 4.1b) to capture the fluctuations driven by turbulent meandering fronts of $\mathcal{O}$ (10 km) near the equator, and larger mesoscale

eddies and filaments $\mathcal{O}$ (10 - 100 km) within the OMZ and along the fringe of the gyre.

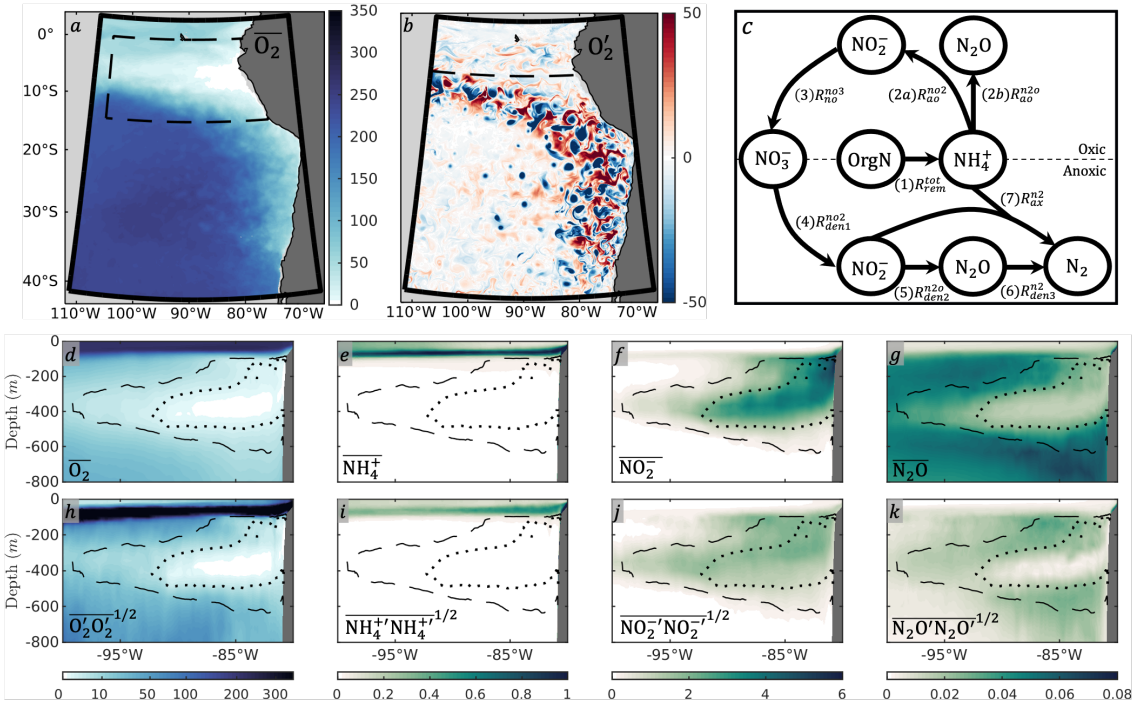

Figure 4.1: (a,b) Mean and eddy O_2 concentrations at 150 m from day 15 of model year 4. The dashed boxed region in panel (a) outlines the OMZ domain, while the dashed line in panel (b) shows the location of the OMZ transect. (c) Schematic of NitrOMZ (ignoring biological uptake): (1) remineralization of organic nitrogen (OrgN) to NH_4^+; (2a,2b) aerobic NH_4^+ oxidation to NO_2^- and N_2O, respectively; (3) NO_2^- oxidation to NO_3^-; (4) NO_3^- reduction to NO_2^-; (5) NO_2^- reduction to N_2O; (6) N_2O reduction to N_2; and (7) anaerobic NH_4^+ oxidation (anammox). (d - g) Transects of averaged monthly mean O_2, NH_4^+, NO_2^-, and N_2O from model years 2 - 11. (h - k) Square root of averaged eddy tracer variances over the same period. The dotted and dashed black curves outline the 1 and 5 mmol O_2 m^{-3} contours, respectively. Units are in mmol m^{-3}.

A persistent oxycline is observed at roughly 100 m depth, coinciding with a maximum in NH_4^+, that overlies an OMZ ranging in thickness from roughly 200 m offshore to nearly 400 m near the coast (Figure 4.1a, b). In the steep suboxic gradients surrounding the OMZ, high concentrations of N_2O accumulate (Figure 4.1g). As O_2 approaches anoxia, characteristic NO_2^- maxima and N_2O minima appear (Figure 4.1f, g). A vigorous mesoscale eddy field drives high heterogeneity in tracer distributions (Figure 4.1b, h-k). Because each tracer is characterized by distinctive mean gradients, eddy fluctuations lead to unique patterns of

tracer variance (Section 4.2.3).

4.3.2 N_2 and N_2O production

In the model, N_2O production (J_{N_2O}, Figure 4.2a) mostly reflects incomplete denitrification, i.e., a slight excess of NO_2^- reduction (R^{n2o}_{den2}) over N_2O reduction (R^{n2}_{den3}) in the suboxic gradients surrounding the OMZ (Figure 4.3b,c). This is consistent with previous studies (Babbin et al., 2015; Ji et al., 2018; Bianchi et al., 2022; McCoy et al., 2023). Despite the higher yield at low O_2 (equation (C.9)), N_2O production by NH_4^+ oxidation (R^{n2o}_{ao}, Figure 4.3a) is significantly smaller than net production by denitrification (McCoy et al., 2023), as suggested by observations (Ji et al., 2015, 2018; Frey et al., 2020), but dominates along the upper oxycline (Figure C.2a). As O_2 approaches anoxia, the denitrification steps become more tightly coupled, leading to net N_2O consumption (J_{N_2}, Figure 4.2b). Further N_2 production is achieved via anammox (R^{n2}_{ax}, Figure 4.3d), which contributes to about 40% of total N loss (Figure C.3a,b), within the range of observational estimates (Dalsgaard et al., 2012; Peng et al., 2016; Babbin et al., 2017).

The eddy-mean decomposition of reactions (Section 4.2.3) reveals that mean N_2O production (J_{N_2O}), which reflects the effect of large-scale tracer distributions, overestimates total N_2O production by an order of magnitude (Figure 4.2c), and is closely compensated by N_2O consumption at eddy scales. The overestimate by mean N_2O production emerges from the much larger difference between mean NO_2^- and N_2O reduction rates (R^{n2o}_{den2} and R^{n2}_{den3}, respectively, Figure 4.3f,g) in the suboxic gradients surrounding the OMZ. This occurs despite the positive sign of their respective eddy reactions (Figure 4.3j,k), which indicates that both NO_2^- and N_2O reduction are enhanced by eddy heterogeneity. Thus, while the mean field approximation underestimates the expression of individual denitrification rates due to the lack of eddies, it overestimates the magnitude of N_2O production from incomplete denitrification.

Integrated over the OMZ domain (outlined in Figure 4.1a), eddy NO_2^- reduction (R^{n2o}_{den2}, Figure 4.3n) consistently contributes roughly 50% to the total reaction (Figure 4.3b), while eddy N_2O reduction (R^{n2}_{den3}) shows a slightly larger contribution to the total ($\sim$60 - 65%,

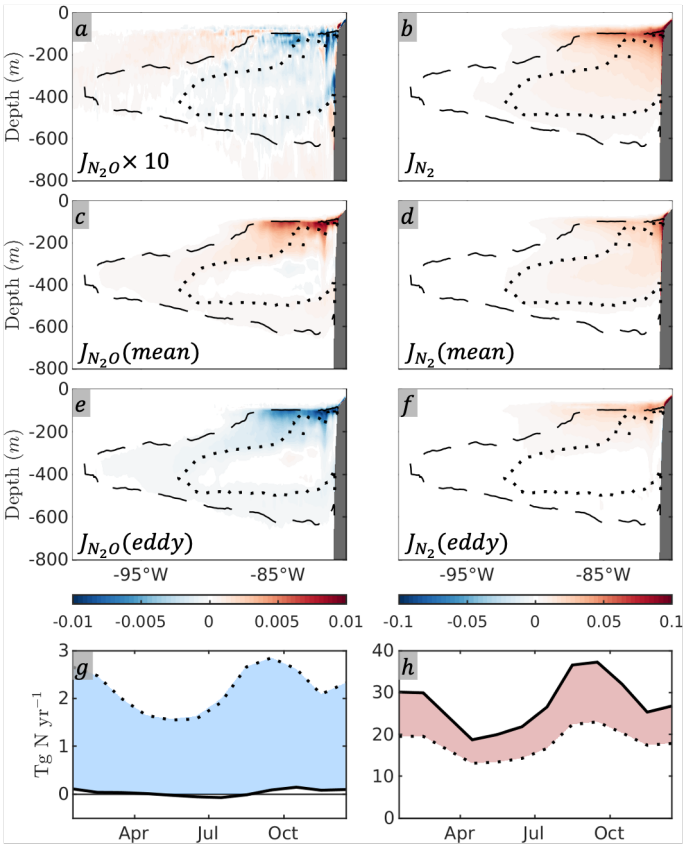

Figure 4.2: (a,c,e) Transects of total, mean, and eddy N_2O production (J_{N_2O}) from model years 2 - 11. (b,d,f) Same as in (a,c,e), but for for N_2 production (J_{N_2}). Units are in mmol N m^{-3} d^{-1}. (g,h) Time-series of monthly averaged integrated total (solid) and mean (dashed) N_2O and N_2 production rates from the OMZ domain (see dashed box in Figure 4.1a, extending to -1000 m), in units of Tg N yr^{-1}. Blue/red shading highlights when eddy reactions contribute negatively/positively to the total reaction rates, respectively.

Figure 4.3c, o). Eddy enhancement of NO_2^- reduction occurs mainly in the upper oxycline (Figure 4.3j), whereas eddy N_2O reduction is strong throughout the suboxic gradients surrounding the OMZ (Figure 4.3k). As a consequence, net eddy N_2O consumption (Figure 4.2e) compensates net mean production (Figure 4.2c) nearly perfectly. This results in a dramatic decrease (91 - 97%) of the net N_2O production compared to the mean field approximation, with net N_2O consumption between June and August (Figure 4.2g). A similar eddy-mean decomposition of N_2O production from NH_4^+ oxidation (R_{ao}^{n2o}, Figure 4.3e,i) reveals a negative and much weaker contribution by eddies.

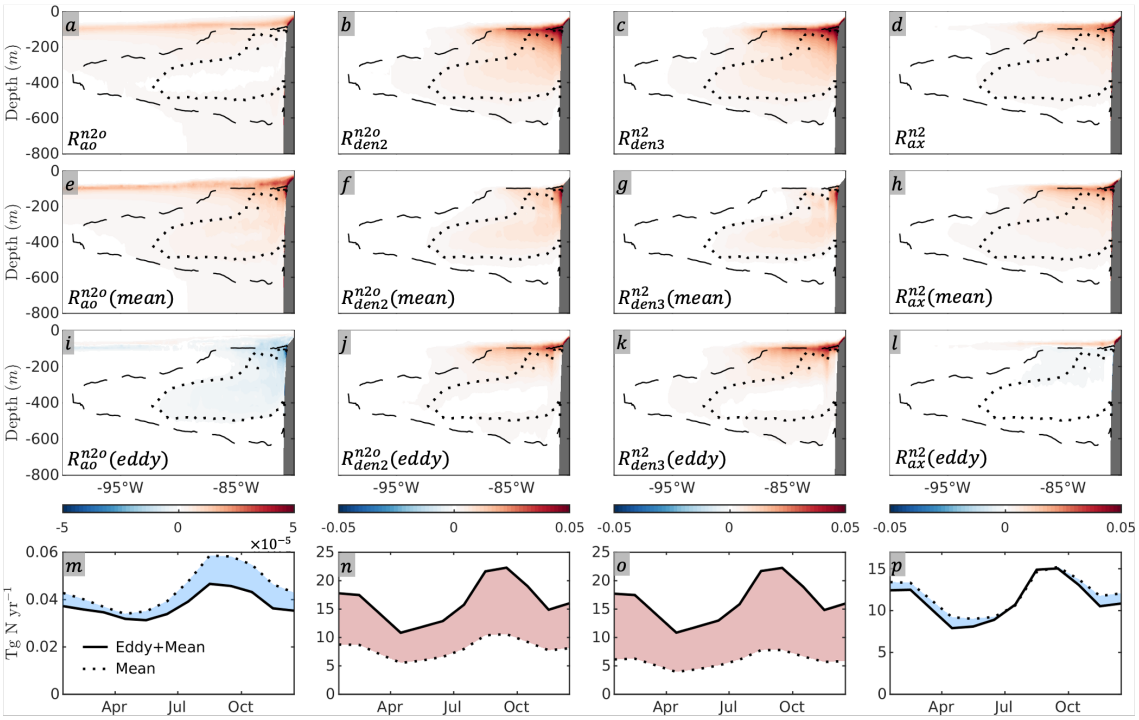

Figure 4.3: Same as in Figure 4.2, but for (a,e,i,m) N_2O production from NH_4^+ oxidation (R_{ao}^{n2o}), (b,f,j,n) NO_2^- reduction to N_2O (R_{den2}^{n2o}), (c,g,k,o) N_2O reduction to N_2 (R_{den3}^{n2}), and (d,h,l,p) anammox (R_{ax}^{n2}) from model years 2 - 11. Units in panels (a - l) are in mmol N m^{-3} d^{-1}.

Because N_2O reduction (R_{den3}^{n2}) is both a sink of N_2O and a source of N_2 (equations (4.1 - 4.2)), these results also highlight the role of environmental heterogeneity in regulating N_2 production (J_{N_2}). In contrast to denitrification, anammox (R_{ax}^{n2}, Figure 4.3h) is well captured by the mean tracer distribution (Figure 4.3d), with a weak positive contribution from eddies along the upper oxycline (Figure 4.3l), and a weak, negative contribution below it. Integrated over the OMZ domain, the eddy contribution is generally negative, peaking in April, and reduces the total reaction by ∼6% on an annual basis. Therefore, by comparison, anammox is less impacted by eddies than denitrification (Figure 4.1h - j). Regardless, because of eddy stimulation of N_2O reduction (R_{den3}^{n2}, Figure 4.3k,o), N_2 production is enhanced annually by ∼53% (Figure 4.2h).

4.3.3 Attributing eddy effects to oxygen variability

To attribute the enhancement of denitrification (R^{n2o}_{den2} and R^{n2}_{den3}) and suppression of nitrification (R^{n2o}_{ao}) and anammox (R^{n2}_{ax}) to specific aspects of eddy-driven heterogeneity, we apply the Taylor series approach outlined in Section 4.2.4. Analysis of individual tracer-pair contributions in Equation (4.6) reveals the dominant role of O_2 fluctuations in enhancing denitrification rates. This is caused by their rapid increase at vanishing O_2 concentrations, despite the relatively weak O_2 variance in the OMZ core (Figure 4.1h).The effect of O_2 fluctuations is strong enough that the magnitude and sign of the eddy N_2O and N_2 production rates (J_{N_2O} and J_{N_2}, respectively, Figure 4.2e, f) are nearly recovered using the contribution from the O_2 variance term alone (Figure 4.4a, b).

The role of O_2 fluctuations is explained schematically in Figure 4.4c. Because of the higher sensitivity to O_2 (Table S1), N_2O reduction (R^{n2}_{den3}, blue curve) increases faster than NO_2^- reduction (R^{n2o}_{den2}, red curve) as O_2 declines. Thus, in the presence of eddies, the amplification of N_2O reduction is greater than that for NO_2^- reduction, and the "window" for N_2O production by incomplete denitrification is reduced relative to a mean field approximation, in agreement with the results in Figure 4.2. Effectively, in the presence of eddies, the last two steps of denitrification become more tightly coupled across the OMZ, leading to a greater N_2O loss.

Figure 4.4c also explains the weaker impact of eddies, and specifically O_2 fluctuations, on anammox (R^{n2}_{ax}, green curve). Because anammox is less sensitive to O_2 than denitrification (Table S1), O_2 fluctuations only slightly enhance the total rate, in particular in the upper oxycline (Figure 4.3l), where the O_2 variance peaks (Figure 4.1h). Additional negative eddy contributions below the oxycline can be attributed to the saturating behavior of NH_4^+ and NO_2^- uptake encapsulated by the Michaelis-Menten dynamics, and more complex functional dependencies related to covariances with O_2' (Figure C.7).

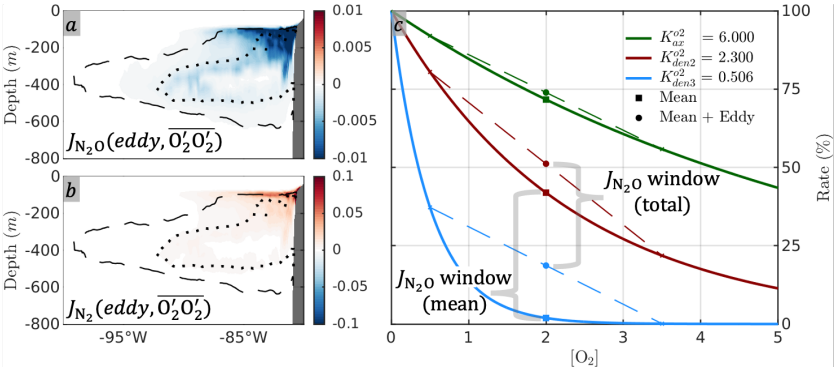

Figure 4.4: (a,b) Reconstructed eddy N_2O and N_2 production following the Taylor series expansion in equation (4.6) using only the contribution from O_2 variance (Figure 4.1h). (c) Schematic of the exponential inhibition by O_2 for anammox (R^{n2}_{ax}, green curve), NO_2^- reduction (R^{n2o}_{den2}, red curve), and N_2O reduction (R^{n2}_{den3}, blue curve); see equations (C.4) and (C.8). The mean field approximation, here assuming $\overline{O_2}$ of 2 mmol m^{-3}, is shown with square markers, while the total inhibition (circle markers) is estimated assuming O_2' of $\pm$ 1.5 mmol m^{-3}. J_{N_2O} windows (mean and total) are defined as the allowance of incomplete denitrification due to a difference in O_2-dependent rate inhibition between R^{n2o}_{den2} and R^{n2}_{den3}.

4.4 Discussion and Conclusions

Models continue to be our most robust tools for extrapolating hypotheses in biogeochemistry to global scales and enabling future projections. Nevertheless, the spatial resolution of most climate and global biogeochemical models prevents accurately resolving processes at the mesoscale and submesoscale. Yet the existing literature reveals a growing body of evidence highlighting the significant role played by mesoscale phenomena in influencing biogeochemistry (McGillicuddy et al., 2007; Mahadevan et al., 2012), and more recently has demonstrated the importance of considering unresolved eddy effects in coarse-grained simulations due to nonlinear biogeochemical reactions (Wallhead et al., 2013; Lévy et al., 2013). Here, we emphasize a similar phenomenon for the reactions controlling N_2 and N_2O production, and therefore N loss, and show their potential to affect the mean state of the ETSP. Together with our results, these studies suggest that large scale physical transports can also depend on eddy-scale reaction dynamics that are not captured by mean field approximations. Using

an eddy-resolving model, we show that eddy fluctuations perturb biogeochemical gradients set by the large scale circulation in the ETSP. The resulting environmental heterogeneity slightly suppresses aerobic and anaerobic NH_4^+ oxidation rates (R_{ao}^{n2o} and R_{ax}^{n2}), but greatly stimulates denitrification rates (R_{den2}^{n2o} and R_{den3}^{n2}), such that denitrification rates occurring at eddy scales are of comparable magnitude to the rates dictated by mean tracer fields, and, in the case of N_2O reduction, even greater (Figure 4.3j,k).

Eddy-driven O_2 variability within the OMZ is the primary driver of these results. Using a Taylor series expansion, we show that anaerobic reactions are enhanced by O_2 fluctuations due to their rapid increase at low O_2. Furthermore, the discrepancy in the magnitude of eddy reactions between denitrification steps is governed by their progressively stronger inhibitions at increasing O_2, while the weaker simulation of anammox by eddies reflects its greater tolerance to O_2 (Dalsgaard et al., 2014). Additionally, anammox is typically NH_4^+ limited in OMZ waters (Dalsgaard et al., 2003; Lam & Kuypers, 2011; Karthäuser et al., 2021), whereas denitrification is typically limited by the availability of organic substrates (Lam & Kuypers, 2011), thus implying denitrification is comparatively more sensitive to O_2 fluctuations. While these results rely on the nitrogen cycle formulations and parameterizations employed herein (Bianchi et al., 2022), they are grounded in the observed progressive sensitivities to O_2 (Dalsgaard et al., 2014). Thus, even though their true sensitivities (and, as a consequence, the magnitude of their associated eddy reactions) remain somewhat uncertain, here we are able to robustly demonstrate a discrepancy in enhancements between denitrification steps. As a consequence, eddy-driven O_2 heterogeneity can be expected to increase N_2 production in OMZs at the expense of reduced N_2O production.

There are other remaining questions regarding the magnitude and significance of eddy reactions in OMZ cycling. As revealed by Lévy et al. (2013), the choice of horizontal resolution likely controls both the magnitude and expression of eddy reactions induced by the mesoscale, in part due to the fact that eddy activity increases at higher resolution (Marchesiello et al., 2003). Our choice of resolution (5 km) well captures mesoscale eddies, and therefore the bulk of eddy kinetic energy in the ETSP (Chelton et al., 2011), but unresolved submesoscale processes may be locally important. For example, intense vertical velocities induced by sub-

mesoscale cross-frontal circulations may supply O_2 to the subsurface (McWilliams, 2016; Lévy et al., 2022), potentially influencing OMZ biogeochemistry near the coast where the oxycline shoals closer to the mixed layer. Higher resolution simulations capable of resolving sub-daily tracer correlations are needed to understand the significance of targeting eddy reactions at these scales. Additionally, since nonlinear terms in the momentum equation are included in our high resolution model, the mean field approximation retains some O_2 in the OMZ due to eddy-advective transport (Czeschel et al., 2011; Gnanadesikan et al., 2013; Bettencourt et al., 2015). This differs from other studies exploring the impact of mesoscale variability on biogeochemistry (e.g., Gruber et al. (2011)), which purposely exclude their influences. Thus, the underestimate of denitrification rates via mean reactions (Figure 4.3f,g) in part arises due to non-zero $\overline{O_2}$ in the OMZ, which slightly complicates our quantification of reactions driven by the low frequency circulation.

Due to computational constraints, a primary goal of ocean modelling is to upscale biogeochemistry and physics at unresolved scales in terms of larger scales to facilitate coarser simulations. Physical parameterizations of eddy transport are widely applied to partially address this challenge (Gent & Mcwilliams, 1990; Fox-Kemper et al., 2008). However, our results robustly suggest a mean field approximation employing an identical parameterization scheme will still greatly overestimate/underestimate N_2O/N_2 production (respectively) from OMZs by neglecting subgrid-scale tracer covariances driven by mesoscale eddies (e.g., Figure 4.1h - k), primarily by misrepresenting the true coupling between denitrification steps in steep O_2 gradients. While biases between coarsened biogeochemical fields and observations are typically addressed through retuning of biogeochemical parameters or via reformatting functional dependencies, the analysis of Wallhead et al. (2013) indicates they may not always be robustly corrected by this approach. Additionally, coarse models tuned to modern ocean observations may fail in predicting the responses to perturbations in a changing ocean, such as the expected expansion of OMZs (Stramma et al., 2008; Schmidtko et al., 2017) or alterations in the partitioning between anoxic and suboxic volumes (Cabré et al., 2015; Bianchi et al., 2018; J. J. Busecke et al., 2019). This effect may be particularly pronounced in OMZ regions, which continue to be poorly resolved in current global Earth system models (Cabré

et al., 2015; J. J. M. Busecke et al., 2022; Séférian et al., 2020).

Despite these challenges, a number of methods to upscale biogeochemistry show promise. In particular, Wallhead et al. (2013) demonstrate that, with knowledge of the functional forms used to represent biogeochemical transformations in ocean models, higher resolution simulations can be used to gather statistical information such as tracer variances and pairwise covariances driven by eddies (e.g., Figure 4.1h - k). This information can in turn can be used to reconstruct eddy reactions via a Taylor series approximation (e.g., Figures 4.4a,b and S8e - h) and "correct" coarse simulations. Our work can assist in guiding efforts to develop scale-dependent eddy reaction parameterizations. Their inclusion will thus ultimately improve the representation of OMZ biogeochemistry in coarse models, for instance by allowing for the presence of aerobic reactions such as NO_2^- oxidation in the core of the OMZ (Buchanan et al., 2023), and expand the influence of anaerobic reactions outside of it such as presented here.

CHAPTER 5

Conclusions

The research presented in this thesis is aimed at improving our understanding of the biogeochemical and physical factors that govern fixed N loss and N_2O outgassing in OMZs. To accomplish this goal, we used observations (Chapter 2) and ocean biogeochemical models (Chapters 3 and 4) to answer the overarching science questions presented in Chapter 1. I summarize these results below.

5.1 Summary of Chapter 2

Chapter 2 described the development of a general method for detecting subsurface anticyclonic eddies (SCVs) from 1D hydrographic profile measurements, which was based on similar approaches from G. C. Johnson & McTaggart (2010) and Z. Zhang et al. (2015). Our methodology exploited shared characteristics among previously identified SCVs from observations and modelling studies. A defining attribute is the doming and bowling of isopycnal surfaces around a weakly-stratified, gradient-wind balanced water mass (McWilliams, 1985; Gordon et al., 2002; Nauw et al., 2006). Additionally, their efficiency in transporting origin waters over vast distances (in part due to their highly nonlinear nature and long lifetimes) suggested that, after propagation from source regions, the core water mass properties of SCVs should strongly contrast with surrounding waters (J. Simpson et al., 1984; McWilliams, 1985; G. C. Johnson & McTaggart, 2010; Collins et al., 2013; Z. Zhang et al., 2015; Schütte et al., 2016). We designed specific detection criteria corresponding to these conditions (Section 2.2), which were based on derived properties extracted from temperature, salinity, and depth measurements, and applied these protocols to the high spatial and temporal resolution

sampling scheme provided by the global Argo float array.

We detected nearly 4000 additional global observations of these subsurface eddies, which included 1716 "spicy" (e.g., characterized by anomalously hot and salty core water masses) and 1258 "minty" (cold, fresh) SCVs throughout the 20+ year Argo record (Figure 2.4). We found subsurface anticyclonic eddies populate vast swaths of the global ocean, with spicy-core SCVs generally outnumbering minty-core detections through the subtropics and mid-latitudes, and vice-versa for high-latitude regions (Figure 2.10). Based on the statistics and water mass characteristics of our detections, we inferred the source waters of regional SCV populations, highlighting several hot-spots of formation that tend to generate long-lived SCVs (Figures 2.4, 2.5, and 2.6). We also provided a first-order estimate of the number of SCVs in the ocean and their potential contributions to regional heat and salt budgets (Figure 2.16). These findings implied a role for SCVs in modulating water properties in the subtropical gyres and mid-latitude subduction regions, which in turn may alter interior water mass characteristics.

Among our global detections, we recovered previously described populations formed from dense water overflows originating from marginal seas (Figure 2.13), such as the Mediterranean (Richardson et al., 2000), the Persian Gulf (Morvan et al., 2019), and the Gulf of Oman (L'Hégaret et al., 2016). Our detections provided further evidence that SCV generation is common at these major outflows (Figure 2.10), and that their propagation plays a non-negligible role in spreading intermediate and deep water masses in the vicinity of these regions (Stewart, 1982; McWilliams, 1985; Bower et al., 1997; Vic et al., 2015). This result was informed through a simple model, based on distributions and scaling arguments (Section 2.5), that revealed the positive heat and salt anomalies induced by SCVs reaches a maximum in these regions (Figure 2.16). Furthermore, statistics of long-lived detections (Figure 2.4) supported previous theory that SCVs generated at eastern boundaries (e.g., the Mediterranean Sea outflow) are more capable of transporting origin waters due to relatively quiescent environments (Bower & Furey, 2012; L'Hégaret et al., 2016). In contrast, SCVs generated near western boundaries (e.g., the Arabian Sea outflow) are more ephemeral due to enhanced horizontal shear induced by mesoscale activity, and a propensity for westward

self-propagation, leading to rapid destruction (Vic et al., 2015; Morvan et al., 2019).

We also found coherent populations of SCVs within regions of mode water formation (Figure 2.14). These included subtropical mode water subduction zones in the vicinity of the Kuroshio, Gulf Stream, East Australian, Brazil, and Aghulhas Current extensions, and equatorward of the ACC (Figure 2.15), where Subantarctic Mode Water is known to form (Talley et al., 2011). The thick, homogeneous cores of our detected SCVs in these regions were in agreement with previous studies (Oka, 2009; Z. Zhang et al., 2015; Xu et al., 2016; Schütte et al., 2016; Li et al., 2017; Barcelo-Llull et al., 2017; Shi et al., 2018), which suggested that SCVs are generated due to meander-driven subduction of low potential vorticity mode water originating from deep winter mixed layers into more stratified adjacent interior waters. This leads to vortex compression that ultimately stimulates anticyclonic motions (Spall, 1995; L. N. Thomas, 2008). Since mode waters relate to thermocline outcropping at upper ocean fronts (Spall, 1995; Gordon et al., 2002; L. N. Thomas, 2008), we further speculated that mode water SCVs may impact remote O_2 and biogeochemical nutrient budgets via periodic injection of ventilated, nutrient-poor waters.

Finally, and most relevant to the nitrogen cycling work presented in Chapters 3 and 4, we highlighted EBUS as significant sources of long-lived and far-reaching SCVs, mirroring results from previous observational (G. C. Johnson & McTaggart, 2010; Pelland et al., 2013) and modelling studies (Molemaker et al., 2015; Frenger et al., 2018). Water mass signatures allowed us to infer their formation within poleward-flowing undercurrents, which characterize EBUS. Shedding of SCVs from EBUS may potentially weaken undercurrent signatures as they flow poleward, as suggested by Pelland et al. (2013). As a consequence, these SCVs may provide a significant source of low-O_2 and high nutrient undercurrent water masses to the adjacent subtropical gyres Frenger et al. (2018). The isolation of these SCV core properties establishes a distinct biogeochemical environment and subsequent biological community compared with the surrounding waters (Löscher et al., 2015; Frenger et al., 2018). As previous studies have shown these SCVs to be hot-spots of fixed N losses and N_2O production (Altabet et al., 2012; Löscher et al., 2015; Arévalo-Martínez et al., 2016; Grundle et al., 2017), we aim to examine their influence to regional biogeochemical budgets in future

projects.

5.2 Summary of Chapter 3

Chapter 3 described the development of a climatological, eddy-resolving simulation of the Eastern Tropical South Pacific that is capable of reproducing the spatial distributions and temporal evolution of observed nitrogen tracers and transformation rates. We demonstrated skill in capturing characteristic large scale biogeochemical tracer gradients (Figures B.9 - B.16). For N cycle tracers, we replicated the observed depletion of NO_3^- and N_2O, and the increase in NO_2^- within the core of the OMZ (Figure 3.4), which emerged due to a strong coupling between denitrification steps at low O_2. The total fixed N loss of 23.3 $Tg\text{N } yr^{-1}$ in the model (Figure 3.5) also matched other estimates from the ETSP (Deutsch et al., 2001; Bianchi et al., 2012; DeVries et al., 2013; Yang et al., 2017), including the partitioning between denitrification and anammox (roughly 58%/42% in this study) as suggested by recent studies (Peng et al., 2016). Thus, the presented model validation suggested our quasi-steady state simulation provides a realistic representation of both the geometry (Figure 3.3) and biogeochemistry of the OMZ in this dynamic region.

A primary objective of this modelling work was to elucidate the respective roles of nitrification and "incomplete" denitrification in local N_2O production and outgassing in the ETSP. To accomplish this, we performed a decomposition of the N_2O tracer in the model to quantify the contributions from these pathways (Section 3.2.4). The presented budget of N_2O (Figure 3.9) found nitrification represents only $\sim$11% of the total biogeochemical N_2O sources on an annual basis, in agreement with recent observations and modeling work Ji et al. (2015); Babbin et al. (2015); Ji et al. (2018); Bianchi et al. (2022). Production from this pathway takes place immediately adjacent to the coast and in the upper ocean (Figure 3.6c) and thus should lead to a more efficient outgassing route. However, we were able to attribute only $\sim$7% of N_2O outgassed to the atmosphere from nitrification in the ETSP (Figure 3.9).

We found the magnitude of step-wise denitrification is primarily controlled by organic matter supply from the euphotic zone (Figure B.7), which varied seasonally. Large net N_2O

consumption rates in the OMZ (Figure 3.6b) agreed with recent measurements (Kock et al., 2016; Casciotti et al., 2018; Kelly et al., 2021) and modeling studies (Bourbonnais et al., 2017), and indicated a short residence time for N_2O produced from NO_2^- reduction. However, a slight decoupling between denitrification steps in the steep O_2 gradients surrounding the anoxic OMZ core ultimately led to significant N_2O accumulation in the domain from incomplete denitrification (Figure 3.6b,f and Figure 3.7a,c). This generated the characteristic double peak structure in N_2O profiles (Figure 3.6e).

Therefore, we found agreement with recent studies (Babbin et al., 2015; Bourbonnais et al., 2017; Ji et al., 2018) in suggesting incomplete denitrification is the most dominant N_2O production pathway in OMZs. However, as observations are often restricted to 1D profile measurements, the simulation afforded us the opportunity to explore this production in a realistic 3D representation of the ETSP OMZ. We found the relative thickness of anoxic and suboxic waters played a key role in determining regions of net N_2O production or consumption via denitrification (Figure 3.6), suggesting OMZ geometry is a major control regulating N_2O outgassing in this region. Near the coast, where high organic matter flux intercepts relatively thin suboxic layers, N_2O consumption was particularly strong (Figures 3.6 and 3.7). In contrast, suboxic layers become thicker offshore, resulting in conditions more favorable to N_2O production.

Our results provided new insights into the role of the large scale physical circulation in redistributing N_2O within the ETSP. As production from denitrification predominantly takes place offshore, this necessitates a role for advective processes (Figure B.5) to generate the large coastal outgassing signal (Figure 3.8). However, a significant fraction ($\sim$68%) of denitrification-derived N_2O was ultimately exported out of our model domain, predominantly along the western boundary near the tropics (Figure B.6b). We speculated that this export may be related to the results of Deutsch et al. (2001) and Carrasco et al. (2017), who together demonstrated that N^* signals (a proxy used to indicate if a water mass has experienced denitrification) propagate far into the western Pacific along the equator. Our results similarly proposed that the biogeochemical influence of OMZs reaches well beyond their immediate vicinity.

Likewise, we attributed the majority of outgassing (∼57%) to a consistent supply of outgassing-favorable N_2O originating from predominantly zonal subsurface currents in the tropical band (Figures 3.6h and B.6d), consistent with the results from Yang et al. (2020). While our regional simulation did not allow us to explicitly attribute this imported N_2O to a source from nitrification or denitrification, it is possible that a significant portion of N_2O outgassed to the atmosphere originates from eastward equatorial currents that act to recirculate N_2O produced by denitrification back into the ETSP. Isotopic measurements along the equator are necessary to gain further insight into this emerging hypothesis.

5.3 Summary of Chapter 4

In Chapter 4, we applied a higher resolution configuration of the ETSP OMZ model (see Chapter 3) to examine how mesoscale-driven environmental heterogeneity augments nitrogen cycle reactions relevant to N_2 and N_2O production in the ETSP. As demonstrated by previous studies (Lévy et al., 2013; Wallhead et al., 2013; Martin et al., 2015), biogeochemical rates estimated from large scale tracer distributions (e.g., "mean field approximations") can fail in representing their true magnitude in a fluctuating environment. This phenomenon arises from the nonlinear nature of biogeochemical interactions (Rovinsky et al., 1997; Brentnall, 2003; Lévy et al., 2013; Martin et al., 2015), which are ubiquitous in the N cycle (e.g., hyperbolic oxidant/reductant uptake kinetics (K. A. Johnson & Goody, 2011), and exponential O_2 inhibition for anaerobic processes (Dalsgaard et al., 2014)).

Our approach to extracting the mesoscale contribution to biogeochemical reactions was based on an eddy-mean decomposition of the continuity equation (Lévy et al., 2013), which describes the evolution of biogeochemical tracers in 3D ocean models. The decomposition required the use of a filter (time, space, or both) to separate larger and lower frequency "mean" scales from smaller, higher frequency "eddy" scales. We chose to filter the 10-year simulation into monthly averages to define our mean circulation, since the wind-driven upwelling signal is considered part of the mean seasonal and regional variability in the ETSP, and since mesoscale eddies and filaments are generally described by time scales of roughly

1 month (Le Traon, 1991; Morrow & Le Traon, 2012). The monthly mean fields were then extracted and used to compute offline "mean" N cycle reactions, analogous to a mean field approximation of reactions such as employed in coarse-grained models Lévy et al. (2013).

We demonstrated that the low frequency circulation maintains the biogeochemical tracer fields and gradients that characterize the ETSP (Figure 4.1d - g), including a persistent, anoxic OMZ volume. Since each heterotrophic denitrification step was released from O_2 inhibition in this layer, a tight coupling led the OMZ to be an important region for local N_2 production (e.g., fixed N loss) from "complete" denitrification. Additionally, the NH_4^+ released from organic matter remineralization (in part via denitrification) was further oxidized with NO_2^- (anammox) in the OMZ, promoting further N_2 accumulation (Figure 4.3d). The circulation also allowed for persistent suboxic gradients to surround the OMZ, where a greater sensitivity to O_2 caused N_2O reduction to be preferentially inhibited, stimulating N_2O accumulation via incomplete denitrification (Figure 4.3c). As in Chapter 3, NH_4^+ oxidation was not a significant N_2O production term, but was locally important in the upper ocean (Figure 4.3a). After integrating these "mean" rates over the OMZ, we attributed approximately 20 N_2 Tg yr^{-1} (Figure 4.3h), and 2 Tg N_2O yr^{-1} (Figure 4.3g), to the influence of the large scale, low frequency circulation in the ETSP.

However, we further demonstrated that small scale features like eddies and filaments stir the large scale gradients, ultimately introducing significant heterogeneity in the system (Figure 4.1b,h - k). This environmental variability drastically augmented N_2 and N_2O production in this region, but by predominantly influencing denitrification rates. We showed NO_2^- reduction (e.g., N_2O production) was enhanced by approximately 50%, while N_2O reduction (e.g., N_2O consumption to N_2) experienced a slightly greater stimulation of approximately 60% (Figure 4.3n,o). This greatly changed the N_2O balance; whereas the large scale circulation was seen to promote incomplete denitrification in suboxic waters, fluctuations induced by eddies led the steps to become more tightly coupled. The result was an enhancement of N_2 production by approximately 50%, but largely at the expense of total N_2O production, which was reduced by approximately 95% (Figure 4.3g,h).

Since the formulation of denitrification rates in our model revealed multiple sources of

nonlinearities, we followed the approach of Lévy et al. (2013) in employing a Taylor series expansion (equation (4.6)) to analyze the eddy tracer correlations underlying these augmentations. Through this exercise, we were able to attribute O_2 variance as the dominant driver of these signals (Figures 4.4a,b, C.5, and C.6). This emerged due to the convexity (e.g., positive curvature) of their respective exponential O_2 inhibition functions at low O_2. As demonstrated in Figure 4.4c), high frequency O_2 fluctuations driven by eddies will magnify anaerobic processes after averaging over oscillating periods. Consequently, a greater sensitivity of N_2O reduction to O_2 (and thus, a locally greater convexity) thus caused a greater amplification than observed for NO_2^- reduction.

We further noted that anammox was overall less influenced by the mesoscale circulation (Figure 4.3l,p), and was slightly diminished (approximately -10%) by heterogeneity, despite a similar, albeit weaker, inhibition to O_2 as in denitrification (Figure 4.4c). We posited that NH_4^+ limitation, as suggested by previous studies (Dalsgaard et al., 2003; Karthäuser et al., 2021), exerted a stronger control on the magnitude of this reaction. In contrast, step-wise denitrification was released from N limitation due to higher OMZ substrate concentrations, and thus was more reactive to O_2 fluctuations. Since uptake of NH_4^+ is governed by Michaelis-Menten uptake kinetics, which is characterized by a concave (e.g., negative curvature) hyperbolic formulation, we demonstrated that variability acted to reduce the reaction set by the large scale circulation, as further demonstrated via the Taylor expansion in Figure C.7.

These results therefore revealed several key findings. Large scale O_2 gradients suggest the region should be a major source of N_2O due to the O_2-dependent decoupling of denitrification rates at low, but non-zero O_2. However, eddies induce significant variability in the system, leading to local amplification of anaerobic rates. However, the variable responses between denitrification steps ultimately allowed these reactions to become more tightly coupled. This suggested that coarse-grained models may (1) underestimate the true magnitude of N_2 production from denitrification, and (2) may greatly overestimate N_2O production from incomplete denitrification within OMZs.

5.4 Ongoing and future work

The modelling work presented herein reflects a progression for current biogeochemical ocean models. Our expanded N cycle assumes a "modular" N cycle, such that the exchanges of dissolved substrates are connected by individual reaction steps (Bianchi et al., 2022). However, the underlying model may need to be re-evaluated as new aspects of the N cycle are uncovered.

For example, recent tracer incubation studies suggest that some heterotrophic organisms carry the ability to reduce NO_3^- directly to N_2O in OMZs, with NO_2^- reduction proceeding entirely within the cell (Ji et al., 2018; Casciotti et al., 2018; Frey et al., 2020). This idea, which contrasts with our "modular" N cycle, may need to be included in future versions of the model, as isotopic evidence indicates this may be a dominant source of N_2O in the ETSP (Casciotti et al., 2018). The measurements from Ji et al. (2018) suggests the N_2O production ratio between NO_3^- reduction and NO_2^- reduction is linked to the ratio between NO_3^- and NO_2^- in OMZs. In order to facilitate the inclusion of N_2O production from NO_3^- in the future, this relationship should be explored further in observational studies and incubation experiments. Uncovering the sensitivity of this process to other environmental factors, such as O_2, is also a priority. We also note that our specific values of the O_2 sensitivities for anaerobic processes (e.g., step-wise denitrification and anammox) are far from well-established, with some experiments showing smaller thresholds (Dalsgaard et al., 2014), and others finding similar or larger thresholds (Ji et al., 2018).

New evidence also suggests that NH_4^+-oxidizing archaea (AOA, which greatly outnumber their bacterial counterparts) can also produce N_2O via a hybrid mechanism (Santoro et al., 2011; Löscher et al., 2012), with a similar enhancement at low O_2 (Trimmer et al., 2016; Santoro et al., 2021). Currently, we only model N_2O production from NH_4^+ using a single O_2-dependent function (Nevison et al., 2003), which is based on the transition in bacterial metabolisms from predominantly hydroxylamine oxidation to nitrifier-denitrification at low O_2 Hooper & Terry (1979); Wrage et al. (2001); Stein & Yung (2003). While our results in Chapters 3 and 4 suggests that nitrification is not a major N_2O source in OMZs, it is

the dominant pathway in the oxygenated ocean (Walter et al., 2006), and should be better constrained to provide a more realistic representation of N_2O production in basin-wide or global models.

Our model also assumes a "system view" by focusing on the biogeochemistry of N transformation reactions (Lam & Kuypers, 2011). However, considering each N cycle reaction is mediated by specialized microorganisms, new analyses are emerging which consider a broader array of traits of the major microbes inhabiting OMZs (Kalvelage et al., 2013; J. Penn et al., 2016; Louca et al., 2016; Zakem et al., 2018; J. L. Penn et al., 2019; Zakem et al., 2020; Sun et al., 2021). These include observations of cell size, carbon quota, stoichiometry, maximum growth rate, biomass yields, and nutrient affinities. Studies have pointed out the value of explicitly resolving the biomass of microbial populations performing these transformations, enabling direct comparisons with molecular observations (Louca et al., 2016). While explicitly simulating microbial biomass requires a number of additional parameters that remain poorly constrained, including their metabolisms in biogeochemical models may reveal more complex feedbacks, such as the competition between microbes for substrates like NO_2^- (e.g., nitrifiers, denitrifiers, and anammox bacteria) (J. L. Penn et al., 2019).

However, despite these current limitations, our model provides a valuable framework to continue exploring theories about the N cycle in both idealized and realistic settings. For example, the lack of interannual forcing in our simulations leaves gaps in understanding ENSO impacts. Since research suggests OMZ geometry and denitrification rates are sensitive to ENSO variability (Yang et al., 2017), N_2O production and outgassing are likely to exhibit significant year-to-year changes. Interannually forced, high-resolution simulations are needed to resolve these questions. Additionally, observations suggest that deoxygenation over the past 50 years has led to expansion of OMZ volumes and shoaling of the upper oxycline (Stramma et al., 2008; Schmidtko et al., 2017). If climate change results in an expansion of anoxic waters (Bianchi et al., 2018; J. J. Busecke et al., 2019), more N_2O would be consumed in the OMZ, leading to negative climate feedback. Conversely, a preferential increase in suboxic waters would increase production from both incomplete denitrification and nitrification, leading to a positive climate feedback (Cabré et al., 2015; Battaglia & Joos,

2018; J. J. Busecke et al., 2019; Kwiatkowski et al., 2020). Employing our expanded N cycle model in future climate simulations could help constrain these emerging questions regarding the partitioning between N_2 and N_2O production in future OMZs.

APPENDIX A

Supporting Information for Chapter 2

A.1 Estimate of SCV spatial density

The following details the rationale for the methods in section 2.5. Given a certain number N_a of Argo profiles in a geographic region (here, 4° by 4° latitude/longitude cells), we can assume a probability p of detecting a SCV with each Argo cast, such that the total number of SCV detections N_d is given by

$$N_\mathrm{d} = p \cdot N_\mathrm{a} \,. \tag{A.1}$$

If we assume that both SCV and Argo profile locations are randomly distributed and uncorrelated within each regional cell, the probability of detection is proportional to the total surface area occupied by SCVs, A_scv, divided by the surface area of the region, A_r:

$$p = \frac{A_\mathrm{scv}}{A_\mathrm{r}} \,. \tag{A.2}$$

If N_scv is the number of detectable SCVs in the region, and assuming that SCVs become detectable at a distance r_d from their center (the 'detectability radius'), the total detectable area occupied by eddies (A_scv) is written as

$$A_\mathrm{scv} = N_\mathrm{scv} \cdot \pi \cdot \overline{r_\mathrm{d}^2} \,, \tag{A.3}$$

where $\overline{r_\mathrm{d}^2}$ denotes the average from all detected SCVs in the region. Combining (A.3) with (A.1) and solving for N_scv gives

$$N_\mathrm{scv} = \frac{N_\mathrm{d}}{N_\mathrm{a}} \cdot \frac{A_\mathrm{r}}{\pi \, \overline{r_\mathrm{d}^2}} \,. \tag{A.4}$$

Using (A.3) and (A.4), we can also define the SCV number density (i.e. the average number of SCVs per unit area) as

$$n_\mathrm{scv} = \frac{N_\mathrm{scv}}{A_\mathrm{r}} = \frac{N_\mathrm{d}}{N_\mathrm{a}} \cdot \frac{1}{\pi \, \overline{r_\mathrm{d}^2}} \,. \tag{A.5}$$

Note that r_d needs to be related to quantities estimated from SCV detections. For simplicity, we can assume that, on average, SCVs are detected at a distance from the center that is proportional to the SCV radial (or length) scale L, and write

$$r_\mathrm{d} = \alpha \cdot L \,, \tag{A.6}$$

where α is a constant of $O(1)$, and L is first baroclinic deformation radius estimated in section 2.2.6. Thus, the SCV spatial density will be given by

$$n_\mathrm{scv} = \frac{N_\mathrm{d}}{N_\mathrm{a}} \cdot \frac{1}{\pi \alpha^2 \overline{L^2}} \,, \tag{A.7}$$

where $\overline{L^2}$ is the average square radius of SCVs detected in the region. Note that the scaling factor α used here is assumed constant for all SCVs. In general, we expect SCV anomalous properties to scale horizontally as Ae^{-x^2/L^2}, where A is the maximum anomaly and x is the distance from the SCV core. Since we assume we can detect SCVs at distances where anomaly values are less than $\frac{A}{e}$, we expect α to be greater than one, but of $O(1)$; a more accurate value for α can be estimated from observations or model simulations of SCVs, which is beyond the scope of this analysis. For illustrative purposes, we set it to 1 and therefore we are likely overestimating n_scv. Thus, (A.7) should be considered an order-of-magnitude, upper bound estimate for use in facilitating comparisons of SCV spatial density between different regions.

A.2 Estimate of SCV hydrographic impacts

To estimate the anomalous heat and salt content caused by the presence of SCVs in a given region, we assume that SCVs carry anomalies of any given property P (e.g. temperature or salinity) with the following three-dimensional structure (McWilliams, 1985; Pelland et al., 2013):

$$P' = P'_\mathrm{o} \cdot e^{-\frac{z^2}{h^2} - \frac{r^2}{L^2}} \,, \tag{A.8}$$

where P'_o is the anomaly in the property P at the center of the SCV, and h and L are the scale height and the first baroclinic deformation radius, respectively, defined in sections 2.2.3

and 2.2.6. The coordinates z and r are a vertical and radial coordinate, respectively, with an origin at the center of the SCV. The total property anomaly integrated over the entire SCV ($\Delta P'$) is thus given by

$$\Delta P' = \int_{-\infty}^{\infty} \int_{-\infty}^{\infty} P' \cdot 2\,\pi\,r\, \cdot dr\,dz\,, \tag{A.9}$$

which can be solved, for each detected SCV, to give:

$$\Delta P' = \pi^{\frac{3}{2}}\, P'_{\mathrm{o}}\, h\, L^2\,. \tag{A.10}$$

Assuming that the number of SCVs that are present in a region with surface area A_{r} is given by (A.4), the property anomaly per unit area ($\delta P'$) caused by SCVs can be written as:

$$\delta P' = \frac{N_{\mathrm{scv}}\,\overline{\Delta P'}}{A_{\mathrm{r}}} = \frac{N_{\mathrm{d}}}{N_{\mathrm{a}}} \cdot \frac{\pi^{\frac{1}{2}}\overline{P'_{\mathrm{o}}\,h\,L^2}}{\alpha^2\overline{L^2}}\,, \tag{A.11}$$

where the overbar represents averages over all detected SCVs in the region. To relate P'_{o} to measured quantities from detected SCVs, for simplicity we assume that the anomaly at the center of the eddy, P'_{o}, is proportional to the detected anomaly P'_{d}, such that:

$$P'_{\mathrm{o}} = \beta\, \cdot P'_{\mathrm{d}}\,, \tag{A.12}$$

where β is a scaling factor greater than one, but likely of $O(1)$, similar to α. Thus we can restate (A.11) as

$$\delta P' = \frac{\beta}{\alpha^2} \cdot \frac{N_{\mathrm{d}}}{N_{\mathrm{a}}} \cdot \frac{\pi^{\frac{1}{2}}\overline{P'_{\mathrm{d}}\,h\,L^2}}{\overline{L^2}}\,, \tag{A.13}$$

which can be further simplified by organizing the constant scaling factors α and β into a constant γ term, given by

$$\gamma = \frac{\beta}{\alpha^2}\,. \tag{A.14}$$

The final form of the equations used in section 2.5 then becomes

$$\delta P' = \gamma \cdot \frac{N_{\mathrm{d}}}{N_{\mathrm{a}}} \cdot \frac{\pi^{\frac{1}{2}}\overline{P'_{\mathrm{d}}\,h\,L^2}}{\overline{L^2}}\,. \tag{A.15}$$

In order to estimate the regional heat and salt anomalies due to the presence of SCVs, we apply (A.15) using an average ocean density (ρ, 1027 kg m^{-3}), the specific heat capacity of

seawater (C_p, 3850 J kg^{-1}°C^{-1}), and the average detected SCV core temperature ($\overline{T_d}'$, °C) and salinity ($\overline{S_d}'$, g kg^{-1}) anomalies to write

$$\delta H' = \gamma\, \rho\, C_{\mathrm{p}}\, \frac{N_{\mathrm{d}}}{N_{\mathrm{a}}}\, \frac{\pi^{\frac{1}{2}} \overline{T'_{\mathrm{d}}\, h\, L^2}}{\overline{L^2}}\,, \tag{A.16}$$

$$\delta S' = \gamma\, \rho\, \frac{N_{\mathrm{d}}}{N_{\mathrm{a}}}\, \frac{\pi^{\frac{1}{2}} \overline{S'_{\mathrm{d}}\, h\, L^2}}{\overline{L^2}}\,. \tag{A.17}$$

To solve (A.15), (A.16) or (A.17), α (as in Appendix A.1) and β are both set to 1 for illustrative purposes. This results in a lower bound estimate for the anomaly effect from SCVs (in the likely case where $\beta > \alpha^2$). Thus, similar to (A.7), the heat and salt impacts from (A.16) and (A.17) are order-of-magnitude estimates used to facilitate comparisons between regions.

A.3 Additional Figures

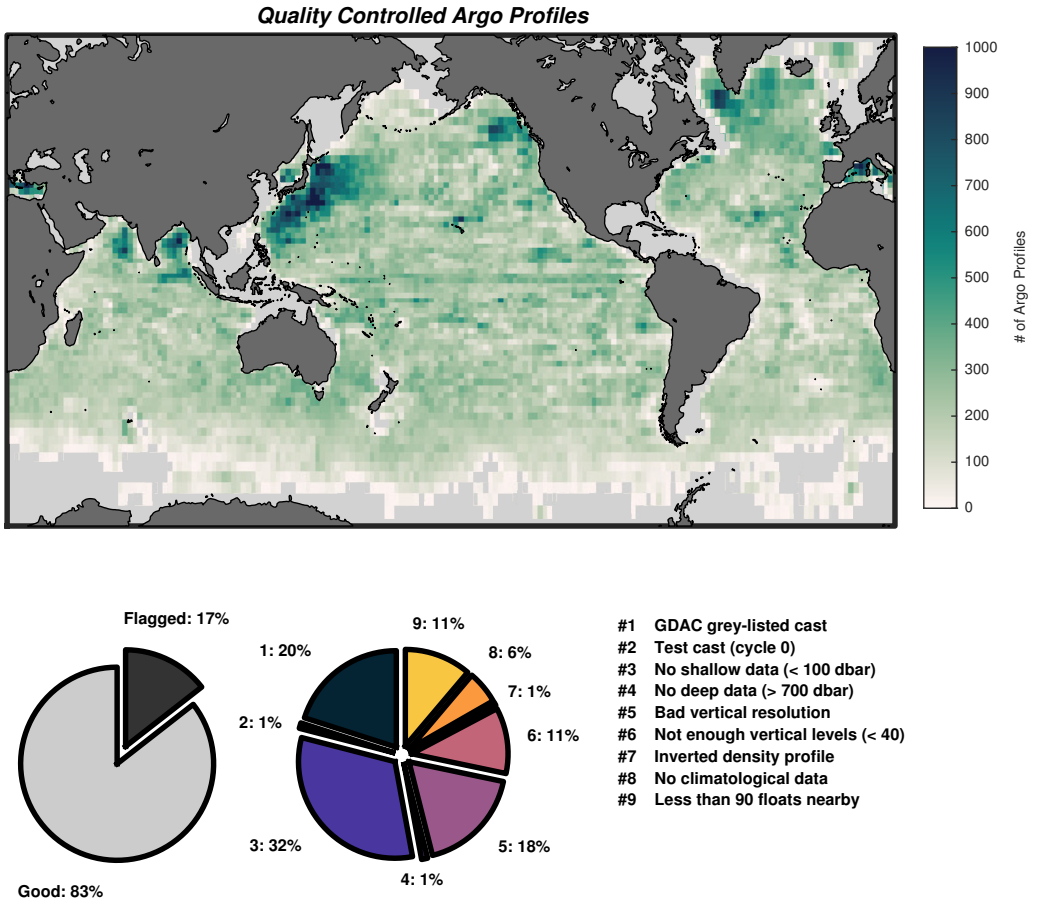

Figure A.1: (top) Number of quality controlled Argo floats per 2°x 2°longitude/latitude grid cell out of a total of 1,992,246 quality controlled float casts. Pie charts show the percentage of all floats rejected (left) and the percentage of floats rejected by each quality control flag (center). A basic description of each quality control flag is shown in the bottom right of the Figure.

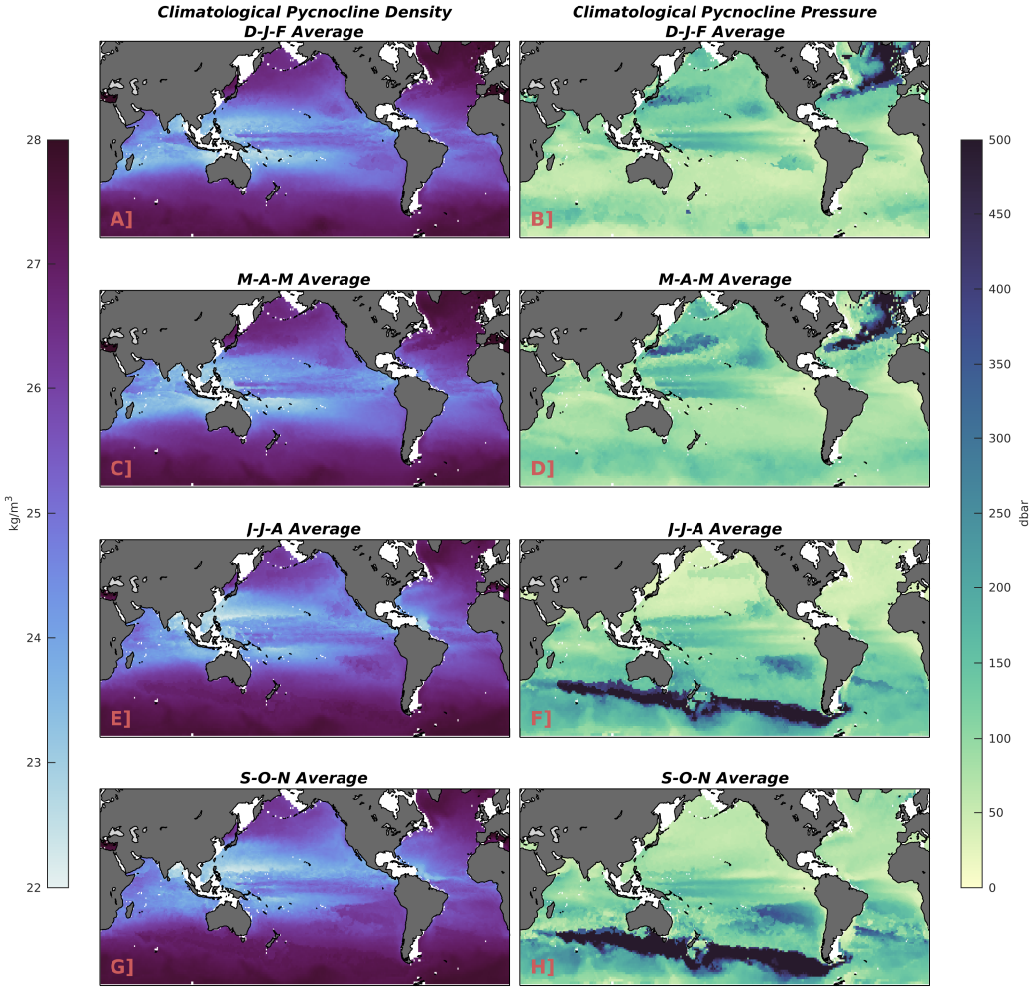

Figure A.2: Roemmich-Gilson (Roemmich & Gilson, 2009) Argo Climatological average mid-pycnocline density and pressure for December-January-February (DJF, panels 'A' and 'E' respectively), March-April-May (MAM, 'B' and 'F'), June-July-August (JJA, 'C' and 'G'), and September-October-November (SON, 'D' and 'H').

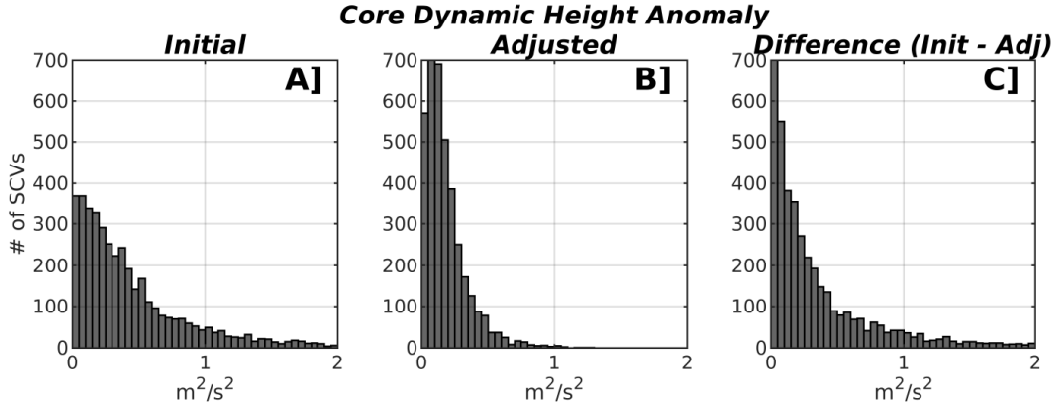

Figure A.3: (A) Histogram of the initial core dynamic height anomaly from all SCVs. (B) Adjusted core dynamic height anomaly after fitting and removing the first baroclinic mode from the initial dynamic height anomaly profile. (C) Difference after removal.

A.4 A global atlas of regional SCVs populations

To provide statistics on coherent populations of spicy-core and minty-core SCVs in greater detail than in the main text, we grouped regional SCV detections within each major oceanic basin. This was accomplished by visually identifying SCVs with similar core properties using Figures 4 through 6 while employing longitude/latitude boxes to gather population statistics (Figure A.4). Each region is labeled according to its basin (North Pacific (NP), South Pacific (SP), North Atlantic (NA), South Atlantic (SA), North Indian (NI), and South Indian (SI)) and it's SCV type (i.e. NP-S1, NP-S2, etc., for spicy-core SCVs and NP-M1, NP-M2, etc., for minty-core SCVs within the North Pacific). Figures A.5 through A.25 provide histograms of core properties and example profiles from within each region.

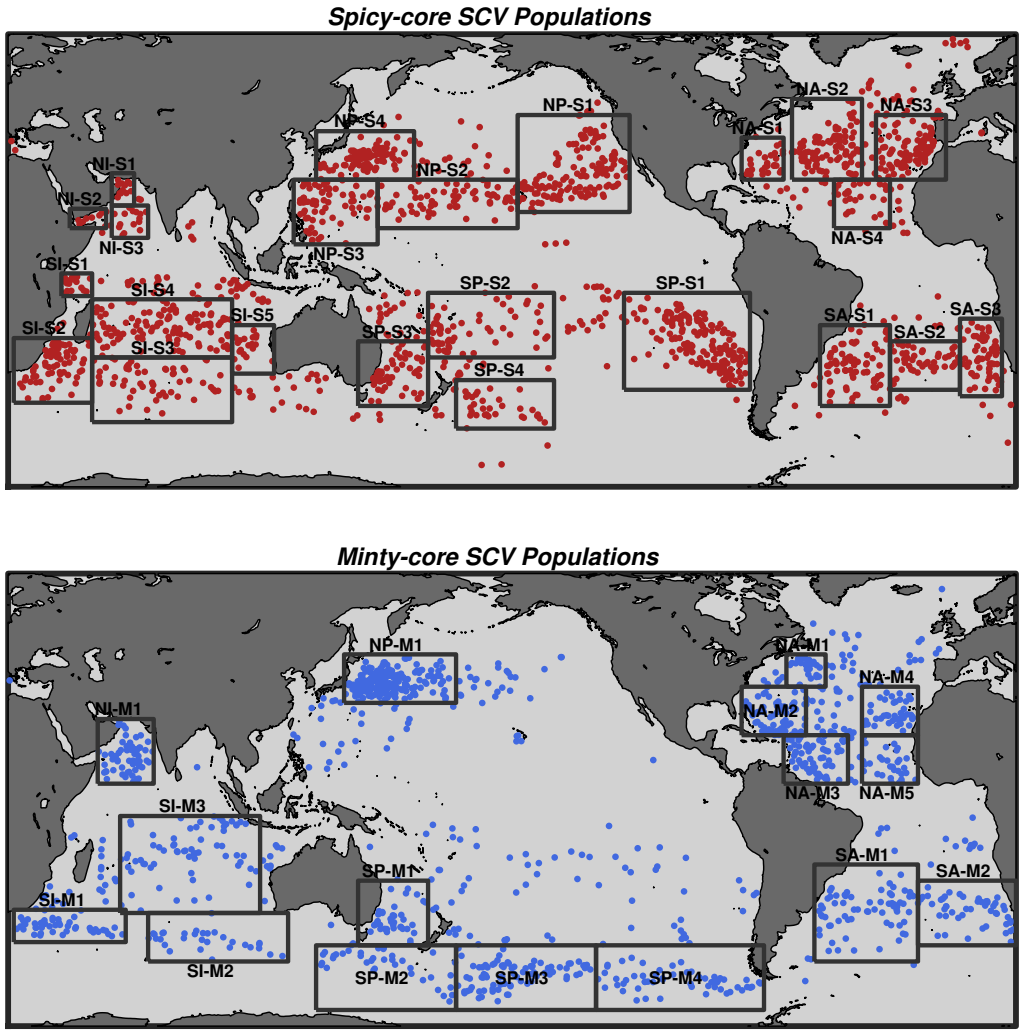

Figure A.4: Locations of identified spicy-core SCV populations (top) and minty-core populations (bottom).

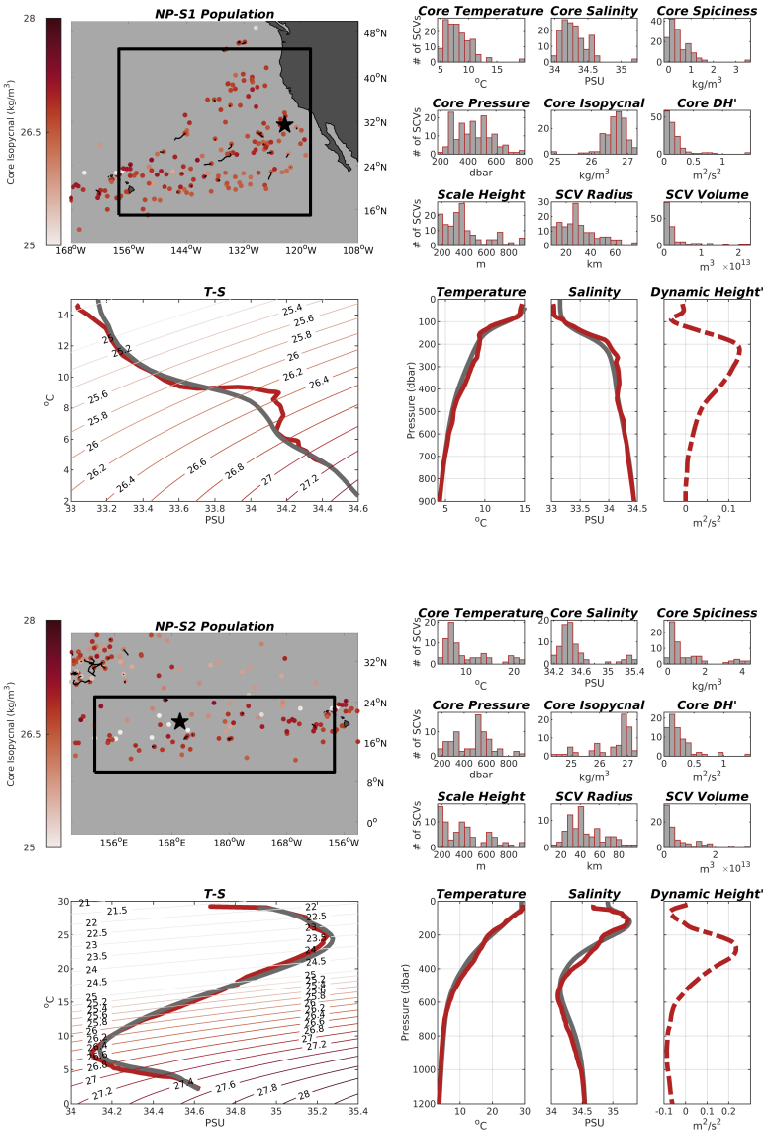

Figure A.5: Spicy-core SCV populations NP-S1 (top, showing Argo float 4900090-128) and NP-S2 (bottom, showing Argo float 2900423-104) from the North Pacific.

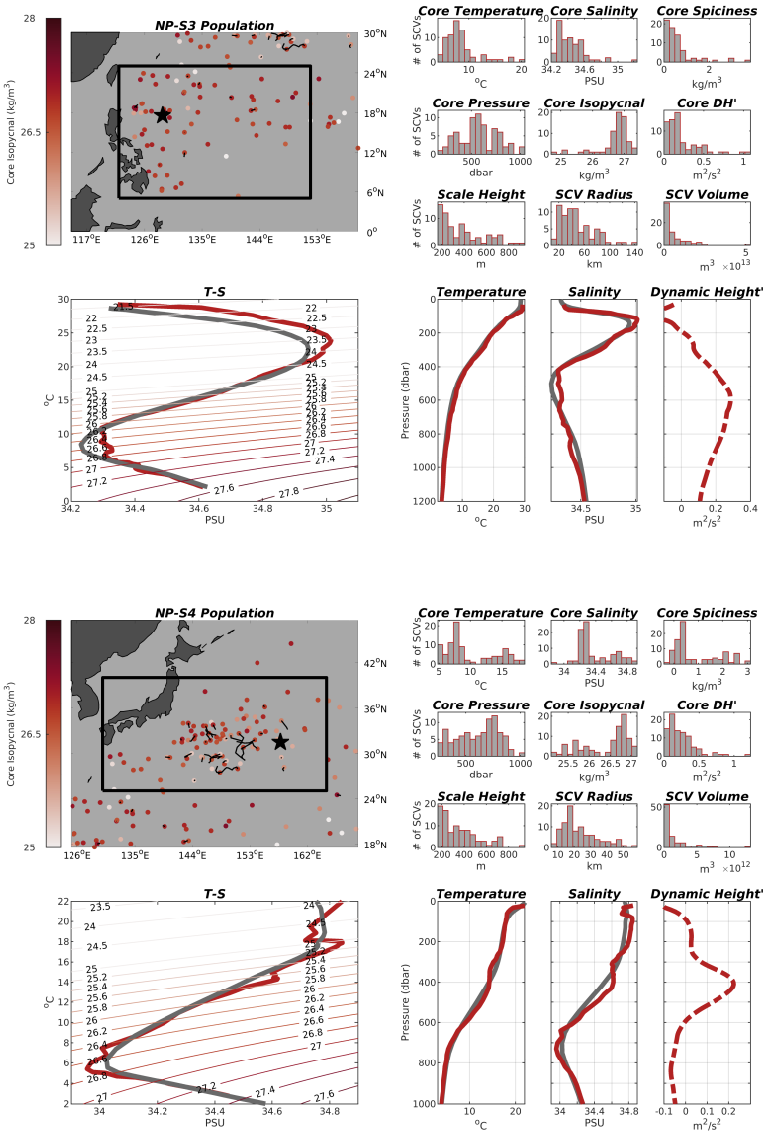

Figure A.6: Spicy-core SCV populations NP-S3 (top, showing Argo float 2900185-62) and NP-S4 (bottom, showing Argo float 2900143-73) from the North Pacific.

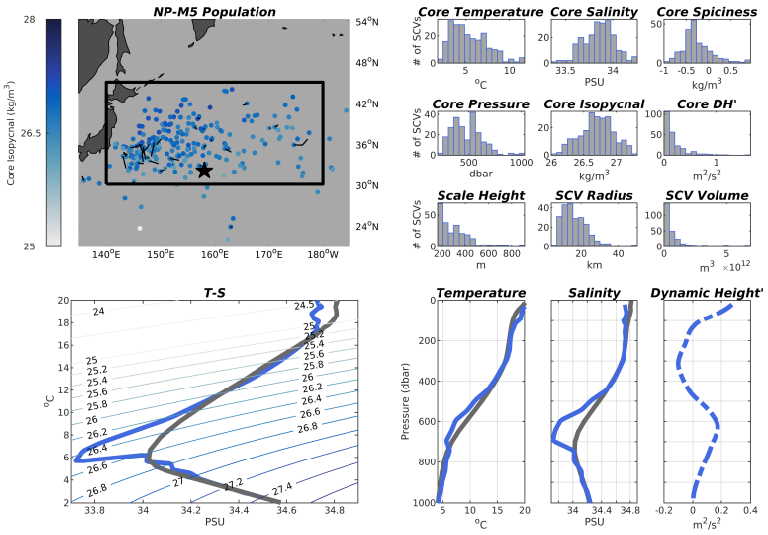

Figure A.7: Minty-core SCV population NP-M1 (showing Argo float 29010-75) from the North Pacific.

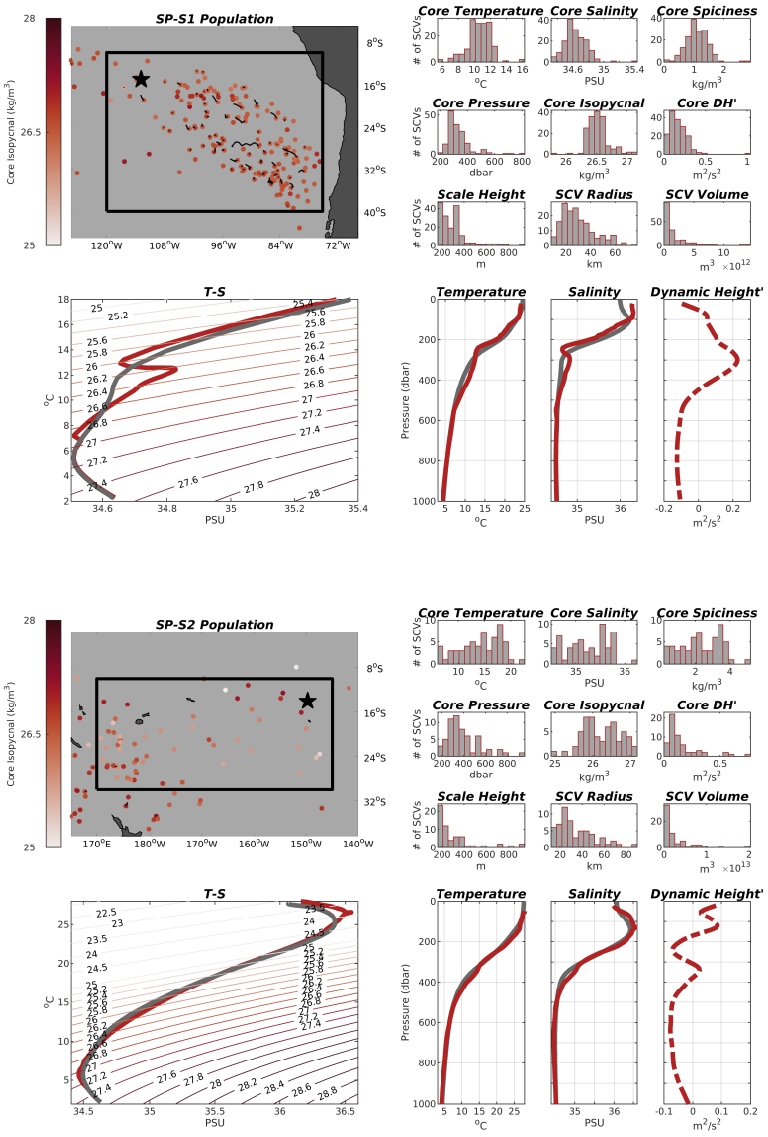

Figure A.8: Spicy-core SCV populations SP-S1 (top, showing Argo float 3900240-45) and SP-S2 (bottom, showing Argo float 5900676-77) from the South Pacific.

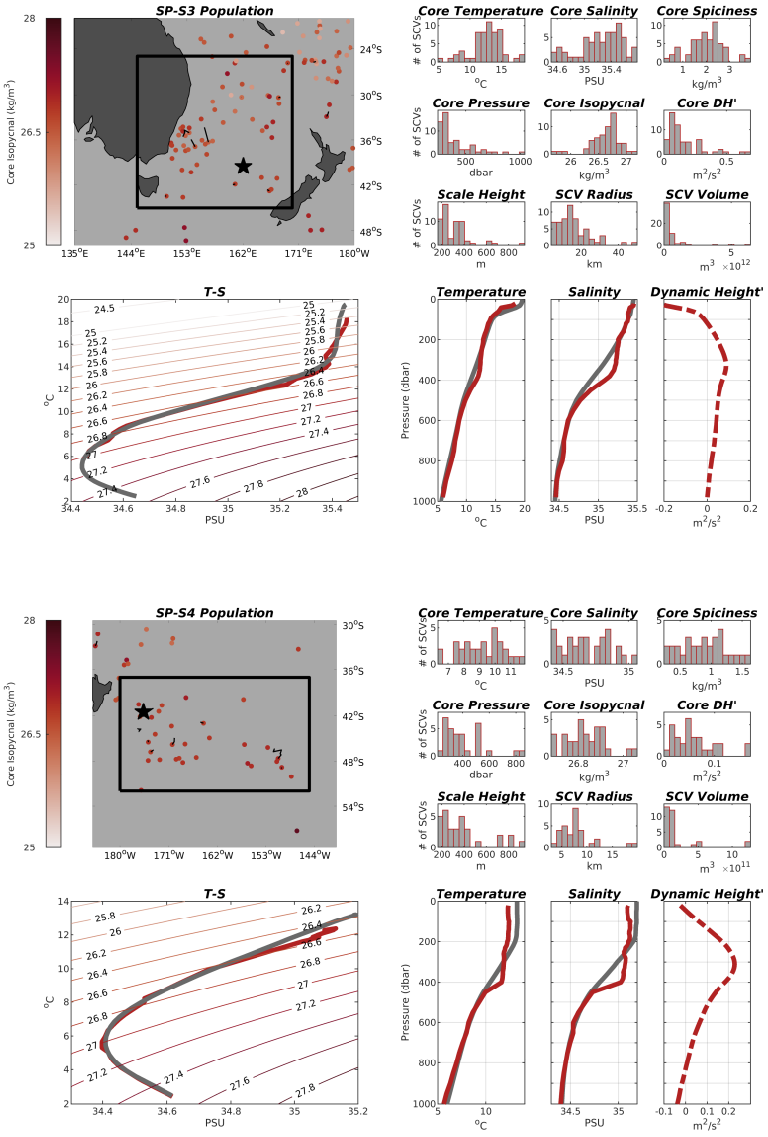

Figure A.9: Spicy-core SCV populations SP-S3 (top, showing Argo float 5901091-15) and SP-S4 (bottom, showing Argo float 3900508-62) from the South Pacific.

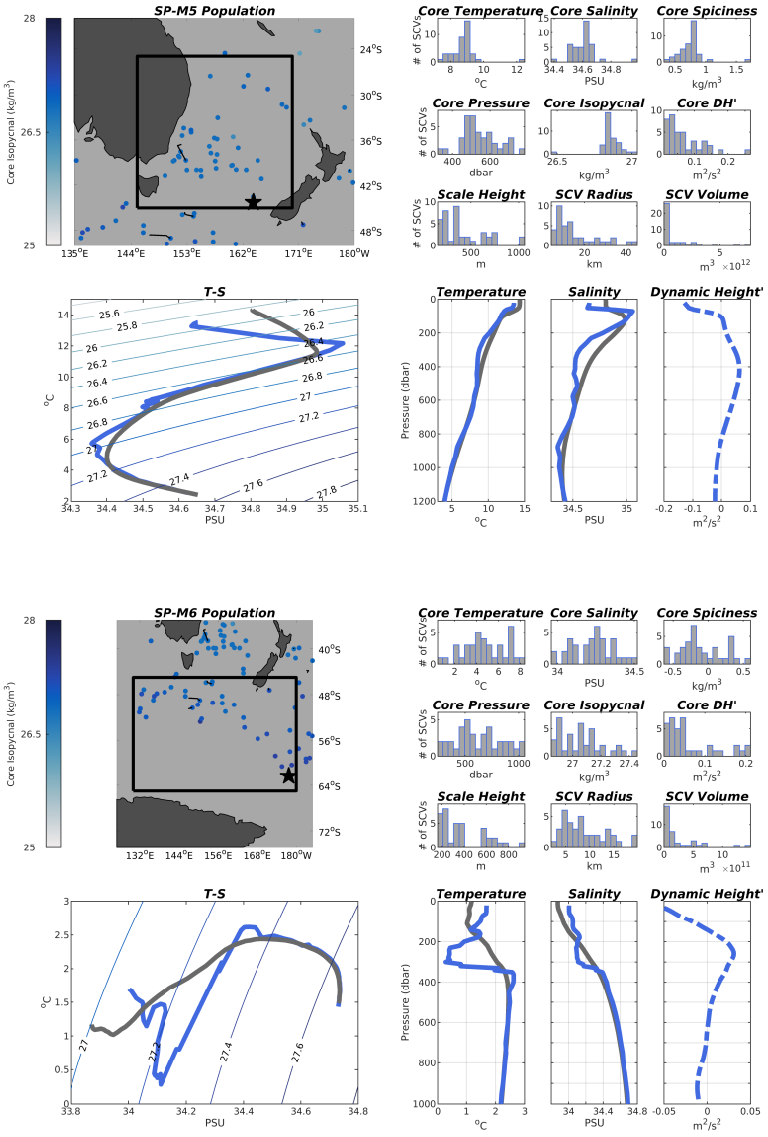

Figure A.10: Minty-core SCV populations SP-M1 (top, showing Argo float 5901269-173) and SP-M2 (bottom, showing Argo float 1901415-65) from the South Pacific.

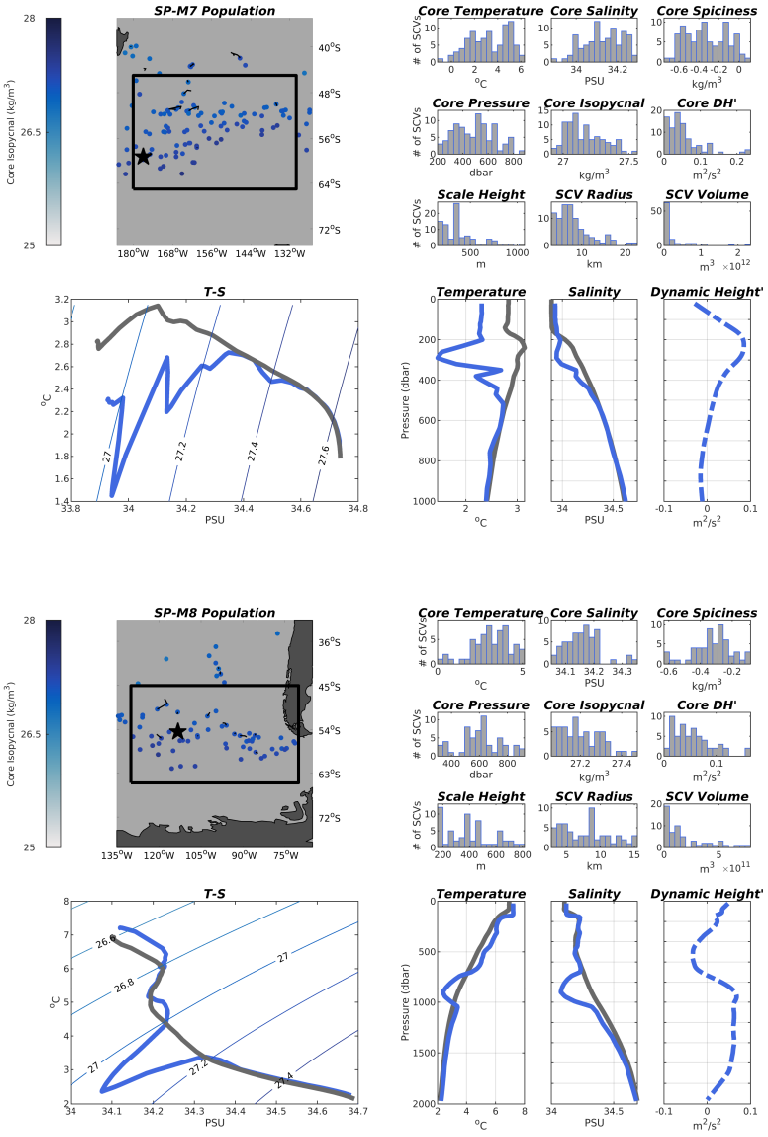

Figure A.11: Minty-core SCV populations SP-M3 (top, showing Argo float 1900805-167) and SP-M4 (bottom, showing Argo float 1900978-349) from the South Pacific.

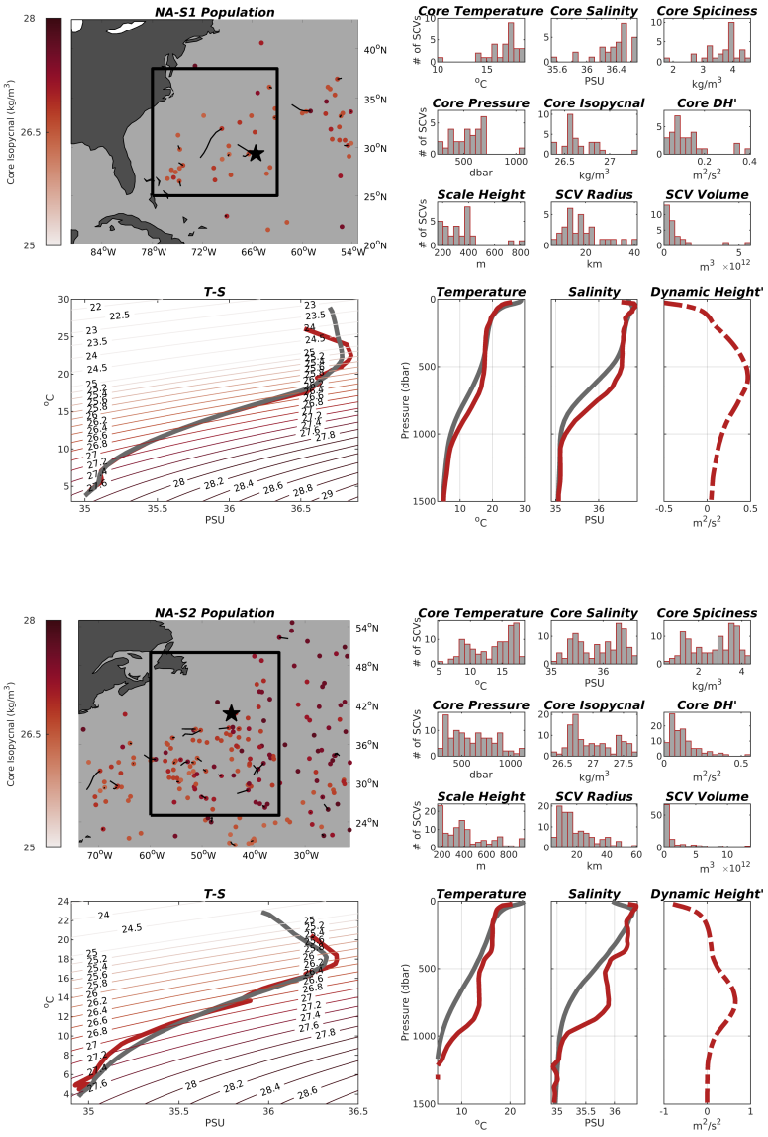

Figure A.12: Spicy-core SCV populations NA-S1 (top, showing Argo float 4900852-174) and NA-S2 (bottom, showing Argo float 69027-150) from the North Atlantic.

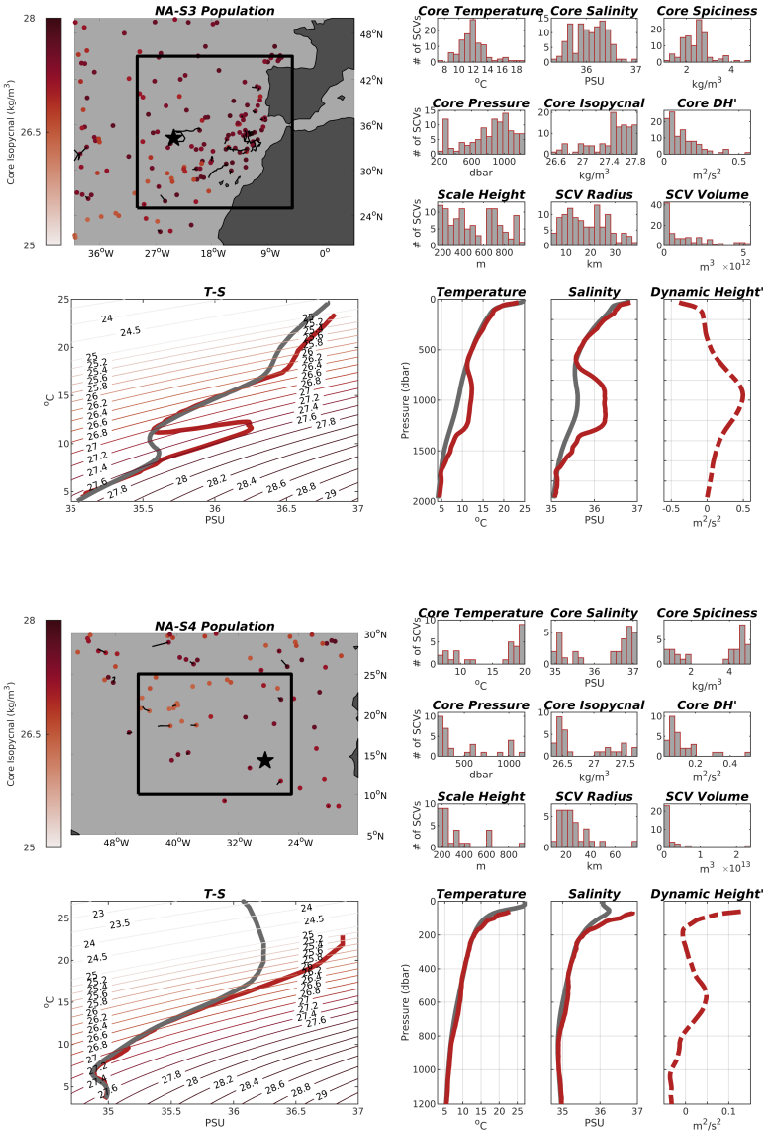

Figure A.13: Spicy-core SCV populations NA-S3 (top, showing Argo float 1900076-2) and NA-S4 (bottom, showing Argo float 3901682-34) from the North Atlantic.

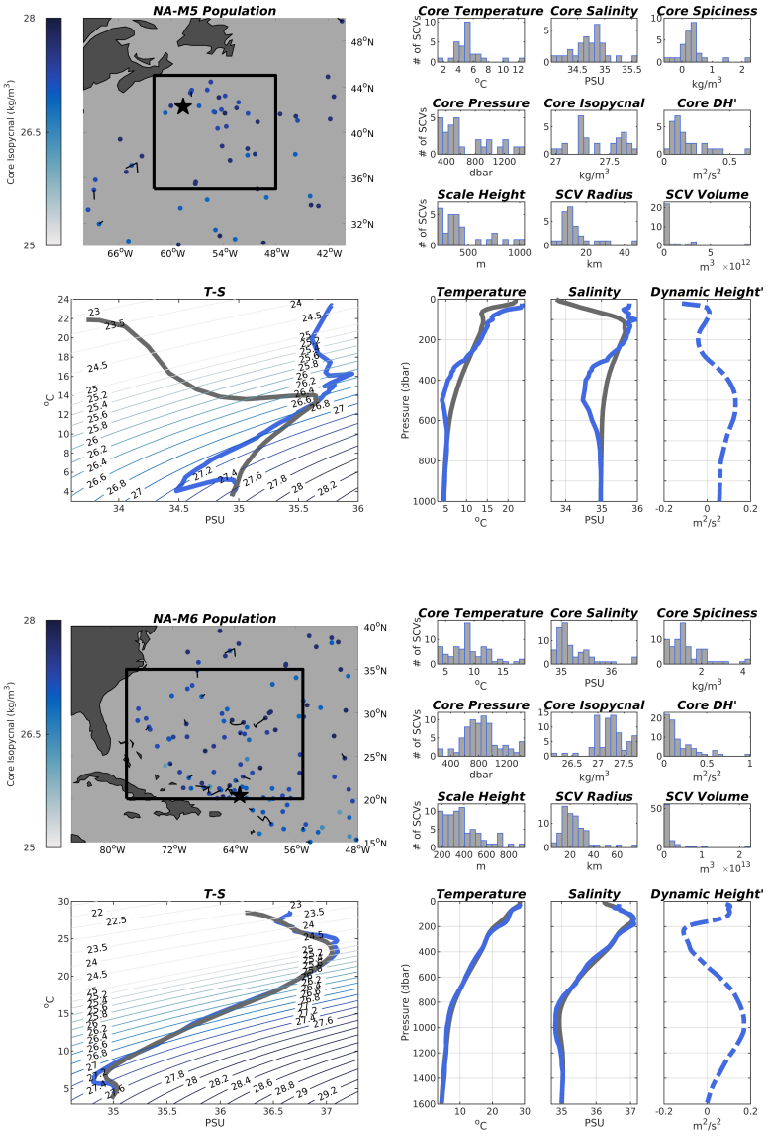

Figure A.14: Minty-core SCV populations NA-M1 (top, showing Argo float 4901102-12) and NA-M2 (bottom, showing Argo float 4900800-61) from the North Atlantic.

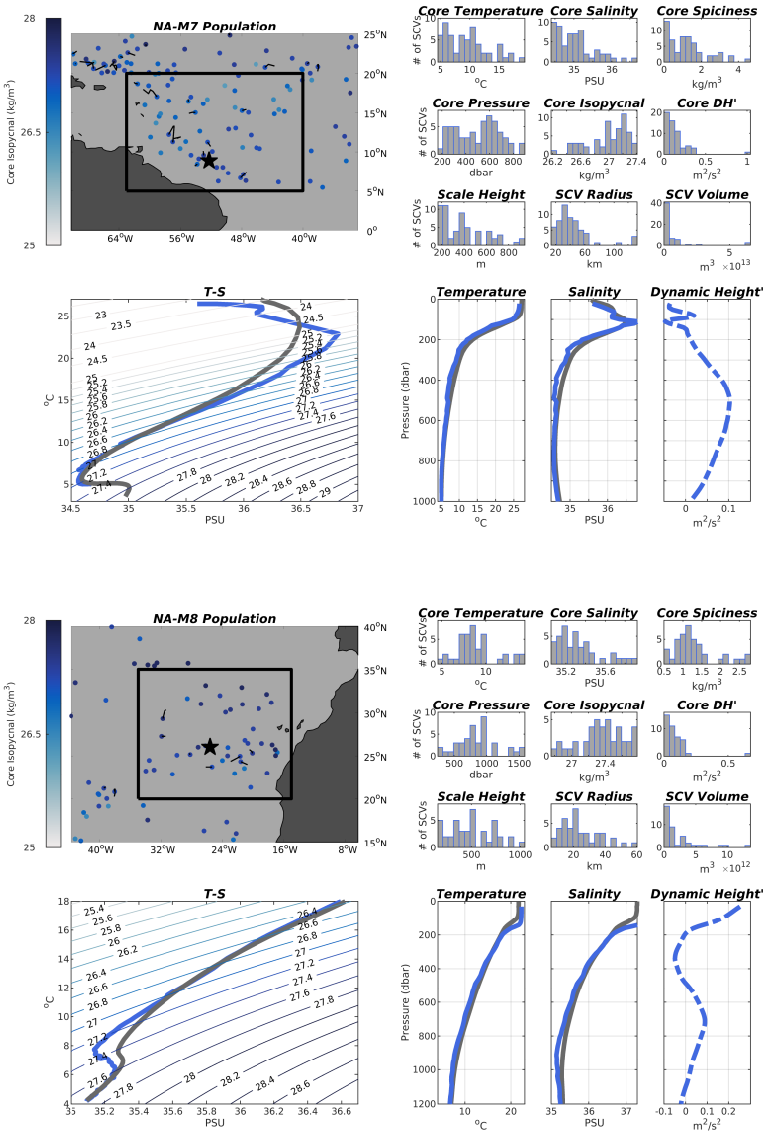

Figure A.15: Minty-core SCV populations NA-M3 (top, showing Argo float 49059-1) and NA-M4 (bottom, showing Argo float 1900067-68) from the North Atlantic.

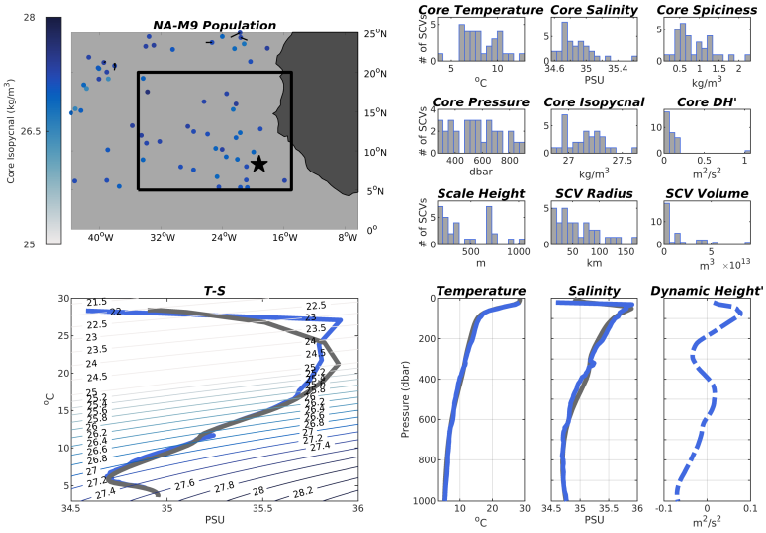

Figure A.16: Minty-core SCV population NA-M5 (showing Argo float 1901540-51) from the North Atlantic.

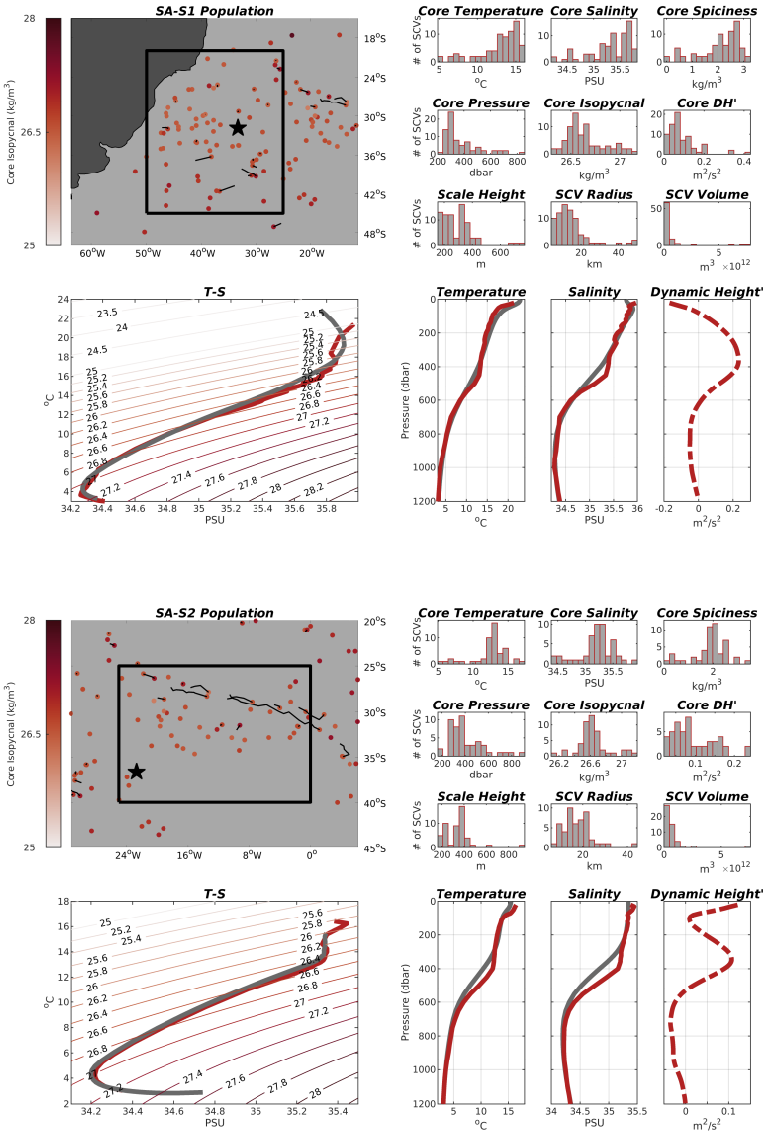

Figure A.17: Spicy-core SCV populations SA-S1 (top, showing Argo float 1900204-130) and SA-S2 (bottom, showing Argo float 1900240-162) from the South Atlantic.

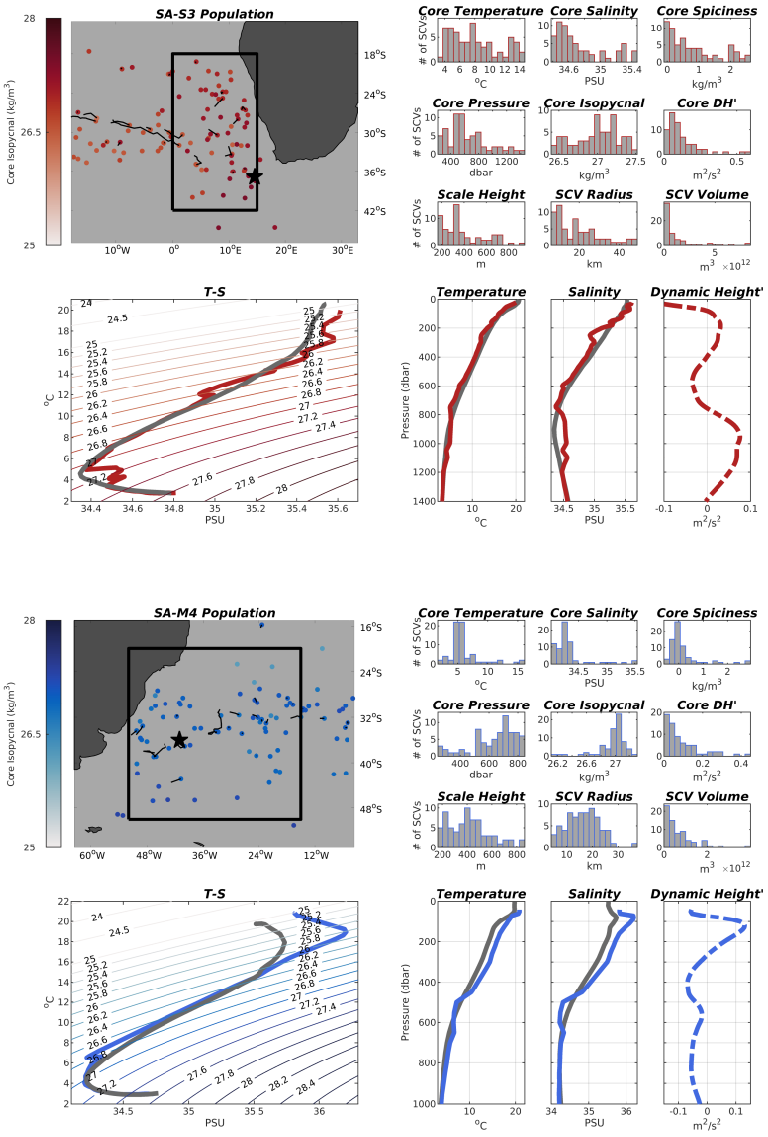

Figure A.18: Spicy-core SCV population SA-S3 (top, showing Argo float 1900221-26) and minty-core population SA-M1 (bottom, showing Argo float 1901268-238) from the South Atlantic.

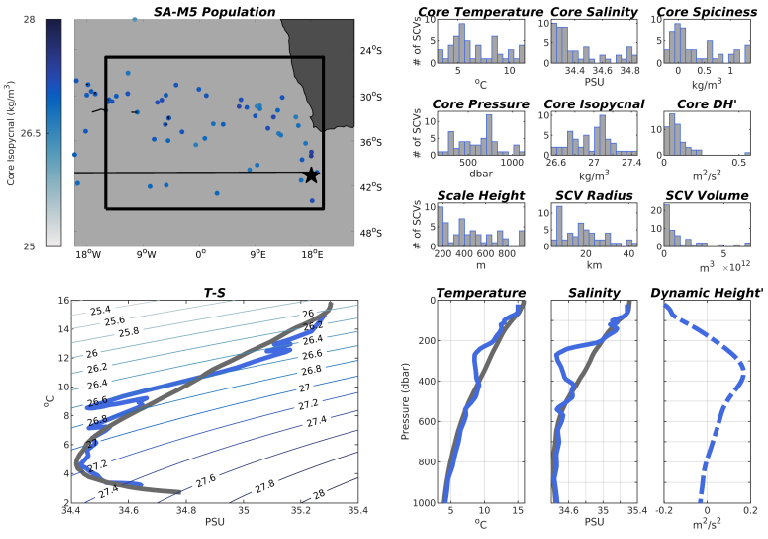

Figure A.19: Minty-core SCV population SA-M2 (showing Argo float 1900692-231) from the South Atlantic.

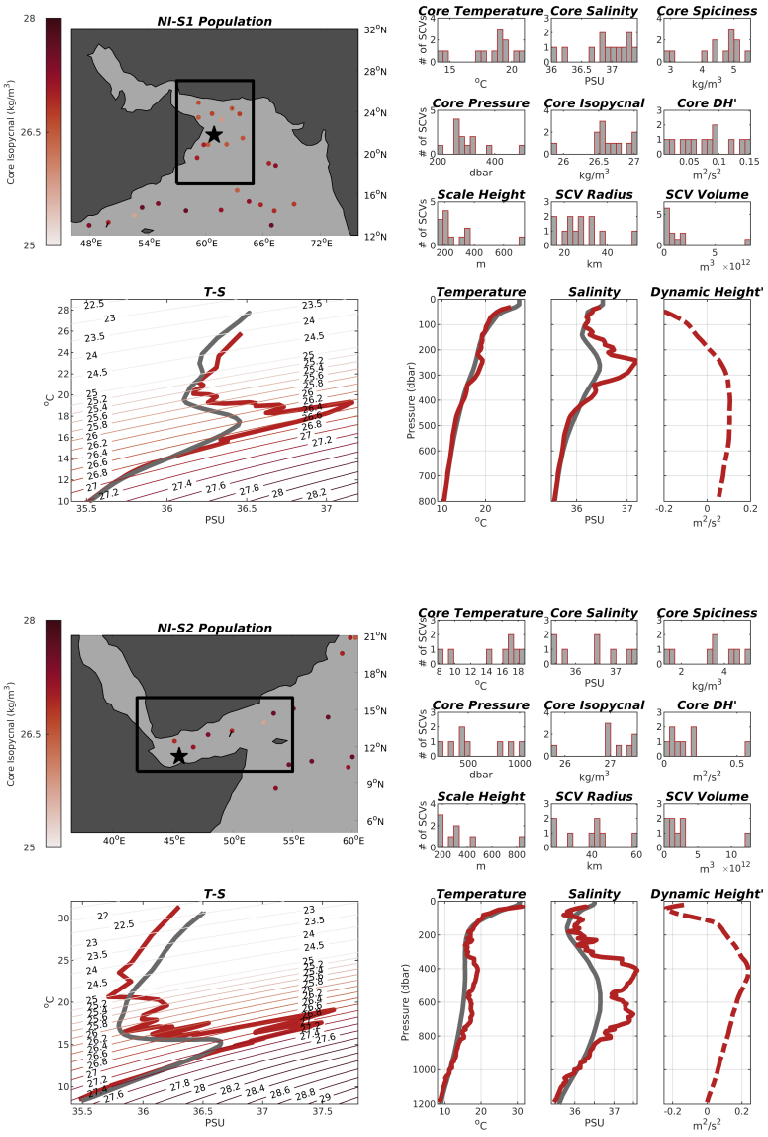

Figure A.20: Spicy-core SCV populations NI-S1 (top, showing Argo float 1901202-48) and NI-S2 (bottom, showing Argo float 6902947-67) from the North Indian.

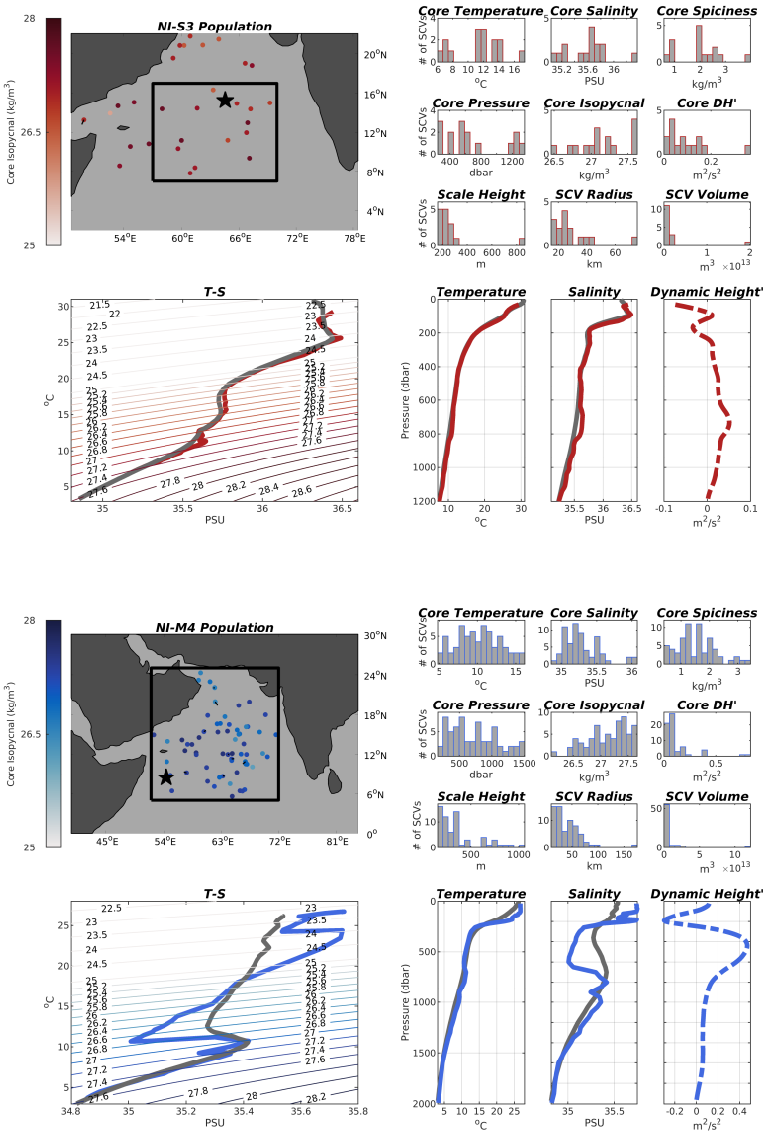

Figure A.21: Spicy-core SCV population NI-S3 (top, showing Argo float 1901186-161) and minty-core population NI-M1 (bottom, showing Argo float 1900372-122) from the North Indian.

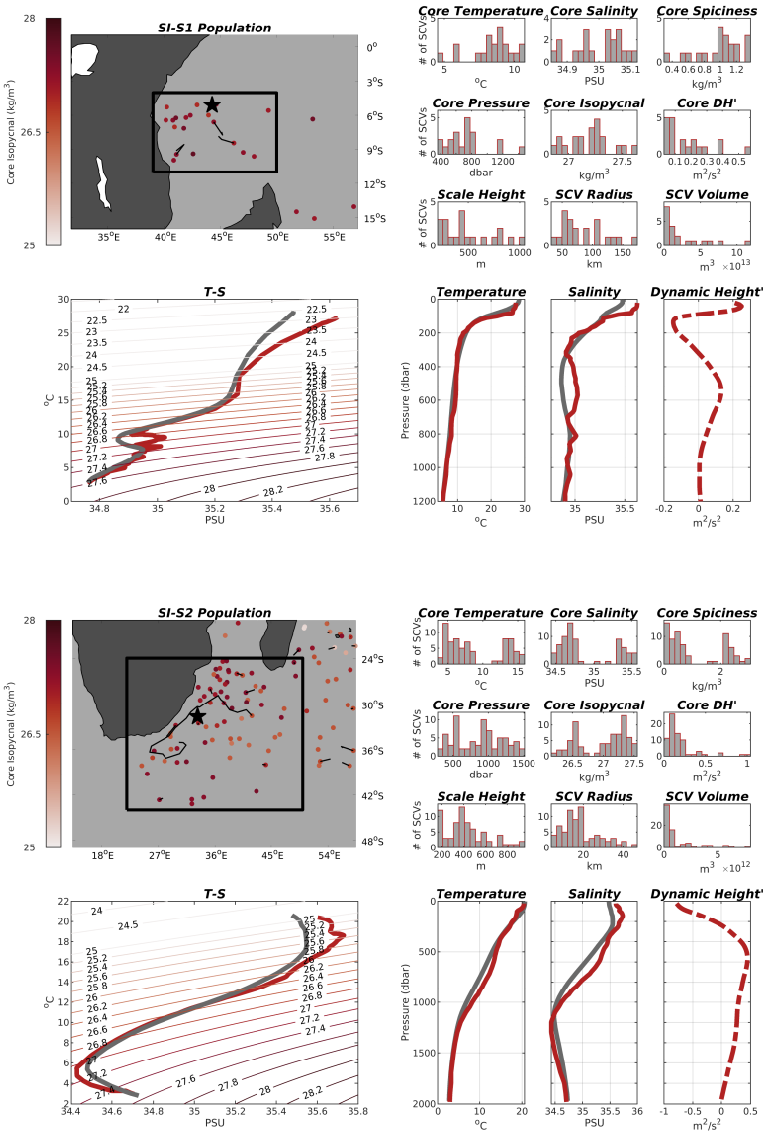

Figure A.22: Spicy-core SCV populations SI-S1 (top, showing Argo float 1900816-135) and SI-S2 (bottom, showing Argo float 1900083-38) from the South Indian.

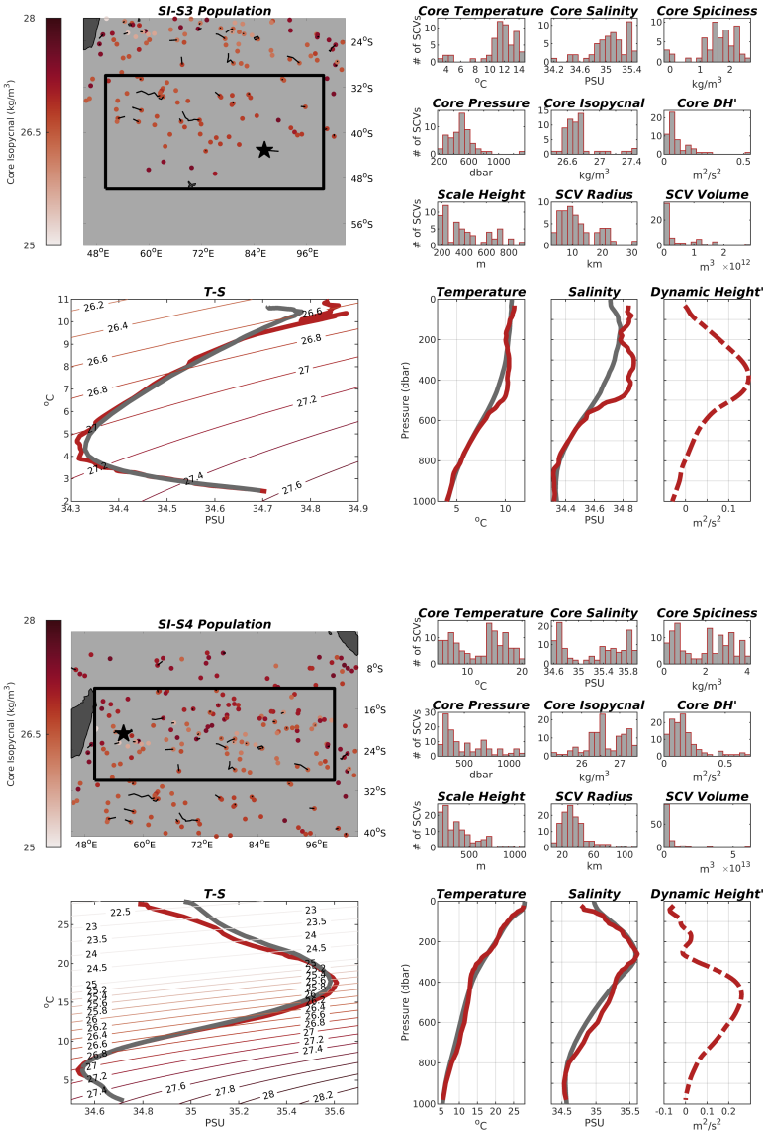

Figure A.23: Spicy-core SCV populations SI-S3 (top, showing Argo float 1900859-134) and SI-S4 (bottom, showing Argo float 1900269-46) from the South Indian.

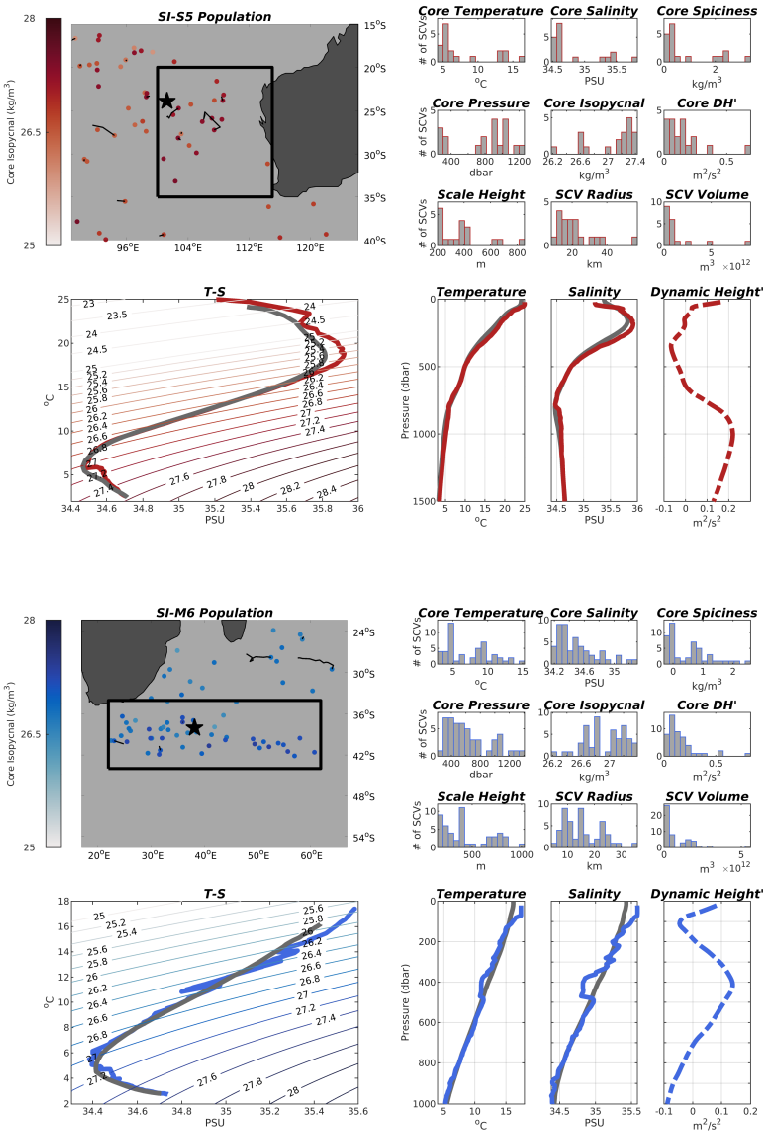

Figure A.24: Spicy-core SCV population SI-S5 (top, showing Argo float 5901205-82) and minty-core population SI-M1 (bottom, showing Argo float 1901664-146) from the South Indian.

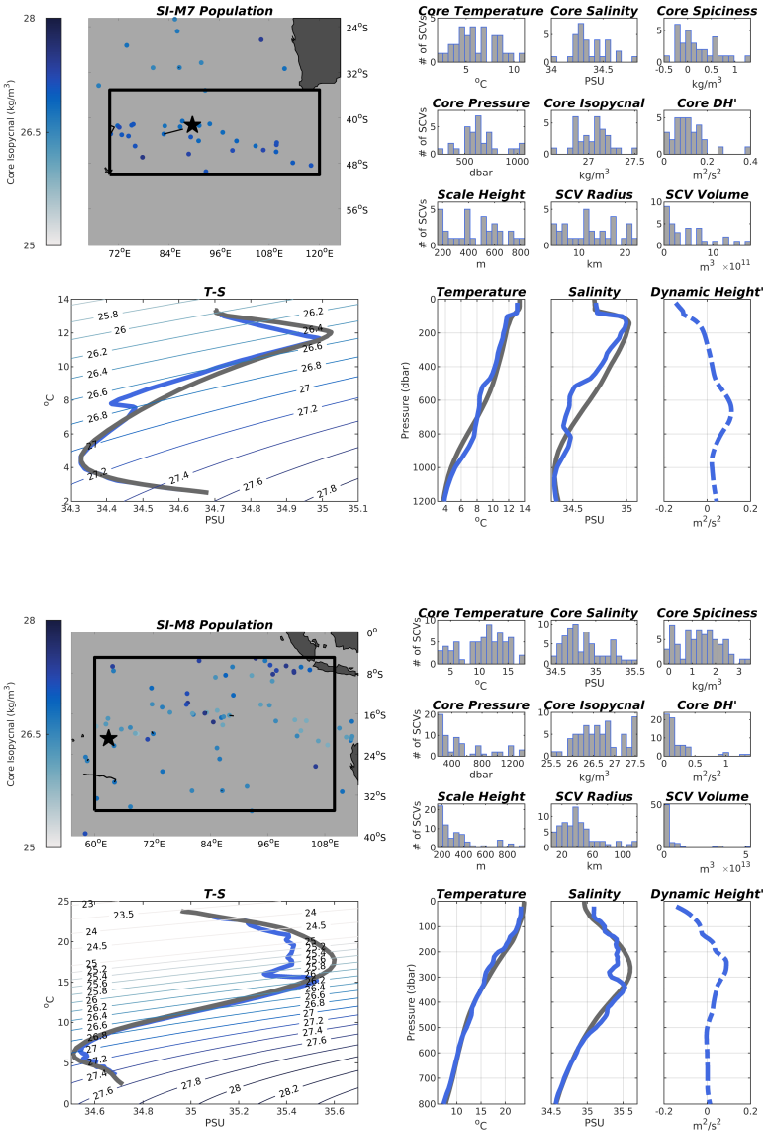

Figure A.25: Minty-core SCV populations SI-M2 (top, showing Argo float 5901251-18) and SI-M3 (bottom, showing Argo float 1900476-66) from the South Indian.

APPENDIX B

Supporting Information for Chapter 3

B.1 Treatment of Organic Matter

In the model, remineralization of sinking particulate OM follows the formulation of Moore et al. (2004), where sinking is implicit and based on the ballast model from Armstrong et al. (2001). Particulate organic carbon (POC) in BEC is produced at each time-step following:

$$R^{poc}_{prod}(z) = (R^{sp}_{graze,poc}(z) + R^{diat}_{graze,poc}(z) + R^{diaz}_{graze,poc}(z)) + (R^{sp}_{agg}(z) + R^{diat}_{agg}(z) + R^{diaz}_{agg}(z)) + (R^{sp}_{loss,poc}(z) + R^{diat}_{loss,poc}(z) + R^{diaz}_{loss,poc}(z)) + f^{d}_{zoo} R^{l}_{zoo}(z).$$

See Table B.2 for descriptions of each rate; further details can be found in Deutsch et al. (2021). POC production is then partitioned into a free and mineral component:

$$R^{poc}_{prod}(z) = R^{free,poc}_{prod}(z) + R^{min,poc}_{prod}(z). \tag{B.1}$$

Following equation (B.1), both free and mineral POC is instantaneously distributed in the water column following one-dimensional steady-state production-remineralization equations. The vertical profile of free POC flux (Φ_{poc}) is calculated as:

$$\Phi_{free,poc}(z) = \Phi_{free,poc}(z_o) e^{-\frac{1}{\lambda_{poc}}(z-z_o)} + \int_{z_o}^{z} R^{prod}_{free,poc}(z) e^{-\frac{1}{\lambda_{poc}}(z-z_o)} dz. \tag{B.2}$$

Here, λ_{poc} is a discretized exponential scale length computed from an initial scale length (γ_{poc}) that is modified by both the local O_2 concentration of layer z:

$$\gamma_{poc} = \begin{cases} \gamma_{poc} * 3.3 & \text{where } O_2 < 5 \text{ mmol/m}^3 \\ \gamma_{poc} * (1 + (3.3-1)(40 - o_2)/35) & \text{where } 5 \text{ mmol/m}^3 < O_2 < 40 \text{ mmol/m}^3 \\ \gamma_{poc} & \text{elsewhere} \end{cases} \tag{B.3}$$

and its thickness dz:

$$\lambda_{poc} = \begin{cases} \gamma_{poc} * (1.0), & \text{where dz <100m} \\ \gamma_{poc} * (1.0 * (2.9 - 1.0) * (-dz - 1.0)/(2.9 - 1.0), & \text{where 100m<dz<250m} \\ \gamma_{poc} * (2.9 * (5.6 - 2.9) * (-dz - 2.9)/(5.6 - 2.9), & \text{where 250m<dz<500m} \\ \gamma_{poc} * (5.6 * (5.7 - 5.6) * (-dz - 5.6)/(5.7 - 5.6), & \text{where 500m<dz<700m} \\ \gamma_{poc} * (5.7). & \text{elsewhere} \end{cases} \quad \text{(B.4)}$$

See Table B.2 for parameter values.

The vertical profile of POC flux for each mineral is calculated as the sum of a soft and hard component (where the hard component is a fraction of the total based on f_{pcaco3}, f_{psio_2}, and f_{dust}, respectively, see Table B.2). The soft component for $CaCO_3$, SiO_2, and dust follow similar remineralization processes as in equation (B.2), whereas the hard components remineralize according to λ_{hard} and $\lambda_{hard,dust}$ (for dust). The fluxes of each mineral are then summed in C units:

$$\begin{aligned} \Phi_{min,poc}(z) = \rho_{pcaco3}(\Phi^{soft}_{pcaco3}(z) + \Phi^{hard}_{pcaco3}(z)) + \\ \rho_{psio_2}(\Phi^{soft}_{psio_2}(z) + \Phi^{hard}_{psio_2}(z)) + \\ \rho_{dust}(\Phi^{soft}_{dust}(z) + \Phi^{hard}_{dust}(z)) \end{aligned}$$

Remineralization at each vertical level is then calculated as the divergence of the POC flux:

$$R^{poc}_{rem}(z) = R^{poc}_{prod}(z) + \frac{d}{dz}(\Phi_{free,poc}(z) + \Phi_{min,poc}(z)) \quad \text{(B.5)}$$

In contrast, dissolved organic carbon (DOC) is an explicit ROMS-BEC tracer and is remineralized (R^{doc}_{rem}) based on a timescale of 15 years with a sharp decrease (6.85%) applied below the euphotic zone as in Frischknecht et al. (2017). Local OM remineralization in the water column (R^{tot}_{rem}) is calculated as the sum of POC and DOC remineralization:

$$R^{tot}_{rem}(z) = R^{poc}_{rem}(z) + R^{doc}_{rem}(z). \quad \text{(B.6)}$$

B.2 NitrOMZ Nitrogen Cycle

The NitrOMZ model expands BEC by including, along with aerobic remineralization (R_{rem}), additional heterotrophic denitrification steps under low-O_2 conditions (Bianchi et al., 2022): NO_3^- reduction (R_{den1}), NO_2^- reduction (R_{den2}), and N_2O reduction (R_{den3}). In order to preserve BEC OM cycle, R_{rem}^{tot} (equation (B.6)) is partitioned into four possible components at each vertical level and time-step:

$$R_{rem}^{tot}(z) = R_{rem}(z) + R_{den1}(z) + R_{den2}(z) + R_{den3}(z) = \sum_{n=1}^{4} R_i(z), \tag{B.7}$$

where i represents one of the four respiration pathways. In practice, we calculate the contribution to total remineralization by each pathway i as:

$$R_i(z) = f_i(z) \cdot R_{rem}^{tot}(z), \tag{B.8}$$

where f_i is the relative fraction of remineralization carried out by the process i. The individual depth-dependent fractions are calculated as:

$$f_i(z) = \frac{r_i(z)}{\sum_{i=1}^{4} r_i(z)}, \tag{B.9}$$

where r_i is the specific heterotrophic respiration rate of the reaction, calculated based on a maximum remineralization rate modulated by a Michaelis-Menten function of the oxidant utilized (O_2, NO_3^-, NO_2^-, and N_2O for R_{rem}, R_{den1}, R_{den2}, and R_{den3}, respectively) and an exponential inhibition by oxygen (ignored for aerobic respiration):

$$r_i(z) = k_i \cdot \frac{[\mathrm{X}](z)}{K_i^X + [\mathrm{X}](z)} \cdot e^{-\frac{\mathrm{O_2}(z)}{K_i^{o2}}}. \tag{B.10}$$

Here, k_i represents the maximum respiration rate for each reaction, K_i^X is the half saturation constant for oxidant $[X]$ uptake, and K_i^{o2} is the scale for inhibition by oxygen.

The chemolithotrophic rates of NH_4^+ oxidation (R_{ao}), NO_2^- oxidation (R_{no}), and anaerobic NH_4^+ oxidation (anammox, R_{ax}) are represented in NitrOMZ using Michaelis-Menten functions for both the oxidants (O_2, O_2, and NO_2^- for K_{ao}, K_{no}, and K_{ax}, respectively) and reductants (NH_4^+, NO_2^-, and NH_4^+, respectively). The general form for R_{ao} and R_{no} is:

$$R_i(z) = k_i \cdot \frac{[\mathrm{X}](z)}{K_i^X + [\mathrm{X}](z)} \cdot \frac{[\mathrm{Y}](z)}{K_i^Y + [\mathrm{Y}](z)}. \tag{B.11}$$

Here, k_i represents the maximum respiration rate for each reaction, and K_i^X and K_i^Y are the half saturation constants for oxidant $[X]$ and reductant $[Y]$ uptake, respectively. Both R_{ao} and R_{no} are also inhibited by light, outlined in B.4. The rate of anammox follows a similar calculation, but with an additional rate-specific exponential O_2 inhibition (K_{ax}^{o2}) term applied, similar to the heterotrophic denitrification steps in equation (B.10). See Table B.4 for parameter values used in this study.

B.3 NitrOMZ Tracer Sources-and-sinks

NitrOMZ represents six major components of the marine nitrogen cycle: N_2, NO_3^-, NO_2^-, N_2O, NH_4^+, and organic nitrogen, which is linked to POC and DOC via fixed stoichiometry. The biogeochemical sources and sinks for each of the remaining tracers (in units of *mmol* m^{-3}) are:

$$\frac{d}{dt}(\mathrm{N_2}) = (Q_{den}^{N:C} \cdot R_{den3}) + R_{ax} + (0.5 \cdot R_{den}^{sed}) \tag{B.12}$$

$$\frac{d}{dt}(\mathrm{NO_3^-}) = R_{no} - (Q_{den}^{N:C} \cdot R_{den1}) - R_{den}^{sed} - R_{up,no_3}^{sp} - R_{up,no_3}^{diat} - R_{up,no_3}^{diaz} \tag{B.13}$$

$$\frac{d}{dt}(\mathrm{NO_2^-}) = R_{ao}^{no_2} - R_{no} + Q_{den}^{N:C}(R_{den1} - R_{den2}) - R_{ax} - R_{up,no_2}^{sp} - R_{up,no_2}^{diat} - R_{up,no_2}^{diaz} \tag{B.14}$$

$$\frac{d}{dt}(\mathrm{N_2O}) = R_{ao}^{n_2o} + (0.5 \cdot Q_{den}^{N:C} \cdot R_{den2}) - (Q_{den}^{N:C} \cdot R_{den3}) \tag{B.15}$$

$$\begin{aligned}\frac{d}{dt}(\mathrm{NH_4^+}) = {} & DON(\tau^{DON}) + DONr(\tau^{DONr}) - R_{ao} - R_{ax} \\ & + Q_{rem}^{N:C}(R_{loss,dic}^{sp} + R_{loss,dic}^{diat} + R_{loss,dic}^{diaz}) \\ & + Q_{rem}^{N:C}(R_{graze,dic}^{sp} + R_{graze,dic}^{diat} + R_{graze,dic}^{diaz} + R_{loss,dic}^{zoo}) \\ & + Q_{rem}^{N:C}(R_{poc}^{rem}(1 - Q^{DONr})) - (R_{up,nh_4}^{sp} + R_{up,nh_4}^{diat} + R_{up,nh_4}^{diaz})\end{aligned} \tag{B.16}$$

(B.17)

Here the symbol d/dt denotes the sum of the local time derivative and the physical transport, and $Q_{rem}^{N:C}$ and $Q_{den}^{N:C}$ represent the approximate nitrogen to carbon ratio from remineralization (16/117) and denitrification (472/2/106), respectively, following Anderson & Sarmiento (1994). The sedimentary denitrification rate (R_{den}^{sed}) follows the same formulation as in Deutsch et al. (2021).

Following the N_2O decomposition described in Section 3.2.4, the N_2O reduction rate decomposition is represented as:

$$R^{den}_{den3} = \frac{N_2O_{den}}{N_2O} \cdot R_{den3} \cdot Q^{N:C}_{den}, \tag{B.18a}$$

$$R^{nit}_{den3} = \frac{N_2O_{nit}}{N_2O} \cdot R_{den3} \cdot Q^{N:C}_{den}, \tag{B.18b}$$

$$R^{bry}_{den3} = \frac{N_2O_{bry}}{N_2O} \cdot R_{den3} \cdot Q^{N:C}_{den}. \tag{B.18c}$$

$$\tag{B.18d}$$

The equations for each of the N_2O tracers (in units of $mmol\ N_2O\ m^{-3}$) are therefore represented as:

$$\frac{d}{dt}(N_2O_{den}) = (0.5 \cdot R_{den2} \cdot Q^{N:C}_{den}) - R^{den}_{den3}, \tag{B.19a}$$

$$\frac{d}{dt}(N_2O_{nit}) = (0.5 \cdot R^{n_2o}_{ao}) - R^{nit}_{den3}, \tag{B.19b}$$

$$\frac{d}{dt}(N_2O_{bry}) = -R^{bry}_{den3}. \tag{B.19c}$$

Descriptions of each nitrogen cycle tracer are presented in Table B.5.

B.4 Light Inhibition

In NitrOMZ, rates of both NH_4^+ and NO_2^- oxidation (R_{ao} and R_{no}, respectively) are photoinhibited by photosynthetically available radiation (PAR) near the surface, modelled in ROMS-BEC using the same formulation as in Frischknecht et al. (2017). Surface PAR (PAR_{in}) is attenuated with depth via a discretized exponential scale length parameter (λ_{par}) computed from an initial surface value (λ_{par_i}):

$$\lambda_{par_i} = max(0.02, Chl_{tot}), \tag{B.20}$$

where Chl_{tot} is the sum of community chlorophyll from diatoms (Chl_{diat}), diazotrophs (Chl_{diaz}), and small phytoplankton (Chl_{sp}). The attenuation coefficient is then further modified depending on the initial value of λ_{par_i}:

$$\lambda_{par}(z) = \begin{cases} 0.0919 \cdot (\lambda_{par_i})^{0.3536} \cdot dz & \text{where } \lambda_{par_i} < 0.13224, \\ 0.1131 \cdot (\lambda_{par_i})^{0.4562} \cdot dz & \text{where } \lambda_{par_i} \geq 0.13224. \end{cases} \tag{B.21}$$

In the initial surface grid cell, attenuation of PAR_{in} from the top of the cell over the cell thickness (m) is calculated as:

$$\mathrm{PAR}_{out}(z) = \mathrm{PAR}_{in}(z) \cdot e^{-\lambda_{par}(z)}. \tag{B.22}$$

For each cell, if both $\mathrm{PAR}_{in}(z)$ and $\mathrm{PAR}_{out}(z)$ are less than the PAR limitation for either rate (PAR^{ao}_{lim} and PAR^{no}_{lim}, here both set to 1 W m^{-2}), then photo-inhibition is avoided and the rates are calculated via equation (B.11). If only $\mathrm{PAR}_{in}(z)$ exceeds PAR limitation, each rate is attenuated via:

$$R_{ao}(z) = R_{ao}(z) \cdot log(\frac{\mathrm{PAR}_{out}(z)/\mathrm{PAR}^{ao}_{lim}}{-\lambda_{par}(z)}) \tag{B.23}$$

$$R_{no}(z) = R_{no}(z) \cdot log(\frac{\mathrm{PAR}_{out}(z)/\mathrm{PAR}^{no}_{lim}}{-\lambda_{par}(z)}). \tag{B.24}$$

Following the calculation, $\mathrm{PAR}_{out}(z)$ is set to $\mathrm{PAR}_{in}(z)$ for the cell below and iterated over the number of depths.

B.5 Biogeochemical Validation

To validate the biogeochemical tracer distributions simulated by ROMS-BEC, we gathered O_2, NO_3^-, PO_4^{-3}, and N^* (defined as $[NO_3^-]$ - $16 \cdot [PO_4^{3-}]$ + 2.9, following Deutsch et al. (2001)) reconstructions from World Ocean Atlas 2018 (H. Garcia et al., 2019) (Figures B.9 - B.12); additional O_2 estimates were provided by Dunn (2012) and Bianchi et al. (2012). Estimates of 3-D NO_2^- and N_2O were obtained from in situ observations (Kock & Bange, 2015; Lauvset et al., 2016), and extrapolated using a machine learning approach as outlined in Yang et al. (2020) (Figures B.13 - B.14). Annually averaged maps of net primary production (NPP) were obtained using three different productivity algorithms, which included the Eppley Vertically Generalized Production Model (Eppley-VGPM) (Behrenfeld & Falkowski, 1997), the updated Carbon-Based Productivity Model (CbPM2) (Behrenfeld et al., 2005) and the Carbon, Absorption, and Fluorescence Euphotic-resolving model (CAFE) (Silsbe et al., 2016) (Figure B.15). Level 3 satellite chlorophyll-a concentration data were obtained from the NASA Ocean Color data center (Figure B.16), with all of the satellite-based data (including NPP) obtained from the Ocean Productivity Group at Oregon State University.

Table B.1: Organic matter cycle rates.

Rates	Description	Units
$R^{sp}_{graze,poc}$	Grazing loss for small phytoplankton routed to POC	mmol C/m^3/s
$R^{diat}_{graze,poc}$	Grazing loss for diatoms routed to POC	mmol C/m^3/s
$R^{diaz}_{graze,poc}$	Grazing loss for diazotrophs routed to POC	mmol C/m^3/s
R^{sp}_{agg}	Aggregation loss of small phytoplankton	mmol C/m^3/s
R^{diat}_{agg}	Aggregation loss of diatoms	mmol C/m^3/s
R^{diaz}_{agg}	Aggregation loss of diazotrophs	mmol C/m^3/s
$R^{sp}_{loss,poc}$	Non-grazing mortality of small phytoplankton routed to POC	mmol C/m^3/s
$R^{diat}_{loss,poc}$	Non-grazing mortality of diatoms routed to POC	mmol C/m^3/s
$R^{diaz}_{loss,poc}$	Non-grazing mortality of diazotrophs routed to POC	mmol C/m^3/s
R^{prod}_{poc}	Amount of particulate organic C produced	mmol C/m^3/s
$R^{prod}_{free,poc}$	Amount of non-mineral particulate organic C produced	mmol C/m^3/s
$R^{prod}_{min,poc}$	Amount of mineral particulate organic C produced	mmol C/m^3/s
R^{rem}_{poc}	Amount of particulate organic C remineralized	mmol C/m^3/s
Φ_{poc}	Incoming particulate C-flux	mmol C/m^3/s
$\Phi_{free,poc}$	Incoming non-mineral particulate C-flux	mmol C/m^3/s
$\Phi_{min,poc}$	Incoming mineral particulate C-flux	mmol C/m^3/s
Φ^{soft}_{pcaco3}	Incoming soft $CaCO_3$ particulate flux	mmol $CaCO_3$/m^3/s
$\Phi^{soft}_{psio_2}$	Incoming soft SiO_2 particulate flux	mmol SiO_2/m^3/s
Φ^{soft}_{dust}	Incoming soft dust flux	mmol C/m^3/s
Φ^{hard}_{pcaco3}	Incoming hard $CaCO_3$ particulate flux	mmol $CaCO_3$/m^3/s
$\Phi^{hard}_{psio_2}$	Incoming hard SiO_2 particulate flux	mmol SiO_2/m^3/s
Φ^{hard}_{dust}	Incoming hard dust flux	mmol C/m^3/s

Table B.2: Organic matter cycle parameters

Parameters	Description	Value	Units
ρ_{pcaco3}	Associated molar ratio of $CaCO_3$ to POC	0.417	mol $CaCO_3$ / mol POC
ρ_{psio_2}	Associated molar ratio of SiO_2 to POC	0.250	mol SiO_2 / mol POC
ρ_{dust}	Associated molar ratio of dust to POC	4163.197	mol dust / mol POC
γ_{poc}	Initial length scale for remineralization of POC	88	m
γ_{pcaco3}	Length scale for remineralization of $CaCO_3$	150	m
γ_{psio_2}	Length scale for remineralization of SiO_2	250	m
γ_{dust}	Length scale for remineralization of dust	200	m
λ_{hard}	Length scale for remineralization of hard subclass	40	km
$\lambda_{hard,dust}$	Length scale for remineralization of hard dust subclass	125	km
f_{poc}	Fraction of POC routed to hard subclass	0	N/A
f_{pcaco3}	Fraction of $CaCO_3$ routed to hard subclass	0.3	N/A
f_{psio_2}	Fraction of SiO_2 routed to hard subclass	0.03	N/A
f_{dust}	Fraction of dust routed to hard subclass	0.97	N/A

Table B.3: Nitrogen cycle rates

Name	Description	Units
R_{rem}	Remineralized particulate organic C	mmol C/m^3/s
R_{ao}^{no2}	Rate of NH_4^+ oxidation to NO_2^-	mmol N/m^3/s
R_{ao}^{n2o}	Rate of NH_4^+ oxidation to N_2O	mmol N/m^3/s
R_{no}	Rate of NO_2^- oxidation to NO_3^-	mmol N/m^3/s
R_{den1}	Rate of NO_3^- reduction to NO_2^-	mmol C/m^3/s
R_{den2}	Rate of NO_2^- reduction to N_2O	mmol C/m^3/s
R_{den3}	Rate of N_2O reduction to N_2	mmol C/m^3/s
R_{ax}	Rate of NH_4^+ and NO_2^- loss to N_2 via anammox	mmol N/m^3/s
R_{den}^{sed}	Rate of sedimentary denitrification	mmol N/m^3/s
$R_{loss,dic}^{sp}$	Non-grazing mortality of small phytoplankton routed to DIC	mmol C/m^3/s
$R_{loss,dic}^{diat}$	Non-grazing mortality of diatoms routed to DIC	mmol C/m^3/s
$R_{loss,dic}^{diaz}$	Non-grazing mortality of diazotrophs routed to DIC	mmol C/m^3/s
$R_{loss,dic}^{zoo}$	Zooplankton mortality routed to DIC	mmol C/m^3/s
$R_{graze,dic}^{sp}$	Grazed mortality of small phytoplankton routed to DIC	mmol C/m^3/s
$R_{graze,dic}^{diat}$	Grazed mortality of diatoms routed to DIC	mmol C/m^3/s
$R_{graze,dic}^{diaz}$	Grazed mortality of diazotrophs routed to DIC	mmol C/m^3/s
R_{up,nh_4}^{sp}	Uptake of NH_4^+ by small phytoplankton	mmol N/m^3/s
R_{up,nh_4}^{diat}	Uptake of NH_4^+ by diatoms	mmol N/m^3/s
R_{up,nh_4}^{diaz}	Uptake of NH_4^+ by diazotrophs	mmol N/m^3/s
R_{up,no_3}^{sp}	Uptake of NO_3^- by small phytoplankton	mmol N/m^3/s
R_{up,no_3}^{diat}	Uptake of NO_3^- by diatoms	mmol N/m^3/s
R_{up,no_3}^{diaz}	Uptake of NO_3^- by diazotrophs	mmol N/m^3/s
R_{up,no_2}^{sp}	Uptake of NO_2^- by small phytoplankton	mmol N/m^3/s
R_{up,no_2}^{diat}	Uptake of NO_2^- by diatoms	mmol N/m^3/s
R_{up,no_2}^{diaz}	Uptake of NO_2^- by diazotrophs	mmol N/m^3/s

Table B.4: Nitrogen cycle parameters

Parameters	Description	Value	Units
k_{rem}	Maximum respiration rate	9.259E-7	mmol C/m^3/s
k_{ao}	Maximum NH_4^+ oxidation rate	5.787E-7	mmol N/m^3/s
k_{no}	Maximum NO_2^- oxidation rate	5.787E-7	mmol N/m^3/s
k_{den1}	Maximum NO_3^- reduction rate	1.852E-7	mmol C/m^3/s
k_{den2}	Maximum NO_2^- reduction rate	9.259E-8	mmol C/m^3/s
k_{den3}	Maximum N_2O reduction rate	5.741E-7	mmol C/m^3/s
k_{ax}	Maximum anaerobic NH_4^+ oxidation rate	5.105E-6	mmol N/m^3/s
K_{rem}^{o2}	Respiration half-saturation constant for O_2 uptake	1.000	mmol O_2/m^3
K_{ao}^{o2}	NH_4^+ oxidation half-saturation constant for O_2 uptake	0.333	mmol N/m^3
$K_{ao}^{nh_4}$	NH_4^+ oxidation half-saturation constant for NH_4^+ uptake	0.305	mmol N/m^3
K_{no}^{o2}	NO_2^- oxidation half-saturation constant for O_2 uptake	0.778	mmol N/m^3
K_{no}^{no2}	NO_2^- oxidation half-saturation constant for NO_2^- uptake	0.509	mmol N/m^3
K_{den1}^{no3}	NO_3^- reduction half-saturation constant for NO_3^- uptake	1.000	mmol N/m^3
K_{den2}^{no2}	NO_2^- reduction half-saturation constant for NO_2^- uptake	0.010	mmol N/m^3
K_{den3}^{n2o}	N_2O reduction half-saturation constant for N_2O uptake	0.159	mmol N/m^3
$K_{ax}^{nh_4}$	NH_4^+ oxidation half-saturation constant for NH_4^+ uptake	0.230	mmol N/m^3
K_{ax}^{no2}	NH_4^+ oxidation half-saturation constant for NO_2^- uptake	0.100	mmol N/m^3
a	O_2-dependent coefficient (Nevison et al., 2003)	0.300	N/A
b	Background coefficient (Nevison et al., 2003)	0.100	N/A
K_{den1}^{o2}	O_2 poisoning constant for NO_3^- reduction	6.000	mmol O_2/m^3
K_{den2}^{o2}	O_2 poisoning constant for NO_2^- reduction	2.300	mmol O_2/m^3
K_{den3}^{o2}	O_2 poisoning constant for N_2O reduction	0.506	mmol O_2/m^3
K_{ax}^{o2}	O_2 poisoning constant for anammox	6.000	mmol O_2/m^3
τ^{DON}	Semi-labile DON remineralization inverse timescale	1.826E-4	1/s
τ^{DONr}	Refractory DON remineralization inverse timescale	2.884E-7	1/s
Q^{DONr}	Fraction of DON to refractory pool	0.0115	N/A
PAR_{lim}^{ao}	PAR limitation for NH_4^+ oxidation	1.000	W/m^2
PAR_{lim}^{no}	PAR limitation for NO_2^- oxidation	1.000	W/m^2

Table B.5: Nitrogen cycle tracers

Name	Description	Units
DON	Dissolved organic nitrogen	mmol N/m^3
DONr	Refractory dissolved organic nitrogen	mmol N/m^3
NH_4^+	Ammonium	mmol N/m^3
NO_2^-	Nitrite	mmol N/m^3
NO_3^-	Nitrate	mmol N/m^3
N_2O	Nitrous oxide	mmol N/m^3
N_2O_{den}	Nitrous oxide sourced from denitrification	mmol N/m^3
N_2O_{nit}	Nitrous oxide sourced from nitrification	mmol N/m^3
N_2O_{bry}	Nitrous oxide sourced from boundaries	mmol N/m^3
N_2	Dinitrogen	mmol N/m^3

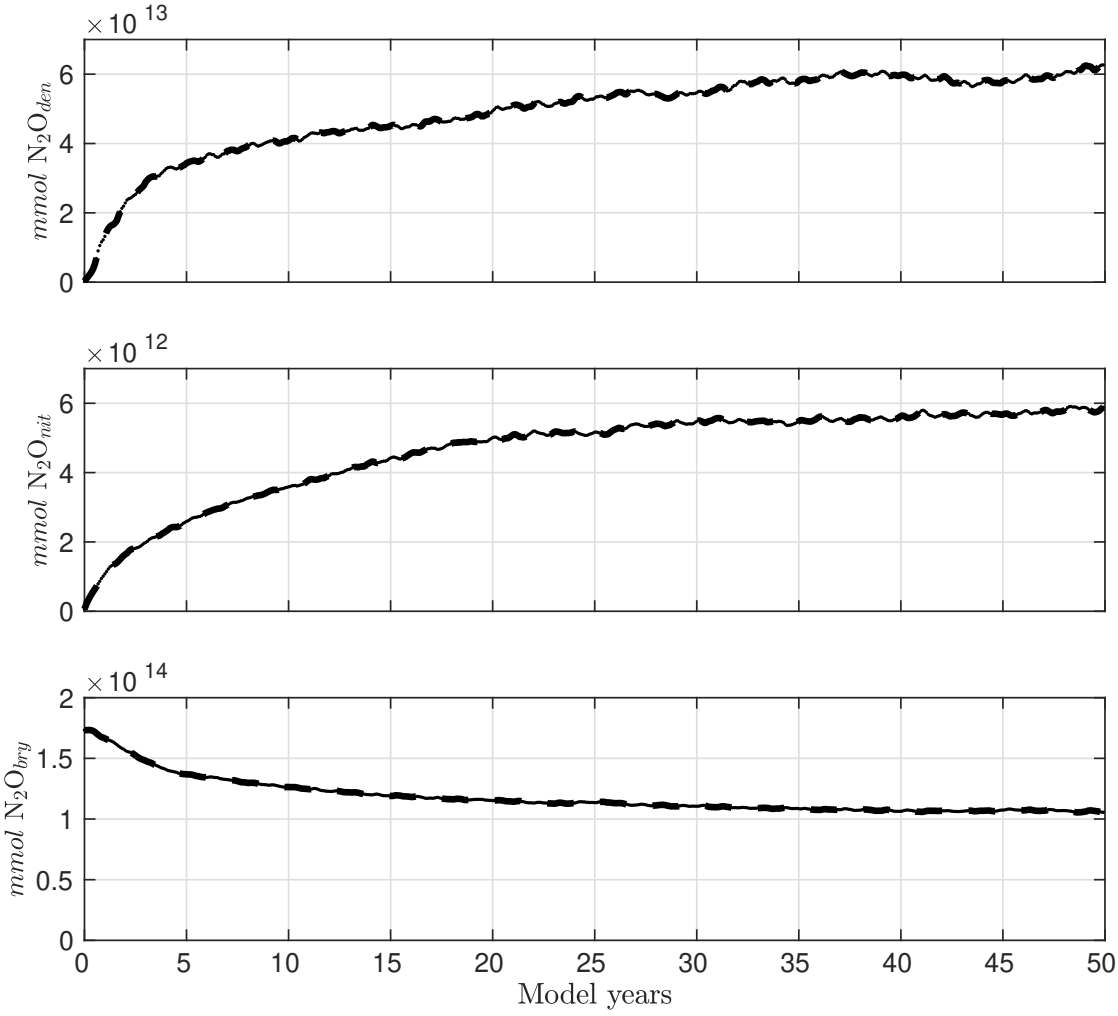

Figure B.1: Integrated N_2O_{nit}, N_2O_{den}, and N_2O_{bry} tracers within the OMZ budget domain for model years 0 - 50.

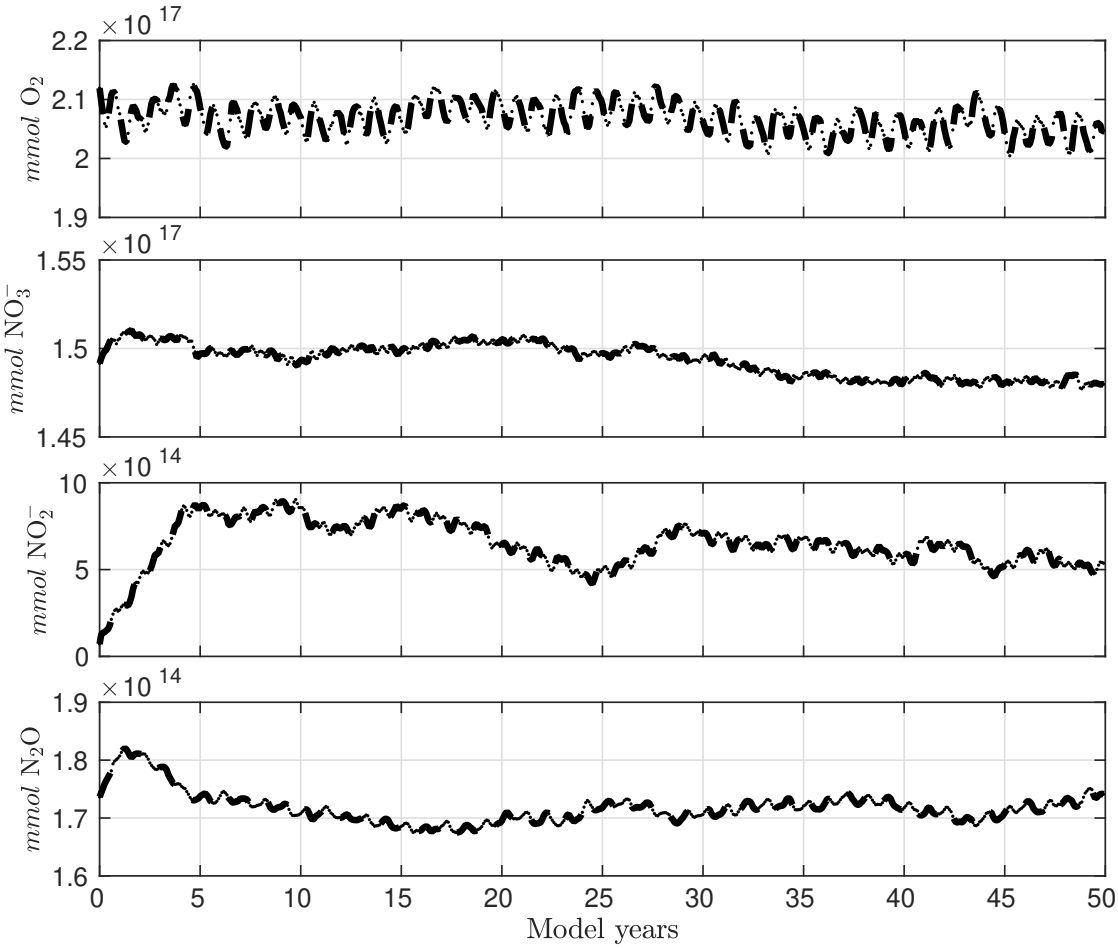

Figure B.2: Integrated O_2, NO_3^-, NO_2^-, and N_2O tracers within the OMZ budget domain for model years 0 - 50.

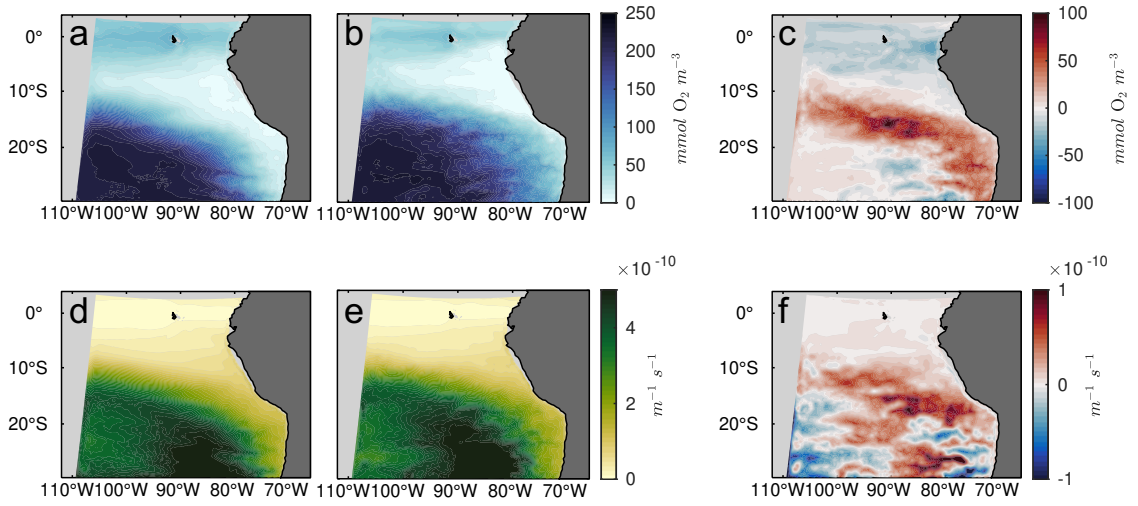

Figure B.3: Annually averaged O_2 at 300 m from model year 1 (a), model year 10 (b), and (c) the difference (year 10 - year 1). (d-f) Same as in (a-c), but for potential vorticity.

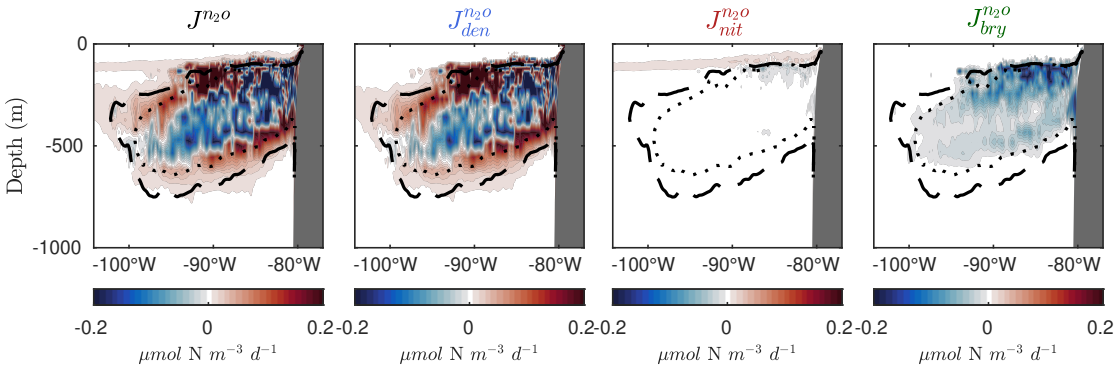

Figure B.4: Averaged net biogeochemical sources-minus-sinks (J) for N_2O (a) and each of the decomposed N_2O tracers (b-e) from model years 41 - 50 along a transect from the coast at 8^oS. The dotted and dashed black curves in highlight the 5 and 10 $mmol$ O_2 m^{-3} contours, respectively.

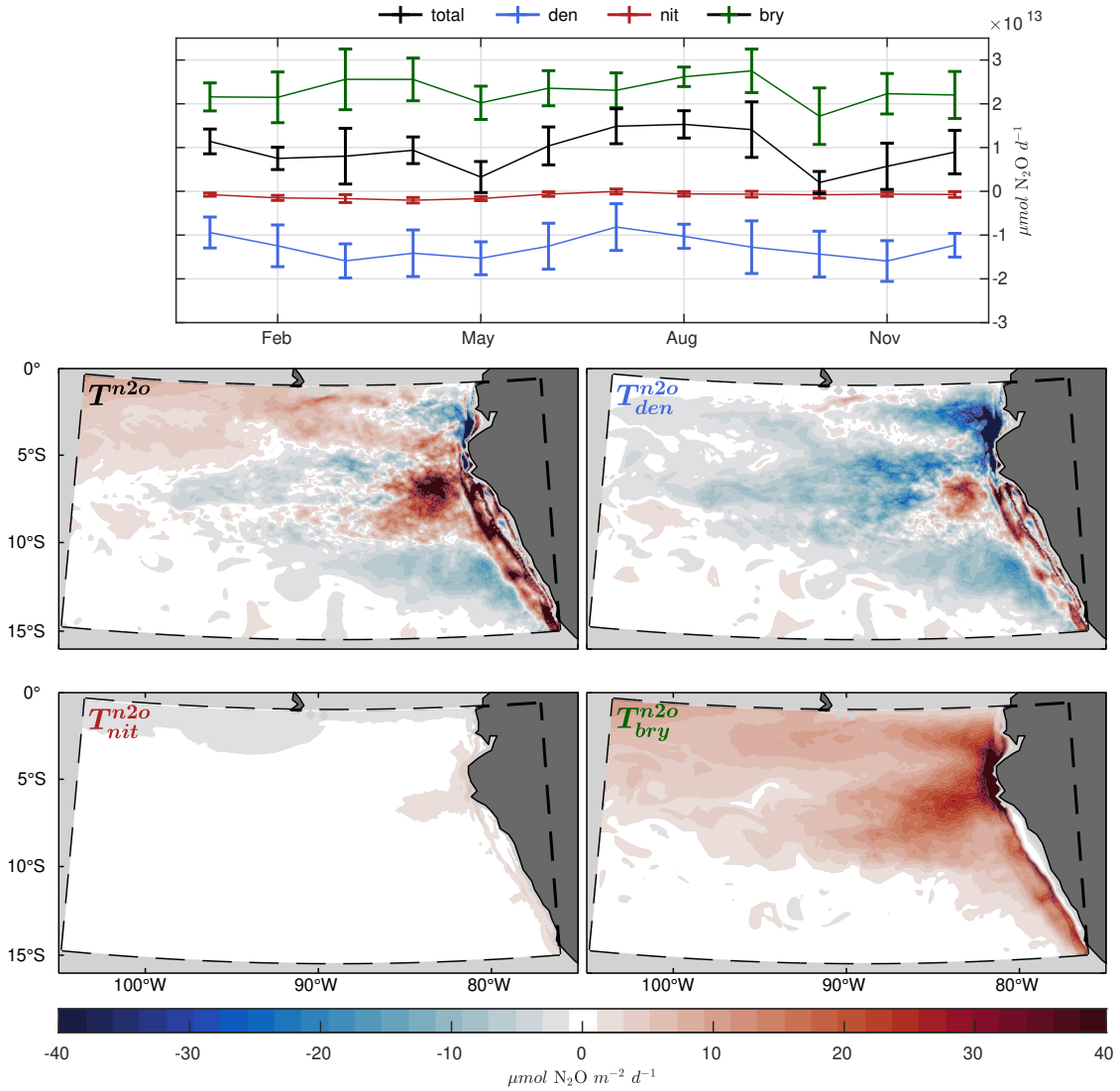

Figure B.5: (top) Time-series of integrated divergence of advective and diffusive fluxes (T terms) for N_2O (black) and each of the decomposed N_2O tracers. Error bars show monthly average and standard deviation from model years 41 - 50. (bottom panels) Vertically integrated divergence of advective and diffusive fluxes for total N_2O and the decomposed N_2O tracers from the OMZ budget domain, averaged from model years 41 - 50.

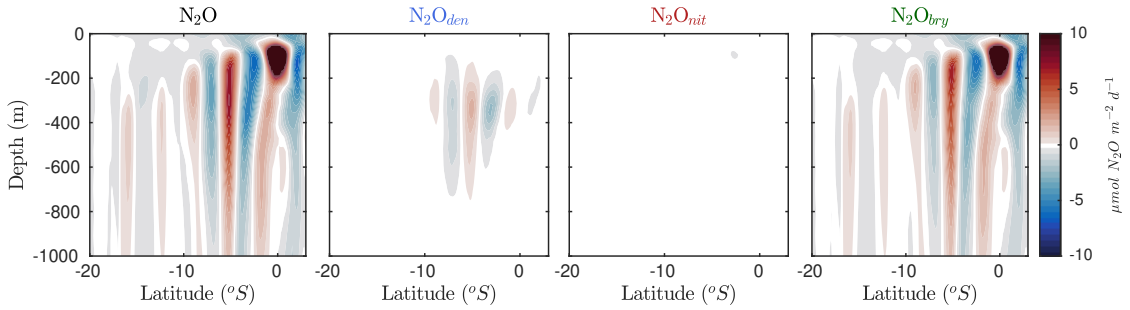

Figure B.6: Annually averaged zonal N_2O transport from the western boundary of the OMZ budget domain (roughly 105^oW) from model years 41 - 50 for (a) N_2O, (b) N_2O_{den}, (c) N_2O_{nit}, (d) N_2O_{bry}.

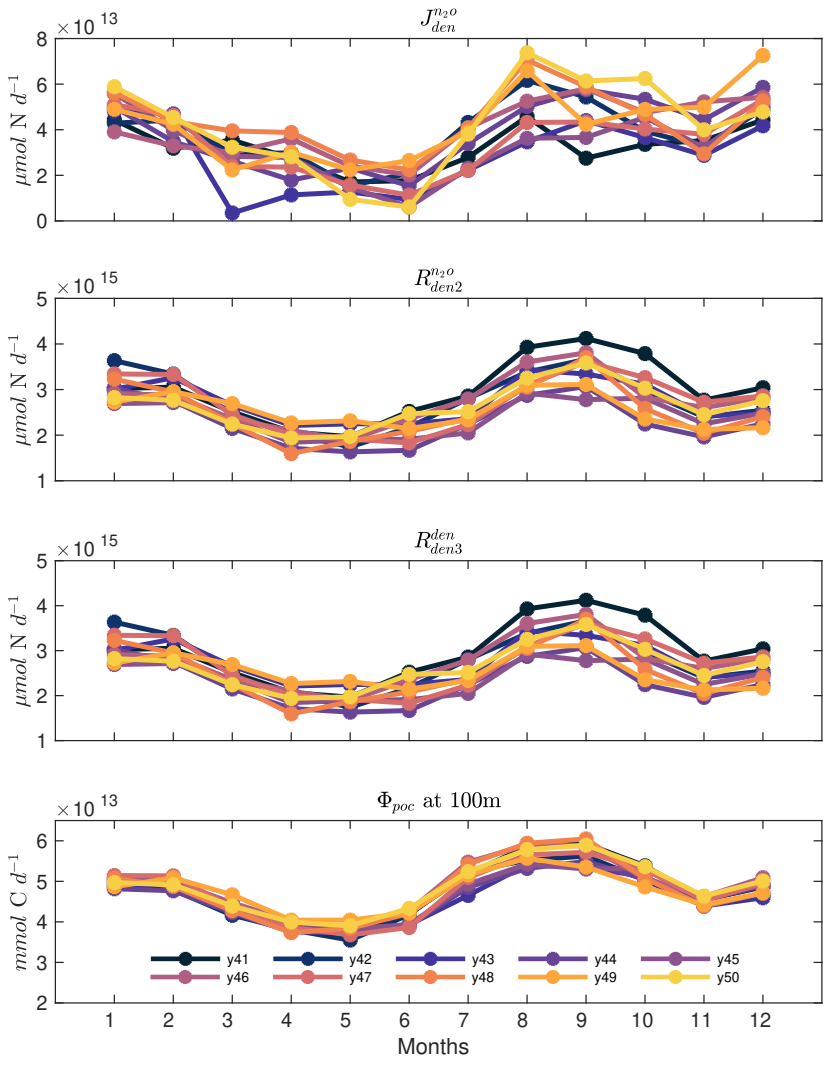

Figure B.7: Integrated net N_2O production rate from denitrification ($J^{n_2o}_{den}$), integrated NO_2^- reduction rate ($R^{n_2o}_{den2}$), integrated N_2O reduction rate of denitrification-sourced N_2O (R^{den3}_{den}), and vertical POC flux (Φ_{poc}) at 100m from the OMZ budget domain for ROMS model years 41 - 50.

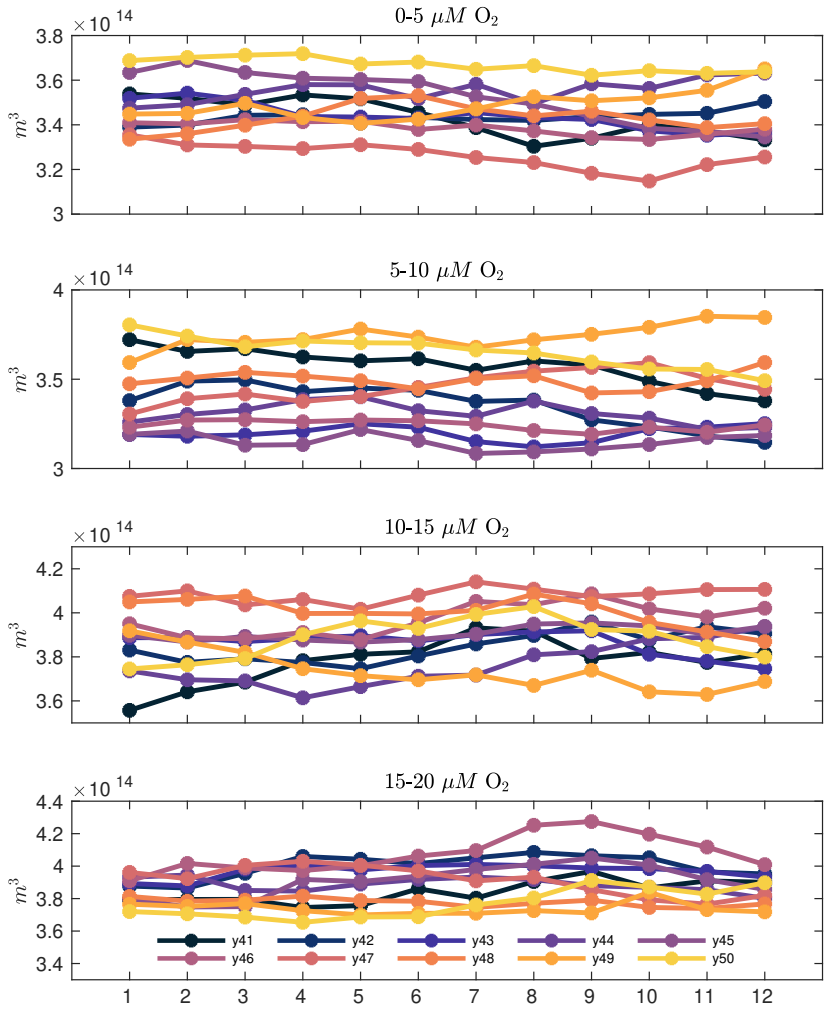

Figure B.8: Volume of the OMZ budget domain occupied by various O_2 thresholds (0 - 5, 5 - 10, 10 - 15, and 15 - 20 $mmol$ O_2 m^{-3}) for ROMS model years 41 - 50.

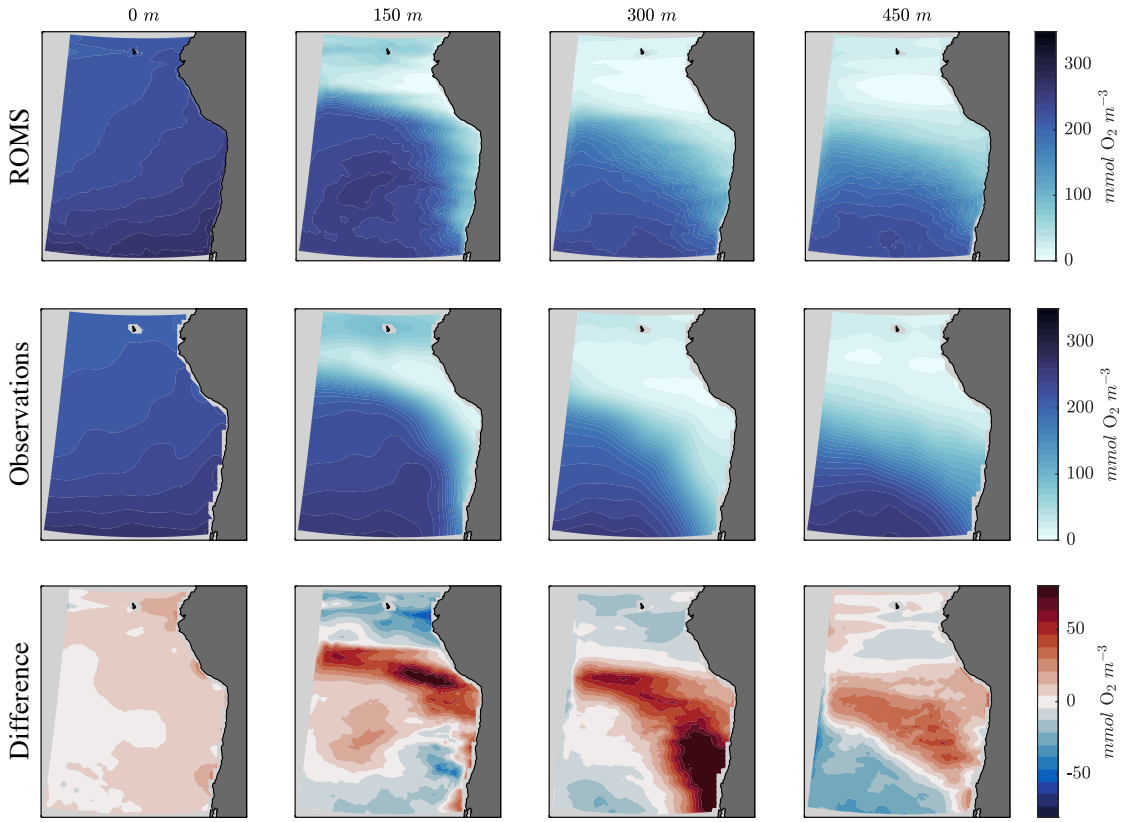

Figure B.9: 0, 150, 300, and 450 m averaged O_2 from (top) ROMS model years 41 - 50, (middle) World Ocean Atlas 2018 O_2 (H. Garcia et al., 2019), and (bottom) their differences (ROMS - WOA18).

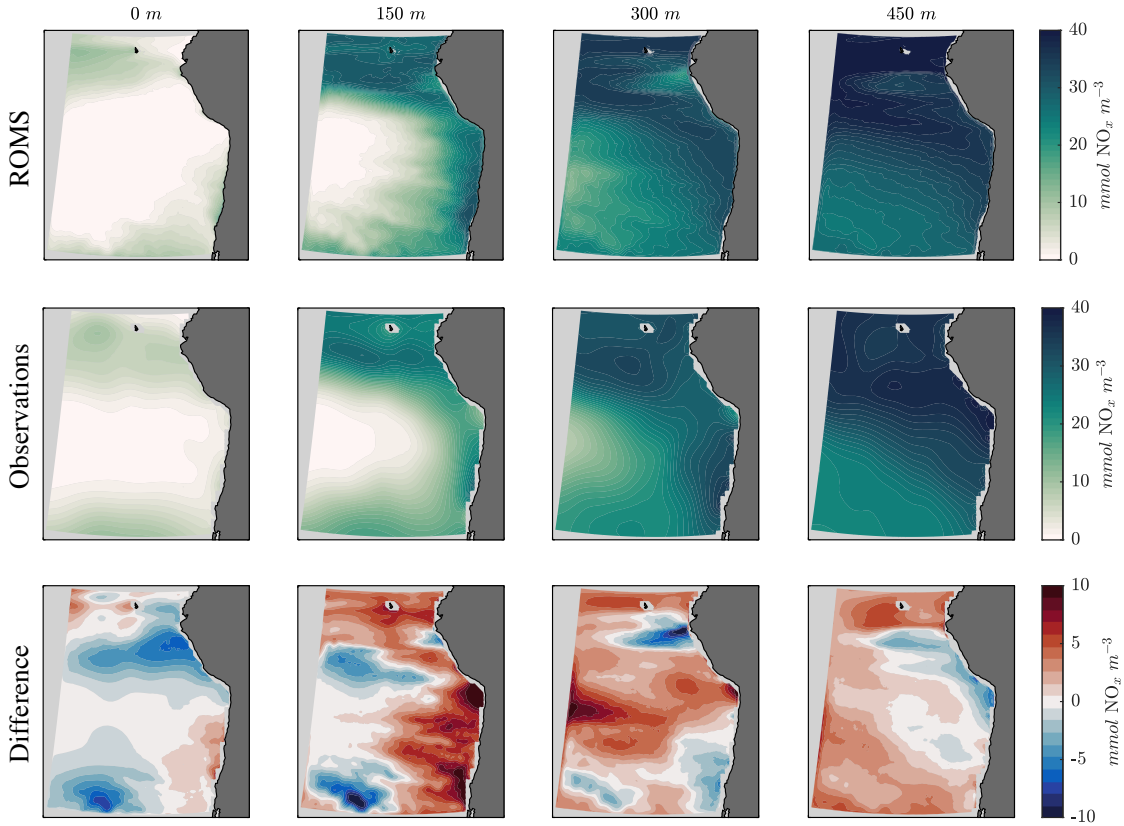

Figure B.10: Same as in Figure B.9, but for nitrate + nitrite (NO_x).

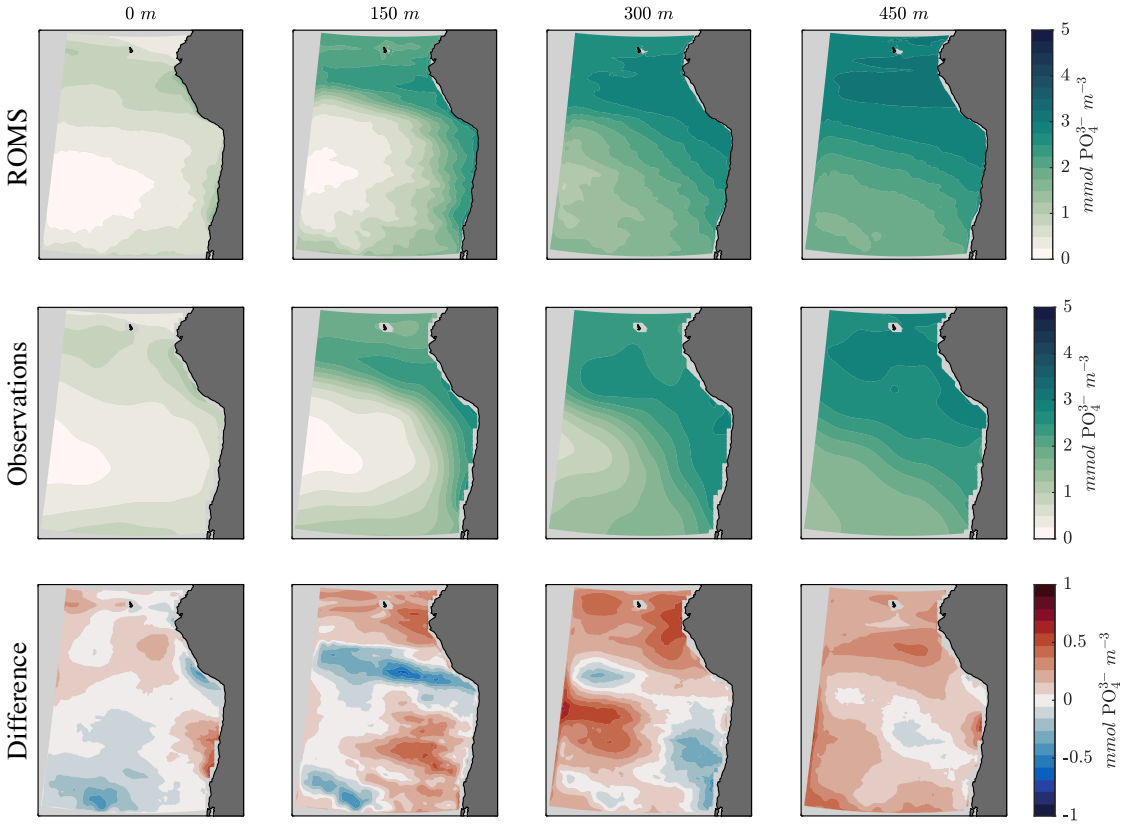

Figure B.11: Same as in Figure B.9, but for phosphate (PO_4^{3-}).

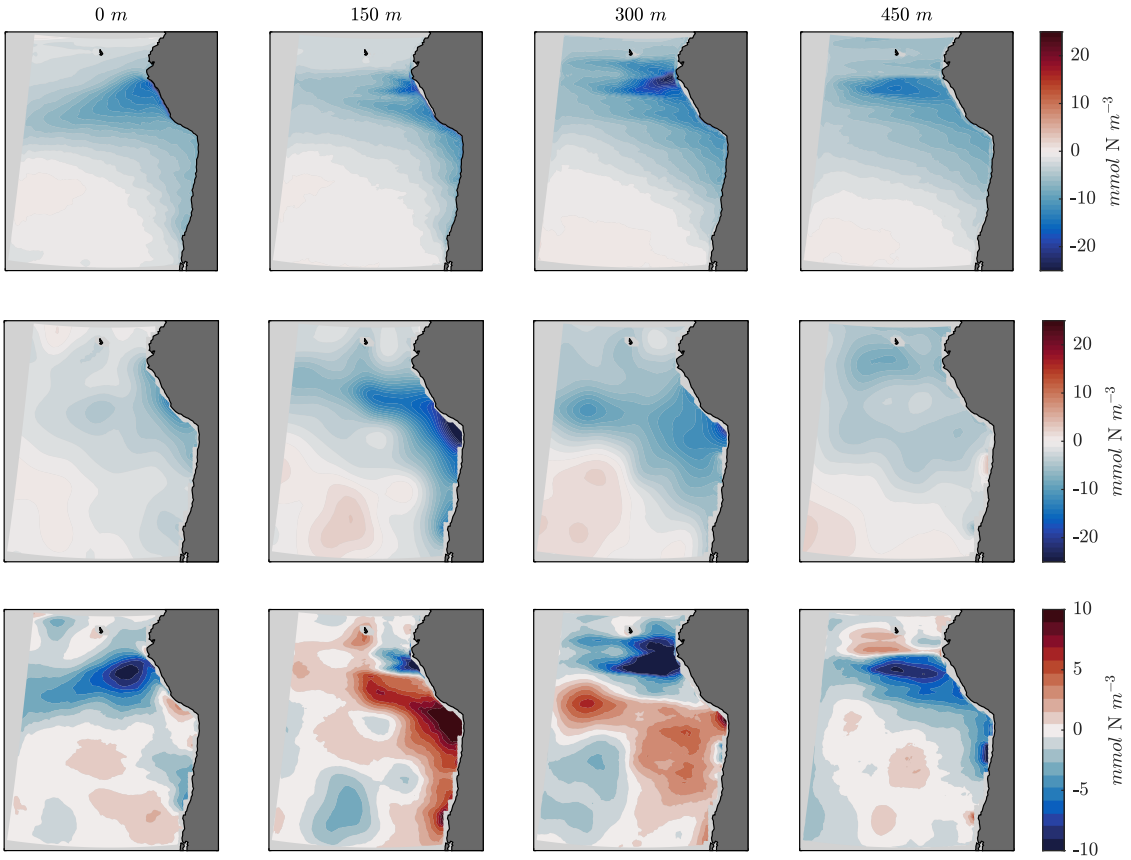

Figure B.12: Same as in Figure B.9, but for N* (here defined as 16·[NO_3^-] - [PO_4^{3-}]).

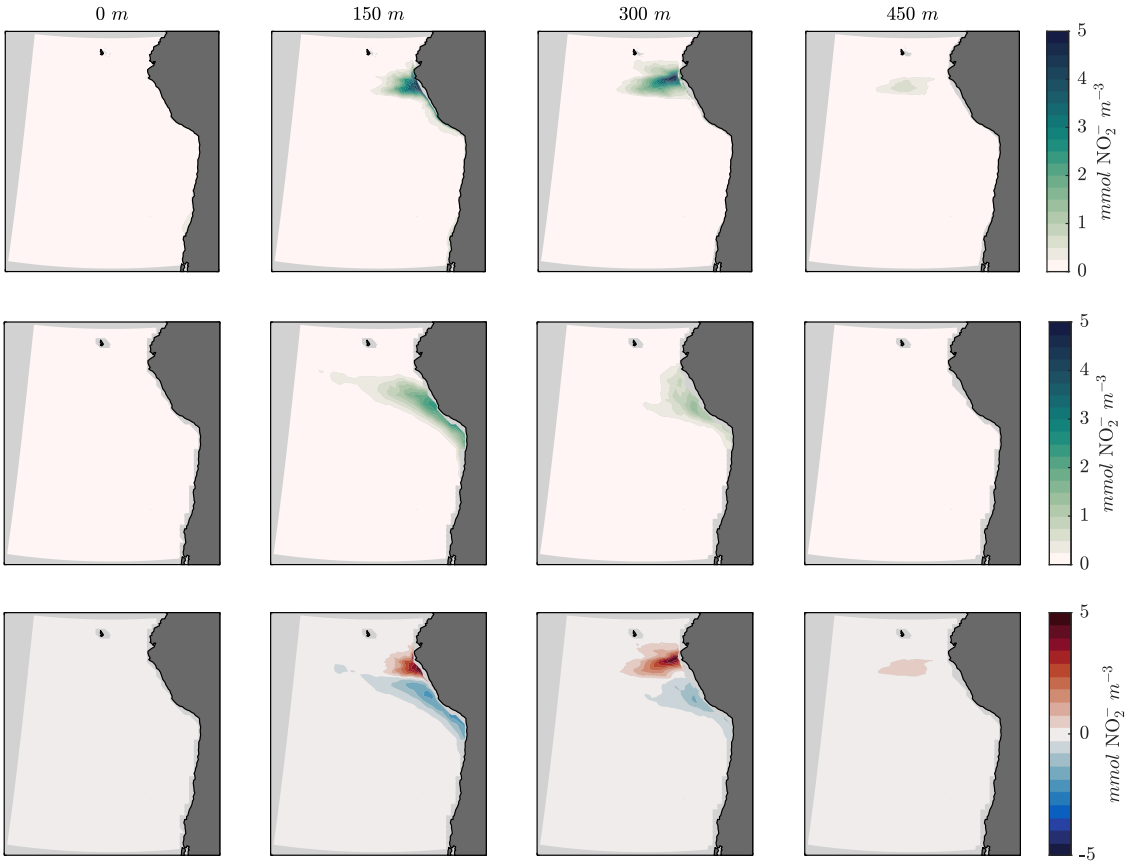

Figure B.13: Same as in Figure B.9, but for NO_2^- comparisons against machine learning estimates.

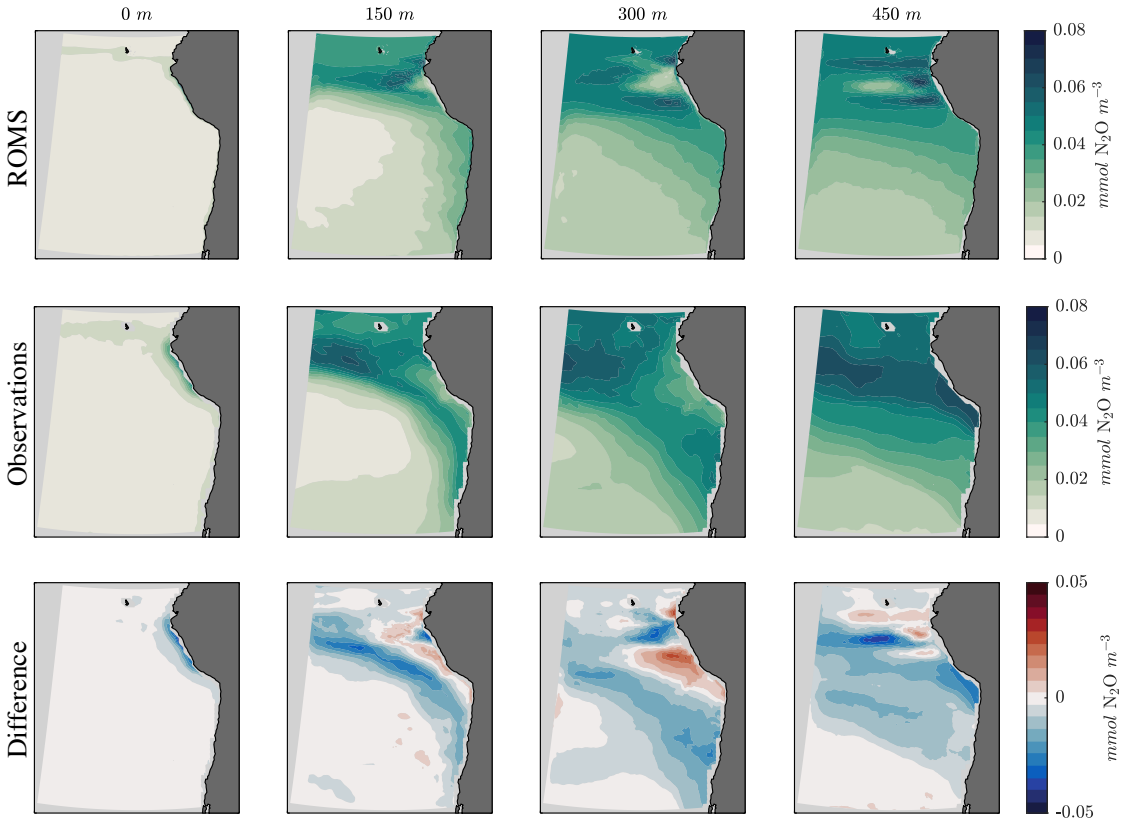

Figure B.14: Same as in Figure B.9, but for N_2O comparisons against machine learning estimates.

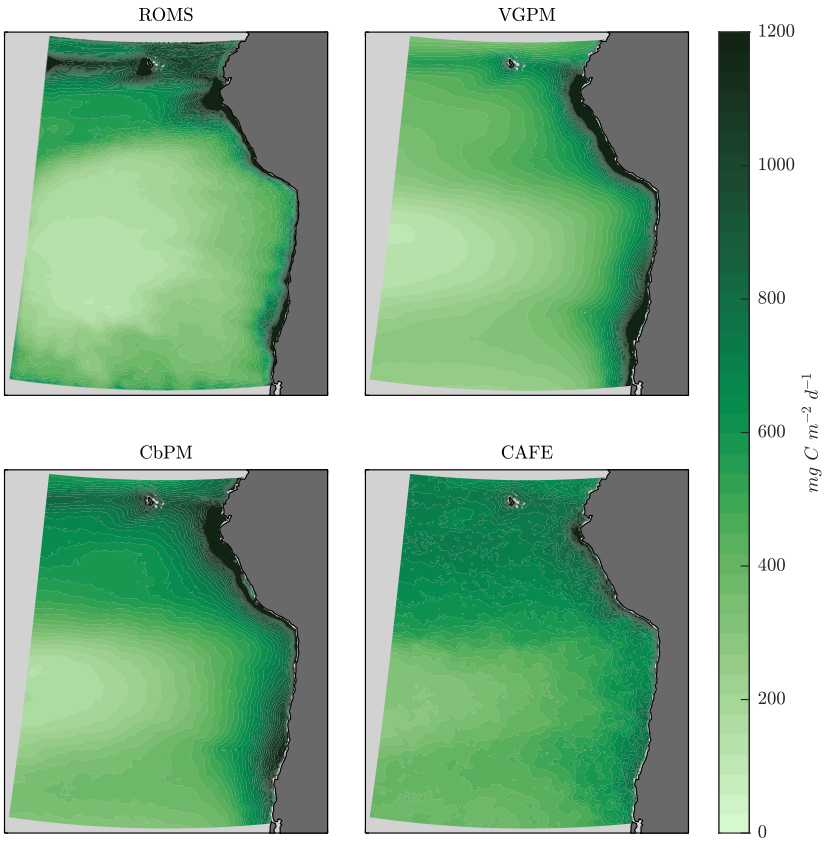

Figure B.15: Averaged net Primary Production (NPP) from (top left) ROMS model years 41 - 50, (top right) the Eppley Vertically Generalized Production Model (Eppley-VGPM, Behrenfeld & Falkowski (1997))), (bottom left) the updated Carbon-Based Productivity Model (CbPM, Behrenfeld et al. (2005)), and (bottom right) the Fluorescence Euphotic-resolving model (CAFE, Silsbe et al. (2016)).

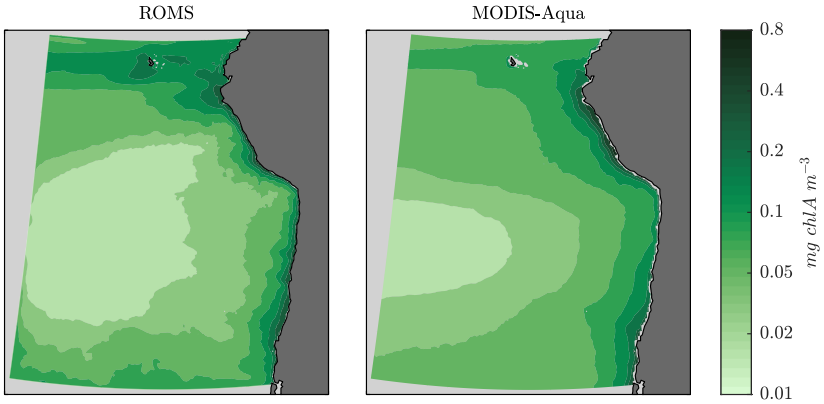

Figure B.16: Averaged surface chlorophyll-A (chlA) from (left) ROMS model years 41 - 50 and (right) MODIS-Aqua.

APPENDIX C

Supporting Information for Chapter 4

C.1 Model Configuration and Forcing

To force the model, we ignore low-frequency interannual variability and focus on climatological steady-state. Initial conditions are extracted from year 50 of the quasi steady-state 10 km resolution solution in McCoy et al. (2023). Monthly climatological boundary forcing (applied at the northern, western, and southern boundaries) for temperature, salinity, surface elevation, and horizontal velocity are taken from an existing Pacific-wide ROMS simulation (Lemarié et al., 2012). Normal-year-forcing of daily freshwater and turbulent heat fluxes are estimated using bulk formulae (Large, 2006) applied to ERA-interim (ERAi) reanalysis data for the year 1979 (Simmons et al., 2006; Dee et al., 2011). Because of known biases in ERAi, which overestimates shortwave and underestimate longwave fluxes (Brodeau et al., 2010), we applied corrections from the DRAKKAR Forcing Set version 5.2 to heat fluxes (Dussin et al., 2014). Daily climatological wind stress is taken from the QuickSCAT-based Scatterometer Climatology of Ocean Winds (Risien & Chelton, 2008).

Boundary forcing of biogeochemical nutrient concentrations (NO_3^-, PO_4^{3-}, $Si(OH)_4$ and O_2) are taken from monthly climatological observations from the 2013 World Ocean Atlas (H. E. Garcia, Boyer, et al., 2013; H. E. Garcia, Locarnini, et al., 2013). NH_4^+, NO_2^-, and N_2 boundary conditions are set to 0 but adjust rapidly within the domain. Iron data are taken from the Community Earth System Model (CESM) as in Deutsch et al. (2021), and DIC and alkalinity from GLODAP (Lauvset et al., 2016), with a reference year of 2002. Boundary forcing of N_2O were generated from a 3-D reconstruction using in situ data from the MEMENTO (Kock & Bange, 2015) database, integrated with additional cruises, using

the same machine-learning approach described in Yang et al. (2020). Air-sea gas exchange of N_2O at the surface is modeled according to Wanninkhof (1992), using a constant atmospheric mixing ratio of 300 ppb, which is taken as a typical concentration for the 20th century.

The treatment of organic matter in the model, and physical and biogeochemical validation is described further in McCoy et al. (2023). Following a 1 year spin-up period to allow the model to adjust to higher resolution, we compared averaged fields from a 10-year model run against the final tracer fields from the previously validated $10km$ resolution model described in McCoy et al. (2023), with no obvious discrepancies in biogeochemical tracer fields emerging due to the switch to higher horizontal resolution.

C.2 NitrOMZ

The NitrOMZ model explicitly resolves the main set of heterotrophic and chemolithotrophic nitrogen cycle transformations associated with the remineralization of sinking organic matter in low O_2 environments (summarized in Figure 4.1c). The model assumes a "modular" N cycle, where individual reaction steps (e.g., individual redox reactions) are represented separately and are connected by exchange of dissolved substrates (Graf et al., 2014; Kuypers et al., 2018).

Heterotrophic reactions in NitrOMZ include aerobic remineralization (R_{rem}) and additional denitrification steps under low-O_2 conditions (Bianchi et al., 2022): NO_3^- reduction (R_{den1}, pathway 4 in Figure 4.1c), NO_2^- reduction (R_{den2}, pathway 5), and N_2O reduction (R_{den3}, pathway 6). In order to preserve the ROMS-BEC organic matter cycle, total remineralization (R_{rem}^{tot}, in units of mmol C m^{-3} s^{-1}, pathway 1 in Figure 4.1c) is partitioned into the four possible components at each vertical level and time-step:

$$R_{rem}^{tot} = \sum_{n=1}^{4} R_i, \tag{C.1}$$

where i represents one of the four respiration pathways (R_{rem}, R_{den1}, R_{den2}, R_{den3}). We calculate the rate-specific contribution to total remineralization by each pathway i as:

$$R_i = f_i \cdot R_{rem}^{tot}, \tag{C.2}$$

where f_i is the relative fraction of remineralization carried out by the process i. The individual depth-dependent fractions are calculated as:

$$f_i = \frac{r_i}{\sum_{n=1}^{4} r_i}, \tag{C.3}$$

where r_i is the specific heterotrophic respiration rate of the reaction:

$$r_i = k_i \cdot \frac{[\mathrm{X}]}{K_i^X + [\mathrm{X}]} \cdot e^{-\frac{\mathrm{O}_2}{K_i^{o2}}}. \tag{C.4}$$

Here, k_i is the maximum rate, K_i^{X} is the half-saturation constant for oxidant [X] (O_2, NO_3^-, NO_2^-, and N_2O for R_{rem}, R_{den1}, R_{den2}, and R_{den3}, respectively) following Michaelis-Menten kinetics (K. A. Johnson & Goody, 2011), and K_i^{o2} is the scale for inhibition by oxygen (ignored for R_{rem}). Each denitrification rate (and anammox, see below) in NitrOMZ is calculated using a step-specific O_2 inhibition term following equation (C.4). Similar to Dalsgaard et al. (2014), Babbin et al. (2015), and Ji et al. (2018), we model a progressive O_2 inhibition of the three denitrification steps ($K_{den1}^{o2} > K_{den2}^{o2} > K_{den3}^{o2}$). As a consequence, complete denitrification to N_2 via N_2O reduction (R_{den3}, pathway 6 in Figure 4.1c) occurs in anoxic waters as each step proceeds unimpeded. However, at low but non-zero O_2, the decoupling of steps allows for N_2O accumulation from incomplete denitrification (i.e. production via R_{den2} > consumption via R_{den3}).

The stoichiometry of each reaction follows the procedure outlined in Paulmier et al. (2009), under the assumption that the composition of organic matter (POC) follows the average oceanic ratios from Anderson & Sarmiento (1994). As a result, the nitrogen to carbon ($Q_{rem}^{N:C}$) and oxygen to carbon ($Q_{rem}^{O:C}$) ratios for aerobic remineralization (R_{rem}) are 16/106 and -472/424 (respectively) whereas the nitrogen to carbon ratio for each denitrification rate ($Q_{den}^{N:C}$) is 472/212 following Anderson & Sarmiento (1994) and Paulmier et al. (2009). Converting denitrification rates from units of mmol C m^{-3} s^{-1} to units of mmol N m^{-3} s^{-1} is therefore represented as:

$$R_{den1}^{no2} = Q_{den}^{N:C} \cdot R_{den1}, \tag{C.5}$$

$$R_{den2}^{n2o} = Q_{den}^{N:C} \cdot R_{den2}, \tag{C.6}$$

$$R_{den3}^{n2} = Q_{den}^{N:C} \cdot R_{den3}. \tag{C.7}$$

Chemolithotrophic reactions in NitrOMZ include NH_4^+ oxidation to both NO_2^- and N_2O (R_{ao}, used interchangeably with NH_3 oxidation, pathway 2 in Figure 4.1c), NO_2^- oxidation to NO_3^- (R_{no}^{no3}, pathway 3), and anaerobic NH_4^+ oxidation with NO_2^- to produce N_2 (anammox, R_{ax}^{n2}, pathway 7). Each rate is based on Michaelis-Menten functions for both the oxidants (O_2, O_2, and NO_2^- for R_{ao}, R_{no}^{no3}, and R_{ax}^{n2}, respectively) and reductants (NH_4^+, NO_2^-, and NH_4^+, respectively), resulting in the general form:

$$R_i = k_i \cdot \frac{[\mathrm{X}]}{K_i^X + [\mathrm{X}]} \cdot \frac{[\mathrm{Y}]}{K_i^Y + [\mathrm{Y}]} \cdot e^{-\frac{\mathrm{O_2}}{K_i^{o2}}}, \tag{C.8}$$

where K_i^Y represents the half-saturation constant for reductant [Y]. Inhibition by oxygen is ignored for both R_{ao} and R_{no}^{no3}, however both are inhibited by PAR as outlined in McCoy et al. (2023). The oxygen to nitrogen ratios for R_{ao} ($Q_{ao}^{O:N}$, 3/2) and R_{no}^{no3} ($Q_{no}^{O:N}$, 1/2) are based on the stoichiometry of the relevant redox reactions. For anammox, NH_4^+ and NO_2^- are combined in 1:1 ratios to produce N_2.

Chemolithotrophic production of N_2O in NitrOMZ is modelled as a by-product of NH_4^+ oxidation (R_{ao}) and is based on the observed relationship between N_2O excess and apparent oxygen utilization, which was consistent with N_2O yields from cultured AOB (Goreau et al., 1980). It implicitly represents a shift in N_2O production as a byproduct of hydroxylamine oxidation at high O_2 to nitrifier-denitrification at low O_2 (Wrage et al., 2001; Stein & Yung, 2003). The partitioning between N_2O and NO_2^- production from R_{ao} is calculated using the function proposed by Nevison et al. (2003):

$$\frac{Y_{ao}^{n2o}}{Y_{ao}^{no2}} = 0.01 \cdot (\frac{a}{[\mathrm{O_2}]} + b). \tag{C.9}$$

N_2O production from NH_4^+ oxidation (R_{ao}^{n2o}, pathway 2b in Figure 4.1c), in units of mmol N_2O m^{-3} s^{-1}, is therefore represented as:

$$R_{ao}^{n2o} = R_{ao} \cdot Y_{ao}^{n2o}, \tag{C.10}$$

with a similar function for NO_2^- production (R_{ao}^{no2}, pathway 2a in Figure 4.1c), but with the product in units of mmol N m^{-3} s^{-1}.

Table C.1: Nitrogen cycle parameters

Name	Description	Value	Units
k_{rem}	Maximum respiration rate	9.259E-7	mmol C/m^3/s
k_{ao}	Maximum NH_4^+ oxidation rate	5.787E-7	mmol N/m^3/s
k_{no}	Maximum NO_2^- oxidation rate	5.787E-7	mmol N/m^3/s
k_{den1}	Maximum NO_3^- reduction rate	1.852E-7	mmol C/m^3/s
k_{den2}	Maximum NO_2^- reduction rate	9.259E-8	mmol C/m^3/s
k_{den3}	Maximum N_2O reduction rate	5.741E-7	mmol C/m^3/s
k_{ax}	Maximum anaerobic NH_4^+ oxidation rate	5.105E-6	mmol N/m^3/s
K_{rem}^{o2}	Respiration half-saturation constant for O_2 uptake	1.000	mmol O_2/m^3
K_{ao}^{o2}	NH_4^+ oxidation half-saturation constant for O_2 uptake	0.333	mmol N/m^3
$K_{ao}^{nh_4}$	NH_4^+ oxidation half-saturation constant for NH_4^+ uptake	0.305	mmol N/m^3
K_{no}^{o2}	NO_2^- oxidation half-saturation constant for O_2 uptake	0.778	mmol N/m^3
$K_{no}^{no_2}$	NO_2^- oxidation half-saturation constant for NO_2^- uptake	0.509	mmol N/m^3
$K_{den1}^{no_3}$	NO_3^- reduction half-saturation constant for NO_3^- uptake	1.000	mmol N/m^3
$K_{den2}^{no_2}$	NO_2^- reduction half-saturation constant for NO_2^- uptake	0.010	mmol N/m^3
$K_{den3}^{n_2o}$	N_2O reduction half-saturation constant for N_2O uptake	0.159	mmol N/m^3
$K_{ax}^{nh_4}$	NH_4^+ oxidation half-saturation constant for NH_4^+ uptake	0.230	mmol N/m^3
$K_{ax}^{no_2}$	NH_4^+ oxidation half-saturation constant for NO_2^- uptake	0.100	mmol N/m^3
a	O_2-dependent coefficient (Nevison et al., 2003)	0.300	N/A
b	Background coefficient (Nevison et al., 2003)	0.100	N/A
K_{den1}^{o2}	O_2 poisoning constant for NO_3^- reduction	6.000	mmol O_2/m^3
K_{den2}^{o2}	O_2 poisoning constant for NO_2^- reduction	2.300	mmol O_2/m^3
K_{den3}^{o2}	O_2 poisoning constant for N_2O reduction	0.506	mmol O_2/m^3
K_{ax}^{o2}	O_2 poisoning constant for anammox	6.000	mmol O_2/m^3

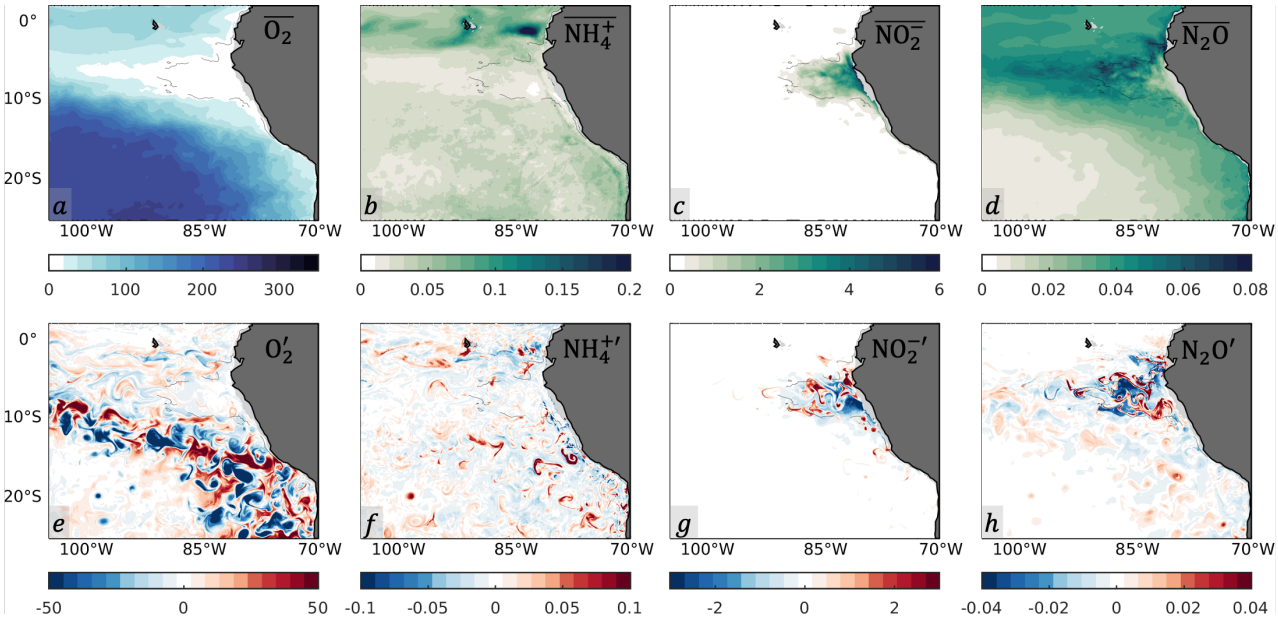

Figure C.1: (top) January climatological mean O_2, NH_4^+, NO_2^-, and N_2O at 150m. (bottom) Same as in the top panels, but for eddy concentrations from day 15 of model year 4. Units are in mmol m^{-3}.

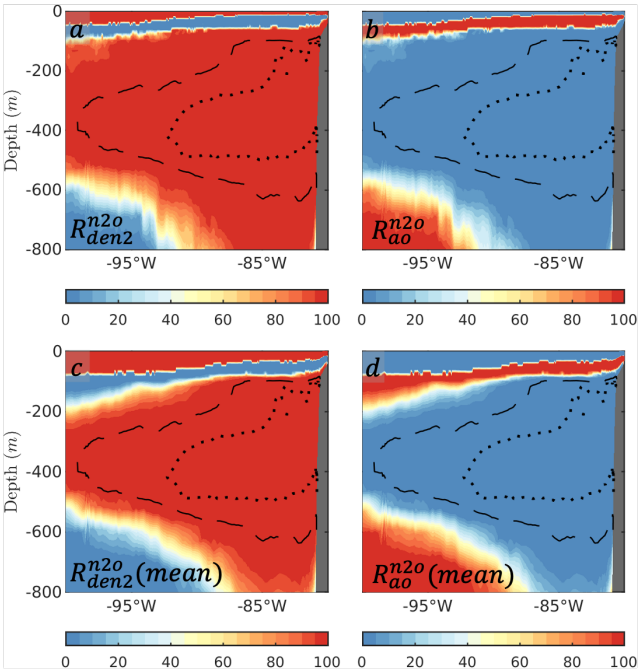

Figure C.2: Transects at approximately -8^{o}S showing the fraction of total averaged N_2O production from (a) NO_2^- reduction and (b) NH_4^+ oxidation. (c,d) Same as in (a,b), but for the fractional contribution to mean N_2O production from mean reactions. Units are in percent (%).

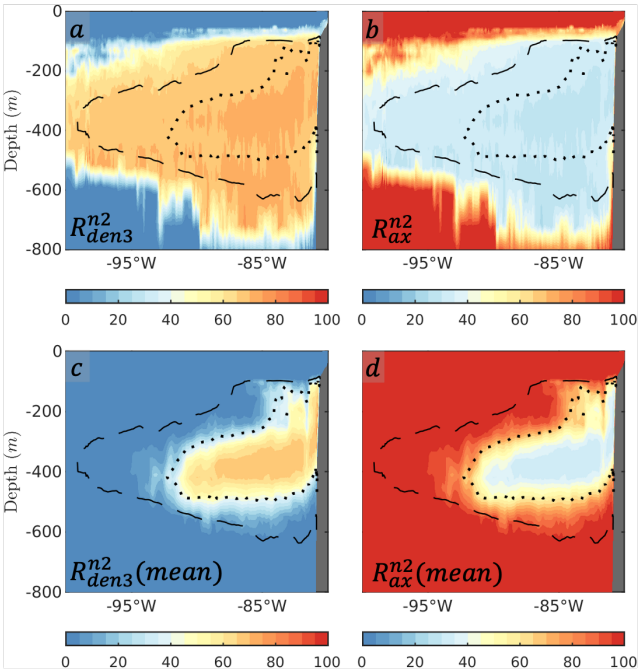

Figure C.3: Transects at approximately -8^{o}S showing the fraction of total averaged N_2 production from (a) N_2O reduction and (b) anammox. (c,d) Same as in (a,b), but for the fractional contribution to mean N_2 production from mean reactions. Units are in percent (%).

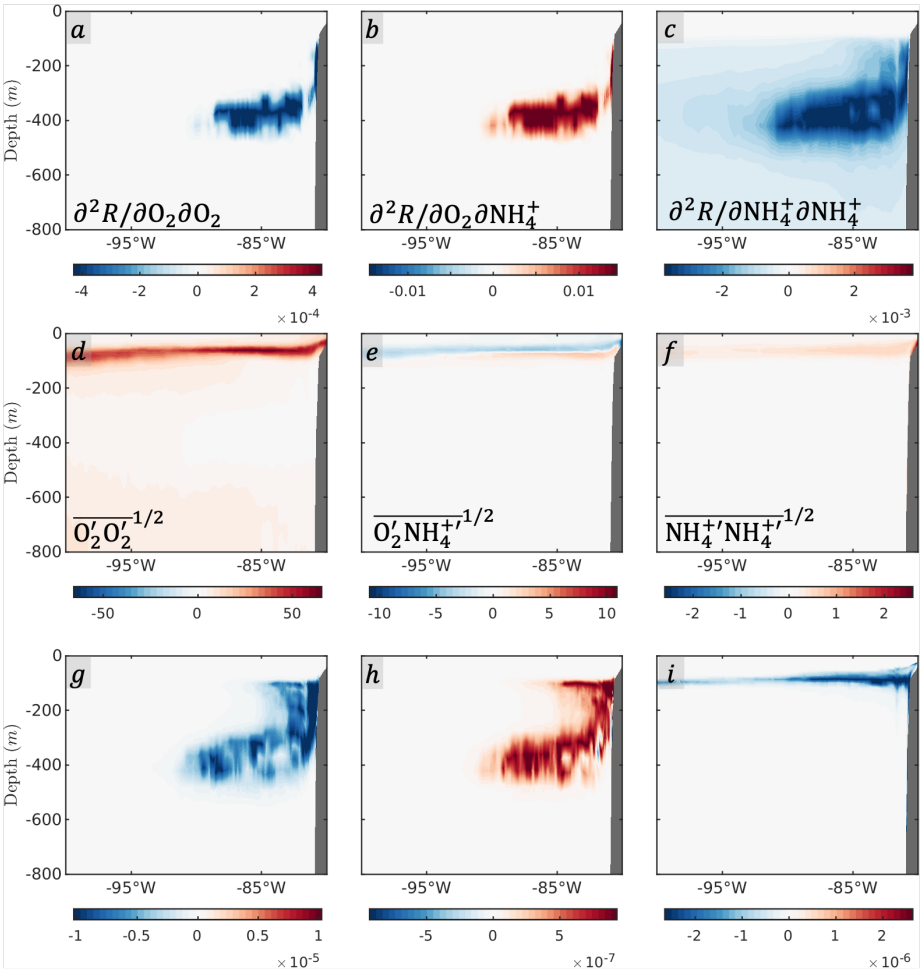

Figure C.4: Transects at approximately -8°S showing (a-c) the curvature of functional dependencies for mean N_2O production from NH_4^+ oxidation (R_{ao}^{n2o}), (d-f) the square root of the associated eddy tracer correlation terms, and (g-i) their products (multiplied by 0.5 following equation (7)), in units of mmol N m^{-3} d^{-1}. The dotted and dashed black curves outline the 1 and 5 mmol O_2 m^{-3} contours, respectively.

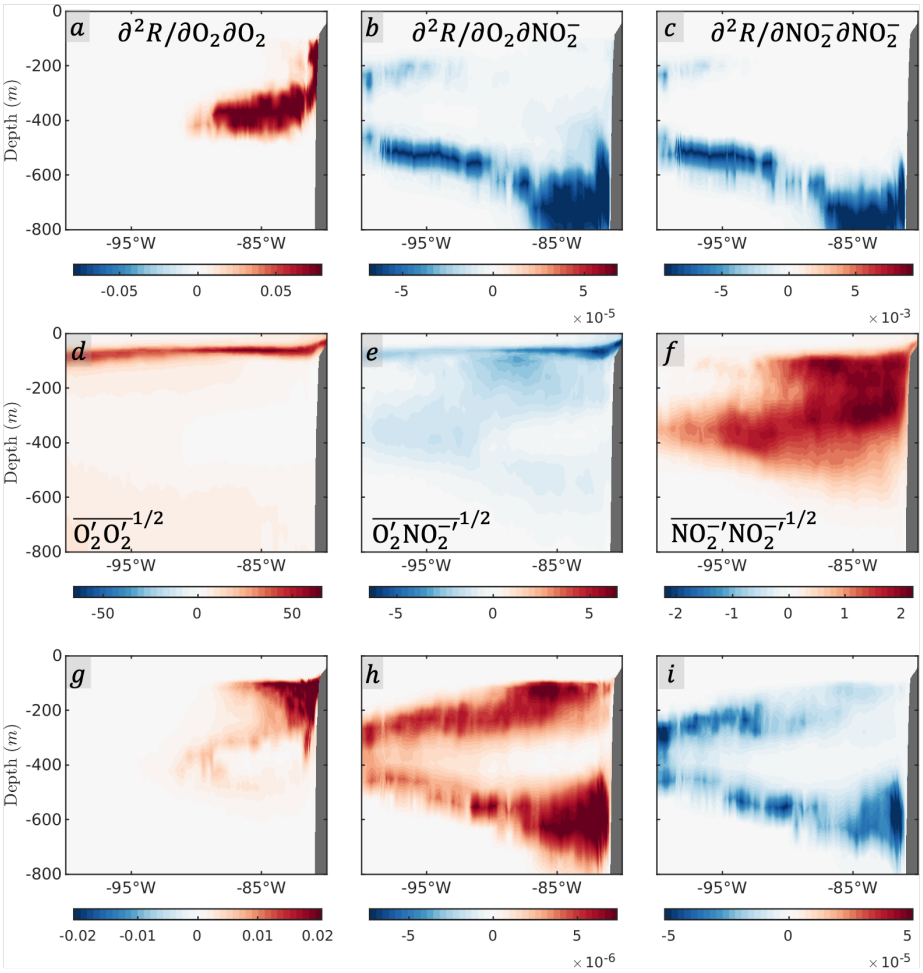

Figure C.5: Same as in Figure C.4, but for mean NO_2^- reduction (R_{den2}^{n2o}).

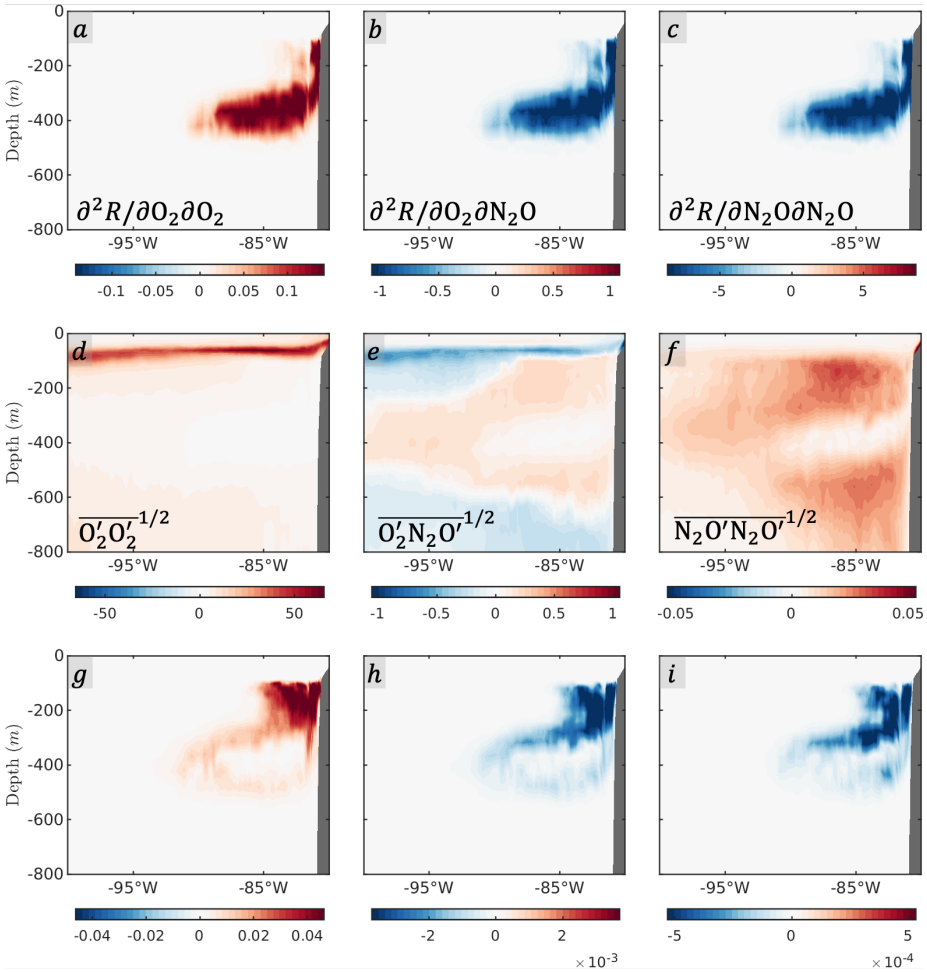

Figure C.6: Same as in Figure C.4, but for mean N_2O reduction (R^{n2}_{den3}).

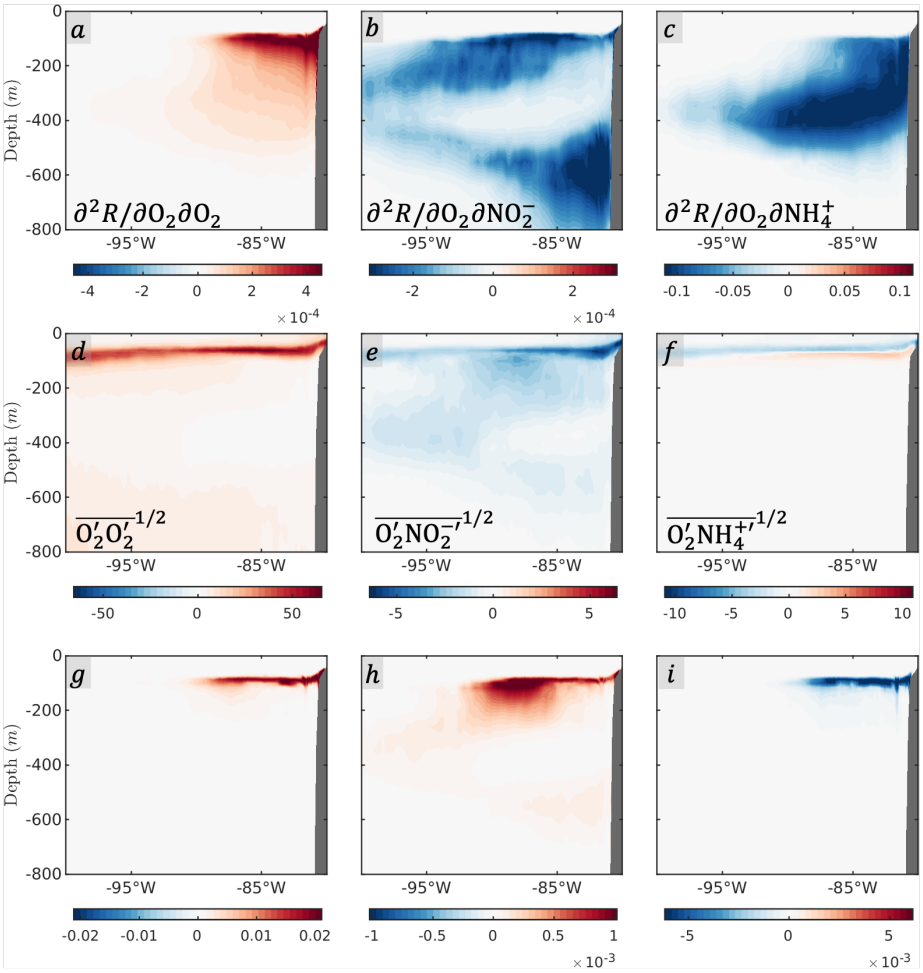

Figure C.7: Same as in Figure C.4, but for mean anammox (R_{ax}^{n2}).

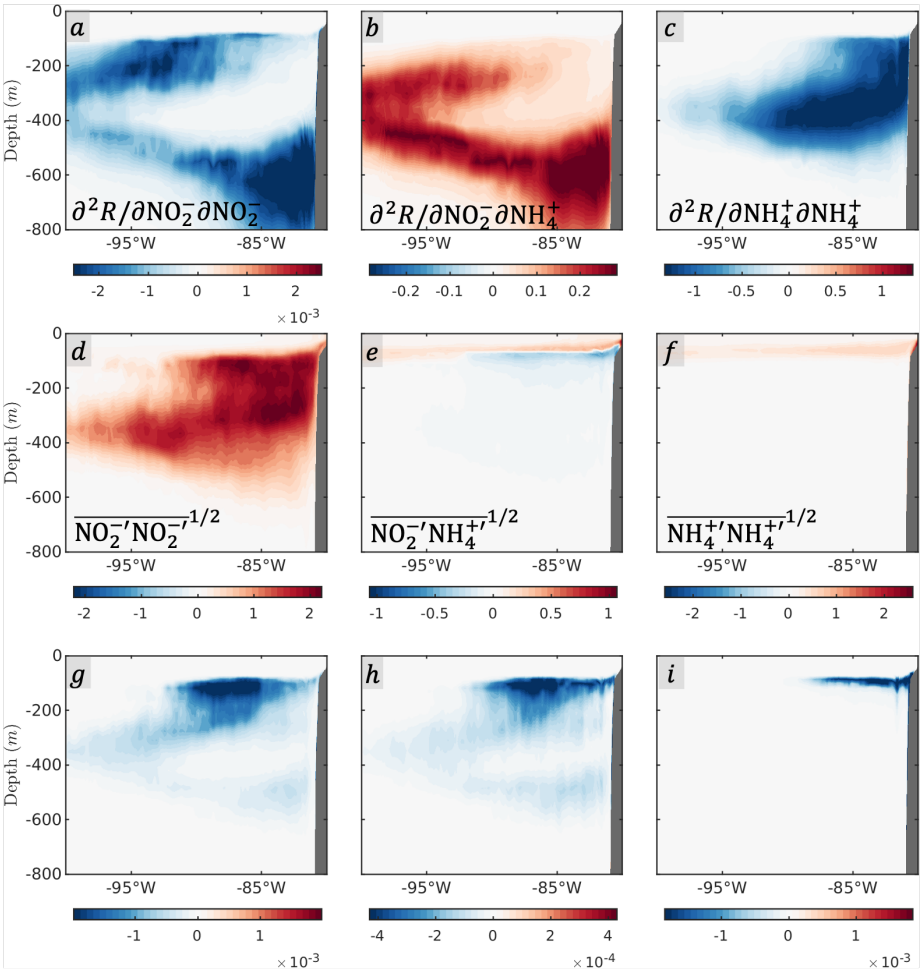

Figure C.7: (continued)

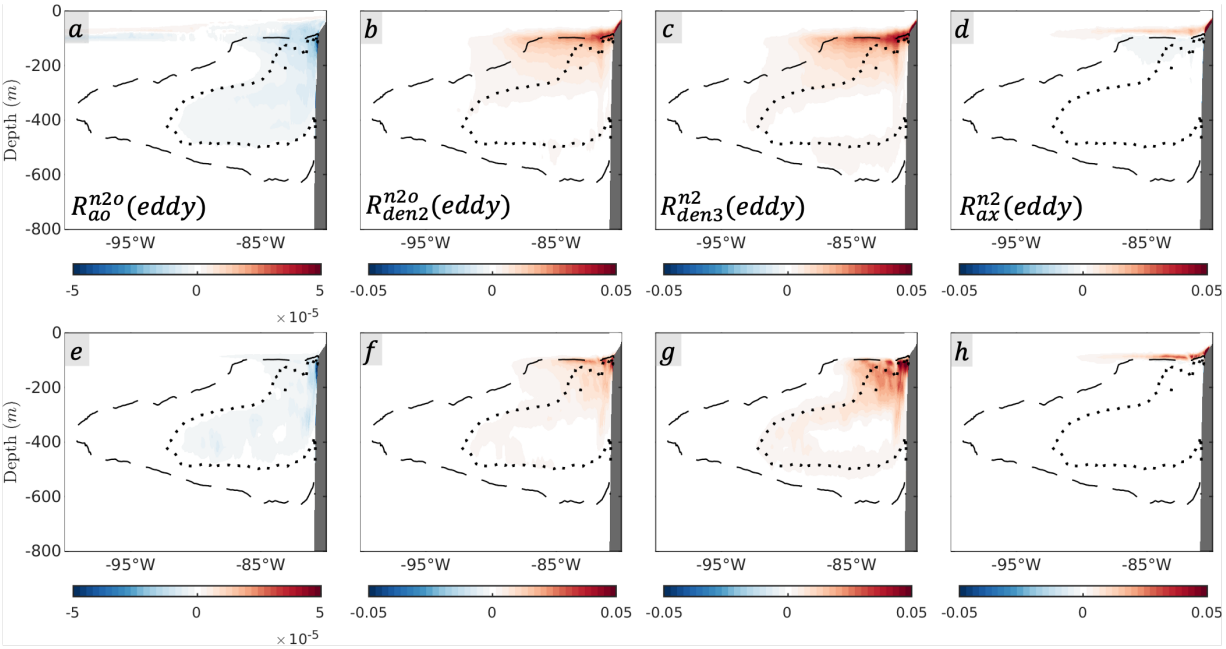

Figure C.8: Transects at approximately -8^{o}S of eddy (a) N_2O production from NH_4^+ oxidation (R^{n2o}_{ao}), (b) NO_2^- reduction to N_2O (R^{n2o}_{den2}), (c) N_2O reduction to N_2 (R^{n2}_{den3}), and (d) anammox (R^{n2}_{ax}) from model years 2 - 11. (e - h) Same as in (a - d), but for the approximate eddy reactions following the Taylor series expansion in equation (7). Units are in mmol N m^{-3} d^{-1}. The dotted and dashed black curves outline the 1 and 5 mmol O_2 m^{-3} contours, respectively.

References

Altabet, M. A., Ryabenko, E., Stramma, L., Wallace, D. W., Frank, M., Grasse, P., & Lavik, G. (2012). An eddy-stimulated hotspot for fixed nitrogen-loss from the Peru oxygen minimum zone. *Biogeosciences*. doi: 10.5194/bg-9-4897-2012

Anderson, L. A., & Sarmiento, J. L. (1994, 3). Redfield ratios of remineralization determined by nutrient data analysis. *Global Biogeochemical Cycles*, *8*(1), 65–80. doi: 10.1029/93GB03318

Arévalo-Martínez, D. L., Kock, A., Löscher, C. R., Schmitz, R. A., Stramma, L., & Bange, H. W. (2015). Influence of mesoscale eddies on the distribution of nitrous oxide in the eastern tropical South Pacific. *Biogeosciences Discussions*, *12*(12), 9243–9273. doi: 10.5194/bgd-12-9243-2015

Arévalo-Martínez, D. L., Kock, A., Löscher, C. R., Schmitz, R. A., Stramma, L., & Bange, H. W. (2016, 2). Influence of mesoscale eddies on the distribution of nitrous oxide in the eastern tropical South Pacific. *Biogeosciences*, *13*(4), 1105–1118. doi: 10.5194/bg-13-1105-2016

Armstrong, R. A., Lee, C., Hedges, J. I., Honjo, S., & Wakeham, S. G. (2001, 1). A new, mechanistic model for organic carbon fluxes in the ocean based on the quantitative association of POC with ballast minerals. *Deep Sea Research Part II: Topical Studies in Oceanography*, *49*(1-3), 219–236. doi: 10.1016/S0967-0645(01)00101-1

Arrigo, K. R. (2005, 9). Marine microorganisms and global nutrient cycles. *Nature*, *437*(7057), 349–355. doi: 10.1038/nature04159

Aumont, O., Ethé, C., Tagliabue, A., Bopp, L., & Gehlen, M. (2015, 8). PISCES-v2: an ocean biogeochemical model for carbon and ecosystem studies. *Geoscientific Model Development*, *8*(8), 2465–2513. doi: 10.5194/gmd-8-2465-2015

Babbin, A. R., Bianchi, D., Jayakumar, A., & Ward, B. B. (2015). Rapid nitrous oxide cycling in the suboxic ocean. *Science*, *348*(6239), 1127–1129. doi: 10.1126/science.aaa8380

Babbin, A. R., Buchwald, C., Morel, F. M., Wankel, S. D., & Ward, B. B. (2020). Nitrite oxidation exceeds reduction and fixed nitrogen loss in anoxic Pacific waters. *Marine Chemistry*, *224*(April). doi: 10.1016/j.marchem.2020.103814

Babbin, A. R., Keil, R. G., Devol, A. H., & Ward, B. B. (2014). Organic matter stoichiometry, flux, and oxygen control nitrogen loss in the ocean. *Science*, *344*(6182), 406–408. doi: 10.1126/science.1248364

Babbin, A. R., Peters, B. D., Mordy, C. W., Widner, B., Casciotti, K. L., & Ward, B. B. (2017). Multiple metabolisms constrain the anaerobic nitrite budget in the Eastern Tropical South Pacific. *Global Biogeochemical Cycles*, *31*(2), 258–271. doi: 10.1002/2016GB005407

Bakun, A. (1990). Global climate change and intensification of coastal ocean upwelling. *Science*, *247*(4939), 198–201.

Bakun, A., & Nelson, C. S. (1991). The seasonal cycle of wind-stress curl in subtropical eastern boundary current regions. *J. Physical Oceanography*, *21*(12), 1815–1834. doi: 10.1175/1520-0485(1991)021⟨1815:TSCOWS⟩2.0.CO;2

Bakun, A., & Parrish, R. H. (1982). Turbulence, transport, and pelagic fish in the california and peru current systems. In *Calcofi* (Vol. 23, pp. 99–112).

Barbosa Aguiar, A. C., Peliz, A., & Carton, X. (2013, 9). A census of Meddies in a long-term high-resolution simulation. *Progress in Oceanography*, *116*, 80–94. doi: 10.1016/j.pocean.2013.06.016

Barcelo-Llull, B., Sangra, P., Pallas-Sanz, E., Barton, E. D., Estrada-Allis, S. N., Martinez-Marrero, A., ... Aristegui, J. (2017, 6). Anatomy of a subtropical intrathermocline eddy. *Deep Sea Research Part I: Oceanographic Research Papers*, *124*, 126–139. doi: 10.1016/j.dsr.2017.03.012

Bashmachnikov, I., Neves, F., Calheiros, T., & Carton, X. (2015, 9). Properties and pathways of Mediterranean water eddies in the Atlantic. *Progress in Oceanography*, *137*, 149–172. doi: 10.1016/j.pocean.2015.06.001

Battaglia, G., & Joos, F. (2018). Marine N2O Emissions From Nitrification and Denitrification Constrained by Modern Observations and Projected in Multimillennial Global Warming Simulations. *Global Biogeochemical Cycles*, *32*(1), 92–121. doi: 10.1002/2017GB005671

Behrenfeld, M. J., Boss, E., Siegel, D. A., & Shea, D. M. (2005, 3). Carbon-based ocean productivity and phytoplankton physiology from space. *Global Biogeochemical Cycles*, *19*(1). doi: 10.1029/2004GB002299

Behrenfeld, M. J., & Falkowski, P. G. (1997, 1). Photosynthetic rates derived from satellite-based chlorophyll concentration. *Limnology and Oceanography*, *42*(1), 1–20. doi: 10.4319/lo.1997.42.1.0001

Bettencourt, J. H., Lopez, C., Hernandez-Garcia, E., Montes, I., Sudre, J., Dewitte, B., ... Garçon, V. (2015, 12). Boundaries of the Peruvian oxygen minimum zone shaped by coherent mesoscale dynamics. *Nature Geoscience*, *8*(12), 937–940. doi: 10.1038/ngeo2570

Bianchi, D., Dunne, J. P., Sarmiento, J. L., & Galbraith, E. D. (2012). Data-based estimates of suboxia, denitrification, and N2O production in the ocean and their sensitivities to dissolved O2. *Global Biogeochemical Cycles*, *26*(January 2016). doi: 10.1029/2011GB004209

Bianchi, D., McCoy, D., & Yang, S. (2022). Formulation, optimization and sensitivity of NitrOMZv1.0, a biogeochemical model of the nitrogen cycle in oceanic oxygen minimum zones. *Geoscientific Model Development Discussions*. doi: 10.5194/gmd-2022-244

Bianchi, D., Weber, T. S., Kiko, R., & Deutsch, C. (2018, 4). Global niche of marine anaerobic metabolisms expanded by particle microenvironments. *Nature Geoscience*, *11*(4), 263–268. doi: 10.1038/s41561-018-0081-0

Bourbonnais, A., Altabet, M. A., Charoenpong, C. N., Larkum, J., Hu, H., Bange, H. W., & Stramma, L. (2015, 6). N-loss isotope effects in the Peru oxygen minimum zone studied using a mesoscale eddy as a natural tracer experiment. *Global Biogeochemical Cycles*, *29*(6), 793–811. doi: 10.1002/2014GB005001

Bourbonnais, A., Letscher, R. T., Bange, H. W., Échevin, V., Larkum, J., Mohn, J., ... Altabet, M. A. (2017, 4). N2O production and consumption from stable isotopic and concentration data in the Peruvian coastal upwelling system. *Global Biogeochemical Cycles*, *31*(4), 678–698. doi: 10.1002/2016GB005567

Bower, A. S., Armi, L., & Ambar, I. (1997, 12). Lagrangian Observations of Meddy Formation during A Mediterranean Undercurrent Seeding Experiment. *Journal of Physical Oceanography*, *27*(12), 2545–2575. doi: 10.1175/1520-0485(1997)027⟨2545:LOOMFD⟩2.0.CO;2

Bower, A. S., & Furey, H. H. (2012, 4). Mesoscale eddies in the Gulf of Aden and their impact on the spreading of Red Sea Outflow Water. *Progress in Oceanography*, *96*(1), 14–39. doi: 10.1016/j.pocean.2011.09.003

Bower, A. S., Hendry, R. M., Amrhein, D. E., & Lilly, J. M. (2013, 1). Direct observations of formation and propagation of subpolar eddies into the Subtropical North Atlantic. *Deep-Sea Research Part II: Topical Studies in Oceanography*, *85*, 15–41. doi: 10.1016/j.dsr2.2012.07.029

Brentnall, S. J. (2003, 2). Plankton patchiness and its effect on larger-scale productivity. *Journal of Plankton Research*, *25*(2), 121–140. doi: 10.1093/plankt/25.2.121

Bristow, L. A., Dalsgaard, T., Tiano, L., Mills, D. B., Bertagnolli, A. D., Wright, J. J., ... Thamdrup, B. (2016). Ammonium and nitrite oxidation at nanomolar oxygen concentrations in oxygen minimum zone waters. *Proceedings of the National Academy of Sciences of the United States of America*, *113*(38), 10601–10606. doi: 10.1073/pnas.1600359113

Brodeau, L., Barnier, B., Treguier, A.-M., Penduff, T., & Gulev, S. (2010, 1). An ERA40-based atmospheric forcing for global ocean circulation models. *Ocean Modelling*, *31*(3-4), 88–104. doi: 10.1016/j.ocemod.2009.10.005

Broecker, W. S., & Peng, T.-H. (1982). *Tracers in the sea* (Vol. 690). Lamont-Doherty Geological Observatory, Columbia University Palisades, New York.

Buchanan, P. J., Sun, X., Weissman, J. L., & Zakem, E. (2023). Oxygen intrusions sustain aerobic nitrite oxidation in anoxic marine zones. *bioRxiv*. doi: 10.1101/2023.02.22.529547

Buchwald, C., Santoro, A. E., Stanley, R. H. R., & Casciotti, K. L. (2015, 12). Nitrogen cycling in the secondary nitrite maximum of the eastern tropical North Pacific off Costa Rica. *Global Biogeochemical Cycles*, *29*(12), 2061–2081. doi: 10.1002/2015GB005187

Busecke, J. J., Resplandy, L., & Dunne, J. P. (2019, 6). The Equatorial Undercurrent and the Oxygen Minimum Zone in the Pacific. *Geophysical Research Letters*, *46*(12), 6716–6725. doi: 10.1029/2019GL082692

Busecke, J. J. M., Resplandy, L., Ditkovsky, S. J., & John, J. G. (2022, 12). Diverging Fates of the Pacific Ocean Oxygen Minimum Zone and Its Core in a Warming World. *AGU Advances*, *3*(6). doi: 10.1029/2021AV000470

Cabré, A., Marinov, I., Bernardello, R., & Bianchi, D. (2015, 9). Oxygen minimum zones in the tropical Pacific across CMIP5 models: Mean state differences and climate change trends. *Biogeosciences*, *12*(18), 5429–5454. doi: 10.5194/bg-12-5429-2015

Canadell, J. G., Scheel Monteiro, P., Costa, M. H., Cotrim da Cunha, L., Cox, P. M., Eliseev, A. V., ... Zickfeld, K. (2021). *Chapter 5: Global Carbon and other Biogeochemical Cycles and Feedbacks. In Climate Change 2021: The Physical Science Basis. Contribution of Working Group I to the Sixth Assessment Report of the Intergovernmental Panel on Climate Change* . Cambridge University Press.

Capone, D., Bronk, D., Mulholland, M. R., & Carpenter, E. (2008). *Nitrogen in the Marine Environment*. Elsevier. doi: 10.1016/B978-0-12-372522-6.X0001-1

Carrasco, C., Karstensen, J., & Farias, L. (2017, 2). On the Nitrous Oxide Accumulation in Intermediate Waters of the Eastern South Pacific Ocean. *Frontiers in Marine Science*, *4*. doi: 10.3389/fmars.2017.00024

Carton, X., L'Hegaret, P., & Baraille, R. (2012). Mesoscale variability of water masses in the Arabian Sea as revealed by ARGO floats. *Ocean Science*, *8*(2), 227–248. doi: 10.5194/os-8-227-2012

Casciotti, K., Forbes, M., Vedamati, J., Peters, B., Martin, T., & Mordy, C. (2018, 10). Nitrous oxide cycling in the Eastern Tropical South Pacific as inferred from isotopic and isotopomeric data. *Deep Sea Research Part II: Topical Studies in Oceanography*, *156*, 155–167. doi: 10.1016/j.dsr2.2018.07.014

Cerovečki, I., Talley, L. D., Mazloff, M. R., & Maze, G. (2013, 7). Subantarctic Mode Water Formation, Destruction, and Export in the Eddy-Permitting Southern Ocean State Estimate. *Journal of Physical Oceanography*, *43*(7), 1485–1511. doi: 10.1175/JPO-D-12-0121.1

Chaigneau, A., Eldin, G., & Dewitte, B. (2009). Eddy activity in the four major upwelling systems from satellite altimetry (1992-2007). *Progress in Oceanography*. doi: 10.1016/j.pocean.2009.07.012

Chaigneau, A., Gizolme, A., & Grados, C. (2008, 10). Mesoscale eddies off Peru in altimeter records: Identification algorithms and eddy spatio-temporal patterns. *Progress in Oceanography*, *79*(2-4), 106–119. doi: 10.1016/j.pocean.2008.10.013

Chaigneau, A., Le Texier, M., Eldin, G., Grados, C., & Pizarro, O. (2011). Vertical structure of mesoscale eddies in the eastern South Pacific Ocean: A composite analysis from altimetry and Argo profiling floats. *Journal of Geophysical Research: Oceans*, *116*(C11). doi: 10.1029/2011JC007134

Chavez, F. P., & Messié, M. (2009). A comparison of Eastern Boundary Upwelling Ecosystems. *Progress in Oceanography*, *83*(1-4), 80–96. doi: 10.1016/j.pocean.2009.07.032

Chelton, D. B., DeSzoeke, R. A., Schlax, M. G., El Naggar, K., & Siwertz, N. (1998, 3). Geographical Variability of the First Baroclinic Rossby Radius of Deformation. *Journal of Physical Oceanography*, *28*(3), 433–460. doi: 10.1175/1520-0485(1998)028⟨0433:GVOTFB⟩2.0.CO;2

Chelton, D. B., Schlax, M. G., & Samelson, R. M. (2011). Global observations of nonlinear mesoscale eddies. *Progress in Oceanography*, *91*(2), 167–216. doi: 10.1016/j.pocean.2011.01.002

Chelton, D. B., Schlax, M. G., Samelson, R. M., & de Szoeke, R. A. (2007, 8). Global observations of large oceanic eddies. *Geophysical Research Letters*, *34*(15). doi: 10.1029/2007GL030812

Codispoti, L. A. (2007, 5). An oceanic fixed nitrogen sink exceeding 400 Tg N. *Biogeosciences*, *4*(2), 233–253. doi: 10.5194/bg-4-233-2007

Codispoti, L. A. (2010). Interesting times for marine N2O. *Science*, *327*(5971), 1339–1340. doi: 10.1126/science.1184945

Codispoti, L. A., Brandes, J. A., Christensen, J. P., Devol, A. H., Naqvi, S. A., Paerl, H. W., & Yoshinari, T. (2001, 12). The oceanic fixed nitrogen and nitrous oxide budgets: Moving targets as we enter the anthropocene? *Scientia Marina*, *65*(S2), 85–105. doi: 10.3989/scimar.2001.65s285

Codispoti, L. A., & Christensen, J. P. (1985, 7). Nitrification, denitrification and nitrous oxide cycling in the eastern tropical South Pacific ocean. *Marine Chemistry*, *16*(4), 277–300. doi: 10.1016/0304-4203(85)90051-9

Cohen, Y., & Gordon, L. I. (1978, 6). Nitrous oxide in the oxygen minimum of the eastern tropical North Pacific: evidence for its consumption during denitrification and possible mechanisms for its production. *Deep Sea Research*, *25*(6), 509–524. doi: 10.1016/0146-6291(78)90640-9

Colas, F., Capet, X., McWilliams, J. C., & Li, Z. (2013, 6). Mesoscale Eddy Buoyancy Flux and Eddy-Induced Circulation in Eastern Boundary Currents. *Journal of Physical Oceanography*, *43*(6), 1073–1095. doi: 10.1175/JPO-D-11-0241.1

Colas, F., C. McWilliams, J., Capet, X., Kurian, J., McWilliams, J. C., Capet, X., & Kurian, J. (2012). Heat balance and eddies in the Peru-Chile current system. *Climate Dynamics*, *39*(1-2), 509–529. doi: 10.1007/s00382-011-1170-6

Collins, C. A., Margolina, T., Rago, T. A., & Ivanov, L. (2013). Looping RAFOS floats in the California Current System. *Deep-Sea Research Part II: Topical Studies in Oceanography*, *85*, 42–61. doi: 10.1016/j.dsr2.2012.07.027

Combes, V., Hormazabal, S., & Di Lorenzo, E. (2015). Interannual variability of the subsurface eddy field in the Southeast Pacific. *Journal of Geophysical Research C: Oceans*, *120*(7), 4907–4924. doi: 10.1002/2014JC010265

Contreras, M., Pizarro, O., Dewitte, B., Sepulveda, H. H., & Renault, L. (2019, 8). Subsurface Mesoscale Eddy Generation in the Ocean off Central Chile. *Journal of Geophysical Research: Oceans*, *124*(8), 5700–5722. doi: 10.1029/2018JC014723

Cornejo, M., & Farías, L. (2012). Following the N2O consumption in the oxygen minimum zone of the eastern South Pacific. *Biogeosciences*, *9*(8), 3205–3212. doi: 10.5194/bg-9-3205-2012

Cushman-Roisin, B., & Beckers, J.-M. (2011). *Introduction to Geophysical Fluid Dynamics* (Second Edi ed.). San Diego: Elsevier Ltd.

Czeschel, R., Stramma, L., Schwarzkopf, F. U., Giese, B. S., Funk, A., & Karstensen, J. (2011, 1). Middepth circulation of the eastern tropical South Pacific and its link to the oxygen minimum zone. *Journal of Geophysical Research*, *116*(C1), C01015. doi: 10.1029/2010JC006565

Dalsgaard, T., Canfield, D. E., Petersen, J., Thamdrup, B., & Acuña-González, J. (2003). N2 production by the anammox reaction in the anoxic water column of Golfo Dulce, Costa Rica. *Nature*, *422*(6932), 606–608. doi: 10.1038/nature01526

Dalsgaard, T., Stewart, F. J., Thamdrup, B., De Brabandere, L., Revsbech, N. P., Ulloa, O., ... Delong, E. F. (2014). Oxygen at nanomolar levels reversibly suppresses process rates and gene expression in anammox and denitrification in the oxygen minimum zone off Northern Chile. *mBio*, *5*(6), 1–14. doi: 10.1128/mBio.01966-14

Dalsgaard, T., Thamdrup, B., Farías, L., & Revsbech, N. P. (2012, 9). Anammox and denitrification in the oxygen minimum zone of the eastern South Pacific. *Limnology and Oceanography*, *57*(5), 1331–1346. doi: 10.4319/lo.2012.57.5.1331

D'Asaro, E. A. (1988, 12). Generation of submesoscale vortices: A new mechanism. *Journal of Geophysical Research*, *93*(C6), 6685. doi: 10.1029/JC093iC06p06685

de Boyer Montégut, C., Madec, G., Fischer, A. S., Lazar, A., & Iudicone, D. (2004). Mixed layer depth over the global ocean: An examination of profile data and a profile-based climatology. *Journal of Geophysical Research C: Oceans*, *109*(12), 1–20. doi: 10.1029/2004JC002378

Dee, D. P., Uppala, S. M., Simmons, A. J., Berrisford, P., Poli, P., Kobayashi, S., ... Vitart, F. (2011). The ERA-Interim reanalysis: Configuration and performance of the data assimilation system. *Quarterly Journal of the Royal Meteorological Society*, *137*(656), 553–597. doi: 10.1002/qj.828

Deutsch, C., Frenzel, H., McWilliams, J. C., Renault, L., Kessouri, F., Howard, E., ... Yang, S. (2021, 8). Biogeochemical variability in the California Current System. *Progress in Oceanography*, *196*, 102565. doi: 10.1016/j.pocean.2021.102565

Deutsch, C., Gruber, N., Key, R. M., Sarmiento, J. L., & Ganachaud, A. (2001, 6). Denitrification and N2 fixation in the Pacific Ocean. *Global Biogeochemical Cycles*, *15*(2), 483–506. doi: 10.1029/2000GB001291

DeVries, T., Deutsch, C., Rafter, P. A., & Primeau, F. (2013, 4). Marine denitrification rates determined from a global 3-D inverse model. *Biogeosciences*, *10*(4), 2481–2496. doi: 10.5194/bg-10-2481-2013

Dewar, W. K., McWilliams, J. C., & Molemaker, M. J. (2015, 5). Centrifugal Instability and Mixing in the California Undercurrent. *Journal of Physical Oceanography*, *45*(5), 1224–1241. doi: 10.1175/JPO-D-13-0269.1

Dewar, W. K., & Meng, H. (1995, 8). The Propagation of Submesoscale Coherent Vortices. *Journal of Physical Oceanography*, *25*(8), 1745–1770. doi: 10.1175/1520-0485(1995)025⟨1745:TPOSCV⟩2.0.CO;2

Dilmahamod, A. F., Aguiar-González, B., Penven, P., Reason, C. J. C., De Ruijter, W. P. M., Malan, N., & Hermes, J. C. (2018, 8). SIDDIES Corridor: A Major East-West Pathway of Long-Lived Surface and Subsurface Eddies Crossing the Subtropical South Indian Ocean. *Journal of Geophysical Research: Oceans*, *123*(8), 5406–5425. doi: 10.1029/2018JC013828

Dugdale, R. C., & Goering, J. J. (1967, 4). Uptake of New and Regenerated Forms of Nitrogen in Primary Productivity. *Limnology and Oceanography*, *12*(2), 196–206. doi: 10.4319/lo.1967.12.2.0196

Dunn, J. (2012, 2). *CSIRO Atlas of Regional Seas (CARS) - 2009.* Tasmanian Partnership for Advanced Computing.

Dussin, R., Barnier, B., & Brodeau, L. (2014). *The Making of the DRAKKAR FORCING SET DFS5* (Tech. Rep. No. May). LGGE, Grenoble, France.

Duteil, O., Frenger, I., & Getzlaff, J. (2021, 10). The riddle of eastern tropical Pacific Ocean oxygen levels: the role of the supply by intermediate-depth waters. *Ocean Science*, *17*(5), 1489–1507. doi: 10.5194/os-17-1489-2021

Duteil, O., Schwarzkopf, F. U., Böning, C. W., & Oschlies, A. (2014, 3). Major role of the equatorial current system in setting oxygen levels in the eastern tropical Atlantic Ocean:

A high-resolution model study. *Geophysical Research Letters*, *41*(6), 2033–2040. doi: 10.1002/2013GL058888

Eppley, R. W., & Peterson, B. J. (1979, 12). Particulate organic matter flux and planktonic new production in the deep ocean. *Nature*, *282*(5740), 677–680. doi: 10.1038/282677a0

Eugster, O., & Gruber, N. (2012, 12). A probabilistic estimate of global marine N-fixation and denitrification. *Global Biogeochemical Cycles*, *26*(4), 2012GB004300. doi: 10.1029/2012GB004300

Falkowski, P. G. (1997, 5). Evolution of the nitrogen cycle and its influence on the biological sequestration of CO2 in the ocean. *Nature*, *387*(6630), 272–275. doi: 10.1038/387272a0

Falkowski, P. G., Ziemann, D., Kolber, Z., & Bienfang, P. K. (1991, 7). Role of eddy pumping in enhancing primary production in the ocean. *Nature*, *352*(6330), 55–58. doi: 10.1038/352055a0

Farías, L., Faúndez, J., Fernández, C., Cornejo, M., Sanhueza, S., & Carrasco, C. (2013, 5). Biological N2O Fixation in the Eastern South Pacific Ocean and Marine Cyanobacterial Cultures. *PLoS ONE*, *8*(5), e63956. doi: 10.1371/journal.pone.0063956

Fasham, M. J. R., Ducklow, H. W., & McKelvie, S. M. (1990, 8). A nitrogen-based model of plankton dynamics in the oceanic mixed layer. *Journal of Marine Research*, *48*(3), 591–639. doi: 10.1357/002224090784984678

Fox-Kemper, B., G. Danabasoglu, Ferrari, R., & Hallberg, R. W. (2008, 9). Parameterizing submesoscale physics in global models. In *Clivar exch.* (Vol. 13).

Fratantoni, D. M., & Richardson, P. L. (2006). The evolution and demise of North Brazil Current rings. *Journal of Physical Oceanography*, *36*(7), 1241–1264. doi: 10.1175/JPO2907.1

Freing, A., Wallace, D. W., & Bange, H. W. (2012). Global oceanic production of nitrous oxide. *Philosophical Transactions of the Royal Society B: Biological Sciences*, *367*(1593), 1245–1255. doi: 10.1098/rstb.2011.0360

Frenger, I., Bianchi, D., Stührenberg, C., Oschlies, A., Dunne, J., Deutsch, C., ... Schütte, F. (2018, 1). Biogeochemical Role of Subsurface Coherent Eddies in the Ocean: Tracer Cannonballs, Hypoxic Storms, and Microbial Stewpots? *Global Biogeochemical Cycles*, *32*(2), 226–249. doi: 10.1002/2017GB005743

Frey, C., Bange, H. W., Achterberg, E. P., Jayakumar, A., Löscher, C. R., Arévalo-Martínez, D. L., ... Ward, B. B. (2020). Regulation of nitrous oxide production in low-oxygen waters off the coast of Peru. *Biogeosciences*, *17*(8), 2263–2287. doi: 10.5194/bg-17-2263-2020

Frischknecht, M., Münnich, M., & Gruber, N. (2017, 1). Local atmospheric forcing driving an unexpected California Current System response during the 2015–2016 El Niño. *Geophysical Research Letters*, *44*(1), 304–311. doi: 10.1002/2016GL071316

Froelich, P., Klinkhammer, G., Bender, M., Luedtke, N., Heath, G., Cullen, D., ... Maynard, V. (1979). Early oxidation of organic matter in pelagic sediments of the eastern equatorial atlantic: suboxic diagenesis. *Geochimica et Cosmochimica Acta*, *43*(7), 1075-1090. doi: https://doi.org/10.1016/0016-7037(79)90095-4

Fuenzalida, R., Schneider, W., Garcés-Vargas, J., Bravo, L., & Lange, C. (2009, 7). Vertical and horizontal extension of the oxygen minimum zone in the eastern South Pacific Ocean. *Deep Sea Research Part II: Topical Studies in Oceanography*, *56*(16), 992–1003. doi: 10.1016/j.dsr2.2008.11.001

Ganesh, S., Parris, D. J., Delong, E. F., & Stewart, F. J. (2014). Metagenomic analysis of size-fractionated picoplankton in a marine oxygen minimum zone. *The ISME Journal*, *8*, 187–211. doi: 10.1038/ismej.2013.144

Garcia, H., Weathers, K., Paver, C., Smolyar, I., Boyer, T., Locarnini, M., ... Reagan, J. (2019). World Ocean Atlas 2018, Volume 3: Dissolved Oxygen, Apparent Oxygen Utilization, and Dissolved Oxygen Saturation. *NOAA Atlas NESDIS*, *83*.

Garcia, H. E., Boyer, T. P., Locarnini, R. A., Antonov, J. I., Mishonov, A. V., Baranova, O. K., ... Johnson, D. R. (2013). World Ocean Atlas 2013. Volume 3: dissolved

oxygen, apparent oxygen utilization, and oxygen saturation. *NOAA Atlas NESDIS 75*, *3*(September), 27.

Garcia, H. E., Locarnini, R., Boyer, T. P., Antonov, J. I., Baranova, O. K., Zweng, M. M., ... Johnson, D. R. (2013). World Ocean Atlas 2013 Volume 4 : Nutrients (phosphate , nitrate , silicate). *NOAA Atlas NESDIS 76*, *4*(September), 396.

Garfield, N., Collins, C. A., Paquette, R. G., & Carter, E. (1999, 4). Lagrangian Exploration of the California Undercurrent, 1992–95. *Journal of Physical Oceanography*, *29*(4), 560–583. doi: 10.1175/1520-0485(1999)029⟨0560:LEOTCU⟩2.0.CO;2

Gaube, P., McGillicuddy, D. J., Chelton, D. B., Behrenfeld, M. J., & Strutton, P. G. (2014, 12). Regional variations in the influence of mesoscale eddies on near-surface chlorophyll. *Journal of Geophysical Research: Oceans*, *119*(12), 8195–8220. doi: 10.1002/2014JC010111

Gaube, P., McGillicuddy, D. J., & Moulin, A. J. (2018). Mesoscale Eddies Modulate Mixed Layer Depth Globally. *Geophysical Research Letters*. doi: 10.1029/2018GL080006

Gent, P. R., & Mcwilliams, J. C. (1990, 1). Isopycnal Mixing in Ocean Circulation Models. *Journal of Physical Oceanography*, *20*(1), 150–155. doi: 10.1175/1520-0485(1990)020⟨0150:IMIOCM⟩2.0.CO;2

Gill, A. (1982). *Atmosphere-Ocean Dynamics*. New York: Academic Press.

Gnanadesikan, A., Bianchi, D., & Pradal, M. A. (2013, 10). Critical role for mesoscale eddy diffusion in supplying oxygen to hypoxic ocean waters. *Geophysical Research Letters*, *40*(19), 5194–5198. doi: 10.1002/GRL.50998

Goodman, L., & Robinson, A. R. (2008, 3). On the theory of advective effects on biological dynamics in the sea. III. The role of turbulence in biological–physical interactions. *Proceedings of the Royal Society A: Mathematical, Physical and Engineering Sciences*, *464*(2091), 555–572. doi: 10.1098/rspa.2007.0251

Gordon, A. L., Giulivi, C. F., Lee, C. M., Furey, H. H., Bower, A., & Talley, L. (2002). Japan/East Sea Intrathermocline Eddies. *Journal of Physical Oceanography*, *32*(6), 1960–1974. doi: 10.1175/1520-0485(2002)032⟨1960:jesie⟩2.0.co;2

Goreau, T. J., Kaplan, W. A., Wofsy, S. C., McElroy, M. B., Valois, F. W., & Watson, S. W. (1980, 9). Production of NO2 and N2O by Nitrifying Bacteria at Reduced Concentrations of Oxygen. *Applied and environmental microbiology*, *40*(3), 526–32. doi: 10.1128/aem.40.3.526-532.1980

Graf, D. R. H., Jones, C. M., & Hallin, S. (2014, 12). Intergenomic Comparisons Highlight Modularity of the Denitrification Pathway and Underpin the Importance of Community Structure for N2O Emissions. *PLoS ONE*, *9*(12), e114118. doi: 10.1371/journal.pone.0114118

Gruber, N. (2004). The Dynamics of the Marine Nitrogen Cycle and its Influence on Atmospheric CO2 Variations. In *The ocean carbon cycle and climate* (pp. 97–148). Dordrecht: Springer Netherlands. doi: 10.1007/978-1-4020-2087-2{_}4

Gruber, N., & Galloway, J. N. (2008, 1). An Earth-system perspective of the global nitrogen cycle. *Nature*, *451*(7176), 293–296. doi: 10.1038/nature06592

Gruber, N., Lachkar, Z., Frenzel, H., Marchesiello, P., Münnich, M., McWilliams, J. C., ... Plattner, G. K. (2011). Eddy-induced reduction of biological production in eastern boundary upwelling systems. *Nature Geoscience*, *4*(11), 787–792. doi: 10.1038/ngeo1273

Gruber, N., & Sarmiento, J. L. (1997, 6). Global patterns of marine nitrogen fixation and denitrification. *Global Biogeochemical Cycles*, *11*(2), 235–266. doi: 10.1029/97GB00077

Grundle, D. S., Löscher, C. R., Krahmann, G., Altabet, M. A., Bange, H. W., Karstensen, J., ... Fiedler, B. (2017). Low oxygen eddies in the eastern tropical North Atlantic: Implications for N2O cycling. *Scientific Reports*, *7*(1), 1–10. doi: 10.1038/s41598-017-04745-y

Hanawa, K., & Talley, L. (2001, 1). Chapter 5.4 Mode waters. *International Geophysics*, *77*, 373–386. doi: 10.1016/S0074-6142(01)80129-7

Hauss, H., Christiansen, S., Schütte, F., Kiko, R., Edvam Lima, M., Rodrigues, E., ... Fiedler, B. (2016, 4). Dead zone or oasis in the open ocean? Zooplankton distribution and migration in low-oxygen modewater eddies. *Biogeosciences*, *13*(6), 1977–1989. doi: 10.5194/bg-13-1977-2016

Hink, L., Lycus, P., Gubry-Rangin, C., Frostegaard, A., Nicol, G. W., Prosser, J. I., & Bakken, L. R. (2017, 12). Kinetics of NH3 -oxidation, NO-turnover, N2O-production and electron flow during oxygen depletion in model bacterial and archaeal ammonia oxidisers. *Environmental Microbiology*, *19*(12), 4882–4896. doi: 10.1111/1462-2920.13914

Hink, L., Nicol, G. W., & Prosser, J. I. (2017, 12). Archaea produce lower yields of N2O than bacteria during aerobic ammonia oxidation in soil. *Environmental Microbiology*, *19*(12), 4829–4837. doi: 10.1111/1462-2920.13282

Hogan, P., & Hurlburt, H. (2011). Why do Intrathermocline Eddies Form in the Japan/East Sea? A Modeling Perspective. *Oceanography*, *19*(3), 134–143. doi: 10.5670/oceanog.2006.50

Hooper, A. B., & Terry, K. (1979, 11). Hydroxylamine oxidoreductase of Nitrosomonas. *Biochimica et Biophysica Acta (BBA) - Enzymology*, *571*(1), 12–20. doi: 10.1016/0005-2744(79)90220-1

Hormazabal, S., Combes, V., Morales, C. E., Correa-Ramirez, M. A., Di Lorenzo, E., & Nuñez, S. (2013). Intrathermocline eddies in the coastal transition zone off central Chile (31-41°S). *Journal of Geophysical Research: Oceans*, *118*(10), 4811–4821. doi: 10.1002/jgrc.20337

Huyer, A. (1983, 1). Coastal upwelling in the California current system. *Progress in Oceanography*, *12*(3), 259–284. doi: 10.1016/0079-6611(83)90010-1

IPCC. (2013). *Climate Change 2013: The Physical Science Basis. Contribution of Working Group I to the Fifth Assessment Report of the Intergovernmental Panel on Climate Change*. Cambridge, United Kingdom and New York, NY, USA: Cambridge University Press. doi: 10.1017/CBO9781107415324

Jacox, M. G., & Edwards, C. A. (2012, 5). Upwelling source depth in the presence of nearshore wind stress curl. *Journal of Geophysical Research: Oceans*, *117*(C5). doi: 10.1029/2011JC007856

Ji, Q., Babbin, A. R., Peng, X., Bowen, J. L., & Ward, B. B. (2015). Nitrogen substrate–dependent nitrous oxide cycling in salt marsh sediments. *Journal of Marine Research*, *73*(3-4), 71–92. doi: 10.1357/002224015815848820

Ji, Q., Buitenhuis, E., Suntharalingam, P., Sarmiento, J. L., & Ward, B. B. (2018). Global Nitrous Oxide Production Determined by Oxygen Sensitivity of Nitrification and Denitrification. *Global Biogeochemical Cycles*, *32*(12), 1790–1802. doi: 10.1029/2018GB005887

Jin, X., & Gruber, N. (2003). Offsetting the radiative benefit of ocean iron fertilization by enhancing N2O emissions. *Geophysical Research Letters*, *30*(24), 1–4. doi: 10.1029/2003GL018458

Jithin, A. K., & Francis, P. A. (2021, 12). Formation of an Intrathermocline Eddy Triggered by the Coastal-Trapped Wave in the Northern Bay of Bengal. *Journal of Geophysical Research: Oceans*, *126*(12). doi: 10.1029/2021JC017725

Johnson, G. C., & McTaggart, K. E. (2010). Equatorial Pacific 13°C Water Eddies in the Eastern Subtropical South Pacific Ocean. *Journal of Physical Oceanography*. doi: 10.1175/2009JPO4287.1

Johnson, G. C., Sloyan, B. M., Kessler, W. S., & McTaggart, K. E. (2002). Direct measurements of upper ocean currents and water properties across the tropical Pacific during the 1990s. *Progress in Oceanography*, *52*(1), 31–61. doi: 10.1016/S0079-6611(02)00021-6

Johnson, K. A., & Goody, R. S. (2011, 10). The Original Michaelis Constant: Translation of the 1913 Michaelis–Menten Paper. *Biochemistry*, *50*(39), 8264–8269. doi: 10.1021/bi201284u

Kalvelage, T., Jensen, M. M., Contreras, S., Revsbech, N. P., Lam, P., Günter, M., ... Kuypers, M. M. (2011). Oxygen sensitivity of anammox and coupled N-cycle processes in oxygen minimum zones. *PLoS ONE*, *6*(12). doi: 10.1371/journal.pone.0029299

Kalvelage, T., Lavik, G., Lam, P., Contreras, S., Arteaga, L., Löscher, C. R., ... Kuypers, M. M. (2013). Nitrogen cycling driven by organic matter export in the South Pacific oxygen minimum zone. *Nature Geoscience*, *6*(3), 228–234. doi: 10.1038/ngeo1739

Kämpf, J., & Chapman, P. (2016). Upwelling systems of the world: A scientific journey to the most productive marine ecosystems. *Upwelling Systems of the World: A Scientific Journey to the Most Productive Marine Ecosystems*, 1–433. doi: 10.1007/978-3-319-42524-5

Karstensen, J., Fiedler, B., Schütte, F., Brandt, P., Körtzinger, A., Fischer, G., ... Wallace, D. (2015, 4). Open ocean dead zones in the tropical North Atlantic Ocean. *Biogeosciences*, *12*(8), 2597–2605. doi: 10.5194/bg-12-2597-2015

Karstensen, J., Schütte, F., Pietri, A., Krahmann, G., Fiedler, B., Grundle, D., ... Visbeck, M. (2017). Upwelling and isolation in oxygen-depleted anticyclonic modewater eddies and implications for nitrate cycling. *Biogeosciences*, *14*(8), 2167–2181. doi: 10.5194/bg-14-2167-2017

Karstensen, J., Stramma, L., & Visbeck, M. (2008, 6). Oxygen minimum zones in the eastern tropical Atlantic and Pacific oceans. *Progress in Oceanography*, *77*(4), 331–350. doi: 10.1016/j.pocean.2007.05.009

Karthäuser, C., Ahmerkamp, S., Marchant, H. K., Bristow, L. A., Hauss, H., Iversen, M. H., ... Kuypers, M. M. M. (2021, 5). Small sinking particles control anammox rates in the Peruvian oxygen minimum zone. *Nature Communications*, *12*(1), 3235. doi: 10.1038/s41467-021-23340-4

Keeling, R. F., Körtzinger, A., & Gruber, N. (2010). Ocean deoxygenation in a warming world. *Annual Review of Marine Science*, *2*(1), 199-229. (PMID: 21141663) doi: 10.1146/annurev.marine.010908.163855

Kelly, C. L., Travis, N. M., Baya, P. A., & Casciotti, K. L. (2021, 2). Quantifying Nitrous Oxide Cycling Regimes in the Eastern Tropical North Pacific Ocean With Isotopomer Analysis. *Global Biogeochemical Cycles*, *35*(2). doi: 10.1029/2020GB006637

Kessler, W. S. (2006, 5). The circulation of the eastern tropical Pacific: A review. *Progress in Oceanography*, *69*(2-4), 181–217. doi: 10.1016/j.pocean.2006.03.009

Klenz, T., Dengler, M., & Brandt, P. (2018). Seasonal Variability of the Mauritania Current and Hydrography at 18°N. *Journal of Geophysical Research: Oceans*, *123*(11), 8122–8137. doi: 10.1029/2018JC014264

Kock, A., Arevalo-Martinez, D. L., Loscher, C. R., & Bange, H. W. (2016). Extreme N2O accumulation in the coastal oxygen minimum zone off Peru. *Biogeosciences*, *13*(3), 827–840. doi: 10.5194/bg-13-827-2016

Kock, A., & Bange, H. (2015, 2). Counting the Ocean's Greenhouse Gas Emissions. *Eos*, *96*. doi: 10.1029/2015EO023665

Könneke, M., Bernhard, A. E., de la Torre, J. R., Walker, C. B., Waterbury, J. B., & Stahl, D. A. (2005, 9). Isolation of an autotrophic ammonia-oxidizing marine archaeon. *Nature*, *437*(7058), 543–546. doi: 10.1038/nature03911

Körner, H., & Zumft, W. G. (1989, 7). Expression of denitrification enzymes in response to the dissolved oxygen level and respiratory substrate in continuous culture of Pseudomonas stutzeri. *Applied and Environmental Microbiology*, *55*(7), 1670–1676. doi: 10.1128/aem.55.7.1670-1676.1989

Kozlowski, J. A., Stieglmeier, M., Schleper, C., Klotz, M. G., & Stein, L. Y. (2016, 8). Pathways and key intermediates required for obligate aerobic ammonia-dependent

chemolithotrophy in bacteria and Thaumarchaeota. *The ISME Journal*, *10*(8), 1836–1845. doi: 10.1038/ismej.2016.2

Krahmann, G., Arévalo-Martínez, D. L., Dale, A. W., Dengler, M., Engel, A., Glock, N., ... Mehrtens, H. (2021, 9). Climate-Biogeochemistry Interactions in the Tropical Ocean: Data Collection and Legacy. *Frontiers in Marine Science*, *8*(September), 1–23. doi: 10.3389/fmars.2021.723304

Kuypers, M. M. M., Marchant, H. K., & Kartal, B. (2018, 5). The microbial nitrogen-cycling network. *Nature Reviews Microbiology*, *16*(5), 263–276. doi: 10.1038/nrmicro.2018.9

Kuypers, M. M. M., Sliekers, A. O., Lavik, G., Schmid, M., Jørgensen, B. B., Kuenen, J. G., ... Jetten, M. S. M. (2003, 4). Anaerobic ammonium oxidation by anammox bacteria in the Black Sea. *Nature*, *422*(6932), 608–611. doi: 10.1038/nature01472

Kwiatkowski, L., Torres, O., Bopp, L., Aumont, O., Chamberlain, M., Christian, J. R., ... Ziehn, T. (2020, 7). Twenty-first century ocean warming, acidification, deoxygenation, and upper-ocean nutrient and primary production decline from CMIP6 model projections. *Biogeosciences*, *17*(13), 3439–3470. doi: 10.5194/bg-17-3439-2020

Kwiecinski, J. V., & Babbin, A. R. (2021, 12). A High-Resolution Atlas of the Eastern Tropical Pacific Oxygen Deficient Zones. *Global Biogeochemical Cycles*, *35*(12). doi: 10.1029/2021GB007001

Lam, P., & Kuypers, M. M. (2011). Microbial Nitrogen Cycling Processes in Oxygen Minimum Zones. *Annual Review of Marine Science*, *3*(1), 317–345. doi: 10.1146/annurev-marine-120709-142814

Lam, P., Lavik, G., Jensen, M. M., van de Vossenberg, J., Schmid, M., Woebken, D., ... Kuypers, M. M. M. (2009, 3). Revising the nitrogen cycle in the Peruvian oxygen minimum zone. *Proceedings of the National Academy of Sciences*, *106*(12), 4752–4757. doi: 10.1073/pnas.0812444106

Landolfi, A., Dietze, H., Koeve, W., & Oschlies, A. (2013, 3). Overlooked runaway feedback in the marine nitrogen cycle: the vicious cycle. *Biogeosciences*, *10*(3), 1351–1363. doi: 10.5194/bg-10-1351-2013

Large, W. B. (2006). Surface Fluxes for Practitioners of Global Ocean Data Assimilation. In E. P. Chassignet & J. Verron (Eds.), *Ocean weather forecasting: An integrated view of oceanography* (pp. 229–270). Dordrecht: Springer Netherlands. doi: 10.1007/1-4020-4028-8_9

Lass, H. U., & Mohrholz, V. (2008). On the interaction between the subtropical gyre and the Subtropical Cell on the shelf of the SE Atlantic. *Journal of Marine Systems*. doi: 10.1016/j.jmarsys.2007.09.008

Lass, H. U., Schmidt, M., Mohrholz, V., & Nausch, G. (2000). Hydrographic and current measurements in the area of the Angola-Benguela Front. *Journal of Physical Oceanography*. doi: 10.1175/1520-0485(2000)030⟨2589:HACMIT⟩2.0.CO;2

Lathuilière, C., Echevin, V., Lévy, M., & Madec, G. (2010). On the role of the mesoscale circulation on an idealized coastal upwelling ecosystem. *Journal of Geophysical Research: Oceans*, *115*(C9).

Lauvset, S. K., Key, R. M., Olsen, A., Van Heuven, S., Velo, A., Lin, X., ... Watelet, S. (2016). A new global interior ocean mapped climatology: The 1° × 1° GLODAP version 2. *Earth System Science Data*, *8*(2), 325–340. doi: 10.5194/essd-8-325-2016

Legg, S., Briegleb, B., Chang, Y., Chassignet, E. P., Danabasoglu, G., Ezer, T., ... Yang, J. (2009). Improving oceanic overflow representation in climate models: The Gravity Current Entrainment Climate Process Team. *Bulletin of the American Meteorological Society*, *90*(5), 657–670. doi: 10.1175/2008BAMS2667.1

Lemarié, F., Kurian, J., Shchepetkin, A. F., Jeroen Molemaker, M., Colas, F., & McWilliams, J. C. (2012). Are there inescapable issues prohibiting the use of terrain-following coordinates in climate models? *Ocean Modelling*, *42*, 57–79. doi: 10.1016/j.ocemod.2011.11.007

Le Traon, P. (1991, Aug). Time scales of mesoscale variability and their relationship with space scales in the north atlantic. *Journal of Marine Research*, *49*(3), 467-492.

Lévy, M., Bopp, L., Karleskind, P., Resplandy, L., Ethe, C., & Pinsard, F. (2013). Physical pathways for carbon transfers between the surface mixed layer and the ocean interior. *Global Biogeochemical Cycles*. doi: 10.1002/gbc.20092

Lévy, M., Couespel, D., Haëck, C., Keerthi, M., Mangolte, I., & Prend, C. J. (2024). The impact of fine-scale currents on biogeochemical cycles in a changing ocean. *Annual Review of Marine Science*, *16*(1). doi: 10.1146/annurev-marine-020723-020531

Lévy, M., Ferrari, R., Franks, P. J. S., Martin, A. P., & Rivière, P. (2012). Bringing physics to life at the submesoscale. *Geophysical Research Letters*, *39*(14).

Lévy, M., Resplandy, L., Palter, J. B., Couespel, D., & Lachkar, Z. (2022). The crucial contribution of mixing to present and future ocean oxygen distribution. In *Ocean mixing* (pp. 329–344). Elsevier. doi: 10.1016/B978-0-12-821512-8.00020-7

L'Hégaret, P., Carton, X., Louazel, S., & Boutin, G. (2016, 5). Mesoscale eddies and submesoscale structures of Persian Gulf Water off the Omani coast in spring 2011. *Ocean Science*, *12*(3), 687–701. doi: 10.5194/os-12-687-2016

Li, C., Zhang, Z., Zhao, W., & Tian, J. (2017, 5). A statistical study on the subthermocline submesoscale eddies in the northwestern Pacific Ocean based on Argo data. *Journal of Geophysical Research: Oceans*, *122*(5), 3586–3598. doi: 10.1002/2016JC012561

Long, A. M., Jurgensen, S. K., Petchel, A. R., Savoie, E. R., & Brum, J. R. (2021, 10). Microbial Ecology of Oxygen Minimum Zones Amidst Ocean Deoxygenation. *Frontiers in Microbiology*, *12*. doi: 10.3389/fmicb.2021.748961

Löscher, C. R., Bourbonnais, A., Dekaezemacker, J., Charoenpong, C. N., Altabet, M. A., Bange, H. W., ... Schmitz, R. (2016, 5). N2 fixation in eddies of the eastern tropical South Pacific Ocean. *Biogeosciences*, *13*(10), 2889–2899. doi: 10.5194/bg-13-2889-2016

Löscher, C. R., Fischer, M. A., Neulinger, S. C., Fiedler, B., Philippi, M., Schütte, F., ... Schmitz, R. A. (2015). Hidden biosphere in an oxygen-deficient Atlantic open ocean eddy: Future implications of ocean deoxygenation on primary production in the eastern tropical North Atlantic. *Biogeosciences Discussions*, *12*(16), 14175–14213. doi: 10.5194/bgd-12-14175-2015

Löscher, C. R., Kock, A., Könneke, M., Laroche, J., Bange, H. W., & Schmitz, R. A. (2012). Production of oceanic nitrous oxide by ammonia-oxidizing archaea. *Biogeosciences*, *9*(7), 2419–2429. doi: 10.5194/bg-9-2419-2012

Louca, S., Hawley, A. K., Katsev, S., Torres-Beltran, M., Bhatia, M. P., Kheirandish, S., ... Hallam, S. J. (2016, 10). Integrating biogeochemistry with multiomic sequence information in a model oxygen minimum zone. *Proceedings of the National Academy of Sciences*, *113*(40). doi: 10.1073/pnas.1602897113

Lukas, R., & Santiago-Mandujano, F. (2001, 8). Extreme water mass anomaly observed in the Hawaii ocean time-series. *Geophysical Research Letters*, *28*(15), 2931–2934. doi: 10.1029/2001GL013099

Luo, Y.-W., Doney, S. C., Anderson, L. A., Benavides, M., Berman-Frank, I., Bode, A., ... Zehr, J. P. (2012, 8). Database of diazotrophs in global ocean: abundance, biomass and nitrogen fixation rates. *Earth System Science Data*, *4*(1), 47–73. doi: 10.5194/essd-4-47-2012

Luyten, J. R., Pedlosky, J., & Stommel, H. (1983, 2). The Ventilated Thermocline. *Journal of Physical Oceanography*, *13*(2), 292–309. doi: 10.1175/1520-0485(1983)013⟨0292:TVT⟩2.0.CO;2

Lynn, R. J., & Simpson, J. J. (1987). The California Current System: The seasonal variability of its physical characteristics. *Journal of Geophysical Research: Oceans (1978–2012)*. doi: 10.1029/JC092iC12p12947

Mahadevan, A., & Campbell, J. W. (2002, 10). Biogeochemical patchiness at the sea surface. *Geophysical Research Letters*, *29*(19), 32–1. doi: 10.1029/2001GL014116

Mahadevan, A., D'asaro, E., Lee, C., & Perry, M. J. (2012). Eddy-driven stratification initiates North Atlantic spring phytoplankton blooms. *Science*, *337*(6090), 54–58.

Manizza, M., Keeling, R. F., & Nevison, C. D. (2012). On the processes controlling the seasonal cycles of the air-sea fluxes of O2 and N2O: A modelling study. *Tellus B: Chemical and Physical Meteorology*, *64*(1), 18429. doi: 10.3402/tellusb.v64i0.18429

Marchesiello, P., McWilliams, J. C., Shchepetkin, A., Physics, P., & Angeles, L. (2003). Equilibrium Structure and Dynamics of the California Current System. *Journal of Physical Oceanography*. doi: 10.1175/1520-0485(2003)33⟨753:ESADOT⟩2.0.CO;2

Martens-Habbena, W., Berube, P. M., Urakawa, H., De La Torre, J. R., & Stahl, D. A. (2009). Ammonia oxidation kinetics determine niche separation of nitrifying Archaea and Bacteria. *Nature*, *461*(7266), 976–979. doi: 10.1038/nature08465

Martin, A. P., Lévy, M., Gennip, S., Pardo, S., Srokosz, M., Allen, J., ... Pidcock, R. (2015, 9). An observational assessment of the influence of mesoscale and submesoscale heterogeneity on ocean biogeochemical reactions. *Global Biogeochemical Cycles*, *29*(9), 1421–1438. doi: 10.1002/2015GB005129

Martinez-Rey, J., Bopp, L., Gehlen, M., Tagliabue, A., & Gruber, N. (2015). Projections of oceanic N2O emissions in the 21st century using the IPSL Earth system model. *Biogeosciences*, *12*(13), 4133–4148. doi: 10.5194/bg-12-4133-2015

McCoy, D., Bianchi, D., & Stewart, A. L. (2020). Global observations of submesoscale coherent vortices in the ocean. *Progress in Oceanography*, *189*(September), 102452. doi: 10.1016/j.pocean.2020.102452

McCoy, D., Damien, P., Clements, D., Yang, S., & Bianchi, D. (2023, 7). Pathways of Nitrous Oxide Production in the Eastern Tropical South Pacific Oxygen Minimum Zone. *Global Biogeochemical Cycles*, *37*(7). doi: 10.1029/2022GB007670

McGillicuddy, D. J. (2014). Formation of Intrathermocline Lenses by Eddy–Wind Interaction. *Journal of Physical Oceanography*, *45*(2), 606–612. doi: 10.1175/jpo-d-14-0221.1

McGillicuddy, D. J., Anderson, L. A., Bates, N. R., Bibby, T., Buesseler, K. O., Carlson, C. A., ... Steinberg, D. K. (2007, 5). Eddy/Wind Interactions Stimulate Extraordinary Mid-Ocean Plankton Blooms. *Science*, *316*(5827), 1021–1026. doi: 10.1126/science.1136256

McWilliams, J. C. (1985). Submesoscale, coherent vortices in the ocean. *Reviews of Geophysics*, *23*(2), 165. doi: 10.1029/RG023i002p00165

McWilliams, J. C. (2016, 5). Submesoscale currents in the ocean. *Proceedings of the Royal Society A: Mathematical, Physical and Engineering Science*, *472*(2189), 20160117. doi: 10.1098/rspa.2016.0117

McWilliams, J. C. (2019). A survey of submesoscale currents. *Geoscience Letters*, *6*(1). doi: 10.1186/s40562-019-0133-3

Ménesguen, C., Hua, B. L., Carton, X., Klingelhoefer, F., Schnürle, P., & Reichert, C. (2012, 3). Arms winding around a meddy seen in seismic reflection data close to the Morocco coastline. *Geophysical Research Letters*, *39*(5), n/a-n/a. doi: 10.1029/2011GL050798

Meunier, T., Tenreiro, M., Pallàs-Sanz, E., Ochoa, J., Ruiz-Angulo, A., Portela, E., ... Carton, X. (2018). Intrathermocline Eddies Embedded Within an Anticyclonic Vortex Ring. *Geophysical Research Letters*, *45*(15), 7624–7633. doi: 10.1029/2018GL077527

Mohrholz, V., Schmidt, M., & Lutjeharms, J. R. (2001). The hydrography and dynamics of the Angola-Benguela Frontal Zone and environment in April 1999. *South African Journal of Science*.

Molemaker, M. J., McWilliams, J. C., & Dewar, W. K. (2015, 3). Submesoscale Instability and Generation of Mesoscale Anticyclones near a Separation of the California Undercurrent. *Journal of Physical Oceanography*, *45*(3), 613–629. doi: 10.1175/JPO-D-13-0225.1

Moore, J. K., Doney, S. C., & Lindsay, K. (2004, 12). Upper ocean ecosystem dynamics and iron cycling in a global three-dimensional model. *Global Biogeochemical Cycles*, *18*(4), n/a-n/a. doi: 10.1029/2004GB002220

Morrow, R., & Le Traon, P.-Y. (2012, 10). Recent advances in observing mesoscale ocean dynamics with satellite altimetry. *Advances in Space Research*, *50*(8), 1062–1076. doi: 10.1016/j.asr.2011.09.033

Morvan, M., L'hégaret, P., Carton, X., Gula, J., Vic, C., De Marez, C., ... Koshel, K. (2019). The life cycle of submesoscale eddies generated by topographic interactions. *Ocean Science*, *15*(6), 1531–1543. doi: 10.5194/os-15-1531-2019

Naqvi, S. W. A., Bange, H. W., Farías, L., Monteiro, P. M. S., Scranton, M. I., & Zhang, J. (2010, 7). Marine hypoxia/anoxia as a source of CH4 and N2O. *Biogeosciences*, *7*(7), 2159–2190. doi: 10.5194/bg-7-2159-2010

Nauw, J. J., van Aken, H. M., Lutjeharms, J. R., & de Ruijter, W. P. (2006). Intrathermocline eddies in the Southern Indian Ocean. *Journal of Geophysical Research: Oceans*, *111*(3), 1–14. doi: 10.1029/2005JC002917

Nevison, C., Butler, J. H., & Elkins, J. W. (2003, 12). Global distribution of N2O and the ΔN2O-AOU yield in the subsurface ocean. *Global Biogeochemical Cycles*, *17*(4), n/a-n/a. doi: 10.1029/2003GB002068

Oka, E. (2009). Seasonal and interannual variation of North Pacific Subtropical Mode Water in 2003-2006. *Journal of Oceanography*, *65*(2), 151–164. doi: 10.1007/s10872-009-0015-y

Oka, E., & Suga, T. (2005). Differential formation and circulation of North Pacific Central Mode Water. *Journal of Physical Oceanography*, *35*(11), 1997–2011. doi: 10.1175/JPO2811.1

Ollitrault, M., & Colin de Verdière, A. (2014, 1). The Ocean General Circulation near 1000-m Depth. *Journal of Physical Oceanography*, *44*(1), 384–409. doi: 10.1175/JPO-D-13-030.1

Orsi, A. H., & Whitworth, T. (2005). *Hydrographic Atlas of the World Ocean Circulation Experiment (WOCE) Volume 1: Southern Ocean.* (Vol. 1). Southampton, U.K.: International WOCE Project Office.

Oschlies, A., Brandt, P., Stramma, L., & Schmidtko, S. (2018). Drivers and mechanisms of ocean deoxygenation. *Nature Geoscience*, *11*(7), 467–473. doi: 10.1038/s41561-018-0152-2

Pajares, S., & Ramos, R. (2019, 11). Processes and Microorganisms Involved in the Marine Nitrogen Cycle: Knowledge and Gaps. *Frontiers in Marine Science*, *6*. doi: 10.3389/fmars.2019.00739

Pasquero, C. (2005). Impact of the spatiotemporal variability of the nutrient flux on primary productivity in the ocean. *Journal of Geophysical Research*, *110*(C7), C07005. doi: 10.1029/2004JC002738

Paulmier, A., Kriest, I., & Oschlies, A. (2009, 5). Stoichiometries of remineralisation and denitrification in global biogeochemical ocean models. *Biogeosciences*, *6*(5), 923–935. doi: 10.5194/bg-6-923-2009

Pegliasco, C., Chaigneau, A., & Morrow, R. (2015, 9). Main eddy vertical structures observed in the four major Eastern Boundary Upwelling Systems. *Journal of Geophysical Research: Oceans*, *120*(9), 6008–6033. doi: 10.1002/2015JC010950

Pelland, N. A., Eriksen, C. C., & Lee, C. M. (2013). Subthermocline Eddies over the Washington Continental Slope as Observed by Seagliders, 2003–09. *Journal of Physical Oceanography*. doi: 10.1175/JPO-D-12-086.1

Peng, X., Fuchsman, C. A., Jayakumar, A., Warner, M. J., Devol, A. H., & Ward, B. B. (2016). Journal of Geophysical Research : Oceans Revisiting nitrification in the Eastern Tropical South Pacific : A focus on controls. *Journal of Geophysical Research: Oceans*, *121*(3), 1667–1684. doi: 10.1002/2015JC011455.Received

Penn, J., Weber, T., & Deutsch, C. (2016, 9). Microbial functional diversity alters the structure and sensitivity of oxygen deficient zones. *Geophysical Research Letters*, *43*(18), 9773–9780. doi: 10.1002/2016GL070438

Penn, J. L., Weber, T., Chang, B. X., & Deutsch, C. (2019, 4). Microbial ecosystem dynamics drive fluctuating nitrogen loss in marine anoxic zones. *Proceedings of the National Academy of Sciences*, *116*(15), 7220–7225. doi: 10.1073/pnas.1818014116

Pennington, J. T., Mahoney, K. L., Kuwahara, V. S., Kolber, D. D., Calienes, R., & Chavez, F. P. (2006, 5). Primary production in the eastern tropical Pacific: A review. *Progress in Oceanography*, *69*(2-4), 285–317. doi: 10.1016/j.pocean.2006.03.012

Prend, C. J., Flierl, G. R., Smith, K. M., & Kaminski, A. K. (2021, 11). Parameterizing Eddy Transport of Biogeochemical Tracers. *Geophysical Research Letters*, *48*(21). doi: 10.1029/2021GL094405

Radko, T., & Sisti, C. (2017). Life and demise of intrathermocline mesoscale vortices. *Journal of Physical Oceanography*, *47*(12), 3087–3103. doi: 10.1175/JPO-D-17-0044.1

Ravishankara, A. R., Daniel, J. S., & Portmann, R. W. (2009, 10). Nitrous Oxide (N2O): The Dominant Ozone-Depleting Substance Emitted in the 21st Century. *Science*, *326*(5949), 123–125. doi: 10.1126/science.1176985

Redfield, A. C., Ketchum, B. H., & Richards, F. A. (1963). The influence of organisms on the composition of sea-water..

Richardson, P., Bower, A., & Zenk, W. (2000, 2). A census of Meddies tracked by floats. *Progress in Oceanography*, *45*(2), 209–250. doi: 10.1016/S0079-6611(99)00053-1

Risien, C. M., & Chelton, D. B. (2008). A global climatology of surface wind and wind stress fields from eight years of QuikSCAT scatterometer data. *Journal of Physical Oceanography*, *38*(11), 2379–2413. doi: 10.1175/2008JPO3881.1

Roemmich, D., & Gilson, J. (2009). The 2004-2008 mean and annual cycle of temperature, salinity, and steric height in the global ocean from the Argo Program. *Progress in Oceanography*. doi: 10.1016/j.pocean.2009.03.004

Rovinsky, A. B., Adiwidjaja, H., Yakhnin, V. Z., & Menzinger, M. (1997, 2). Patchiness and Enhancement of Productivity in Plankton Ecosystems due to the Differential Advection of Predator and Prey. *Oikos*, *78*(1), 101. doi: 10.2307/3545805

Rykaczewski, R. R., & Dunne, J. P. (2010, 11). Enhanced nutrient supply to the California Current Ecosystem with global warming and increased stratification in an earth system model. *Geophysical Research Letters*, *37*(21), n/a-n/a. doi: 10.1029/2010GL045019

Sallée, J.-B., Speer, K., Rintoul, S., & Wijffels, S. (2010, 3). Southern Ocean Thermocline Ventilation. *Journal of Physical Oceanography*, *40*(3), 509–529. doi: 10.1175/2009JPO4291.1

Santoro, A. E., Buchwald, C., Knapp, A. N., Berelson, W. M., Capone, D. G., & Casciotti, K. L. (2021, 2). Nitrification and Nitrous Oxide Production in the Offshore Waters of the Eastern Tropical South Pacific. *Global Biogeochemical Cycles*, *35*(2), 1–35. doi: 10.1029/2020GB006716

Santoro, A. E., Buchwald, C., McIlvin, M. R., & Casciotti, K. L. (2011, 9). Isotopic Signature of N2O Produced by Marine Ammonia-Oxidizing Archaea. *Science*, *333*(6047), 1282–1285. doi: 10.1126/science.1208239

Sarmiento, J. L., Slater, R. D., Fasham, M. J. R., Ducklow, H. W., Toggweiler, J. R., & Evans, G. T. (1993, 6). A seasonal three-dimensional ecosystem model of nitrogen cycling in the North Atlantic Euphotic Zone. *Global Biogeochemical Cycles*, *7*(2), 417–450. doi: 10.1029/93GB00375

Schmidtko, S., Stramma, L., & Visbeck, M. (2017, 2). Decline in global oceanic oxygen content during the past five decades. *Nature*, *542*(7641), 335–339. doi: 10.1038/nature21399

Schneider, W., Fuenzalida, R., Rodríguez-Rubio, E., Garcés-Vargas, J., & Bravo, L. (2003). Characteristics and formation of Eastern South Pacific Intermediate Water. *Geophysical Research Letters*, *30*(11), 1–4. doi: 10.1029/2003GL017086

Schütte, F., Brandt, P., & Karstensen, J. (2016). Occurrence and characteristics of mesoscale eddies in the tropical northeastern Atlantic Ocean. *Ocean Science*, *12*(3), 663–685. doi: 10.5194/os-12-663-2016

Séférian, R., Berthet, S., Yool, A., Palmiéri, J., Bopp, L., Tagliabue, A., ... Yamamoto, A. (2020, 9). Tracking Improvement in Simulated Marine Biogeochemistry Between CMIP5 and CMIP6. *Current Climate Change Reports*, *6*(3), 95–119. doi: 10.1007/s40641-020-00160-0

Shapiro, G., & Meschanov, S. (1991, 1). Distribution and spreading of Red Sea Water and salt lens formation in the northwest Indian Ocean. *Deep Sea Research Part A. Oceanographic Research Papers*, *38*(1), 21–34. doi: 10.1016/0198-0149(91)90052-H

Shchepetkin, A. F. (2015). An adaptive, Courant-number-dependent implicit scheme for vertical advection in oceanic modeling. *Ocean Modelling*, *91*, 38–69.

Shchepetkin, A. F., & McWilliams, J. C. (2005, 1). The regional oceanic modeling system (ROMS): a split-explicit, free-surface, topography-following-coordinate oceanic model. *Ocean Modelling*, *9*(4), 347–404. doi: 10.1016/J.OCEMOD.2004.08.002

Shi, F., Luo, Y., & Xu, L. (2018). Volume and Transport of Eddy-Trapped Mode Water South of the Kuroshio Extension. *Journal of Geophysical Research: Oceans*, *123*(12), 8749–8761. doi: 10.1029/2018JC014176

Siegfried, L., Schmidt, M., Mohrholz, V., Pogrzeba, H., Nardini, P., Böttinger, M., & Scheuermann, G. (2019, 1). The tropical-subtropical coupling in the Southeast Atlantic from the perspective of the northern Benguela upwelling system. *PLOS ONE*, *14*(1), e0210083. doi: 10.1371/journal.pone.0210083

Silsbe, G. M., Behrenfeld, M. J., Halsey, K. H., Milligan, A. J., & Westberry, T. K. (2016, 12). The CAFE model: A net production model for global ocean phytoplankton. *Global Biogeochemical Cycles*, *30*(12), 1756–1777. doi: 10.1002/2016GB005521

Simmons, A., Uppala, S., Dee, D., & Kobayashi, S. (2006). ERA-Interim: New ECMWF reanalysis products from 1989 onwards. *ECMWF Newsletter No. 110*, 25–35.

Simpson, J., Dickey, T., & Koblinsky, C. (1984, 1). An offshore eddy in the California current system Part I: Interior dynamics. *Progress in Oceanography*, *13*(1), 5–49. doi: 10.1016/0079-6611(84)90004-1

Simpson, J. J., & Lynn, R. J. (1990). A mesoscale eddy dipole in the offshore California Current. *Journal of Geophysical Research*, *95*(C8), 13009. doi: 10.1029/JC095iC08p13009

Southwick, O. R., Johnson, E. R., & McDonald, N. R. (2016). A simple model for sheddies: Ocean eddies formed from shed vorticity. *Journal of Physical Oceanography*, *46*(10), 2961–2979. doi: 10.1175/JPO-D-15-0251.1

Spall, M. A. (1995). Frontogenesis, subduction, and cross-front exchange at upper ocean fronts. *Journal of Geophysical Research*, *100*(C2), 2543–2557. doi: 10.1029/94JC02860

Stein, L. Y., & Yung, Y. L. (2003, 5). Production, Isotopic Composition, and Atmospheric Fate of Biologically Produced Nitrous Oxide. *Annual Review of Earth and Planetary Sciences*, *31*(1), 329–356. doi: 10.1146/annurev.earth.31.110502.080901

Steinberg, J. M., Pelland, N. A., & Eriksen, C. C. (2018). Observed Evolution of a California Undercurrent Eddy. *Journal of Physical Oceanography*, *49*(3), 649–674. doi: 10.1175/jpo-d-18-0033.1

Stewart, R. W. (1982). Evolution of Physical Oceanography: Scientific Surveys in Honor of Henry Stommel. *Eos, Transactions American Geophysical Union*, *63*(19), 499. doi: 10.1029/EO063i019p00499-02

Stieglmeier, M., Mooshammer, M., Kitzler, B., Wanek, W., Zechmeister-Boltenstern, S., Richter, A., & Schleper, C. (2014). Aerobic nitrous oxide production through N-nitrosating hybrid formation in ammonia-oxidizing archaea. *ISME Journal*, *8*(5), 1135–1146. doi: 10.1038/ismej.2013.220

Stock, C. A., Dunne, J. P., Fan, S., Ginoux, P., John, J., Krasting, J. P., ... Zadeh, N. (2020, 10). Ocean Biogeochemistry in GFDL's Earth System Model 4.1 and Its Response to Increasing Atmospheric CO ¡sub¿2¡/sub¿. *Journal of Advances in Modeling Earth Systems*, *12*(10). doi: 10.1029/2019MS002043

Stramma, L., Bange, H. W., Czeschel, R., Lorenzo, A., & Frank, M. (2013, 11). On the role of mesoscale eddies for the biological productivity and biogeochemistry in the eastern tropical Pacific Ocean off Peru. *Biogeosciences*, *10*(11), 7293–7306. doi: 10.5194/bg-10-7293-2013

Stramma, L., Johnson, G. C., Firing, E., & Schmidtko, S. (2010, 9). Eastern Pacific oxygen minimum zones: Supply paths and multidecadal changes. *Journal of Geophysical Research*, *115*(C9), C09011. doi: 10.1029/2009JC005976

Stramma, L., Johnson, G. C., Sprintall, J., & Mohrholz, V. (2008, 5). Expanding Oxygen-Minimum Zones in the Tropical Oceans. *Science*, *320*(5876), 655–658. doi: 10.1126/science.1153847

Sun, X., Frey, C., Garcia-Robledo, E., Jayakumar, A., & Ward, B. B. (2021, 5). Microbial niche differentiation explains nitrite oxidation in marine oxygen minimum zones. *The ISME Journal*, *15*(5), 1317–1329. doi: 10.1038/s41396-020-00852-3

Suntharalingam, P., Sarmiento, J. L., & Toggweiler, J. R. (2000). Global significance of nitrous-oxide production and transport from oceanic low-oxygen zones: A modeling study. *Global Biogeochemical Cycles*, *14*(4), 1353–1370. doi: 10.1029/1999GB900100

Szuts, Z. B., Blundell, J. R., Chidichimo, M. P., & Marotzke, J. (2012). A vertical-mode decomposition to investigate low-frequency internal motion across the Atlantic at 26 N. *Ocean Science*, *8*(3), 345–367. doi: 10.5194/os-8-345-2012

Talley, L. D., Pickard, G. L., Emery, W. J., & Swift, J. H. (2011). *Descriptive Physical Oceanography* (6th ed.). Elsevier. doi: 10.1016/C2009-0-24322-4

Thamdrup, B., Dalsgaard, T., & Revsbech, N. P. (2012, 7). Widespread functional anoxia in the oxygen minimum zone of the Eastern South Pacific. *Deep Sea Research Part I: Oceanographic Research Papers*, *65*, 36–45. doi: 10.1016/J.DSR.2012.03.001

Thomas, A. C., Brickley, P., & Weatherbee, R. (2009, 12). Interannual variability in chlorophyll concentrations in the Humboldt and California Current Systems. *Progress in Oceanography*, *83*(1-4), 386–392. doi: 10.1016/j.pocean.2009.07.020

Thomas, L. N. (2008). Formation of intrathermocline eddies at ocean fronts by wind-driven destruction of potential vorticity. *Dynamics of Atmospheres and Oceans*, *45*(3-4), 252–273. doi: 10.1016/j.dynatmoce.2008.02.002

Thomsen, S., Kanzow, T., Krahmann, G., Greatbatch, R. J., Dengler, M., & Lavik, G. (2016, 1). The formation of a subsurface anticyclonic eddy in the Peru-Chile Undercurrent and its impact on the near-coastal salinity, oxygen, and nutrient distributions. *Journal of Geophysical Research: Oceans*, *121*(1), 476–501. doi: 10.1002/2015JC010878

Thomsen, S., Karstensen, J., Kiko, R., Krahmann, G., Dengler, M., & Engel, A. (2019, 3). Remote and local drivers of oxygen and nitrate variability in the shallow oxygen minimum zone off Mauritania in June 2014. *Biogeosciences*, *16*(5), 979–998. doi: 10.5194/bg-16-979-2019

Thomson, R. E., & Krassovski, M. V. (2010, 9). Poleward reach of the California Undercurrent extension. *Journal of Geophysical Research*, *115*(C9), C09027. doi: 10.1029/2010JC006280

Tian, H., Xu, R., Canadell, J. G., Thompson, R. L., Winiwarter, W., Suntharalingam, P., ... Yao, Y. (2020). A comprehensive quantification of global nitrous oxide sources and sinks. *Nature*, *586*(October). doi: 10.1038/s41586-020-2780-0

Trimmer, M., Chronopoulou, P.-M., Maanoja, S. T., Upstill-Goddard, R. C., Kitidis, V., & Purdy, K. J. (2016, 12). Nitrous oxide as a function of oxygen and archaeal gene abundance in the North Pacific. *Nature Communications*, *7*(1), 13451. doi: 10.1038/ncomms13451

Tukey, J. W. (1977). *Exploratory Data Analysis*. Addison-Wesley.

Tyrrell, T. (1999, 8). The relative influences of nitrogen and phosphorus on oceanic primary production. *Nature*, *400*(6744), 525–531. doi: 10.1038/22941

Vic, C., Roullet, G., Capet, X., Carton, X., Molemaker, M. J., & Gula, J. (2015, 10). Eddy-topography interactions and the fate of the Persian Gulf Outflow. *Journal of Geophysical Research: Oceans*, *120*(10), 6700–6717. doi: 10.1002/2015JC011033

Voss, M., Bange, H. W., Dippner, J. W., Middelburg, J. J., Montoya, J. P., & Ward, B. (2013, 7). The marine nitrogen cycle: recent discoveries, uncertainties and the potential relevance of climate change. *Philosophical Transactions of the Royal Society B: Biological Sciences*, *368*(1621), 20130121. doi: 10.1098/rstb.2013.0121

Wallhead, P. J., Garçon, V. C., & Martin, A. P. (2013, 3). Efficient upscaling of ocean biogeochemistry. *Ocean Modelling*, *63*, 40–55. doi: 10.1016/j.ocemod.2012.12.002

Walter, S., Bange, H. W., Breitenbach, U., & Wallace, D. W. R. (2006, 12). Nitrous oxide in the North Atlantic Ocean. *Biogeosciences*, *3*(4), 607–619. doi: 10.5194/bg-3-607-2006

Wang, W.-L., Moore, J. K., Martiny, A. C., & Primeau, F. W. (2019, 2). Convergent estimates of marine nitrogen fixation. *Nature*, *566*(7743), 205–211. doi: 10.1038/s41586-019-0911-2

Wanninkhof, R. (1992). Relationship between wind speed and gas exchange over the ocean. *Journal of Geophysical Research*, *97*(C5), 7373–7382. doi: 10.1029/92JC00188

Ward, B., & Zafiriou, O. (1988, 7). Nitrification and nitric oxide in the oxygen minimum of the eastern tropical North Pacific. *Deep Sea Research Part A. Oceanographic Research Papers*, *35*(7), 1127–1142. doi: 10.1016/0198-0149(88)90005-2

Ward, B. B., Devol, A. H., Rich, J. J., Chang, B. X., Bulow, S. E., Naik, H., ... Jayakumar, A. (2009). Denitrification as the dominant nitrogen loss process in the Arabian Sea. *Nature*, *461*(7260), 78–81. doi: 10.1038/nature08276

Wrage, N., Velthof, G. L., Van Beusichem, M. L., & Oenema, O. (2001). Role of nitrifier denitrification in the production of nitrous oxide. *Soil Biology and Biochemistry*, *33*(12-13), 1723–1732. doi: 10.1016/S0038-0717(01)00096-7

Wunsch, C. (1997). The Vertical Partition of Oceanic Horizontal Kinetic Energy. *Journal of Physical Oceanography*. doi: 10.1175/1520-0485(1997)027⟨1770:TVPOOH⟩2.0.CO;2

Wyrtki, K. (1962, 1). The oxygen minima in relation to ocean circulation. *Deep Sea Research and Oceanographic Abstracts*, *9*(1-2), 11–23. doi: 10.1016/0011-7471(62)90243-7

Xu, L., Li, P., Xie, S.-P., Liu, Q., Liu, C., & Gao, W. (2016, 12). Observing mesoscale eddy effects on mode-water subduction and transport in the North Pacific. *Nature Communications*, *7*(1), 10505. doi: 10.1038/ncomms10505

Yang, S., Chang, B. X., Warner, M. J., Weber, T. S., Bourbonnais, A. M., Santoro, A. E., ... Bianchi, D. (2020). Global reconstruction reduces the uncertainty of oceanic nitrous oxide emissions and reveals a vigorous seasonal cycle. *Proceedings of the National Academy of Sciences of the United States of America*, *117*(22). doi: 10.1073/pnas.1921914117

Yang, S., Gruber, N., Long, M. C., & Vogt, M. (2017, 10). ENSO-Driven Variability of Denitrification and Suboxia in the Eastern Tropical Pacific Ocean. *Global Biogeochemical Cycles*, *31*(10), 1470–1487. doi: 10.1002/2016GB005596

Yoshida, N., Morimoto, H., Hirano, M., Koike, I., Matsuo, S., Wada, E., ... Hattori, A. (1989, 12). Nitrification rates and 15N abundances of N2O and NO3 in the western North Pacific. *Nature*, *342*(6252), 895–897. doi: 10.1038/342895a0

Zakem, E. J., Al-Haj, A., Church, M. J., Van Dijken, G. L., Dutkiewicz, S., Foster, S. Q., ... Follows, M. J. (2018). Ecological control of nitrite in the upper ocean. *Nature Communications*, *9*(1). doi: 10.1038/s41467-018-03553-w

Zakem, E. J., Polz, M. F., & Follows, M. J. (2020, 11). Redox-informed models of global biogeochemical cycles. *Nature Communications*, *11*(1), 5680. doi: 10.1038/s41467-020-19454-w

Zehr, J. P., & Ward, B. B. (2002, 3). Nitrogen Cycling in the Ocean: New Perspectives on Processes and Paradigms. *Applied and Environmental Microbiology*, *68*(3), 1015–1024. doi: 10.1128/AEM.68.3.1015-1024.2002

Zhang, X., Zhang, Z., McWilliams, J. C., Sun, Z., Zhao, W., & Tian, J. (2022, 2). Submesoscale Coherent Vortices Observed in the Northeastern South China Sea. *Journal of Geophysical Research: Oceans*, *127*(2). doi: 10.1029/2021JC018117

Zhang, Z., Li, P., Xu, L., Li, C., Zhao, W., Tian, J., & Qu, T. (2015, 8). Subthermocline eddies observed by rapid-sampling Argo floats in the subtropical northwestern Pacific Ocean in Spring 2014. *Geophysical Research Letters*, *42*(15), 6438–6445. doi: 10.1002/2015GL064601

Zhang, Z., Zhang, Y., & Wang, W. (2017). Three-compartment structure of subsurface-intensified mesoscale eddies in the ocean. *Journal of Geophysical Research: Oceans*. doi: 10.1002/2016JC012376

Zhao, M., Timmermans, M. L., Krishfield, R., & Manucharyan, G. (2018). Partitioning of Kinetic Energy in the Arctic Ocean's Beaufort Gyre. *Journal of Geophysical Research: Oceans*. doi: 10.1029/2018JC014037